



Characterization of the Hydrogen-Dry-Low-NO_x-Micromix-Combustion Principle for Hydrogen-Methane Fuel Mixtures

A thesis submitted in fulfillment of the requirements for the degree of Doctor of Philosophy

Nils Beckmann

Master of Science, FH Aachen University of Applied Sciences
Bachelor of Engineering, FH Aachen University of Applied Sciences

School of Engineering
College of Science, Engineering and Health
RMIT University

August 2019

Declaration

I certify that except where due acknowledgment has been made, the work is that of the author alone; the work has not been submitted previously, in whole or in part, to qualify for any other academic award; the content of the thesis is the result of work which has been carried out since the official commencement date of the approved research program; and, any editorial work, paid or unpaid, carried out by a third party is acknowledged; and, ethics procedures and guidelines have been followed.

Nils Beckmann

10th August 2019

Acknowledgments

First and foremost, I would like to express my deep gratitude to my supervisor Prof. Dr.-Ing. Harald H.-W. Funke for his constant professional support throughout the course of my under- and postgraduate studies. With his trust in my abilities, he offered me this postgraduate research project in the framework of gas turbine combustor research, an area that was somewhat new to me in the beginning. His friendly guidance throughout the last years helped me many times to overcome obstacles along the way and let me evolve on a professional and personal level.

I thank my supervisor Professor Sylvester Abanteriba for accepting me as a candidate in the joint Ph.D. program between RMIT University and Aachen University of Applied Sciences. With the offshore Ph.D. candidature, I not only experienced the many benefits of an international Ph.D. program on a professional side but also found my affection for traveling and exploring the world.

Last but not least, my biggest thank-you goes out to my family and friends. Without their affection and friendship for all those years, which grounded me during hard times, I would not be who and where I am now. Thank you!

Publications

Portions of the material in this thesis have previously appeared in the following publications:

Journal Publications:

- [1] H. H. W. Funke, N. Beckmann, J. Keinz, and S. Abanteriba, “Comparison of Numerical Combustion Models for Hydrogen and Hydrogen-Rich Syngas Applied for Dry-Low-NO_x-Micromix-Combustion,” *J. Eng. Gas Turbines Power*, vol. 140, no. 8, 2018.
- [2] H.H.-W. Funke, N. Beckmann, and S. Abanteriba, “An overview on dry low NO_x Micromix combustor development for hydrogen-rich gas turbine applications,” *International Journal of Hydrogen Energy*, vol. 44, no. 13, pp. 6978–6990, 2019.
- [3] H. H. W. Funke, N. Beckmann, J. Keinz, and S. Abanteriba, “Numerical and Experimental Evaluation of a Dual-Fuel Dry-Low-NO_x Micromix Combustor for Industrial Gas Turbine Applications,” *J. Thermal Sci. Eng. Appl*, vol. 11, no. 1, 2019.

Conference Proceedings:

- [4] H. H.-W. Funke, N. Beckmann, J. Keinz, and S. Abanteriba, “Comparison of Numerical Combustion Models for Hydrogen and Hydrogen-rich Syngas Applied for Dry-Low-NO_x-Micromix-Combustion,” in *Proceedings of the ASME Turbo Expo 2016*, ASME International Gas Turbine Institute, Ed., New York, N.Y.: ASME, 2016.
- [5] H. H.-W. Funke, N. Beckmann, and S. Abanteriba, “A Comparison of Complex Chemistry Mechanisms for Hydrogen Methane Blends Based on the Sandia / Sydney Bluff-Body Flame HM1,” *The University of Sydney, NSW Australia, 11th Asia-Pacific Conference on Combustion*, Dec. 2017.
- [6] H. H.-W. Funke, N. Beckmann, J. Keinz, S. Abanteriba, “Numerical and Experimental Evaluation of a Dual-Fuel Dry-Low-NO_x Micromix Combustor for Industrial Gas Turbine Applications,” in *Proceedings of the ASME Turbo Expo 2017*, ASME International Gas Turbine Institute, Ed., New York, N.Y.: ASME, 2017.
- [7] H. H.-W. Funke, N. Beckmann, S. Abanteriba, “Development and Testing of a FuelFlex Dry-Low-NO_x Micromix Combustor for Industrial Gas Turbine Applications with Variable Hydrogen Methane Mixtures: GT2019-90095,” in *Proceedings of the ASME Turbo Expo 2019*, ASME International Gas Turbine Institute, Ed., New York, N.Y.: ASME, 2019.

Contents

Declaration.....	I
Acknowledgments.....	II
Publications.....	III
List of Figures.....	VII
List of Tables	XII
Nomenclature	XIII
Abstract	1
1 Introduction	2
1.1 The Anthropogenic Greenhouse Effect	2
1.2 Climate Change Mitigation Options	4
1.3 Nitrogen Oxide (NO _x) Emissions.....	6
1.4 The Dry-Low-NO _x Micromix Combustion Principle	7
1.5 Aim & Structure of the Thesis.....	10
2 Low Emission Combustor Research.....	13
2.1 The Challenge of Energy Transition to Renewable Sources.....	13
2.2 Emission Reduction Concepts	16
2.2.1 Catalytic Combustion.....	16
2.2.2 Premixed Combustion.....	17
2.2.3 Diffusion Combustion.....	20
2.2.4 MILD/FLOX Combustion	21
2.2.5 Micromix Combustion.....	22
3 Experimental and Numerical Methods.....	24
3.1 Experimental Setup.....	25
3.1.1 Combustion Chamber Test Stand.....	25
3.1.2 Exhaust Gas Measurement	31

3.2	Numerical Setup	36
3.2.1	Geometric Model	36
3.2.2	Reaction Kinetic Fundamentals	39
3.2.3	Modeling the Reactive Flow Regime	41
3.2.4	Choice of a Suitable Combustion Mechanism for H ₂ /CH ₄ Combustion	45
3.2.5	NO _x Emission Modeling	53
4	Micromix Combustion Principle Designed for H ₂ /CH ₄ Fuel Mixtures	56
4.1	Fuel Characteristics of H ₂ /CH ₄ mixtures	56
4.1.1	Density	57
4.1.2	Lower Heating Value and Stoichiometric Air Requirement	57
4.1.3	Wobbe Index	59
4.2	Baseline Design: 1 st Generation FuelFlex Combustor V1	61
4.2.1	Boundary Conditions	61
4.2.2	Scaling of the Air-Fuel-Equivalence Ratio	63
4.2.3	Definition of the Design Momentum Flux Ratio	64
4.2.4	Aerodynamic Flame Stabilization	67
4.2.5	Combustor Design Process	68
5	Combustion Characteristics of the DLN Micromix Combustion Principle for Variable H ₂ /CH ₄ Fuel Mixtures	70
5.1	Characterization of FuelFlex Combustion with Baseline Geometry V1	73
5.1.1	Visual Flame Appearance	73
5.1.2	Combustion Efficiency	76
5.1.3	Nitrogen Oxide Emissions	82
5.1.4	Conclusion	89
5.2	Optimization of Micromix FuelFlex Combustion	91
5.2.1	Air Gate Velocity Variation	94
5.2.1.1	Nitrogen Oxide Emissions	94
5.2.1.2	Combustion Efficiency	99

5.2.1.3	Influence of the Momentum Flux Ratio J	102
5.2.1.4	Conclusion.....	105
5.2.2	Air Gate Height Variation.....	106
5.2.2.1	Combustion Efficiency.....	106
5.2.2.2	Nitrogen Oxide Emissions.....	107
5.2.2.3	Influence of the Air Gate Height.....	109
5.2.2.4	Conclusion.....	110
5.2.3	Pressure Loss Optimization - V1.1.....	112
5.2.3.1	Pressure Loss.....	112
5.2.3.2	Nitrogen Oxide Emissions.....	112
5.2.3.3	Combustion Efficiency.....	116
5.2.3.4	Conclusion.....	117
6	Conclusion & Outlook.....	119
7	References.....	122
8	Appendix.....	134
8.1	Supplemental Diagrams: NO _x Emissions.....	135
8.2	Supplemental Diagrams: CO Emissions.....	139
8.3	Supplemental Diagrams: CH ₄ Emissions.....	143
8.4	Supplemental Diagrams: H ₂ Emissions.....	147
8.5	Supplemental Diagrams: Combustion Efficiency.....	151
8.6	Flame Images.....	155

List of Figures

Figure 1-1: Development of the world energy consumption [5].....	3
Figure 1-2: Total annual anthropogenic greenhouse gas (GHG) emissions (gigatons of CO ₂ -equivalent per year,) for the period 1970 to 2010 (a) and total anthropogenic greenhouse gas emissions from economic sectors in 2010 (b) [6].....	3
Figure 1-3: Hydrogen production by electrolysis (top) and methanation process (bottom) [23].....	5
Figure 1-4: Relative CO ₂ emissions of H ₂ /CH ₄ fuel mixtures at const. thermal power output.....	6
Figure 1-5: Characteristic flow structure of Jet in Crossflow mixing [43]	8
Figure 1-6: Structural layout (left) and section view of a Micromix combustor (right)	9
Figure 1-7: Schematics of the Micromix combustor geometry, detailing the recirculation zones and aerodynamic flame stabilization	10
Figure 1-8: NO _x emissions of different combustor technologies and fuel types.....	10
Figure 2-1: Electrical storage technologies [51]	14
Figure 2-2: Power-to-gas concept [52]	14
Figure 2-3: GT8 DLN EV multi-burner arrangement [70].....	18
Figure 2-4: Multitube mixer for hydrogen-rich fuels [81]	18
Figure 2-5: Schematic view of the multi-cluster combustor [84]	19
Figure 2-6: Siemens DLE combustion system [86].....	20
Figure 3-1: Interactive research and optimization cycle	24
Figure 3-2: Schematics of the atmospheric test rig.....	25
Figure 3-3: Schematics of the H ₂ /CH ₄ gas mixing facility	26
Figure 3-4: Relative error (dots) between Bronkhorst F-203AV and MicroMotion CMF010 mass flow measurement. Guaranteed error margins indicated as solid lines	27
Figure 3-5: Sectional view of the static mixer showing the interior flow guiding structures	28
Figure 3-6: H ₂ /CH ₄ mixing process in the static mixer illustrated by the velocity field (top) and the molar fraction of H ₂ (bottom).....	28
Figure 3-7: Simulated avg. mixture fraction of H ₂ (bar graph), absolute error of mixture composition (dots) and mixture inhomogeneity (error bars) at mixer outlet for combustor part-load and overload conditions.....	29
Figure 3-8: Combustor equivalence ratio (dots) and power-normalized equivalence ratio (dashed lines) for fuel mixture compositions in the area of interest	30

Figure 3-9: Sketch of a DLN Micromix test-burner, detailing the applied coordinate system and measurement grid	31
Figure 3-10: Relative local deviation from the measured mean NO _x emission level for different combustor equivalence ratios, obtained at a probing location of z = 130 mm	32
Figure 3-11: Exhaust gas measurements of O ₂ (a), CO (b), H ₂ (c) and NO _x corrected to 15 vol.% O ₂ (d) obtained during 3 individual test under constant combustor operating conditions	35
Figure 3-12: Computational domain and coordinate system of the developed slice model	36
Figure 3-13: Visualization of mesh densities for the solution adaptive mesh	37
Figure 3-14: Mesh of solid combustor walls with mass and heat flows	38
Figure 3-15: y+ values on burner walls at the air gate and the fuel inlet	39
Figure 3-16: Energy diagram for a chemical reaction [32]	41
Figure 3-17: Schematics of the Sydney bluff-body burner [118]	46
Figure 3-18: Axial velocity distribution at x=0.065 m simulated with variable C _{1ε} constants	47
Figure 3-19: 2D axisymmetric computational domain and simulation grid	48
Figure 3-20: Relative error of several combustion parameters with respect to the finest mesh	48
Figure 3-21: Simulated temperature distribution (left) and simulated and measured axial temperature profile (right)	49
Figure 3-22: Measured and simulated radial species profiles of O ₂ (a), H ₂ O (b), H ₂ (c), CH ₄ (d), CO ₂ (e), CO (f), OH (g) and NO (h) at the sampling location x=0.013m	50
Figure 3-23: Relative error of cumulated species mass flows m(i) with reference to GRI 3.0 (5) at the domain outlet	52
Figure 3-24: Relative computation time per time step for different reaction mechanisms with reference to GRI 3.0 (5)	52
Figure 4-1: Fuel density for H ₂ /CH ₄ mixtures at T = 298.15 K and p = 1.01325 bar	57
Figure 4-2: Lower heating value and stoichiometric air requirement for H ₂ /CH ₄ mixtures	59
Figure 4-3: Wobbe index for H ₂ /CH ₄ mixtures	59
Figure 4-4: Auxiliary Power Unit – Honeywell Garrett GTCP 36-300	61
Figure 4-5: Design equivalence ratios for MES operation corresponding to Φ _n =0.375	63
Figure 4-6: Schematics of the MMX combustor geometry, detailing JICF mixing	65
Figure 4-7: Relative momentum flux ratio with respect to r(H ₂) = 1	66
Figure 4-8: Recirculation areas at sudden geometry changes [78]	67
Figure 4-9: Flame anchoring characteristics and definition of recirculation zones	67
Figure 4-10: Micromix combustor design process	69
Figure 5-1: Micromix FuelFlex optimization process	71

Figure 5-2: Experimental test schedule.....	72
Figure 5-3: Idealized Micromix flames (a); Flame images at $\Phi_n=0.25$ with $r_{H_2}=1.0, 0.9$ & 0.8 (b).....	73
Figure 5-4: Aerodynamic flame stabilization by counter-rotating vortex pairs.....	74
Figure 5-5: Velocity profile (left) and temperature distribution on a cross-section (right) showing flame separation by cold air penetration.....	74
Figure 5-6: Flame images with variable H_2/CH_4 fuel mixtures for V1	75
Figure 5-7: Experimental results of H_2, CH_4 and CO emissions for variable fuel mixtures.....	77
Figure 5-8: Net molar production rates of $CO, CH_4,$ and CO_2 at $\Phi_n=0.3125$ for $r_{H_2}=0.9$ (a) and $r_{H_2}=0.57$ (b)	79
Figure 5-9: Simulated heat release (left) and temperature (right) on combustor symmetry plane at $\Phi_n=0.375$ for $r_{H_2}=0.9$ and $r_{H_2}=0.57$	80
Figure 5-10: Net CO production rate for 4 operating points with $r_{H_2}=0.57$	81
Figure 5-11: Experimental and simulation results of combustion efficiency for 3 fuel mixtures ..	81
Figure 5-12: Experimental and simulation results of NO/NO_x corrected to 15% O_2 for V1	83
Figure 5-13: Theoretical exhaust gas temperature T_4 for H_2 and CH_4 combustion.....	84
Figure 5-14: Simulated NO mass fraction on the symmetry plane at $\Phi_n=0.375$ for V1	84
Figure 5-15: Simulated temperature (a) and NO distribution (b) at $r_{H_2}=0.9$ for geometry V1.....	86
Figure 5-16: Merged flames anchoring at AGP for $\Phi_n=0.5$ and separated flames at $\Phi_n=0.25$ for geometry V1 and $r_{H_2}=0.9$	87
Figure 5-17: Simulated temperature (a) and NO distribution (b) at $\Phi_n = 0.5$ for geometry V1.....	88
Figure 5-18: Experimental and simulated NO/NO_x emissions at $r_{H_2}=0.9$ for geometry V1	89
Figure 5-19: Design goals in the Micromix optimization process	91
Figure 5-20: NO_x emissions and pressure loss for variable air velocities and $r_{H_2}=0.9$	95
Figure 5-21: Simulated temperature (top) and NO distribution (bottom) on the symmetry plane for V1 and V2 at $r_{H_2}=0.9$	96
Figure 5-22: Formation of hotspots at $\Phi_n=0.375$ and $r_{H_2}=0.9$ for V1 (a) and V2 (b).....	97
Figure 5-23: Velocity profile on symmetry plane and section-wise temperature and vertical velocity distribution for geometry V1 and V2 at $\Phi_n=0.375$ and $r_{H_2}=0.9$	98
Figure 5-24: Experimental and simulation results of H_2, CH_4 and CO emissions for variable fuel mixtures	100
Figure 5-25: Flame images at $r_{H_2}=0.57$ and $\Phi_n = 0.375$ for V1 (a) and V2 (b)	101
Figure 5-26: Experimental results of combustion efficiency for V1 and V2	101
Figure 5-27: Relative momentum flux ratio for variable Φ_n (a) and c_{Air} (b)	103

Figure 5-28: Experimental NO _x results versus \sqrt{J}_{rel} for V1 with varying Φ_n (a) and for V1-V4 at $\Phi_n=0.375$ (b).....	103
Figure 5-29: Experimental NO _x results versus \sqrt{J}_{rel} for V1-V4 for all measured combinations of r_{H_2} and Φ_n	104
Figure 5-30: Experimental results of combustion efficiency for geometry V2 and V2.2.....	107
Figure 5-31: NO _x emissions at full- and overload for V2.1, V2, and V2.2 at $r_{H_2}=0.9$	108
Figure 5-32: Flame images for V2.1 (a), V2 (b), and V2.2 (c) at $r_{H_2}=0.9$ and $\Phi_n=0.5$	108
Figure 5-33: Experimental NO _x results versus \sqrt{J}_{rel} (a) and $\left(\frac{\sqrt{J}}{h_{AGP}}\right)_{rel}$ (b) for V2, V2.1 and V2.2 at varying Φ_n and r_{H_2}	109
Figure 5-34: Experimental results of NO _x corrected to 15% O ₂ for V1 and V1.1	113
Figure 5-35: Flame images for V1 (a) and V1.1 (b) at $\Phi_n = 0.5$ $r_{H_2}=0.9$	113
Figure 5-36: Experimental NO _x results versus $\left(\frac{\sqrt{J}}{h_{AGP}}\right)_{rel}$ for V1 and V1.1 at varying Φ_n and r_{H_2} ..	114
Figure 5-37: Experimental NO _x results versus $\left(\frac{\sqrt{J}}{h_{AGP}}\right)_{rel}$ for all geometries at varying Φ_n and r_{H_2} ..	115
Figure 5-38: Experimental and simulated NO/NO _x emissions for V1 and V1.1 at $r_{H_2}=0.9$	116
Figure 5-39: Experimental results of combustion efficiency for geometry V1 and V1.1.....	116
Figure 8-1: Experimental and simulation results of NO/NO _x corrected to 15% O ₂ for V1	135
Figure 8-2: Experimental and simulation results of NO/NO _x corrected to 15% O ₂ for V2	135
Figure 8-3: Experimental and simulation results of NO/NO _x corrected to 15% O ₂ for V3	136
Figure 8-4: Experimental and simulation results of NO/NO _x corrected to 15% O ₂ for V4	136
Figure 8-5: Experimental and simulation results of NO/NO _x corrected to 15% O ₂ for V2.1	137
Figure 8-6: Experimental and simulation results of NO/NO _x corrected to 15% O ₂ for V2.2	137
Figure 8-7: Experimental and simulation results of NO/NO _x corrected to 15% O ₂ for V1.1	138
Figure 8-8: Experimental and simulation results of mole fraction CO for V1	139
Figure 8-9: Experimental and simulation results of mole fraction CO for V2	139
Figure 8-10: Experimental and simulation results of mole fraction CO for V3	140
Figure 8-11: Experimental and simulation results of mole fraction CO for V4	140
Figure 8-12: Experimental and simulation results of mole fraction CO for V2.1	141
Figure 8-13: Experimental and simulation results of mole fraction CO for V2.2.....	141
Figure 8-14: Experimental and simulation results of mole fraction CO for V1.1	142
Figure 8-15: Experimental and simulation results of mole fraction CH ₄ for V1	143
Figure 8-16: Experimental and simulation results of mole fraction CH ₄ for V2.....	143
Figure 8-17: Experimental and simulation results of mole fraction CH ₄ for V3.....	144

Figure 8-18: Experimental and simulation results of mole fraction CH ₄ for V4.....	144
Figure 8-19: Experimental and simulation results of mole fraction CH ₄ for V2.1.....	145
Figure 8-20: Experimental and simulation results of mole fraction CH ₄ for V2.2.....	145
Figure 8-21: Experimental and simulation results of mole fraction CH ₄ for V1.1.....	146
Figure 8-22: Experimental and simulation results of mole fraction H ₂ for V1.....	147
Figure 8-23: Experimental and simulation results of mole fraction H ₂ for V2.....	147
Figure 8-24: Experimental and simulation results of mole fraction H ₂ for V3.....	148
Figure 8-25: Experimental and simulation results of mole fraction H ₂ for V4.....	148
Figure 8-26: Experimental and simulation results of mole fraction H ₂ for V2.1.....	149
Figure 8-27: Experimental and simulation results of mole fraction H ₂ for V2.2.....	149
Figure 8-28: Experimental and simulation results of mole fraction H ₂ for V1.1.....	150
Figure 8-29: Experimental and simulation results of combustion efficiency η for V1	151
Figure 8-30: Experimental and simulation results of combustion efficiency η for V2.....	151
Figure 8-31: Experimental and simulation results of combustion efficiency η for V3	152
Figure 8-32: Experimental and simulation results of combustion efficiency η for V4.....	152
Figure 8-33: Experimental and simulation results of combustion efficiency η for V2.1	153
Figure 8-34: Experimental and simulation results of combustion efficiency η for V2.2.....	153
Figure 8-35: Experimental and simulation results of combustion efficiency η for V1.1	154
Figure 8-36: Flame images with variable H ₂ /CH ₄ fuel mixtures for V2	155
Figure 8-37: Flame images with variable H ₂ /CH ₄ fuel mixtures for V3	156
Figure 8-38: Flame images with variable H ₂ /CH ₄ fuel mixtures for V4	157
Figure 8-39: Flame images with variable H ₂ /CH ₄ fuel mixtures for V2.1	158
Figure 8-40: Flame images with variable H ₂ /CH ₄ fuel mixtures for V2.2.....	159
Figure 8-41: Flame images with variable H ₂ /CH ₄ fuel mixtures for V1.1	160

List of Tables

Table 1: Temperature development during the expansion of methane (left) and hydrogen (right) under idealized adiabatic conditions. Thermodynamic data obtained from [99]	26
Table 2: Reading (rd) and full scale (f.s.) error sources of gas analysis systems ABB Caldos 27 (H ₂), FID (CH ₄), Magnos 206 (O ₂), URAS (CO/CO ₂) and CLD 700 EL ht. (NO/NO _x) [102, 103]	34
Table 3: Summary of the investigated detailed reaction mechanisms, number of species and reactions	47
Table 4: Arrhenius parameters for the thermal NO reaction mechanism, as described in [108]. Units are m ³ , kmol, s, K	53
Table 5: Summary of general gas composition and properties	60
Table 6: Operational data of the APU Honeywell Garrett GTCP 36-300	62
Table 7: Relative total pressure loss for V1, V1.1, V2, and V2.2 at $\Phi_n = 0.375$ and $r_{H_2} = 0.9$	112
Table 8: Comparison of the combustion characteristics for all tested geometries	118

Nomenclature

Latin Nomenclature

A, A'	Arrhenius parameter
A_{ref}	combustor reference area
b	Arrhenius parameter
c	velocity
$C_{1\epsilon}$	turbulence model coefficient
Da	Damköhler number
d_i	nozzle diameter
E_a	activation energy
g	mass fraction
h	enthalpy
H	humidity
h_{AGP}	air gate height
J	momentum flux ratio
k	reaction rate constant
M	molecular weight
\dot{m}	mass flow
p	pressure
$\Delta p_{\text{t,rel}}$	relative total pressure loss
P	power
PD	power density
\dot{Q}	heat flux
r	volume fraction
R_s	gas constant
T	temperature
t	time
T_3	combustion chamber inlet temperature
T_4	combustion chamber outlet temperature
t_{mix}	mixing time scale
t_{reac}	reaction time scale
u^*	friction velocity
V	volume
$[X]$	molecular concentration of species X
x, y, z	Cartesian coordinates
y	injection depth
y^+	normalized wall distance

Greek Nomenclature

η	combustion efficiency
μ_{JT}	Joule-Thomson coefficient
ν	kinematic viscosity
ρ	density
Φ	equivalence ratio
Φ_n	power normalized equivalence ratio
ψ	mole fraction
ω	production rate

Acronyms

AcUAS	Aachen University of Applied Sciences
AEV	Advanced Environmentally-friendly V-shaped burner
AGP	air guiding panel
APU	Auxiliary Power Unit
CFD	computational fluid dynamics
CH ₄	methane
CO	carbon monoxide
CO ₂	carbon dioxide
div	divergence
DLN	dry low NO _x
DNS	Direct Numerical Simulation
ECS	Environment Control Supply
EV	Environmentally-friendly V-shaped burner
exp.	experiment
f.s.	full scale
FLOX	Flameless Oxidation
FSS	fuel supply segment
GHG	greenhouse gas
Gt	gigaton
H ₂	hydrogen
IGCC	Integrated Gasification Combined Cycle
JICF	jet-in-crossflow
LES	Large Eddy Simulation
LHV	lower heating value
MES	Main Engine Start
MILD	Moderate and Intense Low-oxygen Dilution
MMX	Micromix
MT	multitube
N ₂	nitrogen

NO _x	nitrogen oxides
O ₂	oxygen
ODE	ordinary differential equation
PtG	Power-to-Gas
RANS	Reynolds Averaged Navier-Stokes
rd	reading
SAR	stoichiometric air requirement
sim.	simulation

Indices

0	atmospheric conditions
3	combustion chamber inlet
4	combustion chamber outlet
AGP	air guiding panel
air	air property
APU	Auxiliary Power Unit
b	backward (reaction)
f	forward (reaction)
fuel	fuel property
H ₂ /CH ₄	hydrogen methane fuel mixture property
i, j	indices
JP-1	kerosene
max	maximum
out	outlet
ref	reference
rel	relative
SEG	fuel supply segment
t, tot	total
TB	test burner
therm	thermal

Abstract

With the prospective abatement of fossil energy carriers, gas turbines operated with hydrogen and hydrogen-rich fuel mixtures pave the way for CO₂-free energy production in the future. Low emission gas turbines operated with hydrogen and methane, generated with excess renewable energy by power-to-gas applications, facilitate a direct energy recovery while preserving most of the existing natural gas infrastructure. However, the challenging properties of hydrogen make changes to the gas turbine combustor necessary to enable low emission and flexible-fuel operation. Against this background, the Dry-Low-NO_x-Micromix (MMX) combustion technology has been developed at Aachen University of Applied Sciences (AcUAS) for hydrogen-rich fuels. The diffusion combustion process is based on the phenomenon of jet-in-crossflow-mixing and achieves dry low NO_x emissions by miniaturization of the injection dimensions without dilution. In recent projects at AcUAS, the MMX combustion principle has been optimized for hydrogen and hydrogen-rich syngas (H₂/CO) combustion.

Based on this work, the MMX combustion principle is characterized and optimized for low NO_x combustion with variable fuel mixtures of hydrogen and methane in the framework of this thesis. Hence, a viable bridge technology for near-future hydrogen-enriched methane or natural gas combustion is proposed.

The scientific approach presented in this thesis combines low-pressure combustor testing with numerical analyses carried out with the commercial CFD-code Star-CCM+. Initially, the design process that takes into account the challenging fuel characteristics of variable H₂/CH₄ mixtures is presented. With a first combustor prototype capable of burning a variety of H₂/CH₄ fuel mixtures between 100% hydrogen and 100% methane, a fundamental characterization of the combustion principle under flexible-fuel operation is conducted.

During a subsequent 2-step optimization study the combustion characteristics are successively enhanced, with particular focus on low NO_x emissions at overload conditions and on high combustion efficiencies for methane-rich fuel mixtures and at lean off-design operation. In this process, the dominant influence of the jet-in-crossflow momentum flux ratio as a central design parameter for guaranteeing low NO_x emissions is established. With the final combustor geometry, an optimum concerning fuel flexibility, pressure loss, combustion efficiency, and NO_x emissions is found that generates less than 1.8 ppm NO_x (corrected to 15 vol.% O₂) at the design point with a combustion efficiency exceeding 98% over the entire operating range.

1

Introduction

The demand for mobility and the energy dependence of human life creates a substantial energy requirement which is covered today mostly by fossil fuels. The climatic impact of fossil fuel combustion [1] and the finite and exhaustible quantity of fuel deposits on the planet [2–4] have led many research institutes, universities and the power-producing industry into the development of alternative concepts of sustainable energy generation that also protect the environment.

1.1 The Anthropogenic Greenhouse Effect

In the timeframe from the industrialization in the 18th century until today, human activities, primarily the burning of fossil fuels and clearing of forests, have greatly intensified the natural greenhouse effect. Greenhouse gases (GHG) in the Earth's atmosphere absorb infrared (terrestrial) radiation while shortwave (solar) radiation passes through. The radiation is trapped in the atmosphere that slowly heats up, similar to the effect that can be observed in greenhouses.

The increased concentrations of greenhouse gases in the atmosphere due to anthropogenic action destabilize the climate system. The atmosphere is confronted with a higher amount of energy, which has led to an increase in the average global temperature (approx. 0.85°C in comparison to 1880 [1]). The temperature increase affects the sea level due to the thermal expansion of the oceans and melting of inland ice, rendering coast regions around the world uninhabitable. Further consequences are the acidification of the oceans (absorption of CO₂ reduces the pH-value) and the poleward shift of climate zones with increasing temperature. This has a negative impact on water resources in many regions and leads to altered seasons and large-scaled dying of woods in the middle and higher latitudes. In addition, there is a worsening of the nutrition situation due to crop

failure and augmented crop damage. The anthropogenic climate change is one of the most critical socio-economic problems of our time and a direct consequence of the growing world population and humankind's demand for energy, mobility, and nutrition that relies on intensive mass animal farming.

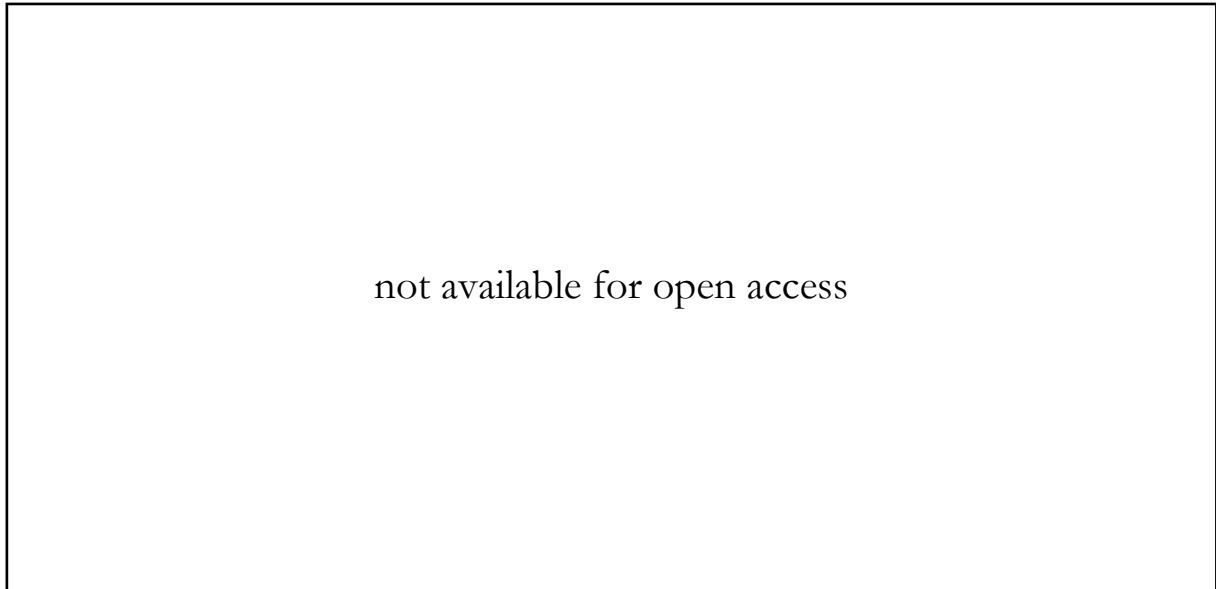


Figure 1-1: Development of the world energy consumption [5]

Along with the world's energy consumption, shown in Figure 1-1, the total annual anthropogenic GHG emissions (presented as gigatons of CO₂ equivalents according to [1]) rise continuously (cf. Figure 1-2 a)). Despite a growing number of climate change mitigation policies, annual GHG emissions grew on average by 1.0 GtCO₂-eq (2.2%) per year, from 2000 to 2010, compared to 0.4 GtCO₂-eq (1.3%) per year, from 1970 to 2000. Total anthropogenic GHG emissions from 2000 to 2010 were the highest in human history and reached 49 GtCO₂-eq/yr in 2010.

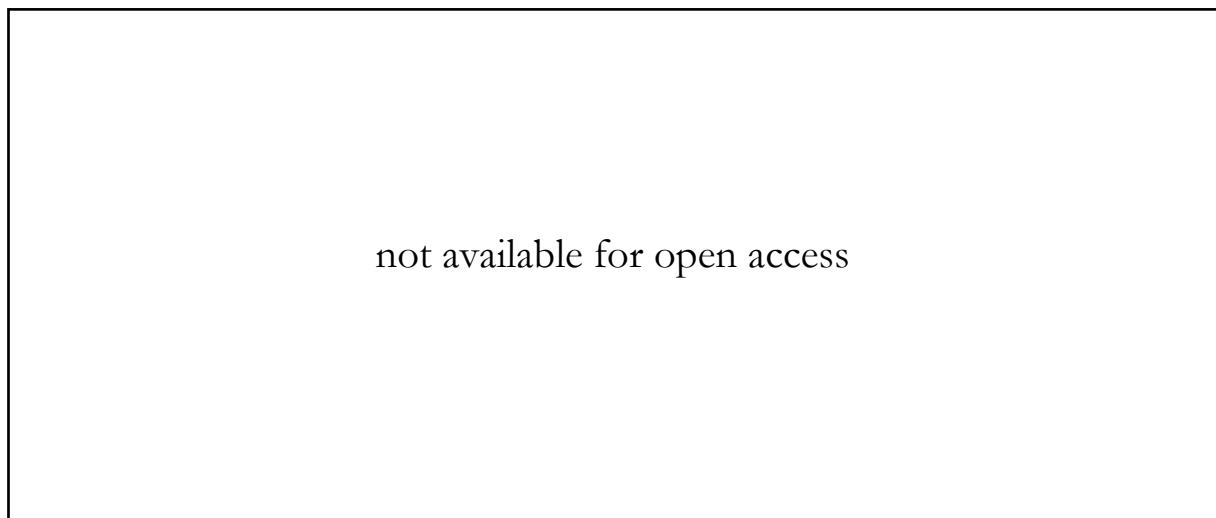


Figure 1-2: Total annual anthropogenic greenhouse gas (GHG) emissions (gigatons of CO₂-equivalent per year,) for the period 1970 to 2010 (a) and total anthropogenic greenhouse gas emissions from economic sectors in 2010 (b) [6]

As Figure 1-2 b) shows, one-third of the overall GHG emissions originate from the production of electricity and heat, another 14% from the transport sector.

CO₂ is the most important anthropogenic GHG and related to fossil fuel combustion and industrial processes. It accounted for 65% of the total anthropogenic GHG emissions in 2010 (cf. Figure 1-2 a)). The climatic impact of CO₂ is global and independent of where the emission occurs. Due to the long residence time of CO₂ in the atmosphere, the current concentration is an accumulation of the emissions from the past 150 years [7]. The climatic impact depends on the concentration and rises proportionally with increasing emissions, as there is only a small saturation effect.

1.2 Climate Change Mitigation Options

Electricity and heat production, along with the transport sector was responsible for 49% of the total annual GHG emissions in 2010 (cf. Figure 1-2 b)). The shift towards renewable energy sources for power production and the use of electricity for transport offers a considerable reduction potential for anthropogenic greenhouse gases.

Power production based on conventional renewable energy sources like solar or wind energy is strongly weather dependent. Thus, the expansion of renewable energy sources requires energy storage technologies for the compensation of the fluctuating and unpredictable energy output of these sources. In times of peak energy production and low demand by the electrical grid, excess renewable energy needs to be transformed into other energy forms and stored, to be retrieved when needed.

Examples of energy storage by conversion of electrical into potential energy are pumped storage hydropower plants. A different concept is the power-to-gas application, which uses excess renewable energy for electrolyzing hydrogen from water or producing methane from hydrogen and carbon dioxide by methanation (cf. Figure 1-3). In contrast to hydrogen produced by steam reforming of natural gas, the currently most efficient and cost-effective production method for hydrogen, green hydrogen or methane produced by excess renewable energy sources is carbon neutral. The synthesized gases are combustible and can be used for reconversion into electrical energy by gas turbines [8–14].

Hydrogen is discussed for decades as a carbon-free energy carrier and offers the potential of reducing greenhouse gas emissions significantly [15–21]. In future power plant development processes and climate change mitigation concepts, hydrogen-fueled gas turbines are regarded as efficient and reliable power systems [22].

For a transition to a reliable, sustainable, ecological, and economic hydrogen-based energy supply,

bridge technologies are needed. Currently, the most commonly employed fuel in gas power plants is natural gas, which, depending on the country of origin, consists of about 80-90% by volume methane (CH_4). The rest consists mostly of longer-chained alkanes like ethane, butane, propane, etc. Methane is a hydrocarbon fuel; thus, its main exhaust gas component is CO_2 . Methane, produced sustainably by methanation or as the product of fermentation processes in biogas facilities, could be directly utilized in low emission combustion engines without increasing its carbon footprint.

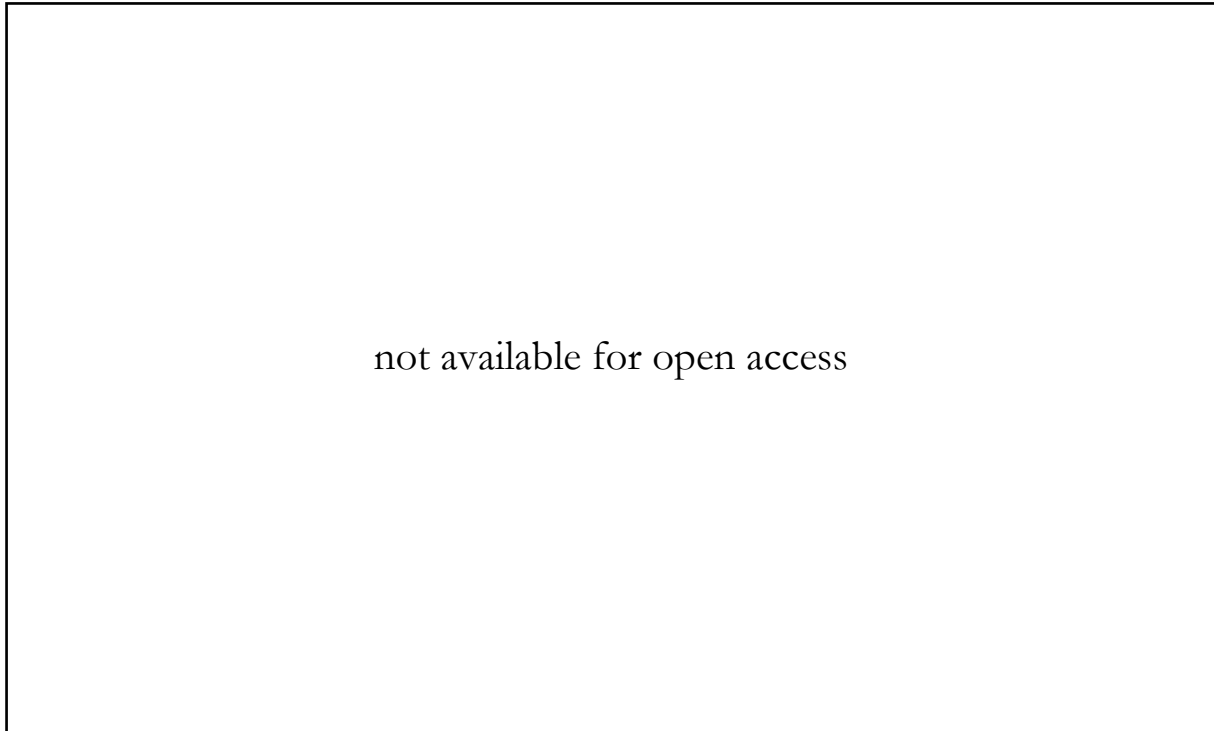


Figure 1-3: Hydrogen production by electrolysis (top) and methanation process (bottom) [23]

From pure natural gas or methane combustion, a gateway to a hydrogen-based power generation is possible by blending increasing amounts of hydrogen into the natural gas grid. A direct feed into the grid and utilization of the hydrogen-natural gas mixture in gas power plants capable of flexible-fuel operation facilitates the direct energy recovery (when H_2 is applied as energy storage) while maintaining most of the existing infrastructure [24].

With an increase of hydrogen in the fuel mixture, the emission of carbon dioxide (CO_2) is reduced (cf. Figure 1-4). The diagram shows the CO_2 reduction potential that high hydrogen combustion offers if the fuel composition of a reference combustor is changed at constant thermal power output. For a reduction of the CO_2 emissions by 50%, the gas turbine fuel must contain approx. 76.5% hydrogen. This underlines that only hydrogen-rich fuel combustion is a very effective way of eliminating CO_2 emissions of gas turbine systems.

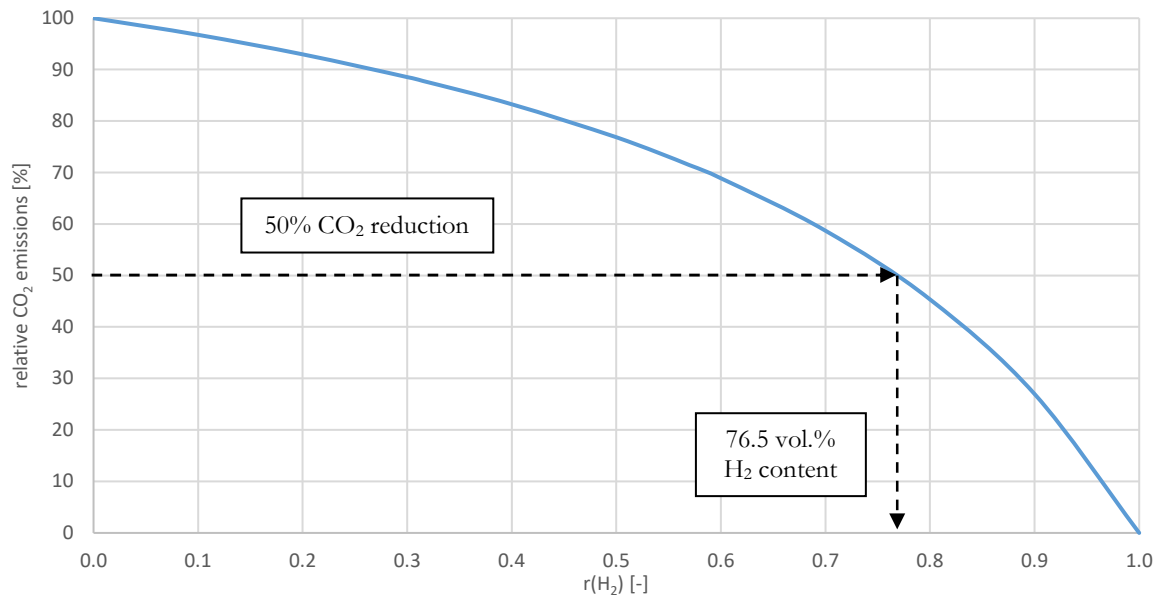


Figure 1-4: Relative CO₂ emissions of H₂/CH₄ fuel mixtures at const. thermal power output

In addition to the apparent CO₂ reduction potential, the admixture of hydrogen enables leaner combustion due to the higher reactivity and flame stability of hydrogen. This improves gas turbine turndown capabilities, required in times of peak load of renewable energies [25].

At constant thermal power output, the combustion temperature for H₂ is decreased (cf. Figure 5-13). Thus, if constant thermal power output is defined as a boundary condition for a gas turbine combustor, this fuel characteristic benefits the lifetime of the combustor and especially turbine parts. When constant turbine inlet temperature is the design goal, higher thermal power output is generated by a hydrogen-fueled gas turbine combustor in comparison to a natural gas alternative.

1.3 Nitrogen Oxide (NO_x) Emissions

Despite reducing CO₂ emissions and their impact on the climate significantly, hydrogen-rich fuel combustion promotes the formation of nitrogen oxides (NO_x). Hydrogen's high reactivity results in rapid heat release and elevated peak temperatures during combustion, which in combination with the temperature dependence of NO_x formation, enables increased NO_x emissions [26–29].

Nitrogen oxides are molecular compounds of nitrogen and oxygen atoms. Primary NO_x sources are the industry, nitrogenous fertilizers, bolt activity and combustion processes. In hydrogen-rich combustion, they are the major pollutants and can only be decreased by optimizing the combustion system for low NO_x performance or by applying dilution of the fuel or the combustor air. Of the many nitrogen oxide species, nitrogen monoxide (NO) and nitrogen dioxide (NO₂) are the most common ones.

Near ground level, NO_x acts as a precursor for the photochemical formation of smog and nitric acid (acid rain). When inhaled, nitric acid forms on the mucous membranes and damages the human respiratory system. Another environmentally harmful reaction of nitrogen oxides in the presence of UV-radiation is the formation of ground-level ozone, an irritating trace gas [30].

There are several NO_x formation pathways that can be differentiated based on the combustion temperature, the equivalence ratio, the type of combustible, concentrations of fuel and air or of intermediate species, or the retention time of precursor species [31–34].

- **Thermal NO:** also known as Zeldovich mechanism is the reaction of atmospheric nitrogen and oxygen at temperatures above 1850 K
- **Prompt NO:** also known as Fenimore mechanism is the formation of NO under fuel-rich conditions via CH-radicals that originate from hydrocarbon-fuels
- **Fuel NO:** formation of nitric oxides by bonded nitrogen in the fuel. Dominant for coal or biomass combustion
- **N_2O formation route:** gains significance in high-pressure areas and for fuel-lean conditions. The reactions feature comparably low activation energies, which do not restrict the mechanism to high-temperature zones like the thermal NO mechanism
- **NNH formation route:** takes place at high concentrations of O- and H-radicals. This formation pathway gains importance in fuel-rich and stoichiometric regions
- **N_2H_3 formation route:** promoted by rich combustion at temperatures below 1500 K

1.4 The Dry-Low- NO_x Micromix Combustion Principle

NO_x emissions can be significantly reduced by applying premixed combustion systems. Lean combustion of homogenous fuel-air mixtures offers a very uniform temperature distribution without high peak temperatures. It thus effectively suppresses the most dominant NO_x formation mechanism via the thermal NO route [35, 36]. The significant low NO_x performance of premixed combustion systems is counteracted by the inherent danger of flashback that increases when highly reactive hydrogen is admixed to natural gas fuel [37].

For achieving low NO_x performance with safety against flashbacks, Aachen University of Applied Sciences (AcUAS) investigates non-premixed gas turbine combustion of hydrogen and hydrogen-rich fuels since the European research projects EQHHPP [38] and CRYOPLANE [39]. In these research projects, the Dry Low NO_x (DLN) Micromix (MMX) combustion principle has been developed and continuously investigated and improved by several follow-up projects since then [34, 40–42].

The DLN MMX principle significantly reduces NO_x formation by miniaturizing the reaction zone and retention time by creating multiple micro diffusion-type flamelets with a typical size of 10-40 mm in length. The combustion process is based on the phenomenon of jet-in-crossflow mixing (JICF). In this mixing process, a smaller gas stream is injected transversely into another, larger stream. Applied to MMX combustion, the smaller secondary fuel jet is deflected and entrained by the air in the primary flow channel, due to the pressure gradient between the upstream and downstream side of the injected fuel jet. By design, the injection takes place at an angle of 90° to the flow direction of the air stream. Figure 1-5 shows the formation of a characteristic counter-rotating vortex pair that arises from the air that is entrained in the fuel jet because of the negative pressure on the downstream side of the injection. The vortices deform the jet and accelerate mixing between fuel and oxidizer.



Figure 1-5: Characteristic flow structure of Jet in Crossflow mixing [43]

After injection and rapid JICF mixing with air, the fuel is burned in miniaturized, diffusion-like flames without using any pre- or post-combustion dilution. Since no premixing of fuel and oxidizer before injection occurs, the risk of flashbacks is avoided.

According to Lefebvre [43], NO_x production is a function of retention time of NO_x forming reactants in the combustion zone, the reaction rate determined by the fuel type and boundary conditions in the combustion chamber and the mixing rate between fuel and oxidizer.

$$\text{NO}_x = A \cdot \left(\frac{p \cdot V}{T \cdot \dot{m}_L} \right) \cdot \exp(z \cdot T) \cdot p^m \cdot \left(\frac{\Delta p}{p} \right)^x \quad 1.1$$

retention time
reaction rate
mixing rate

Thus, intense mixing of fuel and oxidizer and reduction of the residence time of NO_x precursors in the high-temperature domain by miniaturizing the flames results in reduced emissions for MMX combustion.

In Figure 1-6, the structural layout of a typical Micromix combustor and the section view through the center of a fuel injector and the respective air-guiding-panel (AGP) is depicted. Fuel is distributed through the fuel supply segments (FSS) and injected through small nozzles into a crossflow of air. The air enters the Micromix combustor structure from the left, passes the air gate and mixes with the injected fuel jet.

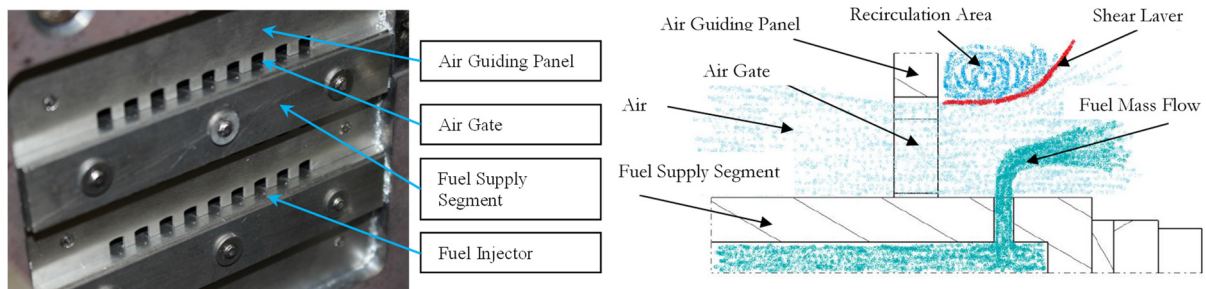


Figure 1-6: Structural layout (left) and section view of a Micromix combustor (right)

The geometry of the fuel supply segments, along with the air guiding panels, which both act as bluff bodies, leads to the formation of counter-rotating vortex pairs, creating an inner and outer recirculation zone during operation of the combustor (cf. Figure 1-7). Their proportions are designed to facilitate flame stabilization and to prevent adjacent flames from merging. Merging of several miniaturized flamelets creates flames with increased expansion, leading to longer residence times of NO_x precursors in the hot reaction zone and significantly promoting NO_x formation.

The inner recirculation zone in front of the AGP is separated from the main flow by a shear layer (cf. Figure 1-6, right). At sufficiently low injection depth of the fuel jet into the air crossflow, the fuel-air-mixture discharges freely into the combustion zone. The residence time of NO_x precursors is low, resulting in low NO_x performance of the combustor. At a critical injection depth, the fuel jet penetrates the shear layer and enters the inner recirculation vortex. The fuel-air-mixture that is formed in the vortex ignites and leads to hot gas recirculation with extended retention times for NO_x precursors at elevated temperatures, resulting in increased NO_x emissions.

The DLN-Micromix technology has been tested and optimized in several research projects with pure hydrogen (H_2) and a defined H_2/CO mixture [44–46]. Figure 1-8 highlights the MMX NO_x reduction potential by comparing the resultant emissions of the small aviation gas turbine Honeywell Garrett GTCP 36-300 operated with conventional kerosene nozzles, with six non-optimized hydrogen nozzles, and with a Micromix hydrogen combustion chamber. The gas turbine operates at a pressure of 6.69 bar (cf. Table 6).

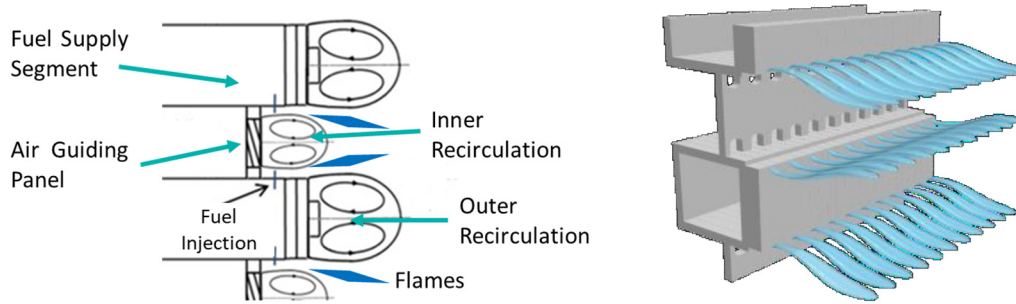


Figure 1-7: Schematics of the Micromix combustor geometry, detailing the recirculation zones and aerodynamic flame stabilization

Due to hydrogen's high reactivity, NO_x emissions increase significantly when changing from kerosene to hydrogen operation with six non-optimized gas nozzles. The conventional nozzles create six large flames with high retention times of NO_x precursors in the high-temperature flame regions, which promotes NO_x formation. When miniaturizing the flames and enhancing the mixing of fuel and oxidizer by Micromix combustion, a NO_x reduction potential of up to 95% is possible at the same operating conditions. The previous research work has proven that Micromix combustion is capable of handling hydrogen's high reactivity while at the same time reducing NO_x emissions significantly.

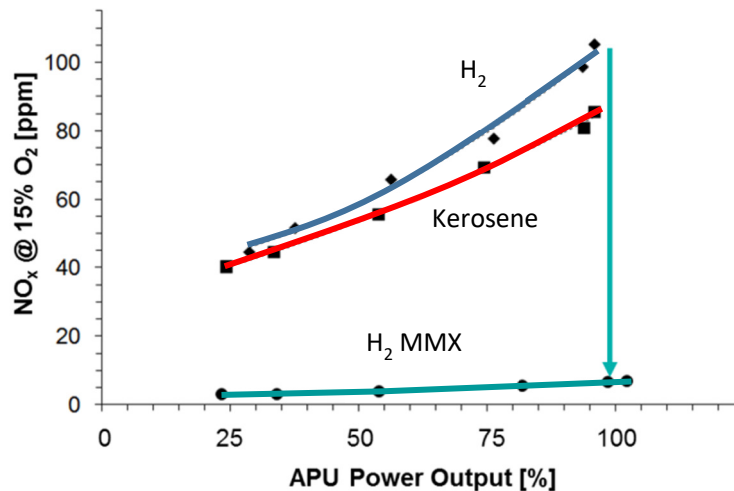


Figure 1-8: NO_x emissions of different combustor technologies and fuel types

1.5 Aim & Structure of the Thesis

In [44, 47], Funke et al. have proven the significant NO_x reduction potential of MMX combustion for lab-scale and industrial-scale gas turbine combustors with hydrogen fuel. Despite hydrogen's high reactivity, stable and safe operation under full-scale gas turbine conditions was achieved by an appropriate choice of the combustion chamber and nozzle geometries. The flame miniaturization applied with the MMX principle effectively reduces NO_x emissions while the non-premixed

combustion system ensures flashback-free operation. During subsequent developments, the combustor's power density has been increased, which benefits manufacturing complexity and costs [41, 48].

Following this successful development, the next advance aimed at dual-fuel operation with hydrogen and a distinct laboratory-scale syngas fuel mixture with 90 vol.% hydrogen and 10 vol.% CO. With a single combustor geometry, combustion of both fuels exceeded 99% combustion efficiency at NO_x emissions lower than 5 ppm (corrected to 15 vol.% O₂) under a variety of gas turbine operating conditions [40, 49].

Based on the recent work at AcUAS, this thesis aims at characterizing the DLN MMX combustion principle under flexible-fuel operation with hydrogen and methane and at establishing design laws that expand the applicable fuel range from pure hydrogen and hydrogen-rich syngas to variable H₂/CH₄ mixtures. By this, a viable bridge technology for near-future hydrogen-enriched methane or natural gas combustion is proposed. The presented results pave the way for a prospective CO₂-free power generation based on low emission gas turbine combustion systems. With the necessary long-term elimination of CO₂ emissions in the power-producing industry, a significant contributor to global climate change can be removed.

Beginning with a comprehensive literature review in chapter 2, recent work in the field of gas turbine research and developments regarding H₂/CH₄ fuels are summarized.

The scientific approach applied in the framework of this thesis combines experimental low-pressure combustor testing with numerical analyses conducted with the commercial CFD-code Star-CCM+. In chapter 3, the fundamentals of modeling the reactive flow regime of a gas turbine combustor, the applied computational models and boundary conditions are described along with the experimental approach used for assessment of the combustion characteristics. Particular focus is laid on the analysis of experimental error sources and the impact of measurement inaccuracies on the results. For a phenomenological interpretation of the experimental results, CFD combustion and flow simulations are used, which also aid in understanding the underlying physical mechanisms. For identification of suitable numerical combustion models capable of predicting the Micromix combustion process fueled with H₂/CH₄ mixtures accurately, a numerical preliminary study based on the bluff-body stabilized flame HM1 by the University of Sydney is presented.

The principal challenges in the flexible fuel adaption of the Micromix combustion system are the combustion properties of the applied fuel mixtures that change significantly over the investigated fuel range. Depending on the fuel mixture composition, the fuel density, the lower heating value, the stoichiometric air requirement, the flammability limits, and the combustor operating point change. This variability requires a multitude of parametric investigations to examine the influences

on combustion stability and exhaust gas emissions. Considering the fuel characteristics of the applied H_2/CH_4 mixtures, the operational boundary conditions, and the geometric restrictions that ensure optimal JICF mixing and flame stabilization, the initial combustor geometry V1 is derived in chapter 4. Since most of the geometric and operational parameters are interdependent, an iterative design process is pursued.

Based on the derived combustor geometry, a numerical and experimental characterization and optimization of the DLN-Micromix technology under flexible-fuel operation is conducted in chapter 5. Initially, the methodology of the extensive parametric test program is explained before the results of a numerical and experimental design space exploration and a successive combustor optimization study are presented and analyzed in detail.

During the initial characterization of flexible-fuel operation with the baseline Micromix FuelFlex combustor V1, presented in chapter 5.1, the applied fuel composition and the combustor's operating point are varied. This process identifies the influence of the fuel mixture composition on the combustion characteristics at variable thermal power output.

Following this initial characterization, the first optimization step (cf. chapter 5.2.1 & 5.2.2) applies an increase in the air gate velocity (and corresponding relative pressure loss) and a modification of the air gate height to reduce NO_x emissions especially at overload conditions and to increase the combustion efficiency at high methane contents

In a second optimization step (cf. chapter 5.2.3), the lessons learned at increased pressure loss are applied to generate the final Micromix FuelFlex combustor geometry, operating at a lower pressure loss with greatly enhanced combustion characteristics.

Throughout this optimization study, a particular focus is laid on the safe combustor operability over a wide fuel range at low NO_x emissions. With the applied approach, the drivers and key design parameters optimizing the MMX operability and low NO_x performance are finally identified.

2

Low Emission Combustor Research

The research on gas turbine combustion systems for the energy sector is driven today by economic but also ecological considerations. With the exhaustible nature of fossil fuel resources on the planet, the foreseeable price development in the coming decades and the climatic impact of exhaust gas components, highly efficient gas turbine systems reduce not only the direct operating costs but also the ecological consequences.

Apart from H_2O , the primary exhaust emission of fossil fuel combustion is CO_2 , a potent greenhouse gas that partly absorbs infrared (terrestrial) radiation in the atmosphere while shortwave (solar) irradiation passes through. It has a direct climatic effect, which proportionally depends on its atmospheric concentration, which has increased significantly since the beginning of industrialization in the 18th century. Reasons are manifold but mainly due to the combustion of fossil energy carriers such as crude oil, natural gas, and coal, as well as the expansion of industrial production, changes in land usage, expansion of livestock production and the population growth. CO_2 is the most important anthropogenic greenhouse gas and globally effective, independent from the place of origin [7].

2.1 The Challenge of Energy Transition to Renewable Sources

In recent decades, there has been a significant increase in global energy consumption in virtually all sectors. Non-renewable sources of energy that rely on fossil energy carriers are still predominant and lead to an aggravation of the anthropogenic climate change. Faced with the consequences on the population, fauna, flora, and climate, a transition to renewable, carbon-neutral energy production is necessary [50].

The weakness of power generation from renewable energy sources (with the exception of mainly hydropower and geothermal energy) is a production that depends on the meteorological conditions, and that is not related to the consumption [51].

Different storage concepts make a transfer of energy from renewable energy sources possible, from times of peak production and low demand to times when adverse weather conditions coincide with high demand by the electrical grid. Additionally, storage of surplus electricity in large quantities and recovery if needed, can be a factor enhancing the network stability of the electrical grid, since variations in the grid frequency can be compensated easily [50].

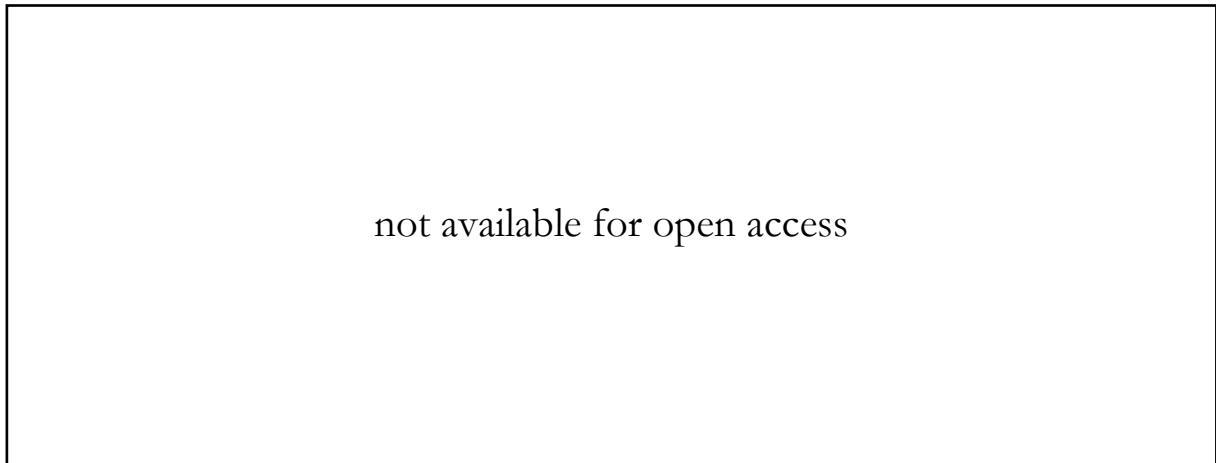


Figure 2-1: Electrical storage technologies [51]

Among the many available energy storage technologies, differentiated by their basic working principles in Figure 2-1, the chemical Power-to-Gas (PtG) technology is of particular interest. It connects the electricity network with the gas network by converting excess electricity into a grid compatible gas in a two-stage process: hydrogen is produced by electrolysis and can be converted with an external CO or CO₂ source to methane via methanation (cf. Figure 2-2).

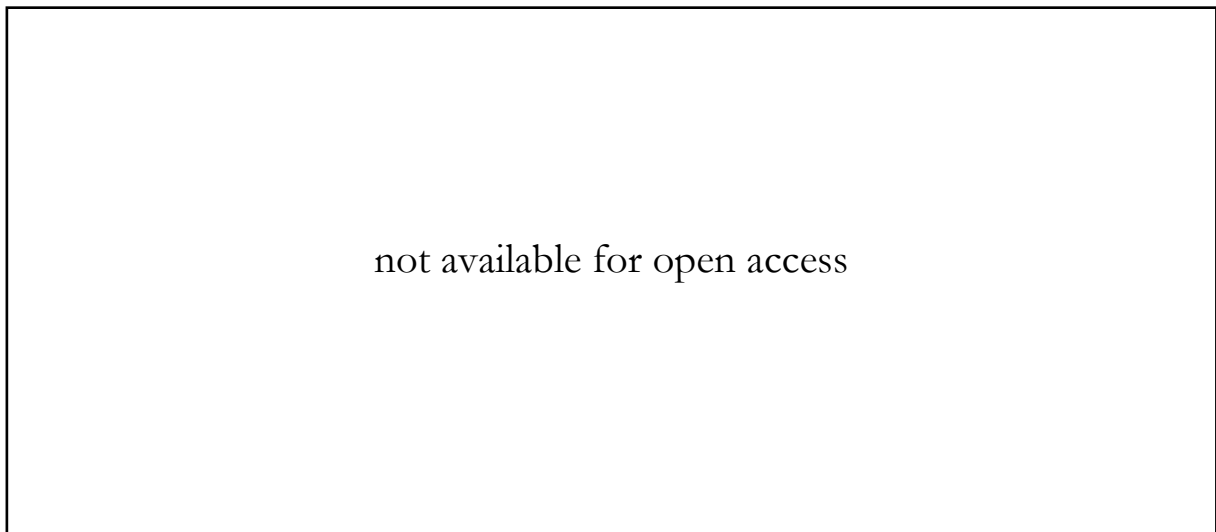


Figure 2-2: Power-to-gas concept [52]

The resulting CH₄, known as substitute natural gas, can be injected into the existing gas grid or gas storages, or it can be utilized directly in all other well-established natural gas facilities. An alternative would be a direct injection of H₂ into the gas grid, which is restricted today by country-specific standards and regulations to a maximum of 0 - 12 vol.% [53].

The use of PtG and of the natural gas grid as storage location is beneficial due to the high capacities already installed, which exceed by far the capacity of all other electrical storage options, presented in Figure 2-1. The main drawbacks of PtG applications are their relatively low efficiency and high costs. This is why nowadays, 96% of the available hydrogen is produced from fossil energy carriers in a process called steam reforming, which emits high levels of CO₂ [52, 53].

Despite the low competitiveness of PtG for hydrogen production in contrast to steam reforming of fossil fuels, it remains highly attractive as a storage concept for excess renewable energy. A direct feed of hydrogen and substitute natural gas into the natural gas grid and combustion in low emission gas turbines facilitate direct energy recovery while maintaining most of the existing natural gas infrastructure [24, 52].

Natural gas that predominantly consists of methane is a well-established fuel in the stationary power generation industry, and the role of hydrogen as a carbon-free energy carrier is discussed for decades for reducing greenhouse gas emissions [15–21].

In the 1950s, hydrogen was first introduced as gas turbine fuel for mainly military applications [36, 54, 55]. However, after the oil crises of 1973 and 1979/80, hydrogen was also considered a potential alternative fuel for gas turbines in civil aero-engine applications [56–58]. In the period that followed, numerous research work was carried out in the area of low-NO_x hydrogen combustors for aircraft engines in the years 1990-2000 [38, 59, 60]. In recent years, all leading manufacturers of gas turbines for the energy sector have been involved in the research and development of gas turbines capable of low-emission combustion of hydrogen-rich fuels [35, 36, 61].

On the way towards a CO₂-free energy supply, a bridge technology is needed that facilitates the transitions from well-established natural gas to hydrogen. Blending increasing amounts of hydrogen into the natural gas is a viable option, but gas turbines have been historically designed and optimized for the use of pure natural gas. Hence, the applied combustion system must be modified to account for flexible-fuel operation with hydrogen-rich fuels [62, 63].

Challenges arise from the changes in lower heating value and in the flame temperature [64, 65]: the first one affects the fuel/air equivalence ratio (cf. chapter 4.2.2). With increasing amounts of hydrogen, leaner combustion is enabled due to hydrogen's higher reactivity and flame stability. This characteristic improves gas turbine turndown capabilities, required in times of peak load of renewable energies [25]. In contrast, the risk of flashbacks is increased when hydrogen is

combusted in a premixed system due to hydrogen's higher flame speed [37].

When increasing the hydrogen share in the fuel, CO₂ emission can be effectively reduced, but due to higher flame temperatures, NO_x formation is promoted during the combustion process [65–69]. This is why especially NO_x reduction strategies are in the focus of the energy-producing industry, particularly when hydrogen-rich fuels are applied [64].

2.2 Emission Reduction Concepts

Already in the 1970s, unburned hydrocarbon, carbon monoxide, and nitrogen oxides emissions were attracting attention, and the first emission regulations were published. In recent decades, overall efficiencies of gas turbines have been largely increased along with service life and reliability, while at the same time, the emissions of pollutant exhaust gases have been significantly reduced. Nonetheless, further research on low-emission combustion systems is essential to meet future requirements concerning the emissions of harmful and climate effective exhaust gas components. In the early 1970s, technologies to achieve low-level NO_x emissions were developed based on water injection in the combustion chamber to lower the combustion temperatures, which soon proved to be a costly way for reducing NO_x emissions. Today, the demand for sustainability, in combination with economic viability, drives the research in the gas turbine industry. Among other things, the industry is confronted with two major challenges: the need for dry low NO_x emissions without inefficient water injection or use of diluents, and the need for fuel flexibility in gas turbines that provide stable combustion with a variety of fuels, including natural gas, syngas, hydrogen and liquid fuels [43, 70].

2.2.1 Catalytic Combustion

An approach to achieving low NO_x emissions without water or steam injection is catalytic combustion [71]. It makes use of catalysts, which are added to the reacting system to increase the reaction rate of chemical conversion processes by reducing the required activation energy. During the catalyzed reaction, the catalyst itself is not consumed and can continue to act at subsequent reactions. When applied to gas turbine combustion processes, a catalyst may be used to enhance fuel preparation by splitting long fuel molecules, by promoting oxidations processes and by decomposing pollutant exhaust gas components [71].

The development of catalytic combustion systems started in the 1970s as an alternative NO_x reduction technology in contrast to water or steam injection. Some work has been done in the field

of catalytic combustion since then, demonstrating NO_x emission levels below 3 ppm [33], but this technology has never been commercialized [72].

This is mainly due to the fact that, despite the enormous research work carried out in the past [71, 73–76], a better NO_x performance than what can be achieved nowadays with more common combustion systems could not be demonstrated. Andrews [33] concludes that due to its limitations, catalytic combustion will not have a significant impact on future gas turbine developments.

2.2.2 Premixed Combustion

The most commonly applied technology today for achieving low NO_x emissions in industrial-scale gas turbines is premixed combustion [77]. Fuel and air are mixed thoroughly before entering the combustion chamber, where combustion occurs with a very homogenous temperature distribution [78, 79].

Döbbeling et al. [70] summarize the development of a low emission combustor technology that is based upon lean, premixed combustion. This approach effectively reduces NO_x emissions in stationary gas turbines by avoiding high flame temperatures, which are the primary drivers for NO_x emissions (cf. chapter 1.3). The demand for ever-higher pressure ratios and turbine inlet temperatures for increasing the overall cycle efficiency of industrial gas turbines competes with the demand for low NO_x emissions. In order to keep the combustion temperature low at a required turbine inlet temperature, the amount of combustor cooling air is kept at a minimum in favor of a higher primary combustor air mass flow. With more air available for fuel-air mixture preparation, leaner combustion is enabled with lower temperatures and resulting in lower NO_x emissions.

The research work resulted in the invention of a compact annular combustion chamber featuring a multi-burner array with a low share of cooling air. By using a multi-burner arrangement in the combustion chamber, fuel staging, switching, and piloting concepts are possible [70]. The first commercially available lean premixed combustion chamber was introduced by Alstom in 1984 in a GT13D gas turbine. With initial NO_x emissions of 32 ppm (corrected to 15 vol.% O₂), research continued and brought forward the Environmentally-friendly V-shaped (EV-) burner with its first application in the heavy-duty GT8 gas turbine by Alstom in 1988 (cf. Figure 2-3). The EV-combustor features dual-fuel operation with gaseous and liquid fuels, which are introduced in the cone-shaped burner where they are premixed with the combustor air. The fuel-air mixture leaves the nozzle, ignites, and stabilizes in the exit plane of the combustor due to vortex breakdown [70]. In Alstom's 200 MW GT13E2 gas turbine, an arrangement of 72 EV-burners is used in an annular combustion chamber design. The EV-burner concept allows natural gas combustion with NO_x

emissions below 25 ppm (corrected to 15 vol.% O₂). Enhancements towards even lower NO_x emission levels could be achieved with the Advanced Environmentally-friendly V-shaped (AEV) burner. In the GT13E2, the AEV technology not only reduces the NO_x emission level under full-load operation to 15 ppm but also decreases the required number of individual burners from 72 EV- to 48 AEV-burners. Additionally, turndown capabilities are improved as the implementation of AEV burners allows low NO_x operation (<25ppm) down to 50% gas turbine load [80].



Figure 2-3: GT8 DLN EV multi-burner arrangement [70]

In [81], York et al. developed and tested a fuel injector designed explicitly for low emission hydrogen-rich fuel combustion. Its multitube (MT) premixer design features small-scale jet-in-crossflow mixing of fuel and air at numerous locations inside of small-diameter tubes. York concludes that micro-mixing injection is capable of achieving homogeneous fuel-air mixtures that benefit low NO_x combustion in premixed combustion systems. The distributed combustor design allows flexible scaling, fuel staging, and flexible-fuel operation.

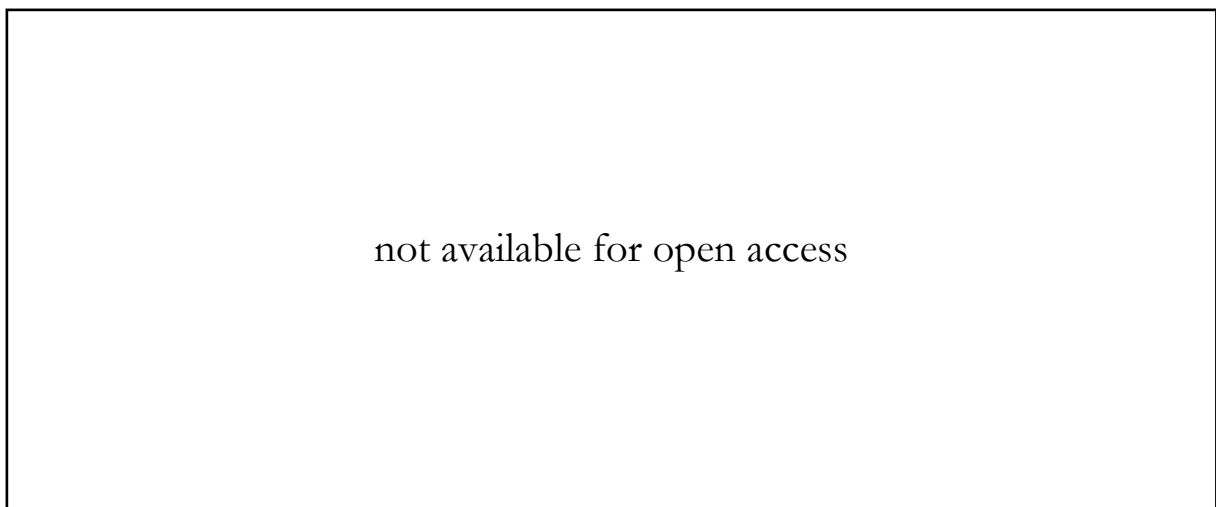


Figure 2-4: Multitube mixer for hydrogen-rich fuels [81]

In a small-scale single nozzle rig the MT burner was tested at realistic gas turbine operating conditions with pressures between 10 and 17 bar, and air inlet temperatures of about 650 K. With an air-side pressure loss of 3.5% across the premixer, the multitube burner operated flashback-free with a 60/40 vol.% H₂/N₂ mixtures and single-digit NO_x emissions (corrected to 15 vol.% O₂). Full-scale testing in an F-class gas turbine confirmed these initial results.

The multitube design highlights the potential of miniaturized premixing based on the jet-in-crossflow approach as a robust dry low-NO_x method for hydrogen-rich fuel combustion in industrial-scale gas turbines.

Hernandez et al. [82] demonstrate ultra-low NO_x emissions below 3ppm for a hydrogen and syngas fuel injector that is based on a radial micro-mixing injection strategy. The proposed design offers the inherent flexibility for accommodating staging and dilution options as well as flexible-fuel operation for future gas turbines. The work of Lee et al. [83] extends the previous work using micro-mixing fuel injectors for hydrogen-rich fuels and highlights essential considerations on flashback avoidance. Radial mixing concepts like presented in [82], offer excellent low NO_x emissions but are prone to flashback phenomena, especially when fueled with pure hydrogen. Adding 25 vol.% of natural gas significantly improves flashback safety at a constant combustor design. With a new axial injection concept, a design is found that is very robust against flashback with the potential for further NO_x emission reduction.

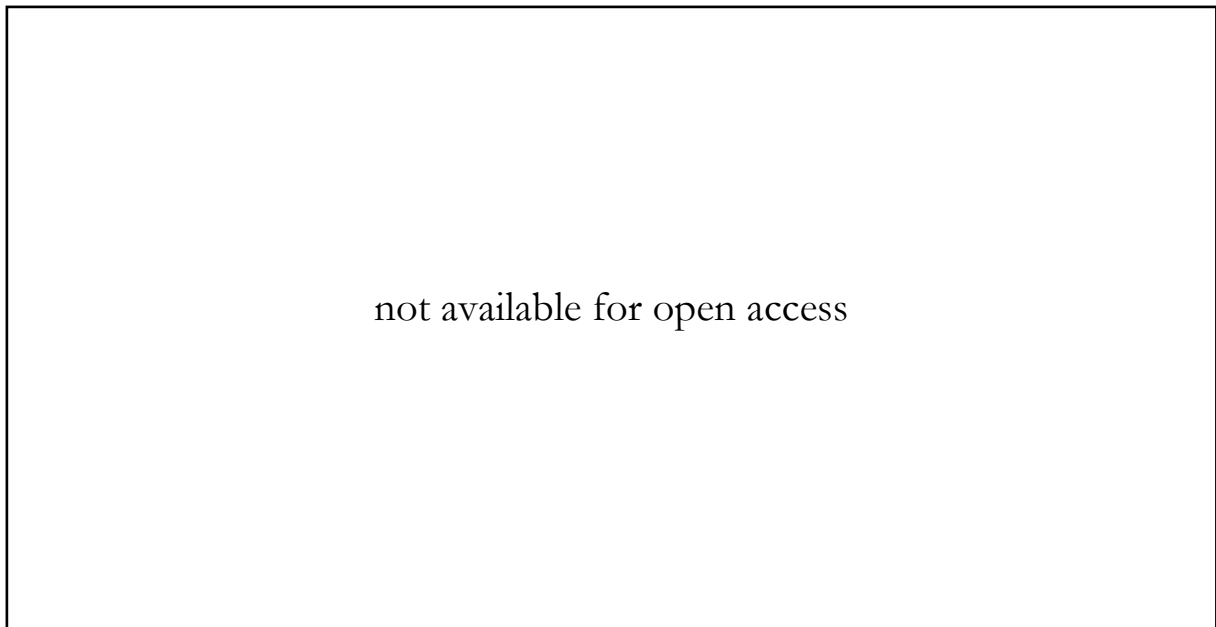


Figure 2-5: Schematic view of the multi-cluster combustor [84]

Dodo et al. [84] and Asai et al. [85] focus on multi-injection combustor concepts for dry low NO_x combustion of hydrogen-rich syngas, especially for Integrated Gasification Combined Cycle (IGCC) applications. They tested fuels consisting of methane, nitrogen, and 40 to 65 vol.%

hydrogen in a prototype multi-cluster combustor at 6 bar operating pressure (cf. Figure 2-5). Operation in an IGCC pilot plant with syngas fuel consisting of CO, H₂ and N₂ confirmed the low NO_x performance demonstrated with the prototype and yielded 10.9 ppm NO_x emission (corrected to 15 vol.% O₂) under full-scale gas turbine conditions.

Lam [86] and Lantz [87] work in the field of dry low emission combustion systems with particular focus on hydrogen-enriched natural gas combustion and fuel-flexibility for industrial-scale gas turbine applications. In their approach, different hydrogen natural gas blends between 0 and 80 vol.% hydrogen in the mixture have been tested in a premixed Siemens DLE combustion system (cf. Figure 2-6).

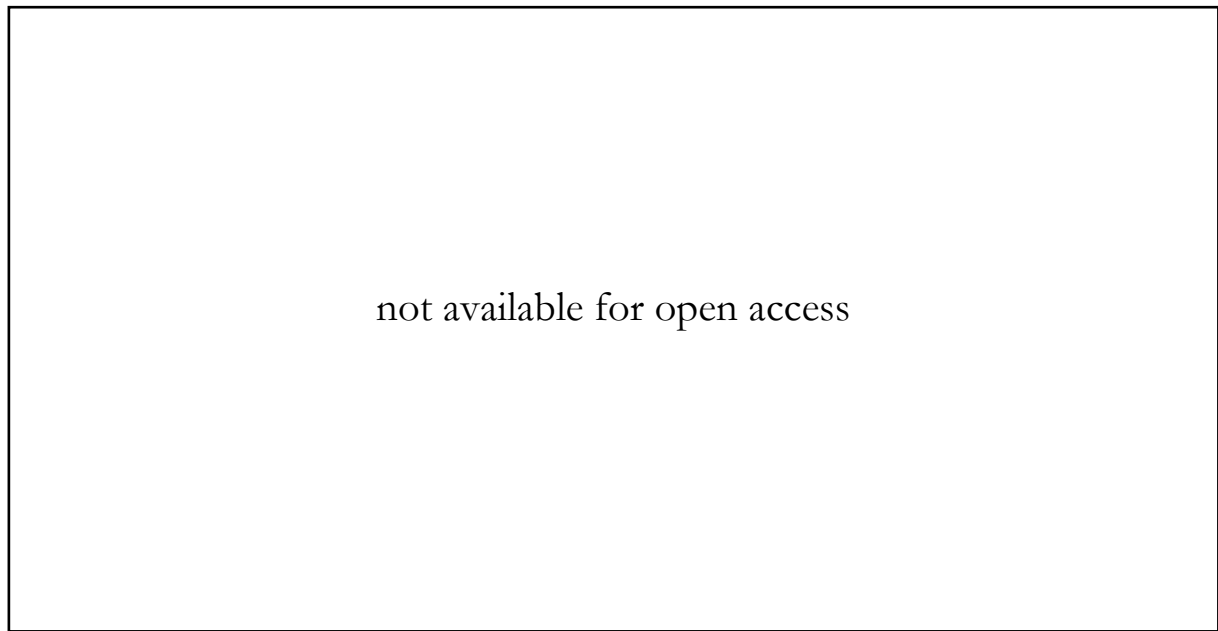


Figure 2-6: Siemens DLE combustion system [86]

Testing was done in an atmospheric test rig under scaled-down gas turbine operating conditions. Hydrogen-enriched natural gas combustion showed increased NO_x emission levels, a consequence of hydrogen's higher reactivity leading to locally increased flame temperatures. From higher temperatures at the burner tip, it was concluded that the flame moves upstream towards the combustor exit plane but without any flashback tendency. The changed flame position and a reduction in the flame size with an increasing amount of added hydrogen in the fuel blend was confirmed by chemiluminescence imaging

2.2.3 Diffusion Combustion

In [88], Iyer et al. investigate premixed and non-premixed combustion of hydrogen-rich fuels. They highlight the necessity for dilution with steam or nitrogen to achieve low NO_x emissions with

diffusion-type flames. Steam turned out to be a more effective diluent than nitrogen and guaranteed NO_x emission levels below 10 ppm at exhaust gas temperatures of approx. 1700 K.

With respect to pure hydrogen combustion in industrial-scale gas turbines, Cerutti et al. [89] aimed at a dual-fuel burner concept that is capable of burning pure hydrogen and pure natural gas. Conceptual diffusion type combustors were evaluated and compared to premixed combustion systems. Experimental test results show NO_x emission of approx. 200 ppm at 15% O_2 for diffusion flame burners with an additional steam dilution of the participating air.

Weiland et al. [90] propose nitrogen dilution of the fuel stream when operating diffusion flame burners with hydrogen-rich fuels rather than steam dilution of the combustor air. By this approach, all of the diluent is forced to pass the flame front where it acts as a heat sink and reduces peak flame temperatures, flame size and hence residence time of NO_x precursors. This effectively reduces overall NO_x emission levels, but the combustor design must account for the inevitable increased fuel volume flows.

Giles et al. [91] and Park et al. [92] both studied NO_x formation in counter-flow diffusion type flames in the presence of different diluents for hydrogen-rich syngas. Giles investigated syngas mixtures with and without hydrocarbons and the effect of dilution with N_2 , H_2O and CO_2 on NO_x formation. The presence of methane in the syngas mixture decreases the peak flame temperature, due to methane's lower reactivity, but increases the formation of prompt NO significantly, due to the presence of CH radicals from the decomposition process of CH_4 . Regarding NO_x emission reduction, steam dilution has proven to be most effective, followed by CO_2 and N_2 . Park [92] conducted combustion and flow simulations based on detailed reaction chemistry to investigate the effect of CO and CO_2 addition to hydrogen-rich fuel on the flame structure and NO emission characteristics. He underlines that diluting the fuel stream with CO_2 effectively reduces NO emissions due to CO_2 's high heat capacity, which suppresses some of the overall reaction rates in the combustion process.

2.2.4 MILD/FLOX Combustion

An innovative alternative to premixed or diffusion combustion for achieving dry low NO_x emissions is Moderate and Intense Low-oxygen Dilution (MILD) combustion [93, 94], which is also called Flameless Oxidation (FLOX) combustion [95]. With a massive dilution of the reactants by recirculation of exhaust gases, pollutant production, especially of CO and NO_x is strictly controlled. The diluted fuel enters the combustor volume at temperatures above the self-ignition temperature. Combustion processes are distributed homogeneously over a large flame volume at

relatively low temperatures, which effectively suppresses thermal NO production.

The concept of MILD-/FLOX-combustion was initially introduced in the 1980s and 1990s for industrial furnace applications and advanced since then, also taking into account the requirements of industrial gas turbine applications [96].

With its high fuel flexibility, it is suited to burn a wide variety of low and high calorific gases, including hydrogen. For hydrogen-rich gases, MILD combustion is of particular interest since the challenging fuel characteristics like high laminar flame speed, adiabatic flame temperature and reactivity are difficult to handle by other conventional gas turbine combustion systems. Derudi et al. [97] showed the potential of MILD combustion when applied to coke oven gas, consisting of 40 vol.% methane and 60 vol.% hydrogen. High combustion efficiencies and low NO_x emissions could be proven for a laboratory-scale burner equipped with a single high-velocity nozzle. Additionally, Sabia et al. [98] demonstrated the beneficial influence of hydrogen addition to natural gas combustion under MILD conditions in terms of reducing thermo-kinetic instabilities.

2.2.5 Micromix Combustion

As can be seen from the previous overview, the current research mainly focuses on the development of premixed low emission gas turbine systems, e.g. [35, 36, 61, 77]. Due to their homogeneous fuel-air mixture, lean combustion with a very homogeneous temperature distribution is possible. Since lean combustion with little inhomogeneities in the local equivalence ratio and temperatures is enabled, NO_x formation is effectively suppressed. Nevertheless, several research groups investigate other concepts like flameless or catalytic burner applications or diffusion flame combustors. The overview has shown that NO_x emissions can be reduced in diffusion-type systems by adding diluents into the air or fuel to reduce peak flame temperatures and the residence time of the reactants in the flame, but this diminishes their efficiency. On the other hand, premixed hydrogen-rich combustion has the vital disadvantage of the risk of flashback during operation due to the high reactivity and flame speed of hydrogen.

This is why the work presented in this thesis focuses on the research gap of ultra-low NO_x combustion with a non-premixed and diluent-free gas turbine combustion system that is capable of burning variable fuel mixtures of hydrogen and methane (up to 100% H₂) in industrial-scale gas turbine applications. In contrast to the majority of industrially available gas turbine combustors, the Micromix principle, investigated in this thesis, achieves dry low NO_x emissions with diffusion flames. Fuel and air are not premixed but introduced separately into the combustion chamber, where they are mixed rapidly by jet-in-crossflow mixing directly before combustion. Due to the

absence of flammable fuel-air mixtures prior to injection, the MMX combustion principle is inherently safe against flashbacks. In contrast to other non-premixed combustion systems, the MMX principle overcomes the described drawbacks for diffusion combustion in terms of NO_x emissions, due to the miniaturization of the injection dimensions, and therefore, does not need dilution of steam or nitrogen.

3

Experimental and Numerical Methods

The research process for investigating and optimizing the DLN Micromix principle for flexible fuel operation with hydrogen and methane mixtures is based on the interactive research and optimization cycle presented in Figure 3-1.

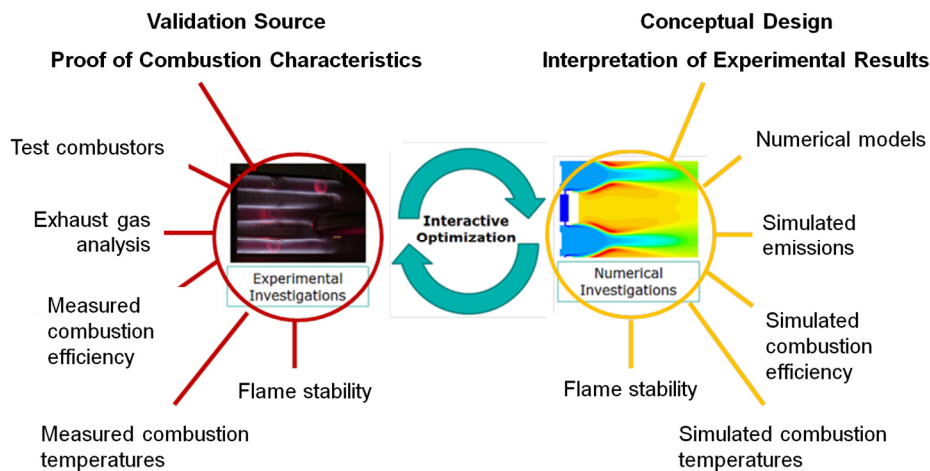


Figure 3-1: Interactive research and optimization cycle

Within this research cycle, 3D combustion and flow simulations are used in the context of parametric studies for generating optimized burner geometries and for the phenomenological interpretation of the experimental results. Experimental investigations with test burners establish the combustion characteristics of the Micromix combustion principle with variable H_2/CH_4 fuel mixtures and provide the basis for validation of the applied numerical methods. In the following, both the experimental and numerical approach is described. Particular focus is laid on the analysis of error sources during the measurement and the impact of measurement inaccuracies on the results.

3.1 Experimental Setup

For the flexible-fuel adaption of the Micromix combustion principle, several experimental parameter variations are necessary (cf. chapter 5). The basis for the design of Micromix gas turbine combustors at AcUAS are the operating conditions of the Auxiliary Power Unit (APU) Honeywell Garrett GTCP 36-300, which acted as a full-scale demonstrator in several preceding studies [34, 40].

Since high-pressure testing during conceptual design is not feasible, a flexible, accessible, and cost-efficient alternative to full-scale gas turbine testing is the application of test burners at atmospheric pressure. Thus, the gas turbine operating conditions are scaled down to fit the atmospheric combustion chamber test rig at AcUAS. In this work, low-pressure testing is applied exclusively. It allows the assessment of the combustion characteristics and the derivation of key design drivers that enable stable combustion with low NO_x emissions under flexible-fuel operation.

3.1.1 Combustion Chamber Test Stand

The atmospheric combustion chamber test stand at AcUAS is displayed in Figure 3-2. The combustor module (test burner) is mounted on the test burner flange and integrated into the atmospheric test rig.

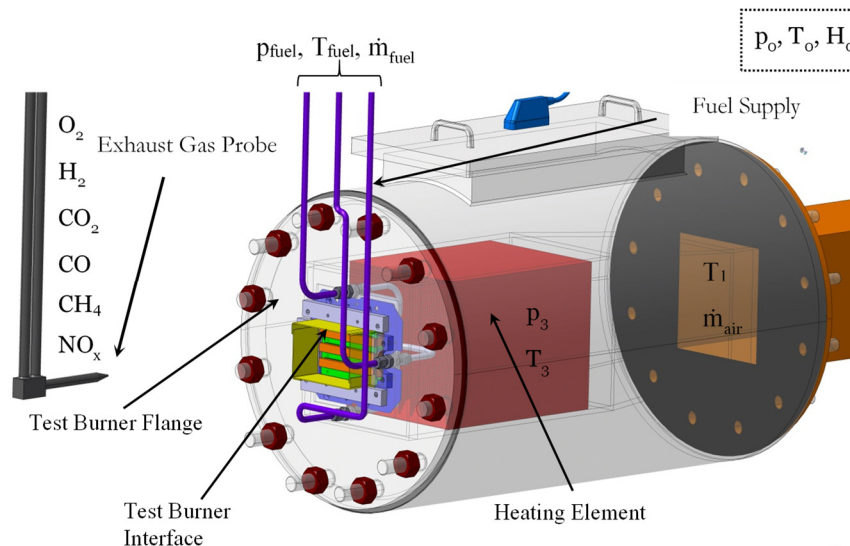


Figure 3-2: Schematics of the atmospheric test rig

The test stand provides ambient air as oxidizer via two radial compressors. The air is preheated by an electric heater to $T_3 \approx 559\text{K}$, corresponding to the combustion chamber inlet temperature of the reference gas turbine Honeywell Garrett GTCP 36-300. Homogenization structures in the

heater ensure a uniform airflow and temperature distribution as inlet boundary condition for the test-burner.

For facilitating flexible-fuel operation, a computer-controlled gas mixing facility, displayed in Figure 3-3, is designed and installed to continuously provide accurate and homogeneous hydrogen methane fuel mixtures to the fuel supply lines of the combustor module.

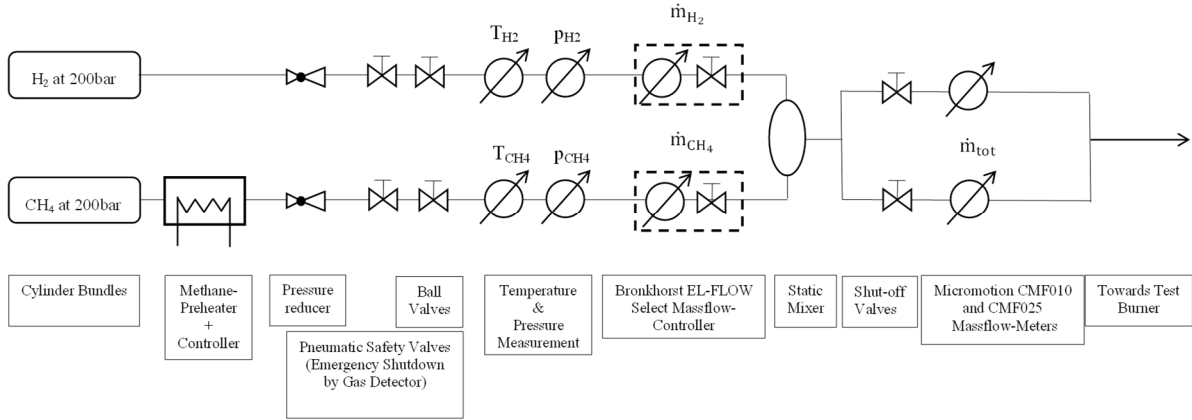


Figure 3-3: Schematics of the H₂/CH₄ gas mixing facility

Gas cylinder bundles supply methane and hydrogen at an initial pressure of 200 bar. Pressure reducers generate a working pressure of approx. 3-5 bar. The expansion of methane within the pressure reducers leads to a significant temperature decrease due to the Joule Thomson Effect. A measure for the change of temperature with a change of pressure at constant enthalpy is the Joule-Thomson-coefficient μ_{JT} which is defined as

$$\mu_{JT} = \left(\frac{\partial T}{\partial p} \right)_h \quad 3.1$$

μ_{JT} is not constant during the expansion but dependent on the current temperature and pressure of the gas.

Table 1: Temperature development during the expansion of methane (left) and hydrogen (right) under idealized adiabatic conditions. Thermodynamic data obtained from [99]

CH ₄			H ₂		
p [bar]	T [K]	μ_{JT} [K/bar]	p [bar]	T [K]	μ_{JT} [K/bar]
200	300.00	0.1588	200	300.00	-0.0405
160	292.74	0.2240	160	301.62	-0.0388
120	282.49	0.3165	120	303.17	-0.0370
80	268.03	0.4444	80	304.65	-0.0351
40	247.91	0.6061	40	306.06	-0.0332
10	228.43	0.7351	10	307.06	-0.0319
1	221.81	0.7719	1	307.34	-0.0316

As can be seen in Table 1, the expansion of the two gas components within a pressure reducer that expands the gas from 200 bar to 10 bar leads to a significant cooling of approximately 71.6 K for methane and negligible heating by approx. 7.1 K for hydrogen. The calculation was performed for an adiabatic change of state. Since in reality, heat flow from the surrounding will reheat the expanded gas, the temperature drop is partly remedied. For guaranteeing a defined set of boundary conditions and the precise and damage-free operation of the installed hardware, a high-pressure gas preheater is integrated into the methane supply. It increases the temperature of the pressurized methane in a way that after expansion, the flow temperature lies in the safe operating range of the installed hardware.

Several ball valves and a set of pneumatic safety valves are integrated into the set-up to safely separate the gas mixing facility from the surrounding test-stand installation (not displayed) and for an emergency shutdown of the whole complex. For recording the fuel boundary conditions, the temperatures and inlet pressures of both fuel components are measured.

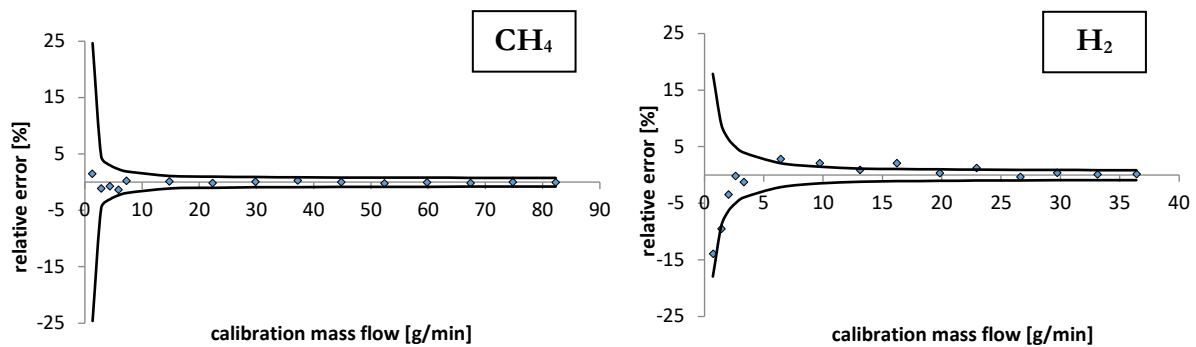


Figure 3-4: Relative error (dots) between Bronkhorst F-203AV and MicroMotion CMF010 mass flow measurement. Guaranteed error margins indicated as solid lines

Precise mixing of the gas flows to a predefined ratio is achieved by measuring and controlling the individual mass flows in their separate supply lines. The main controlling components are two Bronkhorst EL-FLOW Select F-203AV mass flow controllers. They are calibrated against a high precision MicroMotion ELITE CMF010 mass flow meter using multi-point calibration. The results of the calibration process are presented in Figure 3-4 as relative measurement errors between both mass flow meters. Despite four outliers, the calibration proves the guaranteed error margins by the manufacturer, displayed as solid lines. To account for temperature deviations of the supplied fuel streams, a temperature compensation algorithm is implemented. The precisely tuned component streams are guided into a static mixer that ensures good homogeneity of the mixed fuel stream before entering the combustor module. To suppress oscillations of the control loop, the static mixer is designed as an additional reservoir volume, cf. Figure 3-5.

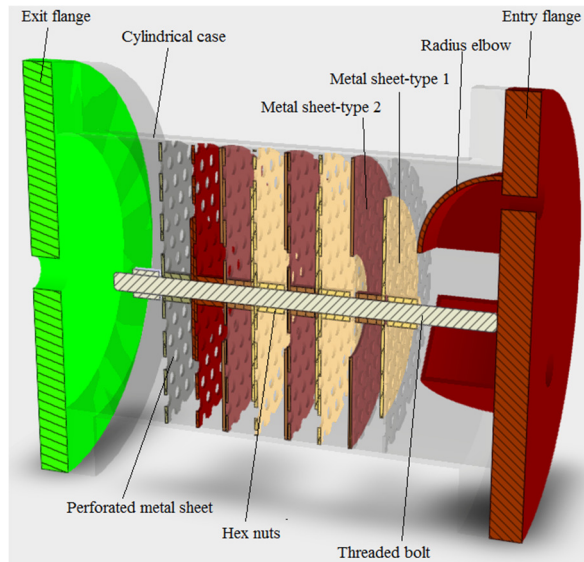


Figure 3-5: Sectional view of the static mixer showing the interior flow guiding structures

Steady Reynolds Averaged Navier-Stokes (RANS) CFD analyses have been carried out to optimize the internal structure of the static mixer for mixture homogeneity at the outlet. The numerical optimization yielded a design that features JICF premixing of the two fuel gas streams in the supply pipes. This initial mixture is directed in a mixing chamber with internal flow guiding structures that force the fluid to change its flow direction several times while passing through perforated metal sheets from one layer to the next.

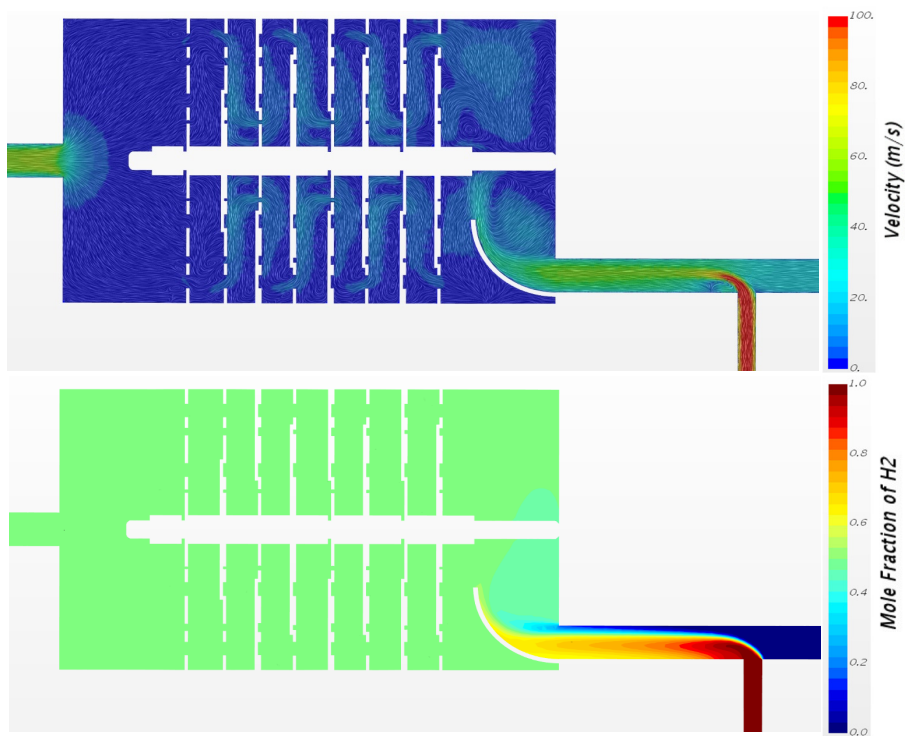


Figure 3-6: H₂/CH₄ mixing process in the static mixer illustrated by the velocity field (top) and the molar fraction of H₂ (bottom)

Figure 3-6 shows the resulting velocity field as well as the development of mixture homogeneity within the static mixer. The mixture inhomogeneity that is defined as the fluctuation margin between the highest and lowest obtained mixture fraction of H_2 at the mixer outlet has been evaluated numerically for three significant fuel mixtures and for fuel mass flows corresponding to combustor part-load and overload operation.

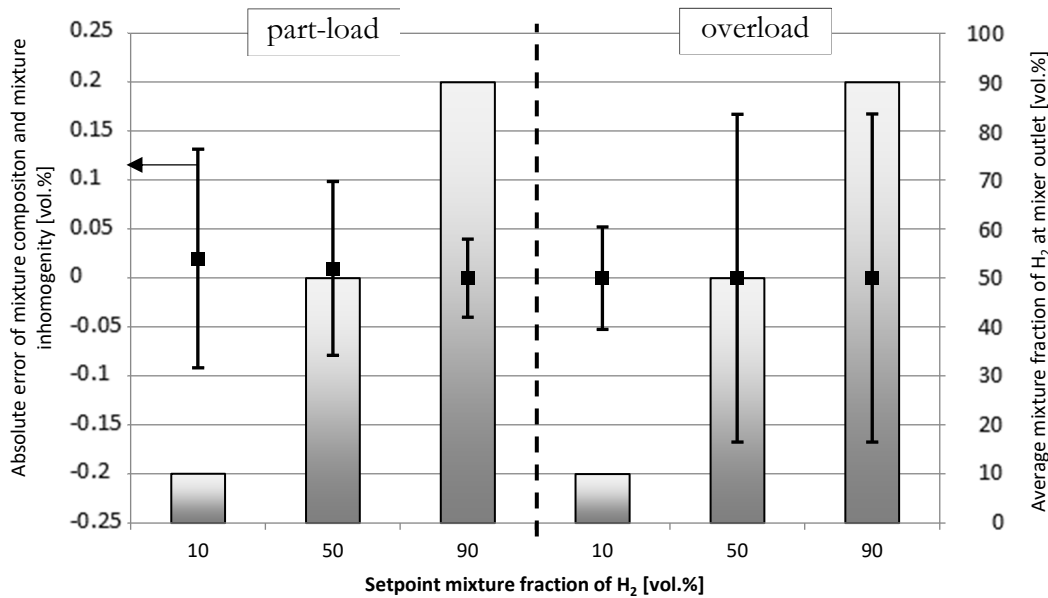


Figure 3-7: Simulated avg. mixture fraction of H_2 (bar graph), absolute error of mixture composition (dots) and mixture inhomogeneity (error bars) at mixer outlet for combustor part-load and overload conditions

As presented in Figure 3-7, the average mixture fraction matches the setpoint precisely for the optimized mixer design. The computed inhomogeneity within the mixer outlet section is less than ± 0.2 vol.% deviation from the average mixture fraction for all investigated fuel mixtures and load cases. These numerical results suggest that the optimized static mixer is capable of producing homogenous gas mixtures in the intended operating range.

After leaving the static mixer, the total mass flow of fuel entering the combustor is acquired by two high precision MicroMotion ELITE mass flow meters (CMF010 and CMF025) of different measurement range for reducing error propagation. The MicroMotion Elite sensors are mass flow meters working on the principle of Coriolis force that originates from the fluid moving through the sensor. They offer very high accuracy and repeatability of mass flow and density measurements for a wide range of gases and liquids.

The air mass flow is adjusted manually and measured by an ABB Sensyflow P mass flow meter. To avoid that deviations of the actual air mass flow from the setpoint affect the combustors operating point, a control system is implemented that directly controls the combustors equivalence ratio. At a set combustors equivalence ratio at constant fuel composition, the following condition is satisfied:

$$\frac{P_{therm}}{\dot{m}_{air}} = \frac{\dot{m}_{fuel} * LHV}{\dot{m}_{air}} = const \quad 3.2$$

The measurement and control accuracy of the applied mass flow controllers influence the mixture composition and accordingly, the combustion parameters like air-fuel ratio, mixture heating value, or the combustion temperature. Based on the measured errors, the influence of these parameters has been evaluated and is presented in the following.

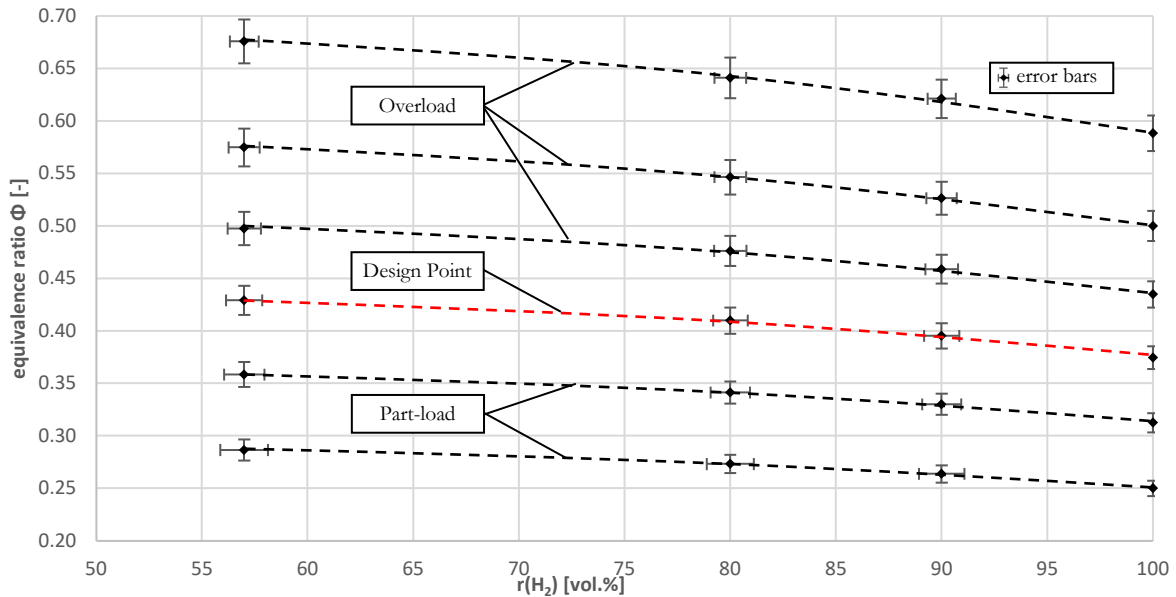


Figure 3-8: Combustor equivalence ratio (dots) and power-normalized equivalence ratio (dashed lines) for fuel mixture compositions in the area of interest

In Figure 3-8, the mixture fractions and equivalence ratios used for design space exploration of the Micromix principle with variable fuel mixtures are plotted. The assessment is limited to hydrogen-rich mixtures between 57 vol.% and 100 vol.% of hydrogen in the fuel, the area of interest for this work. The equivalence ratios highlighted by a red dashed line in the figure, resemble the gas turbine design point (100% thermal power output). The remaining equivalence ratios correspond to gas turbine part-load (67-83% thermal power output) and overload conditions (116-156% thermal power output) (cf. chapter 4). When changing the mixture composition at constant boundary conditions, especially constant thermal power output, a shift of the gas turbine operating point occurs. This apparent shift of the equivalence ratio in Figure 3-8 will be discussed in detail in chapter 4.2.2.

The combination of the air and fuel mass flow measurement errors with the inaccuracies of the stoichiometric air requirement (SAR), dependent on the achievable mixing accuracy, results in an error of the equivalence ratio. This error is smallest for part-load operation with pure hydrogen and increases towards methane-rich combustion at overload conditions. Additionally, the accuracy

of the mass flow controllers installed in the gas mixing facility directly influences the provided mixing accuracy. The fluctuation margin decreases with higher equivalence ratios, due to the increasing fuel mass flows and the resulting lower impact of constant absolute error components. The results confirm that for the fuel mixture composition, a minimum tolerance of ± 0.6 vol.% for overload conditions and maximum tolerance of ± 1.15 vol.% is guaranteed. The equivalence ratio can be determined with a relative accuracy ranging between $\pm 2.9\%$ and $\pm 4.5\%$.

3.1.2 Exhaust Gas Measurement

Optimizing the combustion process for high combustion efficiency and low NO_x emissions is the primary objective of the conducted research. A practical validation approach based on exhaust gas measurements is chosen. For measuring exhaust gas components, an exhaust gas probe is positioned along three axes (x, y, z in Figure 3-9) behind the combustor to take samples from locations that are distributed in a grid at the center outlet area.

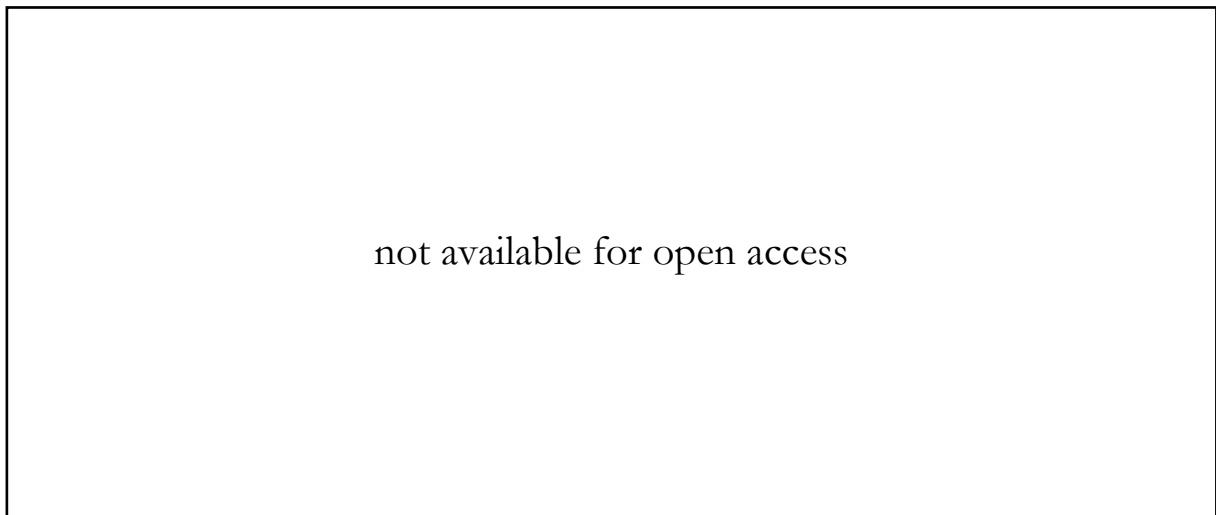


Figure 3-9: Sketch of a DLN Micromix test-burner, detailing the applied coordinate system and measurement grid

An oil flow that is kept at a temperature of 180°C by an oil heater / cooler combination flows through the outer perimeter of the double-walled probe. Keeping the temperature of the applied silicone oil below its cracking temperature of approx. 200°C prevents the oil from degrading during exhaust gas sampling in the hot combustor outlet area ($1000^\circ\text{C} < T_4 < 1800^\circ\text{C}$). At low thermal power output of the combustor that is not sufficient for heating the oil inside the probe, an additional oil heater raises the temperature to 180°C . This avoids condensation of exhaust gas components inside the supply pipes for the gas analyzers. Condensation would lead to concentration changes and consequently, inaccuracies in the exhaust gas analysis. With the specified oil temperature, the probe was initially applied for liquid fuel combustion, where

condensation of long-chained hydrocarbons must be avoided. Since for methane and hydrogen combustion only water vapor is a potential condensable exhaust product, the probe temperature is sufficiently high. In contrast to a low-tech non-heated/non-cooled probe, the double-walled construction and the peripheral devices are much more complex and cost-intensive, but enable operation in a wide exhaust temperature range and avoid inaccuracies in the exhaust gas composition.

At every location, an exhaust gas sample is taken when steady-state conditions are reached. For each equivalence ratio, the arithmetic mean based on measurements at 10 representative locations is obtained. The local measurements cover representative flow phenomena of the combustion process at the edges between the air guiding panel (AGP) and fuel supply segment (FSS), in front of the AGP and FSS, directly in front of an air gate and fuel-nozzle and between adjacent air gates / fuel-nozzles. Therefore, all relevant areas influencing the combustion and mixing process are covered during the measurements. Initial testing has shown that at a probing location of 130 mm behind the combustor face (z-coordinate), a very homogeneous exhaust gas distribution is present, which is favorable for the assessment of combustion characteristics based on the chosen measurement grid.

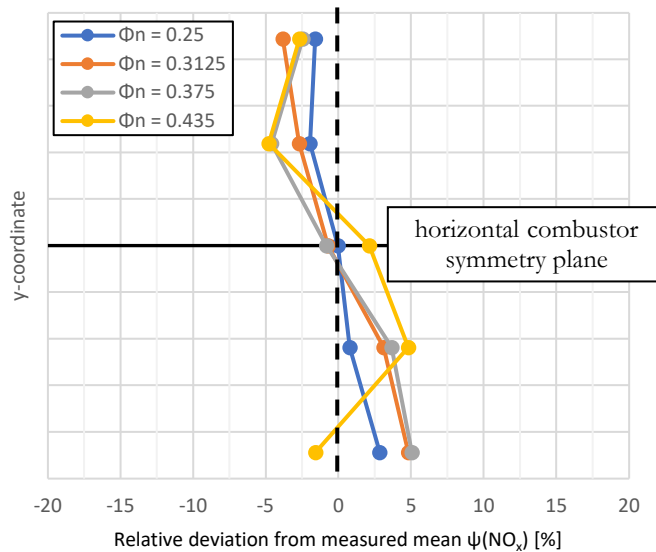


Figure 3-10: Relative local deviation from the measured mean NO_x emission level for different combustor equivalence ratios, obtained at a probing location of $z = 130$ mm

As Figure 3-10 shows, the relative local deviations at the chosen probing location of $z = 130$ mm remain within a margin of $\pm 5\%$ from the mean measurement value of a representative Micromix combustor NO_x measurement. As a result of the present small gradients between adjacent measurement locations, inaccuracies resulting from the chosen approach of arithmetic averaging remain small.

The application of a sealed flame tube that surrounds the combustion area and the definition of the measurement grid in the center region of the test-burner suppress atmospheric influences from the outside (cf. Figure 3-9).

The extracted samples are supplied to the analysis modules of the continuous gas analysis system ABB Advanced Optima AO2020 by heated tubing. They are designed to avoid concentration changes of the different components within the exhaust gas sample and condensation of water in the tubing that could influence the analysis results. After passing through a gas dehydrator, the gas sample is directed to the analyzer modules under controlled pressure conditions. The applied Advanced Optima exhaust gas analysis system determines the amount of unburned hydrogen (ABB Caldos 27), the concentration of O₂ (ABB Magnox 206) and the concentrations of CO and CO₂ (ABB Uras 26). For the determination of NO_x (i.e., NO and NO₂), an Eco Physics CLD 700 EL is used and directly connected to the hot exhaust gas sample. The cross-sensitivity to the remaining water vapor in the sample is below 0.5 percent of the measured value. During exhaust gas measurement, NO can be converted to NO₂ by wall reactions and pressure conditions inside the probe. However, the overall count of NO_x molecules is not affected by this effect [90, 100]. Therefore, only the total NO_x-emissions are given throughout the presented analyses in chapter 5. The obtained NO_x emissions are corrected to an oxygen level in the exhaust gas of 15 vol.%, according to equation 3.3. The correction procedure is based on the European environmental protection standard [101] and ensures comparability between changing ambient and operating conditions of a gas turbine.

$$\psi(NO_x@15\%O_2) = \frac{0.21 - 0.15}{0.21 - r(O_2)} * \psi(NO_x) \quad 3.3$$

To avoid zero or sensitivity drifts affecting the measurement accuracy, all exhaust gas analyzing devices are calibrated using zero-point and reference-point calibration gases, before each test campaign.

In Table 2, systematic and random error sources of the applied gas analysis system are presented. They can be subdivided in:

- **Calibration Gas Tolerance**, resulting from the accuracy of the applied calibration gas
- **Linearity Deviation**, resulting from the deviation of the measurement signal from the assumed linear behavior between 2 calibration points
- **Repeatability**, resulting from the deviation of the measured signal between two successive measurements of the same object at constant boundary conditions.
- **Output Fluctuation**, resulting from component-related fluctuations of the output signal
- **Power Supply Influence**, resulting from fluctuations of the power supply

The device-dependent error sources are full-scale errors. Their reference point is the maximum value of the individual measuring range. In order to minimize these errors, the maximum measuring range is subdivided into several sub-ranges. The calibration gas tolerance results in a relative error dependent on the particular reading. In the presentation of experimental test results in chapter 5, the measurement accuracies of the individual gas analyzers are integrated as error bars.

Table 2: Reading (rd) and full scale (f.s.) error sources of gas analysis systems ABB Caldos 27 (H₂), FID (CH₄), Magnos 206 (O₂), URAS (CO/CO₂) and CLD 700 EL ht. (NO/NO_x) [102, 103]

Type	CALDOS 27	FID	MAGNOS 206	ABB URAS		CLD 700 EL ht.	
Probe Gas	H ₂	CH ₄	O ₂	CO	CO ₂	NO	NO _x
Unit	[vol.%]	[ppm]	[vol.%]	[ppm]	[vol.%]	[ppm]	[ppm]
Calibration Gas (rd)	2.0%	2.0%	0.0%	1.0%	1.0%	5.0%	2.0%
Linearity (f.s.)	2.0%	2.0%	0.5%	0.5%	0.5%	0.5%	0.5%
Repeatability (f.s.)	1.0%	0.5%	50 ppm const.	0.5%	0.5%	1.0%	1.0%
Output Fluctuations (f.s. of smallest measurement range)	0.5%	0.5%	0.5%	0.5%	0.5%	0.5%	0.5%
Power Supply (f.s.)	0.2%	0.2%	0.4%	0.2%	0.2%	0.2%	0.2%
Measurement Ranges	0.5	25	1	10000	5	10	10
	1.5	250	10	100000	15	100	100
	4	2500	25			1000	1000
		25000				10000	10000

In order to consolidate the quality of the measurement results, one test campaign with the initial combustor geometry fueled with a mixture of 90 vol.% H₂ and 10 vol.% CH₄ is repeated 3 times in total. By this approach, the combined reproducibility of the complete combustion chamber test stand, including the newly designed gas mixing facility and the exhaust gas analyzers is evaluated. The resulting exhaust gas measurements are plotted as a function of the combustor equivalence ratio in Figure 3-11. Error bars based on the measurement accuracies in Table 2 are included.

The measurements of the three successively conducted tests match closely. The present small deviations between the obtained measurement results fall well within the guaranteed measurement uncertainty.

The research on Micromix combustion with variable H₂/CH₄ mixtures aims at the identification of key design parameters and their influence on the combustion characteristics. Against this background, the overall accuracy of the combustion chamber test stand, including the newly designed gas mixing facility and the exhaust gas analyzer modules and the demonstrated reproducibility of the experimental setup, allows an adequate discussion of the obtained results.

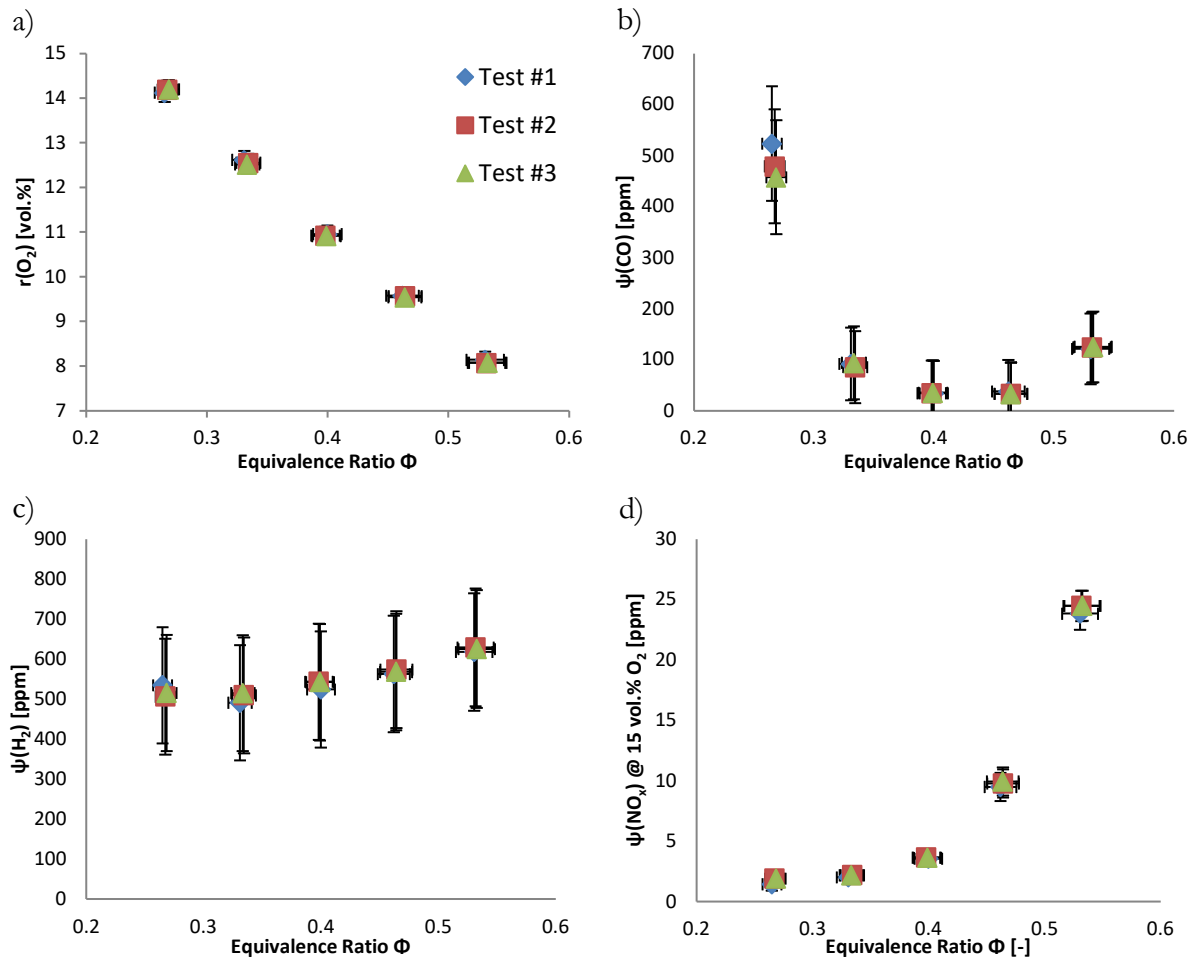


Figure 3-11: Exhaust gas measurements of O_2 (a), CO (b), H_2 (c) and NO_x corrected to 15 vol.% O_2 (d) obtained during 3 individual test under constant combustor operating conditions

3.2 Numerical Setup

The experimental investigation presented in the framework of this thesis is accompanied by combustion and flow simulations using the well-validated commercial CFD code STAR-CCM+. The experiment allows the assessment of the combustion efficiency and exhaust gas composition (especially NO_x and unburned fuel components). The numerical modeling approach, validated through the experimental findings, is used in the scope of parametric studies for predicting combustion characteristics of Micromix combustion with H_2/CH_4 mixtures.

The fundamentals for the applied numerical approach, the computational domain, the meshing procedure, and the chosen combustion models are presented in the following.

3.2.1 Geometric Model

For the extensive parametric studies presented in chapter 5, a simplified, fully parameterized computational model of the investigated combustor is developed. As displayed in Figure 3-12, the geometric model benefits from the symmetric nature of the burner in both lateral and vertical direction. Only a longitudinal burner slice, containing one half of a hydrogen injector and one half of an air gate is simulated. Since no transient effects like vortex shedding are resolved in the chosen steady RANS approach, the use of a symmetrical slice model is justified.

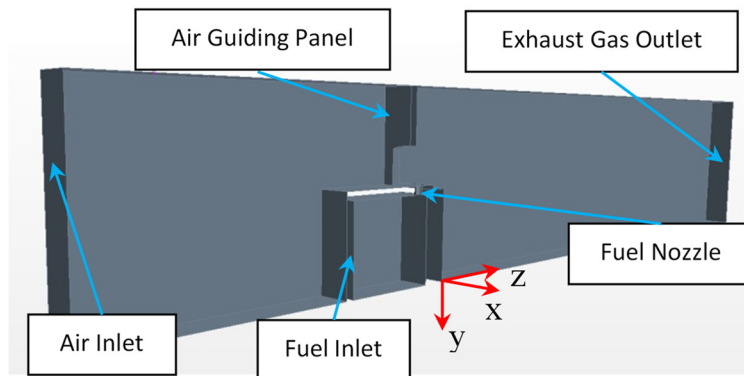


Figure 3-12: Computational domain and coordinate system of the developed slice model

The boundary conditions implemented in the simulations are specified by the parameters of the experimental studies performed at the combustion chamber test stand. The specified fuel mixture of hydrogen and methane and dry air ($r_{\text{O}_2}=0.20949$; $r_{\text{N}_2}=0.79016$; $r_{\text{CO}_2}=0.00035$) as oxidizer are introduced separately into the combustor model via two mass flow inlet boundaries, schematically shown Figure 3-12. To avoid any boundary influences on the mixing and combustion processes, the fuel and air inlet boundaries are set far upstream of the fuel injector and the air guiding panel,

respectively. The air inlet pressure p_3 is 1 bar according to the atmospheric test rig. The air inlet temperature is 559 K, corresponding to the combustion chamber inlet temperature of the APU Honeywell Garrett GTCP 36-300. The fuel inlet temperature is 298.15 K. For the numerical investigation of the test-burner, the design point of the burner and off-design points at overload and part-load conditions are analyzed. The equivalence ratios are set at constant air mass flow by adjusting the fuel mass flow accordingly.

The spatial discretization is performed using an unstructured polyhedral mesh with additional prism layers to account for wall boundary effects. An adaptive local mesh refinement process based on several solution properties is implemented to resolve the reactive flow regime properly. Gao [104] studied the use of adaptive meshing and parallel calculations in her thesis and proposed several measures. For the non-reacting flow properties, she used the density gradient, compressibility (gradient of velocity), and the vorticity to refine the computation grid. For reactive flow, she proposed 4 measures, of which only 3 are applicable for Micromix simulations due to the here applied k- ϵ turbulence model, namely the gradient of specific turbulent kinetic energy, the gradient of mean temperature and the gradient of the mean concentration of species. According to Gao, these measures provide reliable detection of flame fronts and combustion zones for reactive flows.

In her research, these measures showed good results for non-premixed combustion of CH_4 , which corresponds to the research conducted on the Micromix principle. Gradients are used instead of the corresponding physical values for defining the local mesh refinement to reduce numerical errors, which are prone to form where solution properties change drastically within a short amount of time or space [105].

The solution adaptive meshing approach proposed by Gao, applied to the computational model of an MMX combustor, is displayed in Figure 3-13.

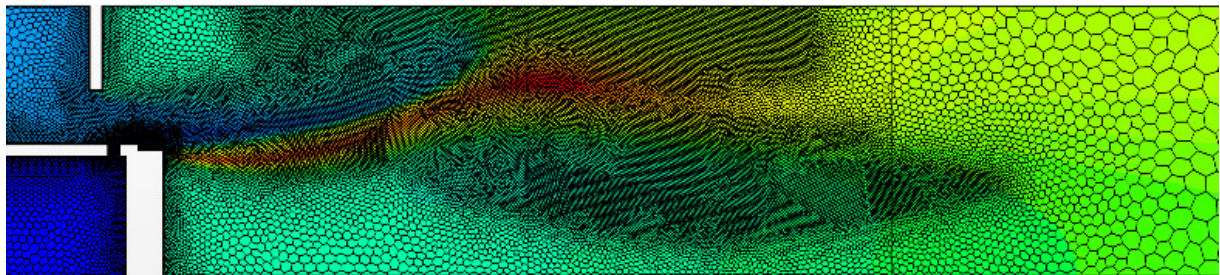


Figure 3-13: Visualization of mesh densities for the solution adaptive mesh

By application of iterative adaptive mesh refinement, unnecessary fine cells are removed in areas where coarse grids are sufficient. The highest mesh densities are locally restricted to the JICF mixing zone, the central flame region, and along the shear layers between vortex structures and the

flame. The adaptive mesh refinement process achieves a reduction of the overall cell count by approx. 50% in comparison to non-adaptive meshes used in the past while maintaining their accuracy [106]. With the solution-adaptive mesh, calculation times for combustion and flow simulations are significantly reduced, facilitating extensive parametric studies.

In order to approach the combustion characteristics of the real gas turbine combustor, which is affected by heat transfer effects, a conjugate heat transfer simulation is included in the numerical approach. By modeling and meshing the solid combustor components as well as the fluid region, heat flows through the combustor walls into the fuel supply and through the air guiding panel into the air supply area are accounted for. Striegan et al. [107] have shown that heat transfer effects influence the fuel temperature and subsequently, the injection velocity and the momentum flux ratio of the jet-in-crossflow mixing. Additionally, heat is subtracted from the main combustion zone. Both effects lead to a change in the simulated temperature profile and the generated NO_x emissions.

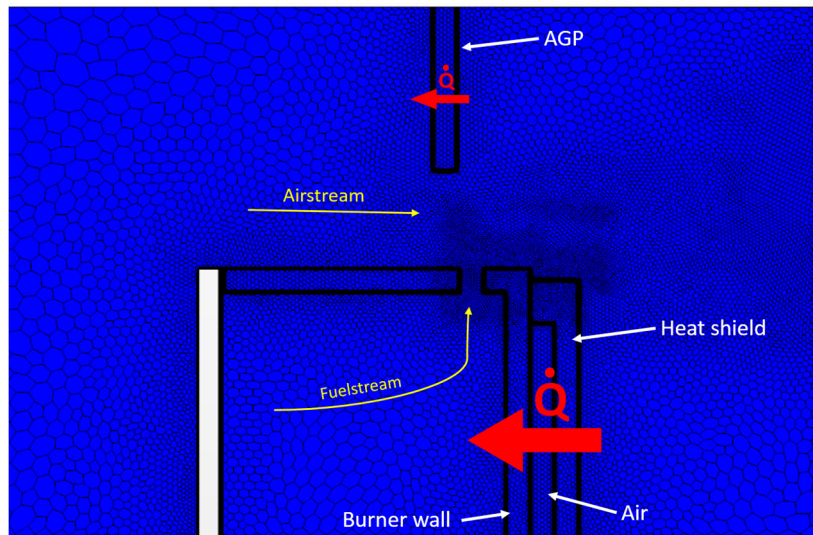


Figure 3-14: Mesh of solid combustor walls with mass and heat flows

In CFD simulations, the wall regions are of particular interest, because they are a source of vorticity in most flow problems. Depending on the chosen modeling approach, the boundary layer needs to be resolved by a fine prism layer mesh. The non-dimensional wall distance y^+ is used to decide whether a given mesh is modeled well enough to simulate the flow near walls.

$$y^+ \equiv \frac{u_* y}{\nu} \quad 3.4$$

Where u_* is the friction velocity derived from the wall shear stress and the fluid density at the wall, y is the distance from the cell to the nearest wall and ν is the local kinematic viscosity of the fluid. The inner region is defined for y^+ values between 0 and 500 and is divided into three subparts:

viscous sublayer, buffer layer, and log-law layer.

In the viscous sublayer ($y^+ < 5$), the velocity parallel to the wall is directly proportional to y^+ . Thus, solving the transport equations all the way to the wall is possible without modeling. The log-law layer ($30 < y^+ < 500$) uses a log-law to calculate the flow velocity and derives the other flow properties from the equilibrium turbulent boundary layer theory. The buffer layer ($5 < y^+ < 30$) is a transition area in which neither model works accurately [108].

In the modeling approach applied for the design process of Micromix combustors, the boundary layer shall be resolved well in order to capture all flow parameters in the air gates and especially in the fuel inlet. Thus y^+ values of 5 or less are required on all combustor walls. As can be seen in Figure 3-15, y^+ values of less than 1 are achieved with the chosen approach of prism layer meshing.

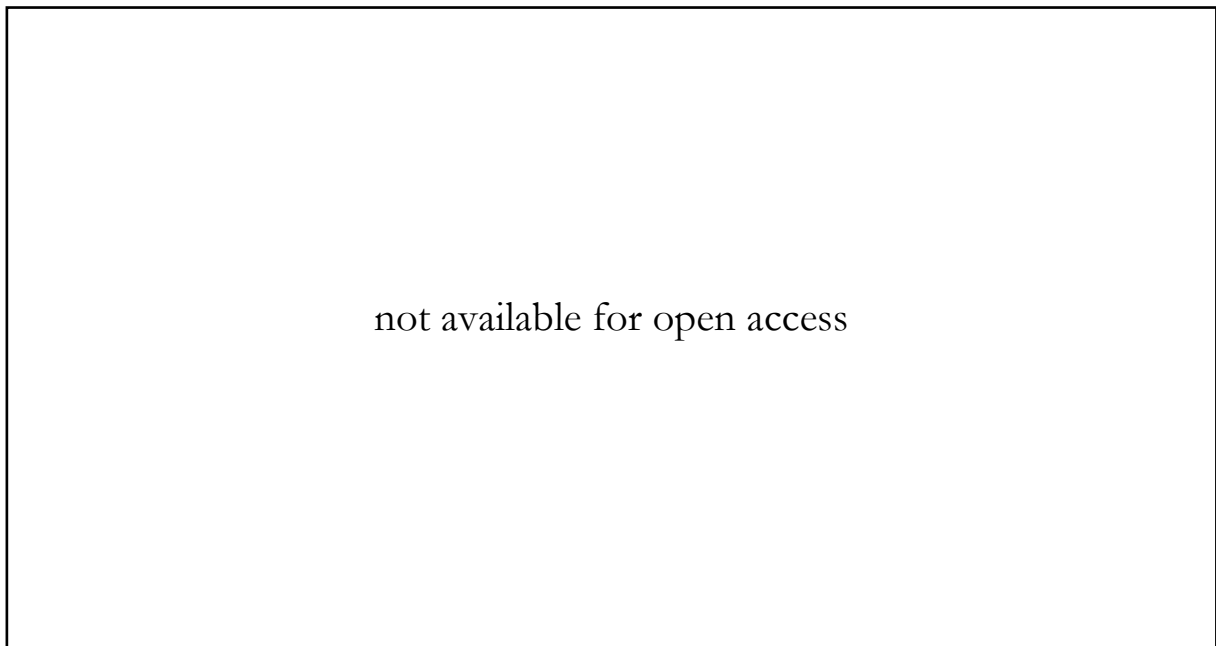


Figure 3-15: y^+ values on burner walls at the air gate and the fuel inlet

3.2.2 Reaction Kinetic Fundamentals

Combustion kinetics are the basis for the applied numerical combustion models as they deliver the reaction rates of the elementary processes occurring on a molecular basis during combustion. In the following, the theoretical background to describe the time dependence of chemical reactions is established. It is applied in subsequent chapters for the discussion of detailed reaction mechanisms, which are the basis for the applied numerical approach.

A chemical reaction begins with the collision of two or more molecules. In endothermic reactions, their kinetic energy is used to break the chemical bonds between atoms. When no recombination occurs, they form new molecules with different characteristics. Exothermic reactions release energy

in the form of heat and take place when the educts (participating molecules in the reaction) are on a higher energy level than the products of the reaction.

Chemical reactions that result directly from intermolecular collisions are called elementary reactions. They take place on the molecular level precisely as the chemical equation describes [32]. The combination / summation of several elementary reactions leads to the formulation of global reactions, characterized by a reaction formula that includes global educts and products but no intermediate species.

The reaction rate describes the rate of formation or consumption of a species in a chemical reaction. It is defined as the concentration change of a given species per time unit. The rate of reaction is proportional to the collision frequency, which in turn is proportional to the involved species concentrations. For elementary reactions, the rate depends solely on the reaction rate constant and the concentration of reactants.

For a general elementary reaction:



the reaction rate for species AB is:

$$-\frac{d[AB]}{dt} = k[AB][C] \quad 3.6$$

Where [AB] and [C] represent the concentration of species AB and C, and k represents the reaction rate constant of the elementary reaction. The negative sign indicates that species AB is being consumed in the forward reaction, thus decreasing in concentration. For chemical reactions that are composed of a forward and a backward reaction, the reaction rate for one involved species can be obtained by:



$$\frac{d[BC]}{dt} = k_f[AB][C] - k_b[BC][A] \quad 3.8$$

There is a strong non-linear dependence between the reaction rate constant and the temperature. Arrhenius proposed an exponential correlation to describe the temperature dependence [109]:

$$k = A * e^{\left(\frac{-E_A}{R_s * T}\right)} \quad 3.9$$

More recently, accurate measurements showed a temperature dependence of the pre-exponential factor A', which is usually small in comparison to the exponential dependence [32].

$$k = A' * T^b * e^{\left(\frac{E_A}{R_s * T}\right)} \quad 3.10$$

The activation energy E_A corresponds to an energy level to be overcome during the reaction (cf. Figure 3-16). Its maximum value corresponds to the bond energies in the molecule, but it can also be much smaller if new bonds are formed simultaneously with the breaking of the old bonds.

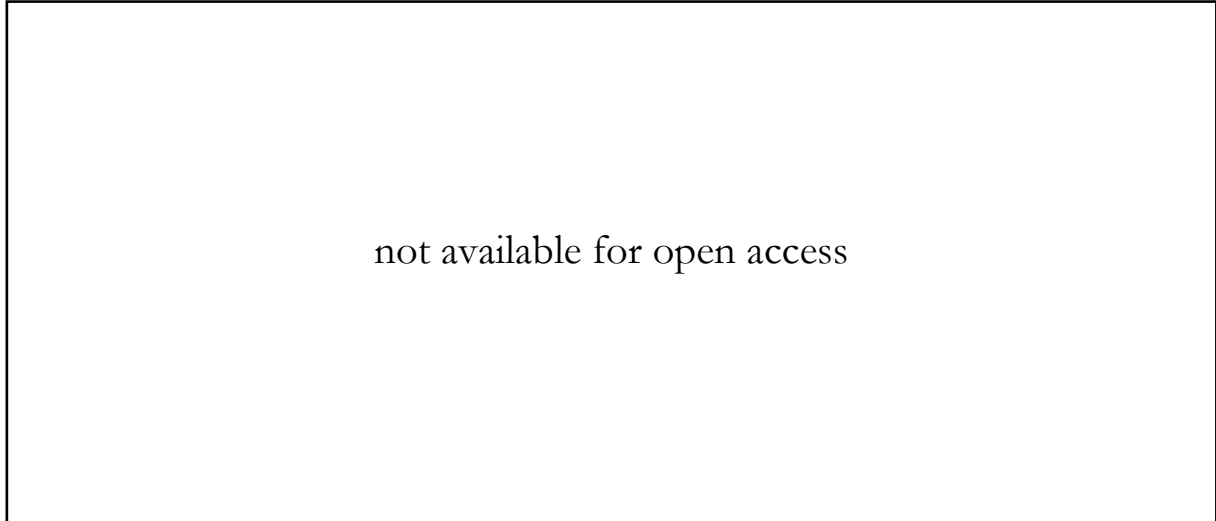


Figure 3-16: Energy diagram for a chemical reaction [32]

The Arrhenius parameters A' , b and E_A are listed for a set of elementary reactions in reaction schemes. They form the basis for describing the time dependence of chemical reactions and thus for the combustion modeling approach discussed in the following.

3.2.3 Modeling the Reactive Flow Regime

During the design process of gas turbine combustors, CFD tools are applied for the numerical prediction of the combustion performance, exhaust emissions, thermal loads, the effectiveness of cooling methods, combustion instabilities, thermoacoustic effects, etc. For the analysis of single design cases or academic combustion problems, sophisticated modeling approaches like Large Eddy (LES) or Direct Numerical Simulations (DNS) are suitable. These provide the most detailed modeling of the flow regime and in combination with a suitable combustion model, are capable of predicting combustion processes most accurately. Due to the excessive computational expense that is necessary to resolve turbulence with little or no modeling, these methods are not feasible for the extensive parametric studies that are pursued during this thesis. For a numerical preliminary study, detailed in chapter 3.2.4 and the extensive parametric studies, detailed in chapter 5, steady and transient simulations based on the well-known Reynolds Averaged Navier Stokes (RANS) equations are performed [110, 111]. Since turbulence effects are not resolved by the numerical grid,

the Reynolds Stress Tensor is modeled by application of a realizable k- ϵ turbulence model [108, 111], which has proven its robustness and accuracy, when applied to the Micromix combustion process in several preceding studies [42, 112]. The RANS approach is basically valid for modeling high turbulence flows, and as the work of Penkner [113] shows, it is able to reproduce jet-in-crossflow characteristics, as present for Micromix combustion.

The flow solver is coupled with combustion models to calculate the reaction state space. They predict the concentrations of the various species present in chemical reactions, as well as the quantities they influence (density, viscosity, and temperature).

A large chemical reaction set, like for hydrocarbon combustion, can span a wide range of time scales. Besides, the turbulent flow field imposes its own limits on length and time scales. These scales range from Kolmogorov and Batchelor scales at the low end, to the large, energy-containing eddy scales at the high end. Resolving these length and time scales in a reacting flow system demands excessive computational resources. Therefore, combustion models are required to account for the processes that occur at length and time scales below what can be resolved on a numerical simulation grid [108]. The four basic types of combustion models in the repository of Star-CCM+ that are suitable for non-premixed combustion cases are:

- Eddy break-up (EBU) models
- Complex Chemistry model
- Presumed Probability Density Function (PPDF) models
- Progress Variable models (Flamelet Generated Manifolds, Steady Laminar Flamelet)

The choice on a specific combustion model is mainly driven by the ratio of turbulent mixing time scale and reaction time scale, described by the turbulent Damköhler number:

$$Da = \frac{t_{mix}}{t_{react}} \quad 3.11$$

For $Da \gg 1$, the flow field is characterized by high reaction rates (low reaction time scales) in combination with high mixing time scales. Therefore, it is only the turbulent mixing that brings together the reacting species, which controls the reaction rate and leads to a purely turbulence driven reacting system. In this case, standard EBU and equilibrium PPDF models are suitable for the simulation approach, since they assume that the reaction occurs instantaneously upon mixing. For $Da \approx 1$, finite rate kinetics must be considered. The overall reaction rate depends on the mixing, that brings the reacting species together, as well as on the individual reaction rates. The adiabatic PPDF model can be extended by the use of the laminar flamelet instead of the equilibrium approach. The EBU model can be extended to account for these effects using reaction rates from

finite-rate kinetics, which are based on mean species concentration and mean temperatures. In the past, a hybrid EBU model coupled with a global reaction equation by Fernández-Galisteo [114] was applied for Micromix combustion of pure hydrogen [44].

A more general approach for modeling finite-rate kinetics that is applied in the framework of this thesis makes use of the complex chemistry model. It can be combined with detailed reaction schemes of varying complexity. It is suitable for simulations, where a detailed description of non-fuel and oxidizer species is required, as well as finite rate kinetics have to be taken into account, for example, for calculating slowly forming species like CO [108]. It is, however, computationally expensive, since the chemical step is solved through ordinary differential equations (ODE).

The applied ODE solver integrates the chemical composition equations based on a homogeneous reactor formulation within each cell. Temperature and pressure-dependent chemical source terms are calculated based on the aforementioned Arrhenius formulation for reaction rates. The individual species transport equations are solved as ordinary differential equations at each time step of the flow field. The formulation of the complex chemistry model shall be briefly discussed here. As described in [108], the general species transport equation for any given species [i] is given as:

$$\frac{\partial}{\partial t} \rho * g_i + \frac{\partial}{\partial x_j} (\rho * c_j * g_i + F_{k,j}) = \omega_i \quad 3.12$$

With $F_{k,j}$ being the diffusive flux component and the source term ω_i , being the rate of production of species [i]. Taking into account the differing time scales for the chemical reactions and the flow field, the general species transport equations are decoupled with the help of an Operator-Splitting Algorithm. At each time step, the chemical state is solved first from the initial state to an intermediate state. Here only the chemical source term is accounted for; thus, no convection or diffusion occurs [108]:

$$g_i^* = g_i + \int_0^\tau r_{k,i} dt \quad 3.13$$

With $r_{k,i}$ being the mean temperature-, pressure- and composition-dependent production rate of species [i]. The reaction source term ω_i applied in the general species transport equation 3.12 depends on the local instantaneous species and temperature distribution as well as on local turbulence effects. As discussed earlier, these effects are not resolved on the numerical grid in RANS calculations. To solve this closure problem, different models are available, which account for these so-called turbulence-chemistry interactions. In the framework of this thesis, the Eddy Dissipation Concept (EDC) by Magnussen is applied [115]. Each cell is divided into a fine structure zone, where all chemical reactions and the dissipation of turbulence energy occur, and a bulk gas zone, where reactions are neglected. Mass transfer exchanges reactant and product species between

both zones. Within the fine structure zone, a well-stirred reactor is applied, taking into account the regarded species, the detailed reaction mechanism, and the ambient conditions.

For the second step of the Operator-Splitting Algorithm, the species transport equation 3.12 is solved with an explicit reaction source term ω_i , given as:

$$\omega_i = \rho * f * \left(\frac{g_i^* - g_i}{\tau} \right) \quad 3.14$$

With g_i^* being the mass fraction at the end of the initial time integration τ . f denotes the mean reaction rate multiplier, which accounts for the turbulence interaction with the reacting system:

$$f = \left(\left[C_1 \left(\frac{v * \tau_{turb}}{L^2} \right)^{0.25} \right]^{-3} - 1 \right)^{-1} \quad 3.15$$

Here, C_1 is the fine structure length constant with a default value of 2.1377, v is the kinematic viscosity, τ_{turb} is the turbulent time-scale, and L is the turbulent length scale. Since turbulent time and length scales are not explicitly solved on the numerical grid, they are retrieved from the applied turbulence model.

Since for the complex chemistry model the computational effort rises with additional species that are explicitly solved by transport equations, detailed reaction calculations are computationally demanding for extensive H_2/CH_4 mechanisms.

A Progress Variable model based on Flamelet Generated Manifolds (FGM) combines the benefits of the detailed reaction mechanism with low computational effort [116]. With this modeling approach, the complexity of the detailed reaction mechanism is decreased by creating a low dimensional manifold parameterized by mixture fraction and a progress variable in the Star-CCM+ workflow. A constant pressure reactor system is applied to generate tabulated chemistry for non-premixed combustion cases. The method takes advantage of the assumption that the chemical processes within this 0D reactor are comparable to a three-dimensional flame. Based on the constant pressure reactor calculations, the combustion progress (temperatures, densities, species concentrations) is tabulated in a preprocessing step. During the actual CFD-simulation, the computational effort is reduced by replacing the full set of transport equations by fewer transport equations for only the controlling variables. Solving these and retracting the information from the tabulated chemistry delivers the necessary results for a combustion simulation like temperature or species profiles [108, 116].

The performance of the hybrid EBU, the FGM, and the complex chemistry model, applied to a recent Micromix combustion test case fueled with hydrogen and hydrogen-rich syngas, was tested in [117]. Due to the lack of the radical species (O, H, OH) in the global reaction approach used in the hybrid EBU model, high deviations between the simulated and the measured NO emissions

were present. Additionally, no reverse reactions are considered by this modeling approach. These are necessary for predicting unburned fuel emissions in the combustor overload regime, where a shift of the equilibrium concentration leads to increased fuel emissions. For the FGM model, coupled with a steady RANS approach applied in [117], a significant underestimation of unburned fuel emissions occurred as well. The FGM model proved to be generally suitable to reduce the computational effort, but the deviations concerning unburned fuel emissions and CO arise from the general tendency towards equilibrium conditions at relatively fast timescales in comparison to the complex chemistry model.

Based on the conducted assessment of the hybrid Eddy Break-Up model, the Flamelet Generated Manifolds approach, and the use of detailed reaction mechanisms in a complex chemistry model, the latter is chosen for the parametric studies presented in chapter 5.

3.2.4 Choice of a Suitable Combustion Mechanism for H₂/CH₄ Combustion

For identification of potential reaction mechanisms, suitable for application in the numerical characterization and optimization process of the Micromix combustion principle, a numerical preliminary study is performed. The validation test case is the bluff-body stabilized flame HM1, investigated in detail by the University of Sydney [118]. It offers a desirable similarity to genuine gas turbine combustors used in the industry (applied H₂/CH₄ fuel mixture, recirculation areas that act as flame holders, fuel injection, etc.) and a broad database of experimental results as well as well-defined boundary conditions.

A schematic drawing of the combustor geometry is displayed in Figure 3-17. It consists of a circular bluff-body with a diameter of 50 mm that is centered in a coflowing stream of air with a velocity of 40 m/s. At its center, an orifice with a 3.6 mm diameter is located to act as a fuel nozzle. The combustor is fueled with a mixture of 50 vol.% methane and 50 vol.% hydrogen at a velocity of 118 m/s. In the wake region of the bluff body, hot gas recirculation stabilizes the flame to the burner face. At sufficiently high fuel velocities, the jet flow penetrates through the recirculation zone and forms a jet-like flame further downstream.

Experimental test data is provided by the Clean Combustion Research Group at the University of Sydney [118]. Laser Doppler Velocimetry (LDV) is used for the simultaneous measurement of the axial and radial velocity components. 400 data points are recorded at each location. The measurements are made at different axial locations in the recirculation zone, with radial measurements at 1 mm increments. For the measurement of temperatures as well as major and minor species of the mixing field, the Raman/Rayleigh/LIF technique is used. Measured species

are N_2 , O_2 , CH_4 , CO , CO_2 , H_2 , H_2O , OH , and NO . The concentrations are deduced from inelastic Raman scattering, while the temperature is obtained from the Rayleigh signal. The laser-induced fluorescence technique is applied for the two minor species NO and OH . Typically, 800 data points are collected at each measurement location across the full width of the flame. The mixture fraction for each data point is calculated from the measured mass fractions of all species.

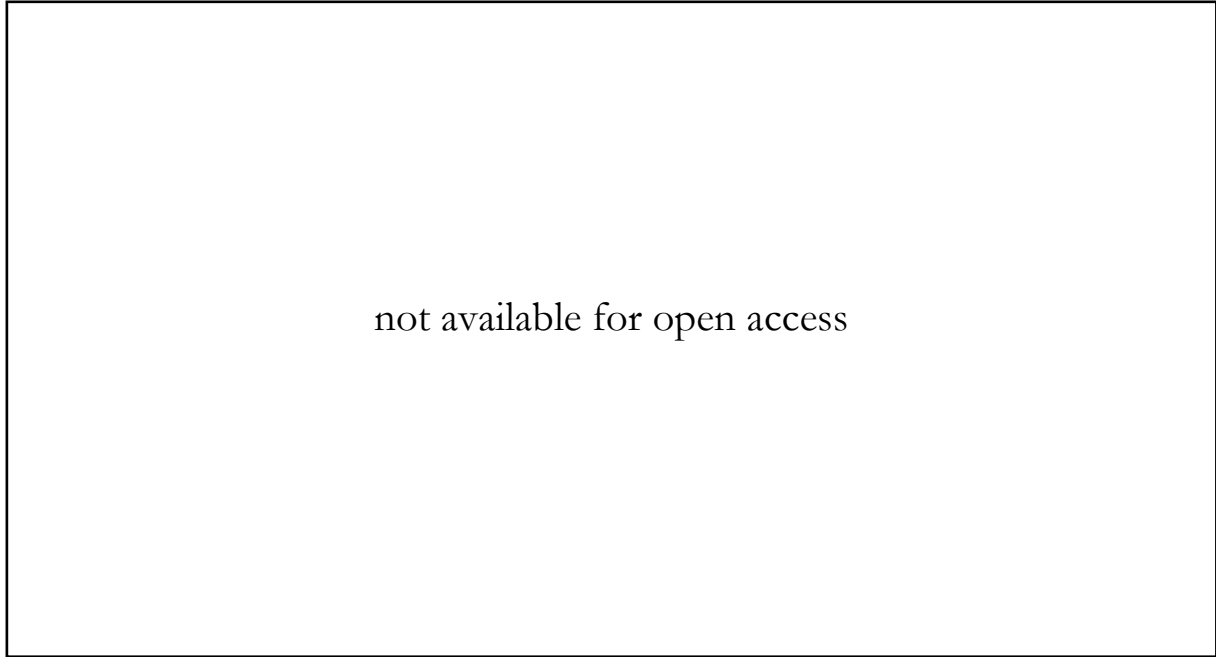


Figure 3-17: Schematics of the Sydney bluff-body burner [118]

The preliminary study focuses on the impact of different detailed reaction mechanisms with variable complexity on the numerical solution of the presented experimental test case. The reactive flow regime is solved by the commercial CFD-code Star-CCM+ with the application of a three-dimensional, unsteady, pressure-based RANS solver using the standard k - ϵ -turbulence model with all y^+ wall treatment.

Since numerical simulations using the standard k - ϵ -model tend to overestimate the turbulence dissipation within the recirculation areas of the bluff-body flame, the $C_{1\epsilon}$ constant is changed to a value of 1.6 based on [119]. Figure 3-18 shows a comparison of the axial velocity for the two $C_{1\epsilon}$ values with measurement data obtained at an axial location of 0.065 m. It can be seen that a value of 1.44 tends to underestimate the central fuel jet velocity, while the 1.6 value reproduces the course of the velocity distribution closely.

The chemical reactions of the combustion process are solved by a complex chemistry model described in detail in the preceding chapter. The 6 reaction mechanisms applied by the complex chemistry model for this study range in complexity between 16 and 118 species and between 41 and 665 reactions, respectively (cf. Table 3).

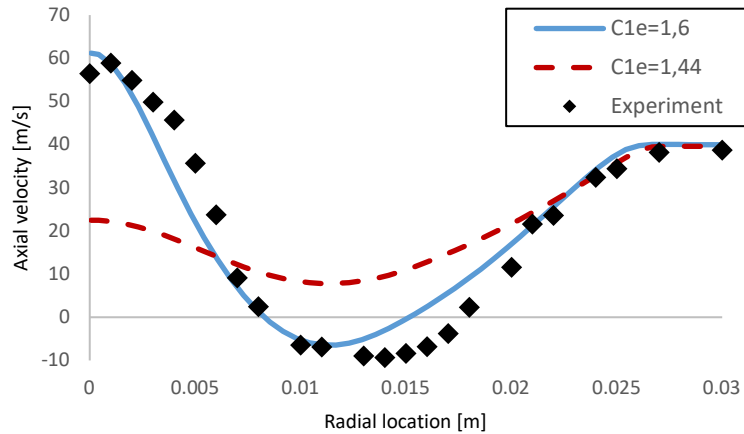


Figure 3-18: Axial velocity distribution at $x=0.065$ m simulated with variable C_{1e} constants

The mechanisms chosen are GRI 3.0 (5), derivatives of GRI 3.0 and GRI 1.2 ranging down from 30 to 17 species (2)-(4), a skeletal reaction mechanism with 16 species (1) and a comprehensive mechanism from the National University of Ireland Galway (6). The GRI3.0 (5) and the DRM 22 (3) mechanisms have already been applied successfully in the numerical simulation of hydrogen/methane combustion [120–123]. The GRI 3.0 (5) provides detailed mechanisms for nitrogen oxide formation. For the remaining mechanisms, a thermal NO model based on the extended Zeldovich equations is applied (cf. chapter 3.2.5). For modeling of turbulence-chemistry interactions, the Eddy Dissipation Concept (EDC) [115] is used.

Table 3: Summary of the investigated detailed reaction mechanisms, number of species and reactions

No.	Name	Species	Reactions	References
1	Star-CCM+ internal CH ₄ mechanism	16	41	[124]
2	Star-CCM+ internal CH ₄ mechanism	17	73	[125]
3	DRM22	24	104	[126]
4	Star-CCM+ internal CH ₄ mechanism	30	184	[127]
5	GRI 3.0	53	325	[128]
6	NUI Galway	118	665	[129]

The boundary conditions used in the simulations are specified based on the experimental data [118]. For capturing the effect of conjugate heat transfer, the computational domain is composed of a fluid region and a solid region that represents the ceramic bluff-body (cf. Figure 3-19). Due to the fully symmetrical nature of the bluff-body flame, a 2D axisymmetric mesh is generated. The mesh density is varied between the fuel pipe, flame region, and co-flow.

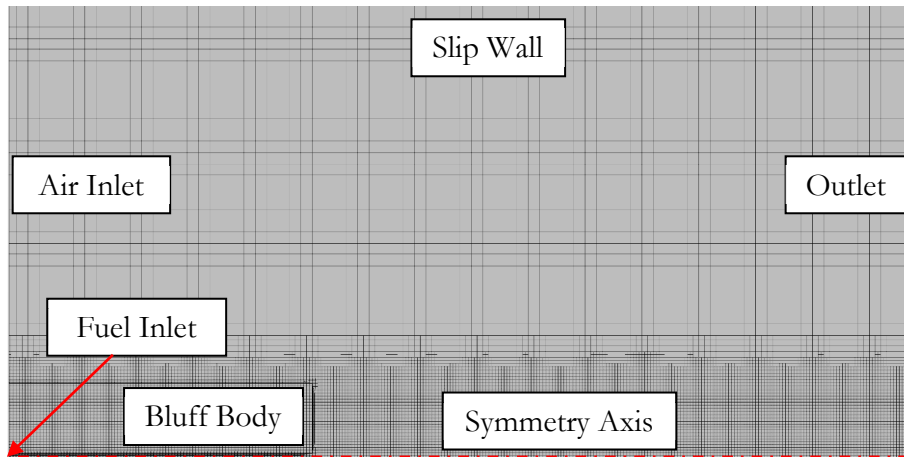


Figure 3-19: 2D axisymmetric computational domain and simulation grid

A mesh dependency study targeting several exhaust gas components (volume fraction of H_2 , CH_4 , O_2 , H_2O , and CO_2) and temperatures (mean outlet temperature and maximum flame temperature) is performed for 5 different mesh sizes ranging between 10k and 110k cells (cf. Figure 3-20). Mesh independence is achieved with a total cell count of approx. 48k cells, including a prism layer mesh to resolve the boundary layer.

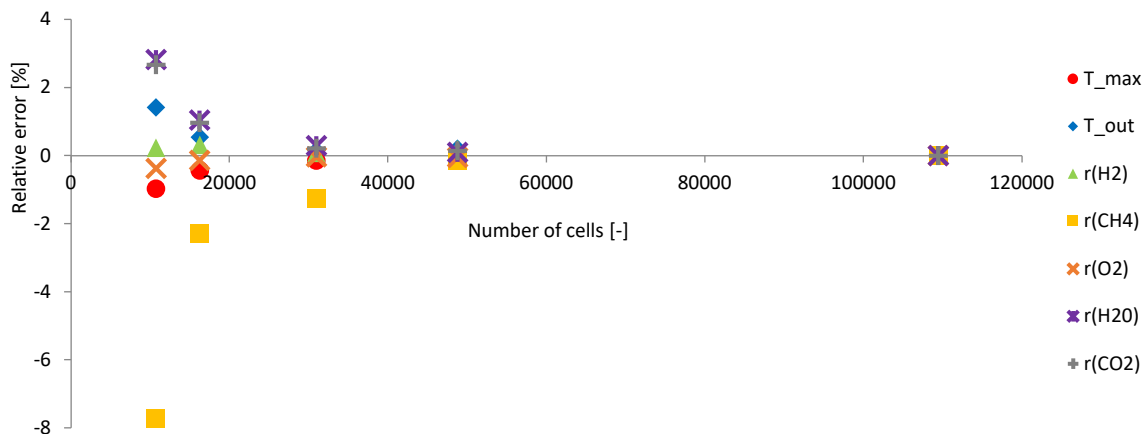


Figure 3-20: Relative error of several combustion parameters with respect to the finest mesh

In Figure 3-21, the simulated temperature distribution of the HM1 flame is displayed along with the simulated and measured axial temperature profile for the domain spreading between 0.1 m upstream and 0.2 m downstream of the bluff-body face. All investigated reaction mechanisms predict nearly the same axial temperature profile that is shifted slightly downstream in the axial direction when compared to the experimental results. This shift might be a result of the chosen simplified turbulence modeling approach, which is constant between all tested combustion models. The following evaluation of the radial species profiles obtained with the 6 different reaction mechanisms is performed at an axial location of $x = 0.013$ m. Here the influence of the turbulence model constant $C_{1\epsilon}$ on the velocity and species profiles is small compared to farther downstream

locations, and potential inaccuracies in modeling the turbulence dissipation have little impact on the results.

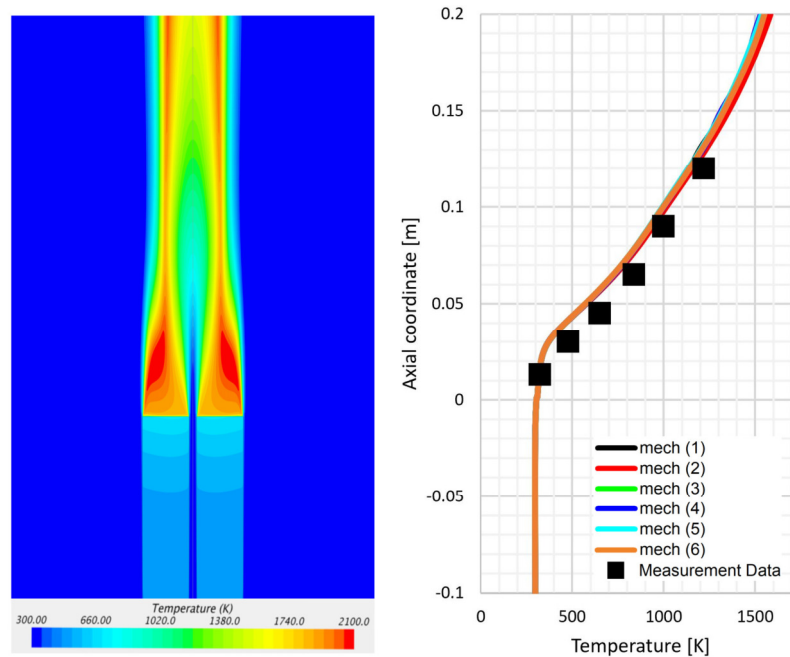


Figure 3-21: Simulated temperature distribution (left) and simulated and measured axial temperature profile (right)

Figure 3-22 a) and b) show the radial species profiles of O_2 and H_2O . The simulated primary exhaust emissions are in close agreement with each other and with the measurement data.

The species profiles of H_2 and CH_4 are displayed in Figure 3-22 c) and d). There is a slight underestimation of the concentration level in front of the bluff-body face. In the wake region of the bluff-body, mixing of fuel and co-flowing air occurs by transport processes, e.g., convection and diffusion. Apart from present measurement errors, the chosen turbulence modeling approach can reduce the mixing or spreading effect of fuel components in the vortex region, leading to deviations. Additionally, the peak concentration of H_2 inside the fuel jet is slightly overestimated by all applied combustion mechanisms. The peak concentration of CH_4 is well modeled.

As Figure 3-22 e) shows, CO_2 emissions are in good agreement between simulation and experimental results. Significant differences between the individual reaction mechanisms are present for the CO profile, displayed in Figure 3-22 f). The differences are due to the varying fidelity of the CO chemistry integrated in the investigated reaction mechanisms.

The highest deviations are present for the peak OH concentrations in the shear layer between the bluff-body wake and the co-flowing air (cf. Figure 3-22 g). The experiment shows a small peak at this location, which is significantly overestimated by the coinciding simulation results.

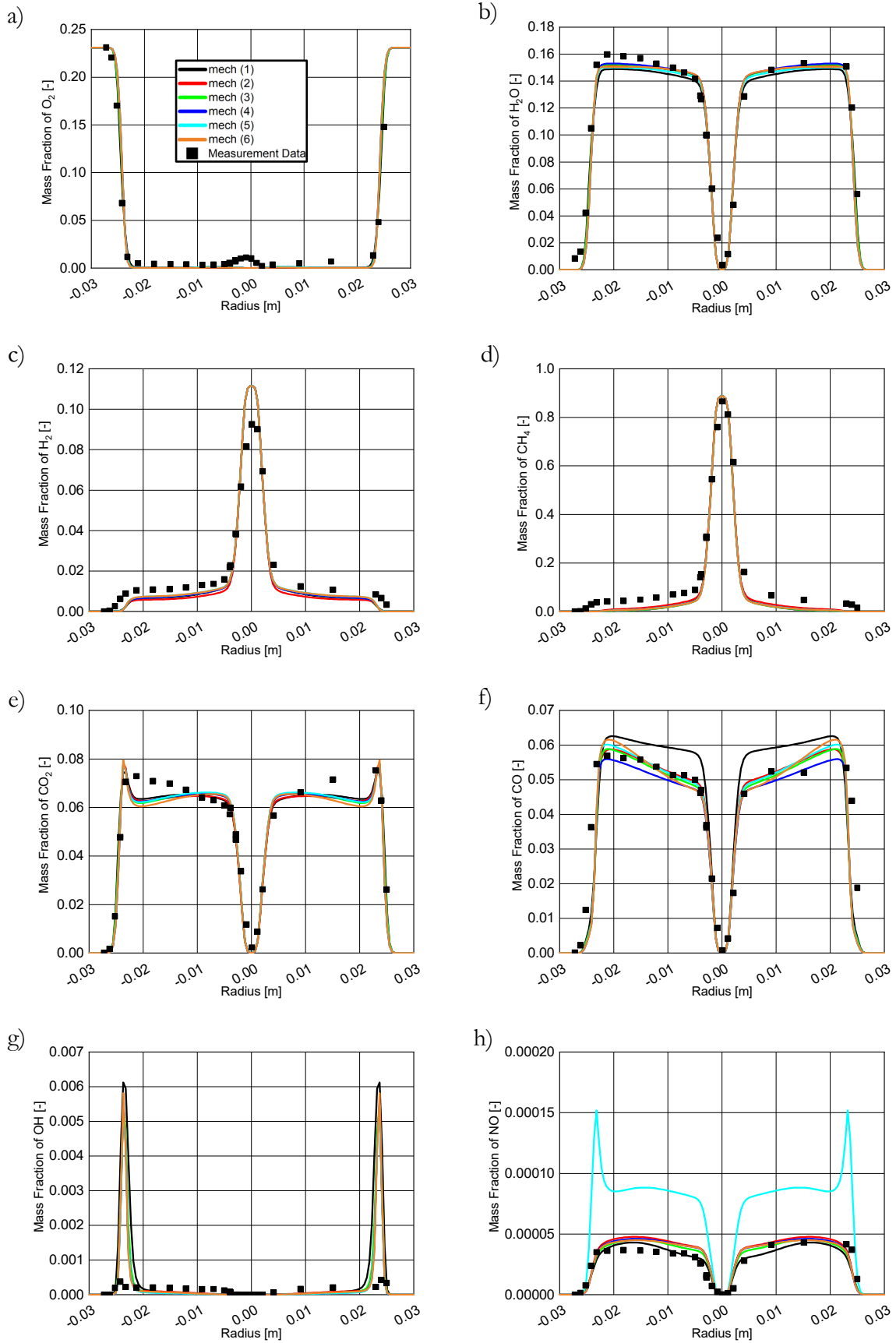


Figure 3-22: Measured and simulated radial species profiles of O_2 (a), H_2O (b), H_2 (c), CH_4 (d), CO_2 (e), CO (f), OH (g) and NO (h) at the sampling location $x=0.013\text{m}$

The results suggest that especially OH radicals are highly sensitive towards the chosen turbulence modeling approach independent of the significantly varying combustion mechanisms.

The radial distribution of NO is displayed in Figure 3-22 h). All models applying the thermal NO approach (1,2,3,4,6) yield comparable results that match the experimental results closely. The more elaborate mechanism GRI 3.0 (5) incorporates additional formation pathways (thermal NO, NH, NNH, N₂O, and prompt NO_x) that overestimate the NO emissions drastically when implemented with the chosen modeling approach.

When comparing the numerical and experimental results, not only the simplifications of the numerical approach but also the inaccuracies of the measurement have to be taken into account. There are several sources of error that need to be considered in evaluating the overall accuracy of laser-based measurements of species concentrations in flames. These are photon noise, interference errors, and spatial resolution. Photon noise is associated with the number of photons n collected by a given detector at each laser pulse and decreases proportionally to $\frac{1}{n^{0.5}}$. This noise is expected to become significant at species mole fractions less than a few percent [118]. The interference error depends on the magnitude of the fluorescence or chemiluminescence interference with the measured species. The error due to spatial resolution is not considered to be substantial. The overall measurement errors are highly dependent on the combustion conditions and the measured species. Typical error levels are reported in [118] and achieve maximum values of 12.5% for H₂ measurement under lean conditions.

For evaluating the differences in the overall combustion progress within the simulated domain, an analysis is carried out based on the cumulated exhaust mass flows per species. This parameter isolates the total production or consumption of a single species independent of the overall exhaust gas composition. It is calculated from the mass flow averaged mass fraction of the individual species at the domain outlet and the total exhaust gas mass flow. Figure 3-23 shows the relative deviation of the investigated mechanisms for the different species exhaust mass flows with reference to the simulation result of the well-established GRI 3.0 (5) mechanism.

Concerning the primary exhaust emissions O₂, H₂O and CO₂, all mechanisms except for (1) show deviations less than 1% between each other. The deviations of the GRI 1.2 and GRI 3.0 derivatives (2-4) with respect to the GRI 3.0 results (5) decrease with increasing species count. The deviations produced by mechanism (3) do not exceed 2.7%, whereas mechanism (4) shows nearly identical results as the GRI 3.0 (rel. error < 0.11%). Since the more elaborate mechanisms (5) and (6) have been developed independently with varying validation goals, the apparent deviations are comprehensible. The results of these 2 mechanisms fall in an error margin of less than 5%.

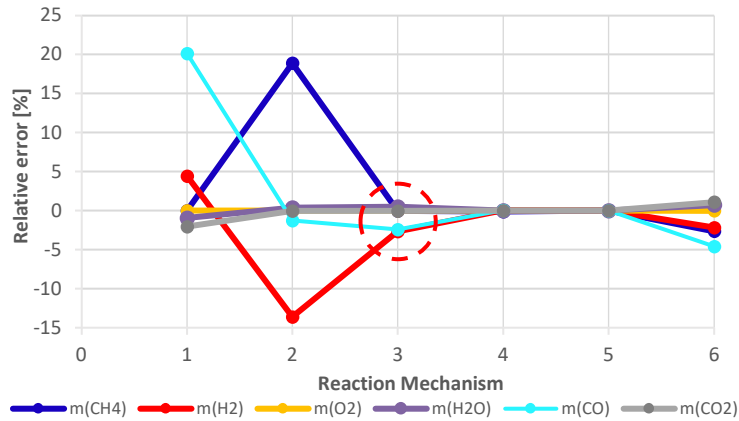


Figure 3-23: Relative error of cumulated species mass flows $m(i)$ with reference to GRI 3.0 (5) at the domain outlet

As time is a limiting factor for extensive parametric studies, a particular focus is laid on the computational expense of each mechanism to choose a reaction set that delivers the best compromise between accuracy and computation time. Figure 3-24 shows a comparison of the relative computation times with reference to GRI 3.0 (5).

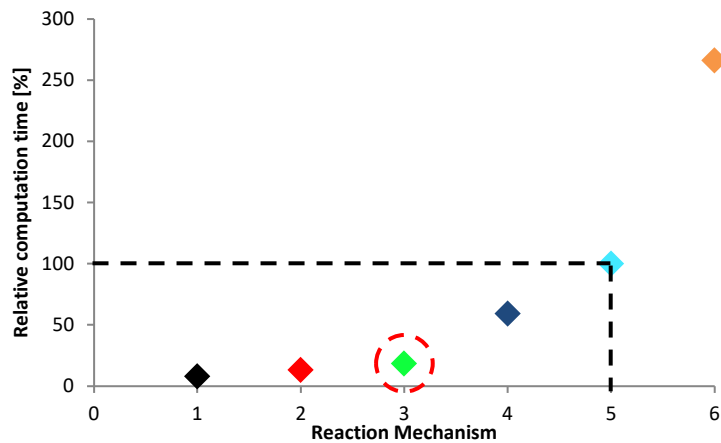


Figure 3-24: Relative computation time per time step for different reaction mechanisms with reference to GRI 3.0 (5)

Apparently, mechanism (4), which shows a good representation of the investigated test case, and closely matches the GRI3.0 results, reduces the computational time by approx. 40%. However, with the minor deviations displayed throughout this preliminary study and with a reduction of the computational time by approx. 80%, the DRM22 mechanism (3) is chosen for the numerical parametric studies presented in chapter 5.

3.2.5 NO_x Emission Modeling

The commercial CFD-code Star-CCM+ that is applied for the numerical design space exploration accompanying the experimental testing in chapter 5 offers emission models that treat NO formation as a general indicator of the overall NO_x emissions of a combustion system. The three formation pathways that are accounted for are fuel, thermal, and prompt NO. The transport equation that is used to solve for NO_x is the same for all models, with the addition of reacting source terms to account for each formation pathway [108]. Since the NO concentration is usually low compared to other species in combustion systems, it is generally agreed that NO chemistry has negligible influence and can be decoupled from the main combustion and flow field calculations. The species NO is therefore implemented as a passive scalar with source terms defined by the regarded formation pathways.

The first emission model treats fuel NO, which is the product of converting bonded nitrogen in the hydrocarbon fuel into nitric oxide. The fuel NO-formation mechanism is dominant for coal combustion since coal includes around 1% of bonded nitrogen. As fuel NO is irrelevant for the combustion of hydrogen and methane, it will not be treated further in the present thesis [32].

As a suitable indicator for NO_x emissions under lean hydrogen combustion with the MMX combustion principle, the thermal NO model has been applied in the past with success [117]. It is based on the extended Zeldovich mechanism. Crucial for this NO formation mechanism is the concentration of oxygen molecules that is available during combustion. At 1850 K and more, the dissociation of the oxygen molecules increases with rising temperature. This leads to a higher concentration of atomic oxygen, which accelerates NO formation. The first two reactions of the thermal NO pathway take place in oxygen-rich (lean) regions of the flame.

Table 4: Arrhenius parameters for the thermal NO reaction mechanism, as described in [108]. Units are m³, kmol, s, K

	Forward			Backward		
	A'	b	E _A /R _s	A'	b	E _A /R _s
(1) $N_2 + O \xrightleftharpoons[k_{-1}]{k_1} NO + N$	1.8E11	0.0	38370	3.8E10	0.0	425
(2) $N + O_2 \xrightleftharpoons[k_{-2}]{k_2} NO + O$	1.8E07	1.0	4680	3.8E06	1.0	20820
(3) $N + OH \xrightleftharpoons[k_{-3}]{k_3} NO + H$	7.1E10	0.0	450	1.7E11	0.0	24560

They are displayed in Table 4 along with the coefficients A' , b , and E_A/R_s of the advanced Arrhenius equation 3.10 used for the applied thermal NO model. In fuel-rich zones of the flame and above 1850K, the third displayed elementary reaction is predominant. The name “thermal NO” is derived from the required activation energy due to the forceful triple bond of N_2 .

Thermal NO has proven in the past to be a suitable indicator of the general NO_x emission characteristic of experimentally investigated test burner configurations, and due to its post-processing capability allows a fast prediction prior to testing. Within Star-CCM+, the thermal NO model is implemented as a passive scalar with a source term derived from the three reaction equations stated above.

$$\begin{aligned} \frac{d[NO]}{dt} = & k_1[O][N_2] + k_2[N][O_2] + k_3[N][OH] - k_{-1}[NO][N] - k_{-2}[NO][O] \\ & - k_{-3}[NO][H] \end{aligned} \quad 3.16$$

For the application of the thermal NO production rate in hybrid EBU models that do not incorporate radical species, partial equilibrium assumptions need to be applied to calculate the concentrations of $[O]$, $[H]$ and $[OH]$. For detailed reaction mechanisms, this is unnecessary, since the radical concentrations are directly computed during the simulation. For the remaining unknown radical $[N]$, a quasi-steady-state assumption is introduced, since the activation energy for the reaction of N is low compared to reaction (1).

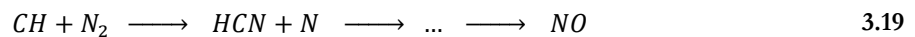
$$[N] = \frac{k_1[O][N_2] + k_{-2}[NO][O] + k_{-3}[NO][H]}{k_{-1}[NO] + k_2[O_2] + k_3[OH]} \quad 3.17$$

Thus, the total rate of NO production is given by

$$\begin{aligned} \frac{d[NO]}{dt} = & k_1[O][N_2] + (k_2[O_2] + k_3[OH] - k_{-1}[NO]) \\ & * \frac{k_1[O][N_2] + k_{-2}[NO][O] + k_{-3}[NO][H]}{k_{-1}[NO] + k_2[O_2] + k_3[OH]} - k_{-2}[NO][O] \\ & - k_{-3}[NO][H] \end{aligned} \quad 3.18$$

This formulation serves as the source term for the passive scalar formulation of the NO mass fraction in the computational domain.

The last formation route available is regarded by the prompt NO model. The formation of prompt NO is related to the radical CH , which can react in various ways. The intermediately formed CH reacts with ambient nitrogen to HCN and further to NO .



Since the formation is based on the existence of CH radicals, which can react in many different ways, a description of the formation process is much more complicated. Prompt NO is formed predominantly under fuel-rich conditions [32], which are not present during lean MMX combustion of hydrogen methane mixtures. Initial preliminary studies that accounted for thermal

and prompt NO in H₂/CH₄ MMX combustion confirmed this theoretical assessment. This is why the prompt NO model is omitted for the parametric studies conducted in chapter 5.

For the sake of comparability with the experimental results, the obtained NO emissions are corrected to 15 vol.% O₂ in the exhaust gas according to equation 3.3.

4

Micromix Combustion Principle Designed for H₂/CH₄ Fuel Mixtures

The DLN Micromix combustion principle has been initially developed for the low NO_x combustion of pure hydrogen. In recent years Micromix combustion has proven its potential for low emission combustion of hydrogen and hydrogen-rich syngas in many preceding studies [44–46]. The aim of this thesis is the exploration of the applicable fuel range towards variable mixtures of hydrogen and methane and characterization of the combustion principle under flexible-fuel operation.

For the 1st generation FuelFlex Micromix combustor, the premier design goal is fuel flexibility between 0% and 100% H₂. To adapt the Micromix principle towards variable H₂/CH₄ mixtures, the fuel parameters depending on the gas mixture composition must be determined. In the following, the main combustion characteristics are summarized, which are essential for the design process of a gas turbine combustor.

4.1 Fuel Characteristics of H₂/CH₄ mixtures

The blending of methane into pure hydrogen has a significant impact on the fuel properties and in consequence, on the combustion characteristics when applied to gas turbine combustors. Hydrogen and methane differ significantly in their molar mass, stoichiometric air requirement, lower heating value, and lean ignition limits.

4.1.1 Density

Based on the molecular weights of hydrogen ($M_{H_2}=2.0159 \frac{kg}{kmol}$) and methane ($M_{CH_4}=16.043 \frac{kg}{kmol}$), the molecular weight of any given H₂/CH₄ mixture is defined by equation 4.1.

$$M_{H_2/CH_4} = r_{H_2} * M_{H_2} + r_{CH_4} * M_{CH_4} \quad 4.1$$

With the molecular weight of the mixture M_{H_2/CH_4} defined, the composition-dependent fuel density can be calculated by equation 4.2, if ideal gas behavior is assumed.

$$\rho_{H_2/CH_4} = \frac{p}{\frac{R_s}{M_{H_2/CH_4}} * T} \quad 4.2$$

Based on the gas constant R_s , and temperature and pressure boundary conditions set to the reference conditions used in the combustor design process in chapter 4.2 ($T=298.15K$; $p=1.01325$ bar), the fuel density is illustrated in Figure 4-1 as a linear function of the mixture composition.

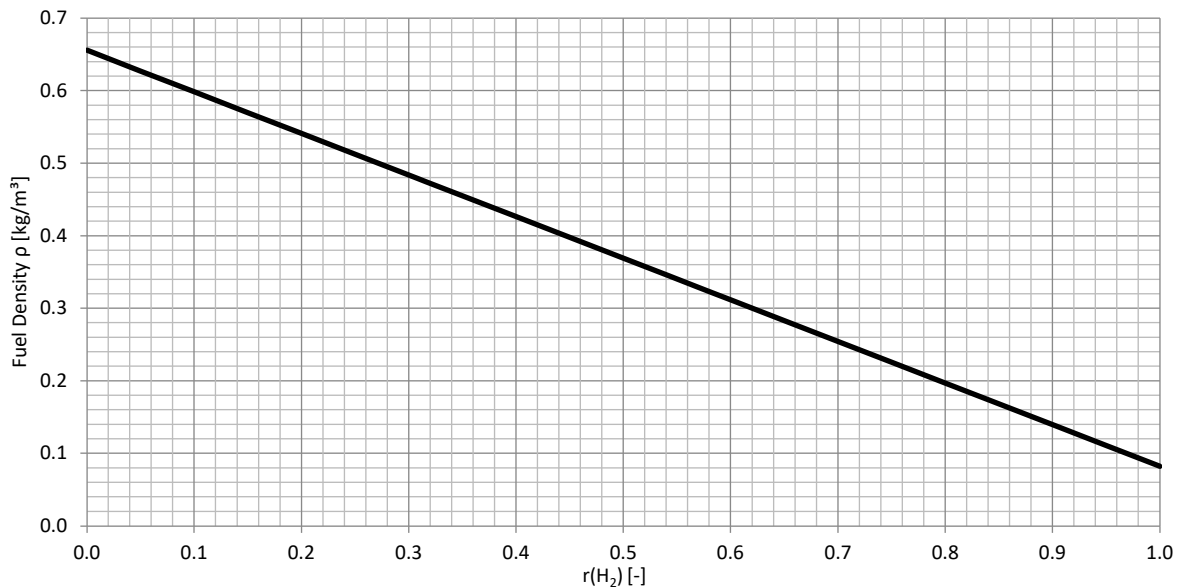


Figure 4-1: Fuel density for H₂/CH₄ mixtures at $T = 298.15$ K and $p = 1.01325$ bar

4.1.2 Lower Heating Value and Stoichiometric Air Requirement

The lower heating value (LHV) is a measure for the energy density of the fuel. It is defined as the amount of heat released by combusting a specified quantity of fuel at initially 25 °C (298 K) and returning the temperature of the combustion products in the end to 150 °C, at which the water component of the combustion products is still in the vapor state. Thus, the latent heat of vaporization of water in the reaction products is not recovered.

The LHV of variable H₂/CH₄ mixtures can be defined based on the LHVs of the individual components ($LHV_{H_2} = 119.6 \frac{MJ}{kg}$; $LHV_{CH_4} = 49.9 \frac{MJ}{kg}$) and their respective mass fractions in the fuel:

$$LHV_{H_2/CH_4} = g_{H_2} * LHV_{H_2} + g_{CH_4} * LHV_{CH_4} \quad 4.3$$

Since throughout this thesis, fuel mixtures are defined by their volumetric composition, the mass fractions needed for the stated definition are calculated based on equation 4.4.

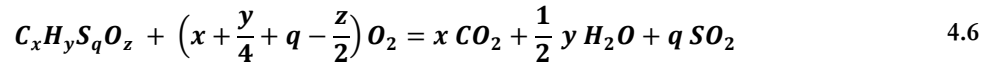
$$g_i = \frac{m_i}{\sum m_j} = \frac{r_i * M_i}{\sum r_j * M_j} \quad 4.4$$

The same linear dependence on the mass-specific mixture composition is also present for the stoichiometric air requirement (SAR).

$$SAR_{H_2/CH_4} = g_{H_2} * SAR_{H_2} + g_{CH_4} * SAR_{CH_4} \quad 4.5$$

The SAR describes the stoichiometric air-to-fuel ratio, the amount of air required for stoichiometric combustion of a specific fuel. It can be derived from the chemical equation for stoichiometric combustion, by knowledge of the molecular composition of a pure fuel.

With the general reaction equation for complete combustion



and the mass fractions of the atomic fuel components

$$c = \frac{M_C}{M_{fuel}} \cdot x \quad h = \frac{M_H}{M_{fuel}} \cdot y \quad s = \frac{M_S}{M_{fuel}} \cdot q \quad o = \frac{M_O}{M_{fuel}} \cdot z \quad 4.7$$

the stoichiometric air requirement is calculated:

$$SAR = \frac{1}{g_{O_2,air}} \cdot \left[\frac{M_{O_2}}{M_C} \cdot c + \frac{M_{O_2}}{M_H} \cdot \frac{h}{4} + \frac{M_{O_2}}{M_S} \cdot s - \frac{M_{O_2}}{M_O} \cdot \frac{o}{2} \right] \quad 4.8$$

For mixtures of hydrogen and methane, the trend displayed in Figure 4-2 is established. The LHVs for hydrogen methane mixtures range between $119.6 \frac{MJ}{kg}$ and $49.9 \frac{MJ}{kg}$, the SAR between 34.2 and 17.2. Due to the significant difference in molecular weight between both fuel components, the hydrogen mass fraction rises sharply towards hydrogen-rich fuels. This, in turn, leads to the illustrated steep increase of the LHV and the SAR at mixture compositions between 80 vol.% and 100 vol.% of hydrogen in the fuel (cf. Figure 4-2). Blending hydrogen with only 20 vol.% CH₄ results in a reduction of the LHV by 38.7% and of the SAR by 33.1%

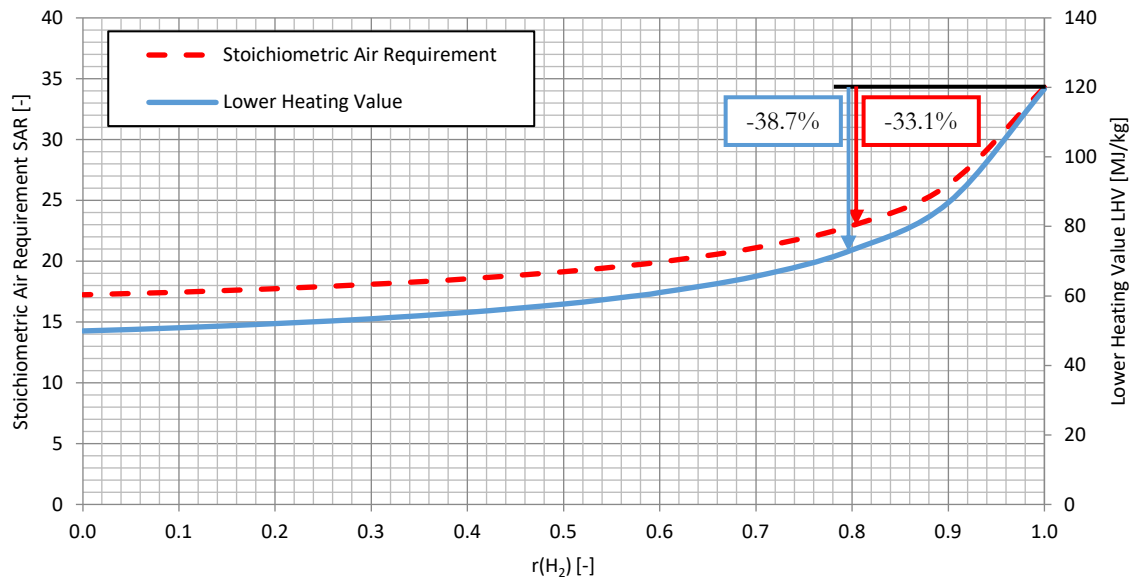


Figure 4-2: Lower heating value and stoichiometric air requirement for H₂/CH₄ mixtures

4.1.3 Wobbe Index

The Wobbe Index WI is a measure for the interchangeability of gaseous fuels. It is used to compare the thermal energy output of different composition fuel gases in combustors. If two fuels have the same Wobbe Index, then for a constant combustor geometry at given pressure and temperature boundary conditions, the thermal energy output is identical as well. The Wobbe Index for fuel compositions between 0 and 100 vol.% of hydrogen in the fuel is plotted in Figure 4-3.

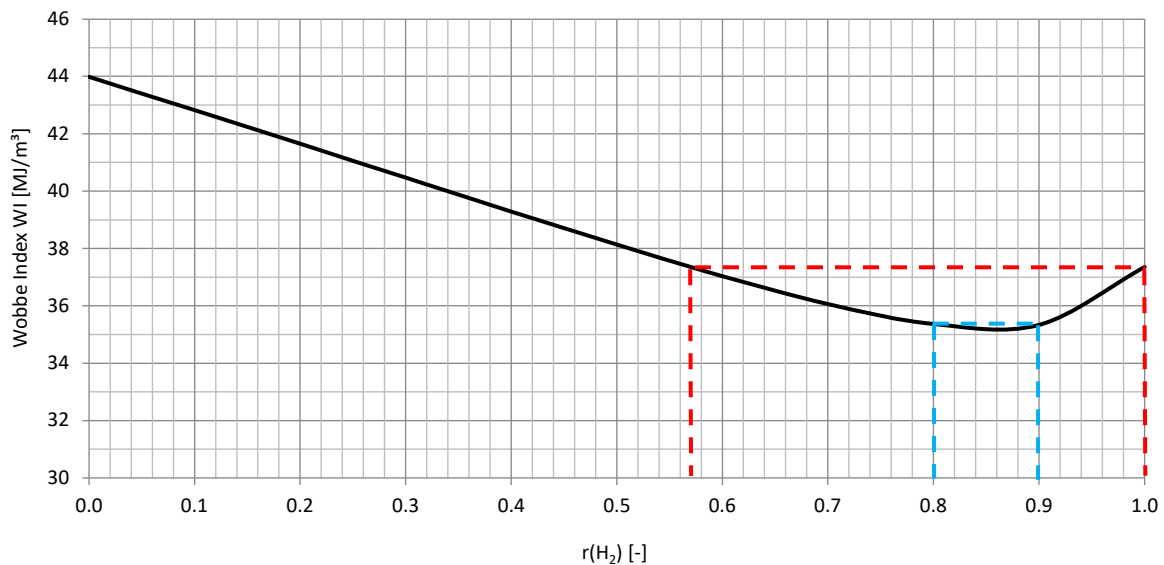


Figure 4-3: Wobbe index for H₂/CH₄ mixtures

In the fuel range between 100 vol.% and 57 vol.% of hydrogen in the mixture, the Wobbe Index stays nearly constant with deviations less than 6%, suggesting good interchangeability between the applied fuel mixtures. Due to the particular course displayed in Figure 4-3, a fuel mixture with 57% H₂ yields the same Wobbe Index as pure hydrogen fuel. The same holds for the two highlighted mixtures with 80% and 90% H₂. Towards methane-rich mixtures, the change in density, SAR and LHV leads to a significant increase in the Wobbe index (cf. Table 5)

Table 5: Summary of general gas composition and properties

r_{H2}	[-]	1	0.9	0.8	0.57	0
r_{CH4}	[-]	0	0.1	0.2	0.43	1
LHV	$\left[\frac{MJ}{kg}\right]$	119.6	86.9	73.2	59.9	49.9
SAR	$\left[\frac{kg_{air}}{kg_{fuel}}\right]$	34.3	26.3	22.9	19.7	17.2
ρ at T=298 K p=1.013 bar	$\left[\frac{kg}{m^3}\right]$	0.082	0.140	0.197	0.329	0.656
Wi	$\left[\frac{MJ}{m^3}\right]$	37.4	35.3	35.4	37.4	44.0

The significant deviations in WI between pure hydrogen and pure methane imply that the interchangeability between both fuels is not given if a constant combustor geometry is applied. There are optimal combustor geometries for each fuel, but for flexible fuel operation over a wide fuel range, compromises need to be made.

4.2 Baseline Design: 1st Generation FuelFlex Combustor V1

As presented in the previous chapters, the challenges in the flexible-fuel adaption of the Micromix combustion principle are the characteristics of the applied fuel mixtures that change significantly over the investigated mixture range. In the first step, the initial design process aims at generating a geometry that operates at a wide fuel range with acceptable emission levels and combustion efficiency. Based on this initial geometry, the fundamental characterization of the Micromix combustion principle fueled with H₂/CH₄ is conducted (cf. chapter 5.1).

4.2.1 Boundary Conditions

The boundary conditions for the structural layout of the first flexible-fuel Micromix combustor are the operating conditions of the Auxiliary Power Unit Honeywell Garrett GTCP 36-300. This small aviation gas turbine acted as a full-scale demonstrator in several preceding studies [34, 40].

The APU Honeywell Garrett GTCP 36-300 is a compact gas turbine, used for the supply of electricity and pressurized air in the Airbus A320 family on the ground and in emergencies. Since the APU is operated at approximately constant speed at all operating points, the air mass flow remains constant during operation while the fuel mass flow is adapted to the particular load condition.

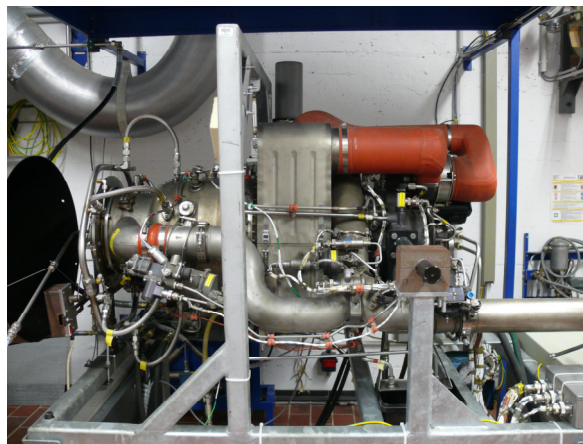


Figure 4-4: Auxiliary Power Unit – Honeywell Garrett GTCP 36-300

The control of the APU provides two operating modes:

- Environment Control Supply (ECS)
- Main Engine Start (MES)

ECS operation is used to power the electrical and pneumatic consumers of the aircraft, such as the air-conditioning system or the lighting system. In this mode, a total power output of 333 kW is

provided at a speed of 99%. MES operation is used during start-up of the main engines and is characterized by a maximum power output of 370 kW at a speed of 101%. Due to the higher power consumption in MES mode, this operating point defines the boundary conditions for the design of Micromix combustors. The essential data is given in Table 6.

Table 6: Operational data of the APU Honeywell Garrett GTCP 36-300

		ECS	MES
maximum power output	P	333 kW	370 kW
engine speed	n	62570 min ⁻¹	63830 min ⁻¹
combustion chamber inlet pressure	p_3	6.44 bar	6.69 bar
combustion chamber inlet temperature	T_3	549 K	559 K
air mass flow	\dot{m}_{air}	1.77 kg/s	1.79 kg/s
kerosene fuel mass flow	\dot{m}_{JP-1}	136 kg/h	149 kg/h

For the development of new Micromix combustors, high-pressure testing is not feasible. Thus, the operating conditions of the APU are scaled down to atmospheric conditions to facilitate testing in an atmospheric combustion chamber test stand. The air mass flow needed for atmospheric testing is scaled down from the air mass flow delivered by the APU based on Mach's similarity:

$$\dot{m}_{air,TB} = \dot{m}_{air,APU} \cdot \frac{p_{3,TB}}{p_{3,APU}} \cdot \sqrt{\frac{T_{3,APU}}{T_{3,TB}}} \quad 4.9$$

The fuel mass flows are scaled down accordingly.

The APU boundary conditions, combustor design space, thermal power output, and operating pressure define the basic geometry of the Micromix combustor. The three parameters can be summarized in the power density PD that describes the required thermal power P_{ref} in a combustor related to the available design space A_{ref} of the combustion chamber section and the operational parameters of a gas turbine p_{ref} .

$$PD = \frac{P_{ref}}{A_{ref} * p_{ref}} \quad 4.10$$

It is one of the key design parameters since it acts as a similarity relation between different combustor designs and between high- and low-pressure testing conditions. For a compact design, high thermal power output on a small combustor design space and thus high power densities are favorable. With the given boundary conditions, construction of a combustor module suitable for the APU Honeywell Garrett GTCP 36-300 determines the design power density to a fixed value of $7.6 \frac{MW}{m^2 * bar}$.

4.2.2 Scaling of the Air-Fuel-Equivalence Ratio

When converting the gas turbine operating conditions from kerosene (JP-1) to H₂/CH₄ operation, the following requirement for a constant thermal power output of the combustion chamber between both fuels needs to be fulfilled:

$$\dot{Q}_{JP-1} = \dot{Q}_{H_2/CH_4} \quad 4.11$$

$$\dot{m}_{JP-1} * LHV_{JP-1} = \dot{m}_{H_2/CH_4} * LHV_{H_2/CH_4} \quad 4.12$$

The stated requirement holds true for constant combustion efficiencies. Since gas turbine operation in the power-producing industry is only reasonable at combustion efficiencies close to 100%, this assumption is justified. Eq. 4.11 and 4.12 yield for the fuel mass flow in flexible-fuel operation:

$$\dot{m}_{H_2/CH_4} = \frac{\dot{m}_{JP-1} * LHV_{JP-1}}{LHV_{H_2/CH_4}} \quad 4.13$$

Based on the air mass flow provided by the compressor, the scaled fuel mass flows, and the mixture dependent stoichiometric air requirement, the scaled equivalence ratio is obtained:

$$\Phi_{H_2/CH_4} = \frac{SAR_{H_2/CH_4} * \dot{m}_{H_2/CH_4}}{\dot{m}_{air}} \quad 4.14$$

The equivalence ratio Φ indicates the amount of air participating in the combustion process. If the amount of air is higher than the amount required for stoichiometric combustion, values of $\Phi < 1$ are achieved (lean combustion). In contrast, values of $\Phi > 1.0$, in turn, indicate a lack of air (rich combustion).

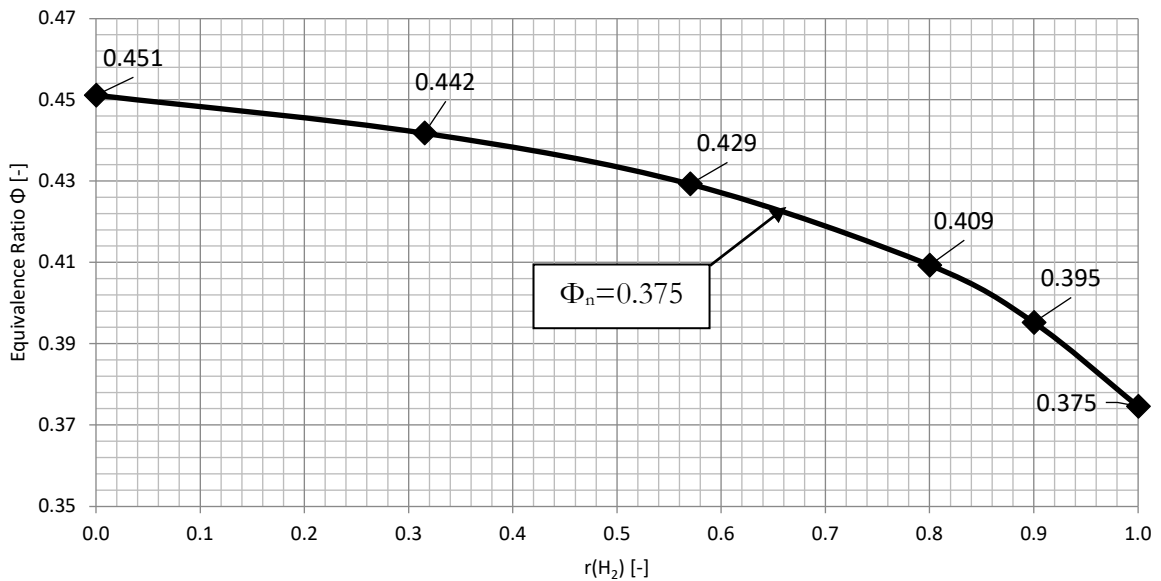


Figure 4-5: Design equivalence ratios for MES operation corresponding to $\Phi_n=0.375$

In Figure 4-5, the resulting equivalence ratios are plotted for MES conditions operated with H₂/CH₄ mixtures. Changing the mixture composition at constant boundary conditions, especially constant thermal power output, yields a shift of the gas turbine operating point. High hydrogen contents in the fuel facilitate leaner combustion due to the beneficial fuel characteristics of hydrogen, which also improves gas turbine turndown capabilities.

In the framework of this thesis, the gas turbine combustor is addressed as an isolated component. With the applied boundary condition of constant thermal power output, the shift of the operating point and of the thermal design point (equivalence ratio, exhaust gas temperature) is discussed. For an engine integration, the change in the operating conditions of the combustion chamber results in real engine effects like alteration of the operational point in the gas turbine compressor map that goes along a shift of the performance requirements of the turbine. In [130], Funke et al. address these real engine integration effects for kerosene, hydrogen and methane operation of a small aviation gas turbine.

For better comparability between the different operating conditions at varying mixture compositions, the power-normalized equivalence ratio Φ_n with reference to pure hydrogen is introduced.

$$\dot{Q}_{H_2} = \dot{Q}_{H_2/CH_4} \quad 4.15$$

$$\dot{m}_{H_2} * LHV_{H_2} = \dot{m}_{H_2/CH_4} * LHV_{H_2/CH_4} \quad 4.16$$

$$\Phi = \frac{\dot{m}_{fuel} * SAR}{\dot{m}_{air}} \quad 4.17$$

$$\Phi_n = \Phi_{H_2/CH_4} * \left(\frac{SAR}{LHV}\right)_{H_2} * \left(\frac{LHV}{SAR}\right)_{H_2/CH_4} \quad 4.18$$

It is derived by the requirement of constant thermal power output between a combustor fueled with a specific mixture of hydrogen and methane and the same combustor fueled with pure hydrogen at constant air mass flow. For one gas turbine load condition, the normalized equivalence ratio is constant for all mixture compositions. All fuel compositions yield the same thermal power output as hydrogen combustion at a given equivalence ratio Φ , if for these mixtures the normalized equivalence ratio Φ_n is set to the hydrogen value (cf. Figure 4-5).

4.2.3 Definition of the Design Momentum Flux Ratio

The DLN Micromix combustion principle is a non-premixed combustion system. Mixing of fuel and oxidizer occurs directly before combustion via JICF injection of a fuel jet into an airflow (cf. Figure 4-6). Thus, the central design focus is the jet-in-crossflow mixing, characterized by the

injection depth y . According to equation 4.19 and 4.20, y is controlled by the nozzle diameter, the fuel and air velocities, and their respective densities. These quantities are determined by the combustor geometry and the boundary conditions [43]. The density and velocity ratios are summarized in the momentum flux ratio J .

$$y \propto d_i \cdot \sqrt{J} \quad 4.19$$

$$J = \frac{\rho_{fuel} \cdot c_{fuel}^2}{\rho_{air} \cdot c_{air}^2} \quad 4.20$$

At sufficiently low injection depth of the fuel jet into the air crossflow, the fuel-air-mixture discharges freely into the combustion zone. The residence time of NO_x precursors is low, resulting in low NO_x emissions of the combustor.

At a critical injection depth y_{crit} , the fuel jet penetrates the shear layer and enters the inner recirculation vortex (cf. Figure 4-6). The fuel-air-mixture that is formed in the vortex ignites and leads to hot gas recirculation and vertical flame merging with extended retention times for NO_x precursors at elevated temperatures, resulting in increased NO_x emissions. In contrast, insufficient injection depth reduces the fuel-air-mixture quality and ultimately, part-load stability.

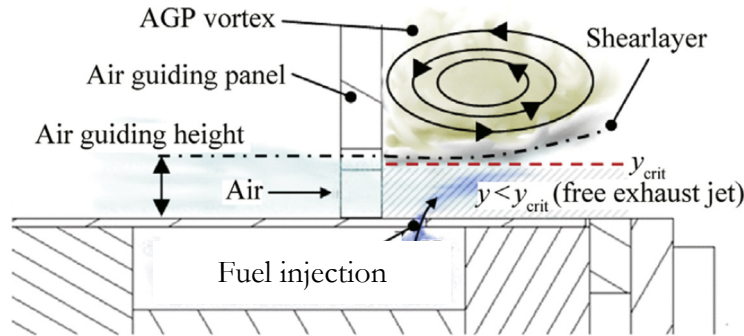


Figure 4-6: Schematics of the MMX combustor geometry, detailing JICF mixing

The injection of the secondary flow into the primary flow causes a deflection of the injected gas. The flow of the injected gas asymptotically approaches a maximum height or a maximum penetration depth with increasing run length. For JICF mixing of two air streams, this maximum injection depth can be calculated by the following expression according to Ballal and Lefebvre [43]:

$$y_{max} = 1.15 \cdot d_i \cdot \sqrt{\frac{\rho_1 \cdot c_1^2}{\rho_2 \cdot c_2^2}} = 1.15 \cdot d_i \cdot \sqrt{J} \quad 4.21$$

The prefactor of 1.15 holds for air-in-air injection. The publication by Norster [131] confirms that different gas combinations also have different pre-factors for calculating the maximum penetration depth. By studies of air-in-air and propane-in-air injection, Norster has demonstrated that propane

features a different pre-factor than air. For the initial design process, higher pre-factors for calculating the maximum penetration depth in hydrogen and methane operation are applied based on previous experimental experience [34, 40]. In the present thesis, the injection depth remains a theoretical design parameter for the sizing of the air guiding panel geometry. A detailed experimental assessment and quantification is not the scope of this thesis, since no experimental methods for measuring injection depths, like for example particle image velocimetry were available. The momentum flux ratio J proved to be a suitable substitute that can be assessed readily in the experiment and in the simulation. This is why it is chosen for the analyses conducted in the following chapters.

The momentum flux ratio J changes as a function of the fuel mixture composition for a given set of geometrical and operational boundary conditions. In Figure 4-7, this dependency is shown for momentum flux ratios that have been normalized according to equation 4.22. The momentum flux ratios used throughout this thesis are referred to the momentum flux ratio obtained with the initial combustor geometry V1, operating at an equivalence ratio of $\Phi=0.375$ with pure hydrogen fuel.

$$J_{rel} = \frac{J}{J_{V1, r_{H2}=1; \Phi_n=0.375}} * 100\% \quad 4.22$$

The highest values of J_{rel} are present for fuel mixtures between 80 and 90 vol.% H₂, implying that these mixtures are most critical for hot gas recirculation as a consequence of the mixture-dependent increased injection depth. Apart from its low LHV and lower reactivity in comparison to hydrogen-rich fuels, pure methane offers the lowest momentum flux ratio. In consequence, part-load stability issues may arise due to a reduced fuel-air mixture quality caused by insufficient injection depth.

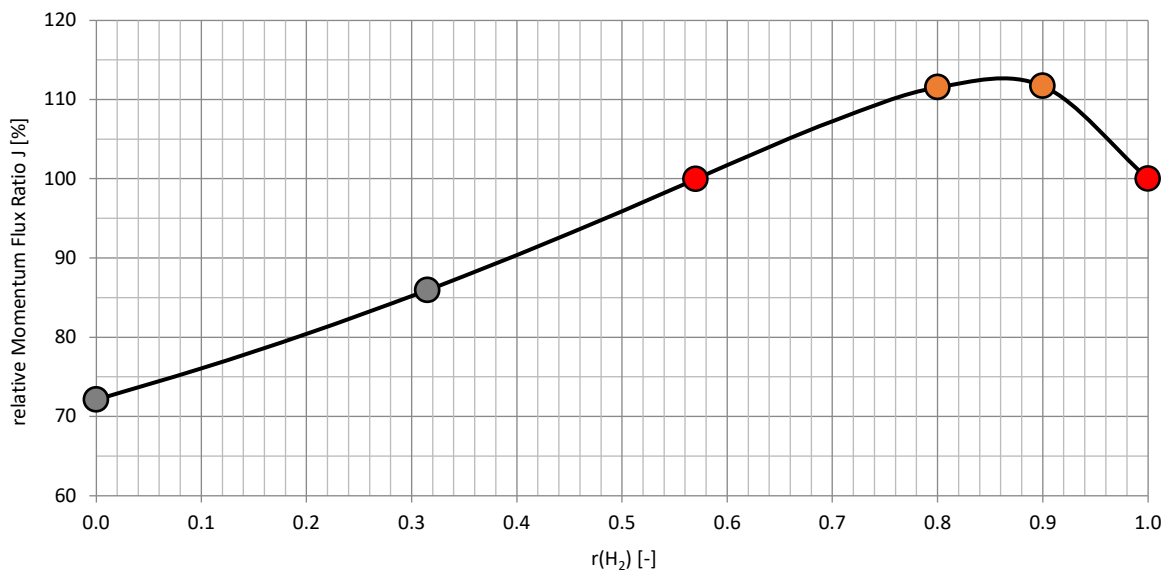


Figure 4-7: Relative momentum flux ratio with respect to $r(H_2) = 1$

In Figure 4-7, two sets of mixtures are highlighted by red and orange dots. They offer the possibility to achieve a constant momentum flux ratio with two different fuel mixture compositions. For these mixtures, not only the momentum flux ratio but also the Wobbe index is constant, as presented in Table 5. In total six mixtures ($r_{H_2}=1, 0.9, 0.8, 0.57, 0.315, 0$) are chosen for further investigation. For the initial Micromix FuelFlex combustor geometry, a momentum flux ratio at the combustor design point is chosen that lies in the range of experience from preceding studies. This defines the injector nozzle dimensions and the size of the air-gates. Throughout this thesis, all other momentum flux ratios are normalized by this momentum flux ratio of pure hydrogen in preheated air at $\Phi=0.375$ with the given initial MMX FuelFlex combustor geometry.

4.2.4 Aerodynamic Flame Stabilization

Stable flame anchoring and precise positioning of the flame is a primary design goal in the construction process. For flame anchoring, stabilization, and positioning, recirculation vortices are used that can be created by the use of Carnot-buffets at sudden geometry changes (cf. Figure 4-8).

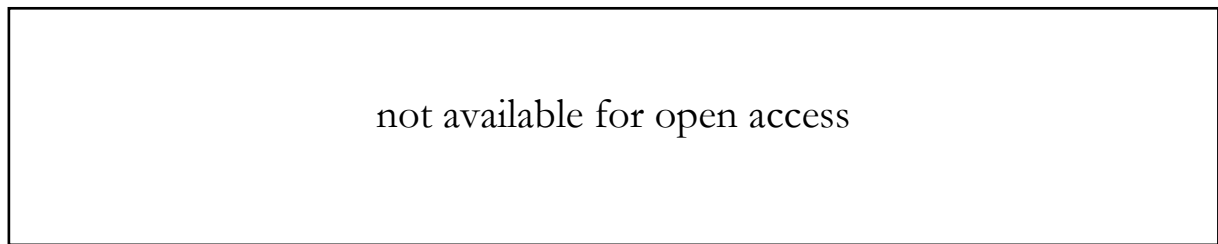


Figure 4-8: Recirculation areas at sudden geometry changes [78]

During the operation of an MMX combustor, the combustor geometry generates recirculation zones downstream of each AGP and burner segment, as shown in Figure 4-9. These recirculation areas are essential for the flame anchoring and are the main aerodynamic feature that ensures stabilization and separation of the created micro-flames.

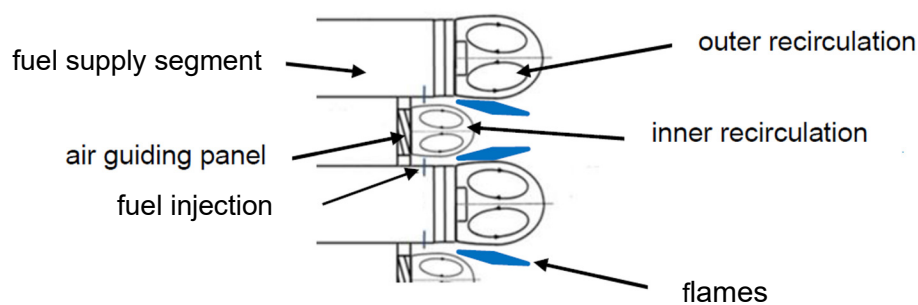


Figure 4-9: Flame anchoring characteristics and definition of recirculation zones

The aerodynamic flame stabilization is a result of the interaction between the inner recirculation zone behind the air guiding panels and the outer recirculation zone of the adjacent fuel supply segments. Both inner and outer recirculation areas must be designed to hold the flames between the resulting vortices in the desired position and to prevent them from merging with each other.

The size and shape of the established recirculation zones are influenced by the geometry of the combustor segment and the air guiding panel. The blockage ratios describe the geometrical properties that influence the size of the counter-rotating vortex pair and ultimately, the flame shape and orientation. The blockage ratio of the AGP (BR_{AGP}), the blockage ratio of the fuel supply segment (BR_{FSS}), and the Blockage Ratio Dimension Ratio (BRDR) are defined according to Figure 4-10. The latter is a similarity parameter between different combustor geometries and introduced to define the interaction of the inner and outer recirculation vortices to each other.

The generated recirculation zones need to stabilize the flame over the entire operating range from part-load to overload, and to separate the flames from each other to avoid flame merging, the formation of hotspots and increased NO_x emissions. Vertical flame separation is mostly controlled by the blockage ratios and the blockage-ratio-dimension-ratio, the horizontal merging of flames is considered in the combustor design by the distance between adjacent injector nozzles.

4.2.5 Combustor Design Process

An initial combustor geometry is derived by considering the fuel characteristics of the applied H₂/CH₄ mixtures, the operational boundary conditions, and the geometric restrictions that ensure optimal jet-in-crossflow mixing and flame stabilization. Since most of the geometric and operational parameters are interdependent, an iterative design process based on the schematics shown in Figure 4-10 is performed.

The injection depth y is controlled by the momentum flux ratio J of the fuel/air jet-in-crossflow. The momentum flux ratio is dependent on the densities of the applied fuel and air and their respective velocities, which are again controlled by the size of the air guiding panel gate and the fuel nozzle diameter. With a fixed design momentum flux ratio and constant boundary conditions (power density, type of fuel, temperatures, pressures), the fuel nozzle diameter and the area of the air gate are fixed.

For safe operation without flame merging and hot gas recirculation, the air gate height is designed to exceed the critical injection depth, which prevents penetration of the shear layer by the fuel jet. During an iterative matching process, the air gate geometry is adjusted to the flame stabilization requirements formulated by the design blockage ratios and the blockage ratio dimension ratio.

In the end, an initial test burner geometry is derived based on the APU boundary conditions, the chosen fuel range, the design momentum flux ratios, and the design blockage ratios. It is constructed for flexible fuel operation with H₂/CH₄ mixtures between 0 and 100 vol.% H₂, at a combustor power density (PD) of $7.6 \frac{\text{MW}}{\text{m}^2 \cdot \text{bar}}$. In the following discussion, this initial geometry is labeled “V1”.

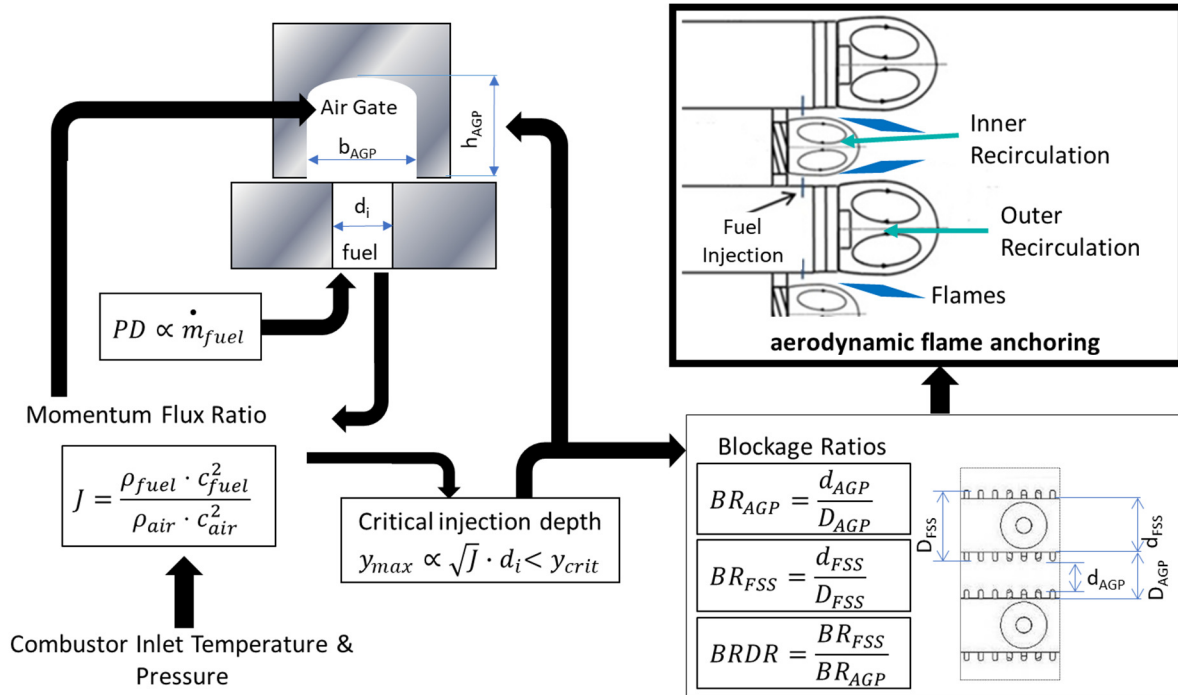


Figure 4-10: Micromix combustor design process

Due to intellectual property restrictions related to the sizing and construction of Micromix gas turbine combustors, no explicit geometry data is presented throughout this thesis. Where this data is required for an assessment of the tested design variations, the parameters are normalized and given as relative values.

5

Combustion Characteristics of the DLN Micromix Combustion Principle for Variable H₂/CH₄ Fuel Mixtures

This chapter covers the evaluation and optimization process of Micromix gas turbine combustors capable of burning variable fuel mixtures of hydrogen and methane. As presented in the previous chapter, the design of a FuelFlex Micromix combustor is driven by three key-parameters or design considerations:

- Applicable fuel compositions
- Momentum flux ratio J of the jet-in-crossflow mixing
- Air gate velocity / combustor pressure loss

For the characterization of the combustion process with variable H₂/CH₄ fuel mixtures, a testing methodology is applied that is suitable for analyzing the impact of the main design parameters and operating conditions on the safe operating range, combustion efficiency, and NO_x emissions. Detailed analyses by experimental testing and numerical simulations are performed, giving indications on critical phenomena influencing flexible-fuel Micromix combustion. Based on the findings of testing and simulating the baseline geometry, an optimization process is presented that, in the end, leads to an enhancement of the combustion efficiency and to a reduction of the pollutant emission level.

During the initial characterization of flexible-fuel operation with the baseline Micromix FuelFlex combustor V1, presented in chapter 5.1, the applied fuel composition and the combustor's operating point are varied. This process identifies the influence of the fuel mixture composition on

the combustion characteristics at variable thermal power output. For this evaluation, a variation of the equivalence ratio is conducted to represent gas turbine part-load, full-load, and overload conditions. In total, 6 operating points are considered that stretch from $\Phi_n=0.25$ (part-load) over $\Phi_n=0.375$ (design point) to $\Phi_n=0.588$ (overload). Six different fuel mixtures are chosen based on the nonlinear course of momentum flux ratio versus fuel mixture composition (cf. chapter 4.2.3). With the two sets of fuels yielding constant momentum flux ratios at changed mixture composition (cf. Figure 4-7), the influence of the momentum flux ratio is decoupled from the mixture composition during the analysis of the experimental results.

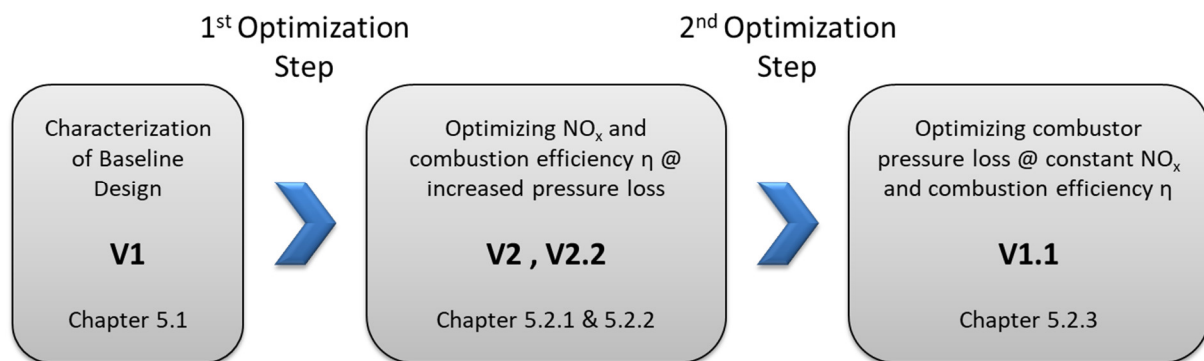


Figure 5-1: Micromix FuelFlex optimization process

Following this initial characterization, the first optimization step applies an increase in the air gate velocity (and corresponding relative pressure loss) to reduce NO_x emissions, especially at overload conditions, and to increase the combustion efficiency at high methane contents (cf. Figure 5-1). The first part of this optimization, presented in chapter 5.2.1, evaluates the influence of the air gate velocity on the combustion characteristics. Three additional air gate geometries allow relative air velocities between 87.5% and 125% with the baseline design (V1) operating at 100%. For each new combustor geometry (V2, V3, V4), a design space exploration with variable fuel mixture composition and combustor operating point is conducted. For the optimum design V2, operating at 125% relative air velocity, a modification of the air gate geometry is applied to widen the safe operating range at overload conditions (cf. chapter 5.2.2)

In a second optimization step, presented in chapter 5.2.3, the lessons learned during this first optimization at increased pressure loss are applied to generate the final Micromix FuelFlex combustor geometry V1.1. It operates at a comparable pressure loss as V1 with significantly improved combustion characteristics in terms of lower NO_x emissions, a wider operating range, and higher combustion efficiencies at high methane contents.

The parameter variations applied for the characterization and optimization of the Micromix combustion process under flexible-fuel operation are summarized in the test schedule, shown in

Figure 5-2. At each combination of parameters (equivalence ratio / mixture composition / combustor variant), 10 datasets are acquired over the measurement grid displayed in Figure 3-9. With a total of 222 possible combinations, evaluated experimentally and numerically, this amounts to 2220 experimental datasets consisting of the measured exhaust gases and all boundary conditions.

		Geometry	Design Air Gate Velocity	Tested Fuel Composition $r(H_2)$	Operating Point	# of scheduled Datasets
		[-]	[%]	[-]	[-]	[-]
Characterization of Baseline Design	Chapter 5.1	V1	100	0 - 1.0	part load ($\Phi_n=0.25 ; 0.3125$) full load ($\Phi_n=0.375$) overload ($\Phi_n=0.43 ; 0.5 ; 0.588$)	360
Air Gate Velocity Variation	Chapter 5.2.1	V2	125	0 - 1.0	part load ($\Phi_n=0.25 ; 0.3125$) full load ($\Phi_n=0.375$) overload ($\Phi_n=0.43 ; 0.5 ; 0.588$)	360
		V3	112.5	0.315 - 1.0	part load ($\Phi_n=0.25 ; 0.3125$) full load ($\Phi_n=0.375$) overload ($\Phi_n=0.43 ; 0.5 ; 0.588$)	300
		V4	87.5	0.315 - 1.0	part load ($\Phi_n=0.25 ; 0.3125$) full load ($\Phi_n=0.375$) overload ($\Phi_n=0.43 ; 0.5 ; 0.588$)	300
AGP Height Variation	Chapter 5.2.2	V2.1	125	0.315 - 1.0	part load ($\Phi_n=0.25 ; 0.3125$) full load ($\Phi_n=0.375$) overload ($\Phi_n=0.43 ; 0.5 ; 0.588$)	300
		V2.2	125	0.315 - 1.0	part load ($\Phi_n=0.25 ; 0.3125$) full load ($\Phi_n=0.375$) overload ($\Phi_n=0.43 ; 0.5 ; 0.588$)	300
Pressure Loss Optimization	Chapter 5.2.3	V1.1	100	0.315 - 1.0	part load ($\Phi_n=0.25 ; 0.3125$) full load ($\Phi_n=0.375$) overload ($\Phi_n=0.43 ; 0.5 ; 0.588$)	300
Total number of scheduled Datasets						2220

Figure 5-2: Experimental test schedule

5.1 Characterization of FuelFlex Combustion with Baseline Geometry V1

With the first generation Micromix FuelFlex combustor, a design space exploration is performed. In the following experimental and numerical evaluation, the baseline combustor geometry V1 is tested at atmospheric pressure at operating conditions correlating to the design point of the reference gas turbine Honeywell Garrett GTCP 36-300 at $\Phi_n=0.375$ and part- and overload conditions (cf. chapter 4.2.2). For a general characterization of the MMX combustion process under flexible-fuel operation, the fuel mixture composition is varied between 0 vol.% and 100 vol.% hydrogen in the fuel.

5.1.1 Visual Flame Appearance

To assure high combustion efficiency, low pressure losses, and low pollutant emissions, the design laws for DLN Micromix combustor modules aim at generating clearly separated micro flames that are stabilized aerodynamically by vortex systems. Aerodynamic flame separation prevents adjacent micro-flames from merging. Merging of adjoining flames results in the formation of a reduced number of large-scale flames, increasing the residence time of NO_x precursors in the hot reaction zone and significantly promoting NO_x formation.

Figure 5-3 shows exemplary images of miniaturized flames at part-load operation ($\Phi_n=0.25$) for 3 hydrogen-rich fuels, along with a sketch of idealized Micromix flames. The images show clearly separated flamelets with no tendency of flame merging, as required by the design laws.

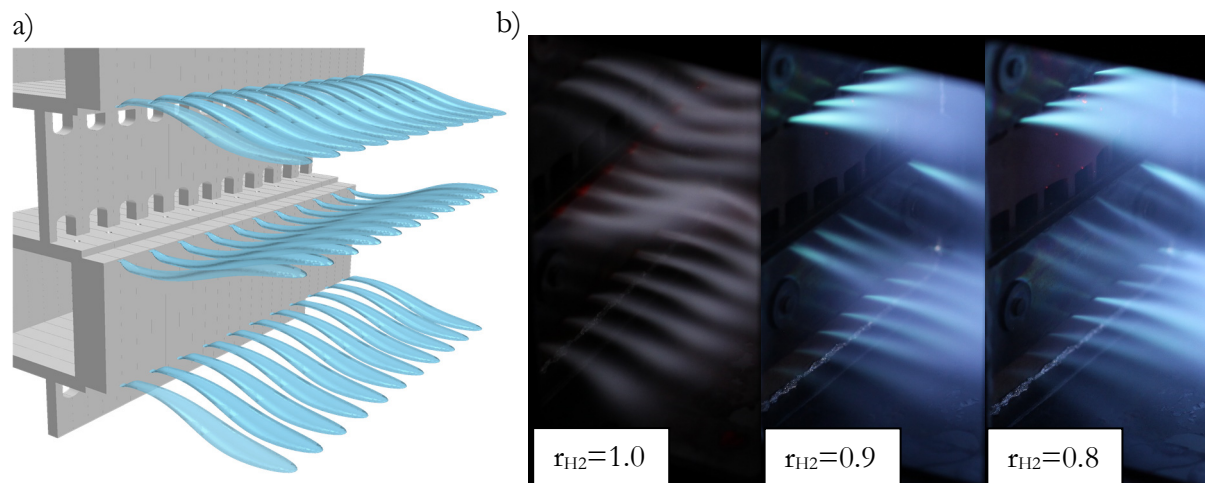


Figure 5-3: Idealized Micromix flames (a); Flame images at $\Phi_n=0.25$ with $r_{H_2}=1.0, 0.9$ & 0.8 (b)

The visible light emissions of pure hydrogen flames are considerably weaker than those of hydrocarbon blend fuels at the same operating point but nonetheless clearly visible. According to Schefer et al. [132], the blue to violet emission of hydrogen flames results from the radiation of

OH* molecules in the upper range of ultraviolet light emissions at around 400 nm and from excited H₂O molecules at around 600 to 900 nm. When CH₄ is admixed to pure hydrogen, the flames get an intense blue color due to the added radiation of CH* radicals [133, 134].

The flames, depicted in Figure 5-3, are stabilized aerodynamically by vortex structures that form in the wake region of the fuel supply segment and the air guiding panel. These flow structures, depicted in Figure 5-4 as streamlines, also provide flame separation that prevents the Micromix flames from merging vertically.

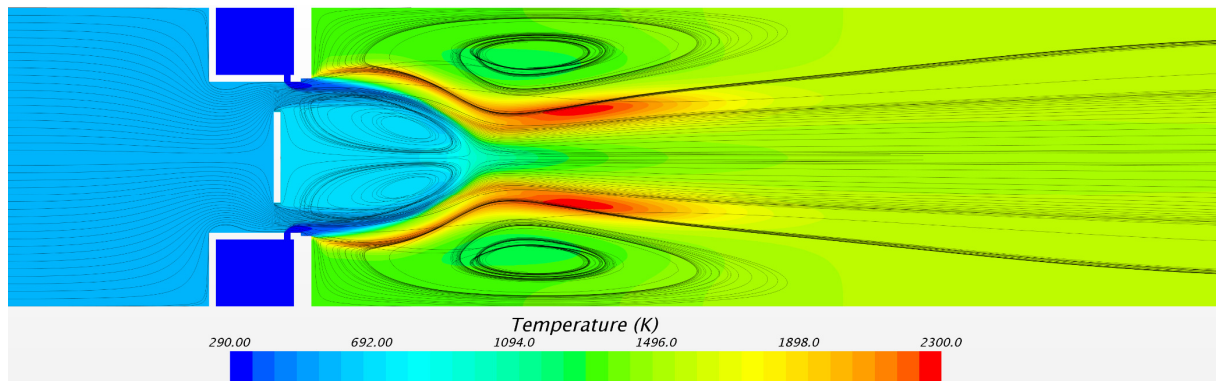


Figure 5-4: Aerodynamic flame stabilization by counter-rotating vortex pairs

In a horizontal direction, the flames are separated by a coflowing stream of air, shown in Figure 5-5. After passing the air guiding panel, the excess air that does not take part in the combustion process encases the individual flames and provides cold air to the lower recirculation zone.

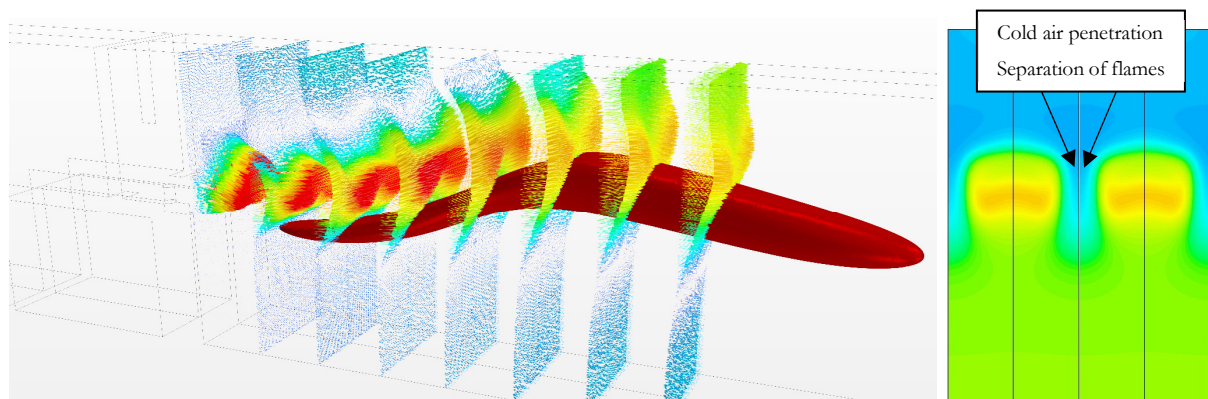


Figure 5-5: Velocity profile (left) and temperature distribution on a cross-section (right) showing flame separation by cold air penetration

Figure 5-6 shows the visual flame appearance of Micromix flames for the entire design space exploration conducted with the MMX baseline geometry V1. Six different H₂/CH₄ fuel mixtures were tested at the combustor design point at $\Phi_n=0.375$ and in total 4 off-design points.

		Design Point				
Φ_n r_{H2}	0.5	0.435	0.375	0.3125	0.25	
1.0						
0.9						
0.8						
0.57					Flame Blow Out	
0.315				Flame Blow Out	Flame Blow Out	
0.0				Flame Blow Out	Flame Blow Out	

Figure 5-6: Flame images with variable H₂/CH₄ fuel mixtures for V1

The first Micromix combustor prototype designed for flexible fuel operation shows satisfactory operational behavior with miniaturized Micromix flames over a wide fuel and operating range. However, there are three combustion phenomena that need to be discussed in the following:

- I. At part-load operation with fuel mixtures between 0 and 57 vol.% H₂ in the fuel, flame blow out occurs.
- II. As the methane content in the fuel mixture is increased (r_{H_2} reduced) at constant thermal power output ($\Phi_n = \text{const.}$), the Micromix flames become more extensive in volume and length.
- III. Testing at overload conditions at $\Phi_n = 0.588$ is not possible due to overheating of the air guiding panel. Even at $\Phi_n = 0.5$ vertical flame merging and hot gas recirculation occurs, clearly visible for 100 vol.% H₂ ($r_{H_2} = 1.0$) by the large orange flame in the center of the combustor module.

5.1.2 Combustion Efficiency

For assessing the combustion characteristics of the combustor module V1 with particular focus on the part-load performance, the unburned fuel and carbon monoxide emissions and the overall combustion efficiencies are evaluated. In Figure 5-7, the obtained unburned H₂ and CH₄ emissions, as well as the carbon monoxide emissions are plotted as a function of the hydrogen content in the fuel.

For the 100% and 90% H₂ mixture, no increased emissions of fuel components occur at part-load operation. With a growing amount of CH₄ in the fuel (r_{H_2} reduced), the general emission level of unburned H₂ ($\psi(H_2)$) and CH₄ ($\psi(CH_4)$), as well as CO ($\psi(CO)$) is increased and the steep gradient at lean off-design, present for all considered emissions, is shifted towards increased equivalence ratios. Except for $\Phi_n = 0.25$, CH₄ is fully consumed at Micromix combustion with 80% and 90% H₂ in the fuel. 57% H₂ is the first fuel mixture that shows unburned CH₄ molecules at the combustor outlet, even at the design point. Between 80% and 90% H₂ in the fuel, the combustion process allows a full decomposition of the introduced amount of CH₄ but no complete conversion into H₂O and CO₂, proven by the present amount of CO and H₂ in the exhaust gas.

H₂ is not only introduced as part of the fuel mixture, but also an intermediate species in the decomposition of CH₄. Thus, increased amounts of H₂ in the exhaust not only result from incomplete combustion of the introduced fuel, but also from H₂ as intermediate species that is not oxidized during subsequent reactions.

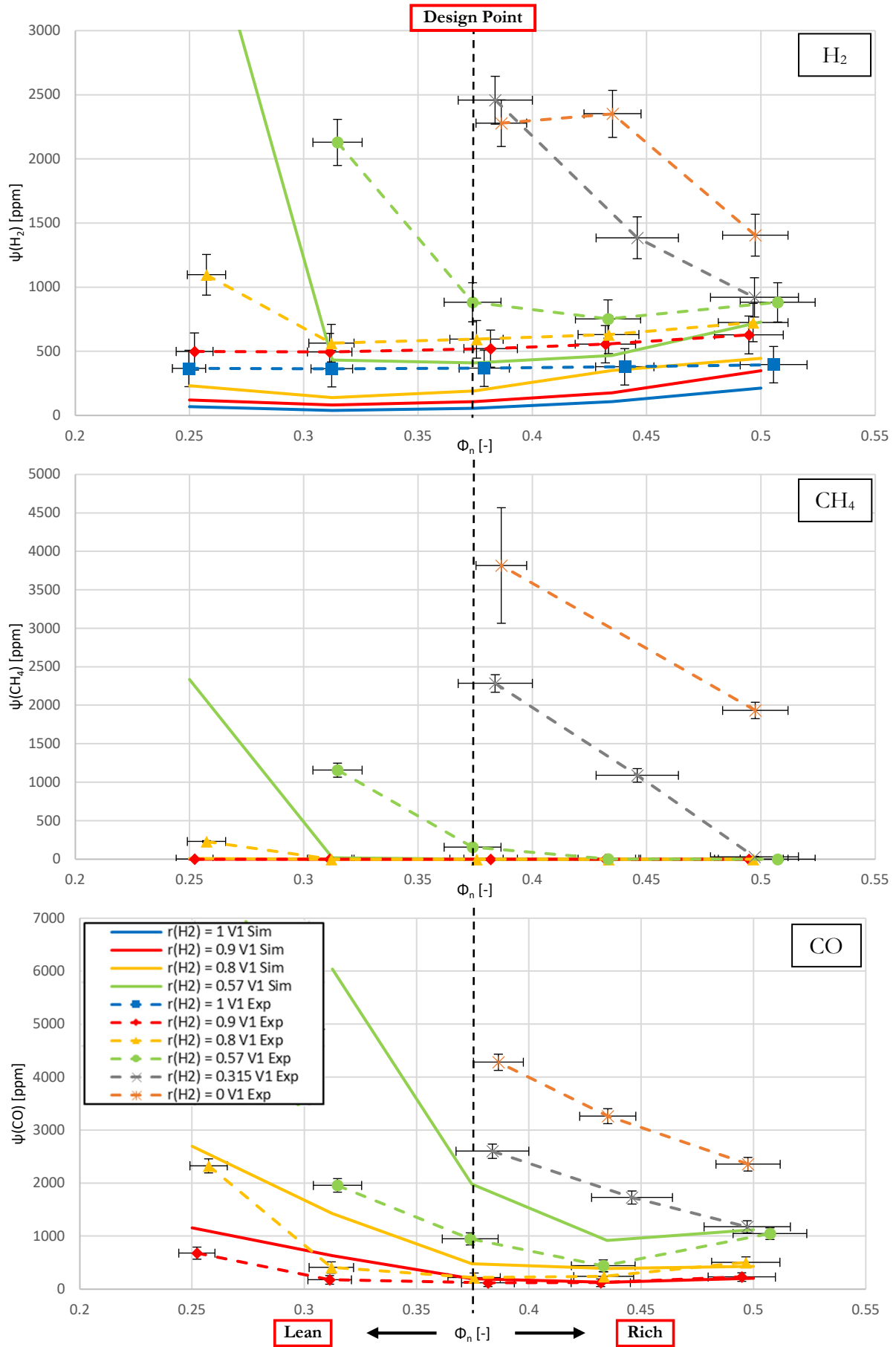


Figure 5-7: Experimental results of H₂, CH₄ and CO emissions for variable fuel mixtures

In [117], Funke et al. have investigated the slight increase of H₂ emissions towards rich combustion conditions based on equilibrium and 0D reactor calculations. It can be attributed to the limited reaction time and a shift of the H₂ equilibrium concentration resulting from changed reaction rates of forward and reverse reactions at higher equivalence ratios.

During incomplete combustion of hydrocarbon fuels, full oxidation of carbon atoms to CO₂ is partly inhibited, leading to the increased emission of carbon monoxide (CO). Incomplete combustion occurs if the ambient conditions (e.g., pressure, temperature, equivalence ratio, turbulence, etc.) are not sufficient for complete oxidation.

When comparing the simulation and experimental results, the simulated unburned fuel emissions H₂ and CH₄ fall below the experimental levels and the location of the steep increase of emission is shifted towards leaner combustion conditions. Thus, the simulation predicts a more complete combustion than is present in reality. Concerning CO emissions, a certain overestimation of the emission level occurs. The present deviations are, among other things, a result of the chosen modeling approach using steady RANS-simulations. Especially flame quenching resulting from local aerodynamic effects and mixing effects that cause elevated unburned fuel emission levels is presumably not accurately predicted by the numerical approach. Additionally, the mutual influence between individual MMX flames, the impact of the surrounding flame tube and imperfections of the combustor geometry that occur within certain tolerances during manufacturing, assembly, and operation are not considered. Since the general combustion physics and the emission trends of all emissions are very well captured by the applied numerical approach, a phenomenological description of the underlying combustion physics is reasonable.

The emission of unburned fuel components and CO are related to the reactivity of the applied fuel mixtures. The physical principles that result in increased emissions towards higher concentrations of methane, and towards lean off-design are described in the following based on the simulated production rates of CO₂, CH₄, and CO within the combustor domain. They are plotted as a function of the axial z-coordinate, defined in Figure 3-12.

Figure 5-8 a) shows the net molar production rates for the specified species at lean off-design for a fuel composition of 90% H₂. In both the experiment and the simulation, this operating point yields no CH₄ in the exhaust gas and little CO emissions. CO is continuously produced and consumed within the Micromix flame. As Figure 5-8 a) indicates, there is a region in the early flame stage where CO production is dominant ($z < 25$ mm), whereas further downstream CO consumption dominates. As can be seen from the consumption rate of CH₄ in this early stage of the flame, CH₄ is broken down rapidly into intermediate species like CH₃, CH₂, CH, etc. and ultimately partly oxidized to CO. According to the production rate of CO₂ that is also maximal in

this flame region, a part of the readily produced CO is directly oxidized further to CO₂. Following this early stage, where all CH₄ is broken down, and a major part of CO₂ is produced, a second reaction zone is present. Here the decomposition of CH₄ is already at an end, leaving only intermediate species to react further downstream. The amount of CO that is still present at the end of the first stage is consumed until the end of the considered reaction zone, located at a distance of 130 mm from the burner face. This leaves no CH₄ and only minor CO emission in the exhaust gas.

When looking at the net molar production rates for a 57% H₂ fuel at the part-load operating point $\Phi_n=0.3125$, there is a change in the expansion of the reaction zones (cf. Figure 5-8 b)). With increasing amount of methane in the fuel, the second stage where CH₄ decomposition is already finished, and CO consumption becomes dominant, is shifted downstream. In the early flame stage, CH₄ is rapidly consumed, leading to high CO and CO₂ production rates.

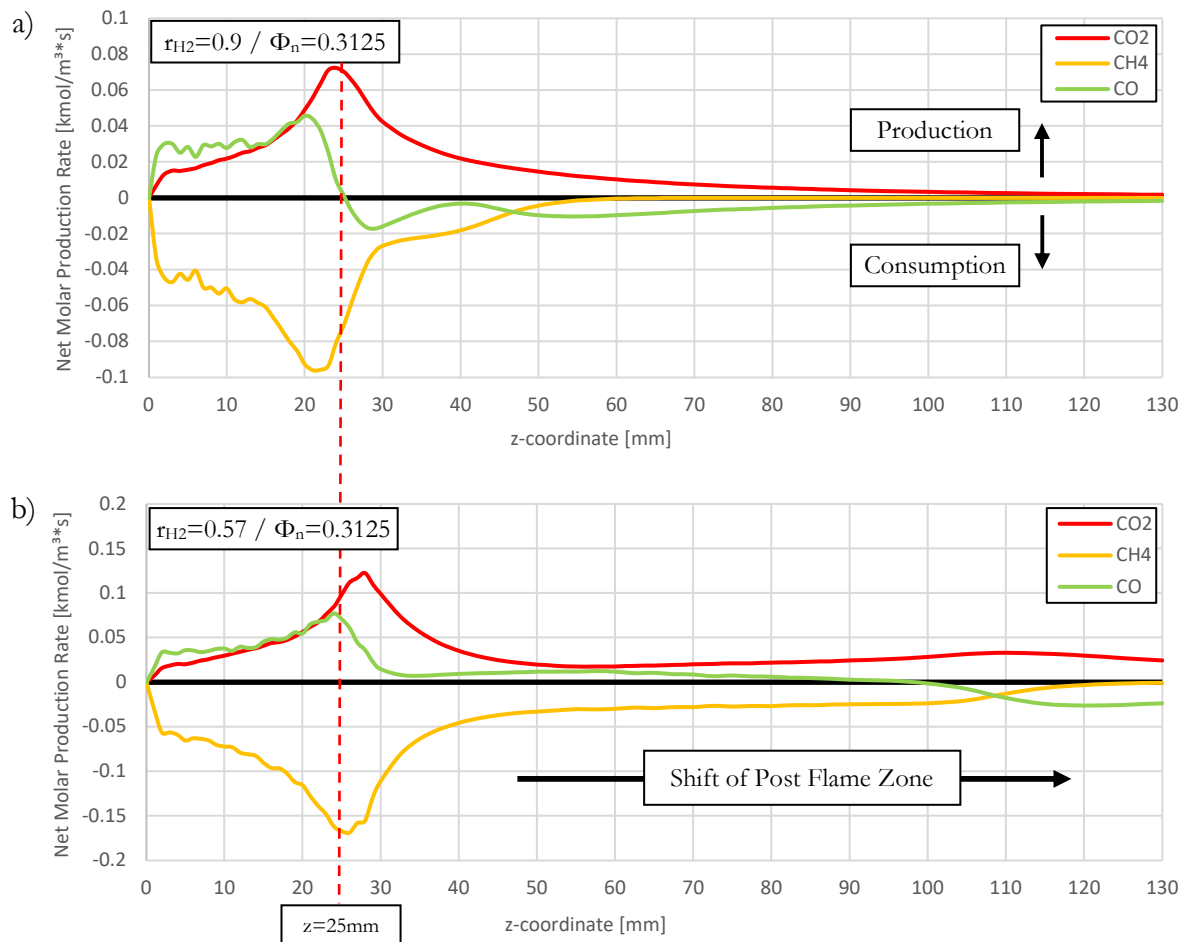


Figure 5-8: Net molar production rates of CO, CH₄, and CO₂ at $\Phi_n=0.3125$ for $r_{H_2}=0.9$ (a) and $r_{H_2}=0.57$ (b)

The leftover CH₄ slowly reacts further until at $z = 120$ mm, it is fully consumed. In this intermediate flame stage, CH₄ decomposition leads to further production of CO and CO₂. Only in a post-flame zone located at $z > 100$ mm, CO consumption becomes dominant. Here the leftover CO reacts to

CO₂. The integral of the CO₂ production rate indicates that this post flame zone is one of the major production zones for CO₂.

The simulated change in the flame expansion with an increasing amount of CH₄ in the fuel is also clearly visible during the experimental combustor testing (cf. red boxes in Figure 5-6). Hydrogen-rich flames are small and become more extensive as the methane content in the fuel is increased. The change of the flame shape and size is a result of the changed reactivity of the applied fuel. Here, the reactivity is evaluated by simulating the local heat release rates at a power-normalized equivalence ratio of 0.375 with pure hydrogen and a 57 vol.% hydrogen fuel mixture. The local heat release and temperature distribution on the central combustor symmetry plane are shown in Figure 5-9.

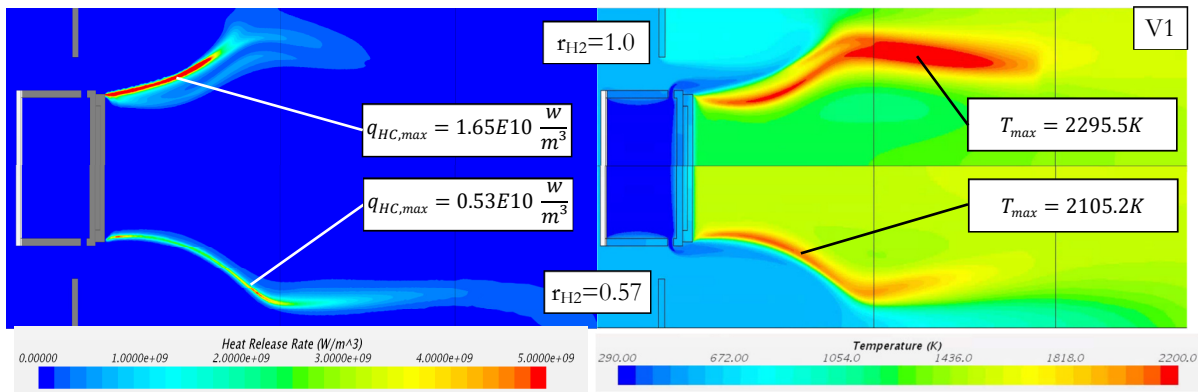


Figure 5-9: Simulated heat release (left) and temperature (right) on combustor symmetry plane at $\Phi_n=0.375$ for $r_{H_2}=0.9$ and $r_{H_2}=0.57$

The maximum heat release rate for hydrogen combustion is tripled in comparison to the 57% H₂ case, whereas the overall thermal power output is nearly constant ($\Phi_n=\text{const}$, $\eta\approx\text{const}$). Additionally, the heat release zone is much more confined. Since heat release rate and local combustion temperature are interconnected, also the simulated peak temperatures are reduced at $r_{H_2}=0.57$, as methane is added to the hydrogen fuel. With lower temperatures, all reaction processes within the flame happen at increased timescales, leading to extended Micromix flames and increased emissions of unburned fuel components and CO, as seen during experimental testing.

When changing the combustor operating point from part-load to the design point and beyond, the thermal power output and interconnected, the combustion temperatures are increased. As can be seen from Figure 5-10, this results in a reduced axial expansion of the flame zone (indicated by the consumption of CO) and ultimately reduced unburned fuel and CO emissions (cf. Figure 5-7).

The presence of hydrocarbons, hydrogen, or carbon monoxide in the exhaust gas, reduces the combustion efficiency since their chemical energy is not released during combustion. Apart from that, CO emissions need to be held at a minimum since it is toxic for humans and animals.

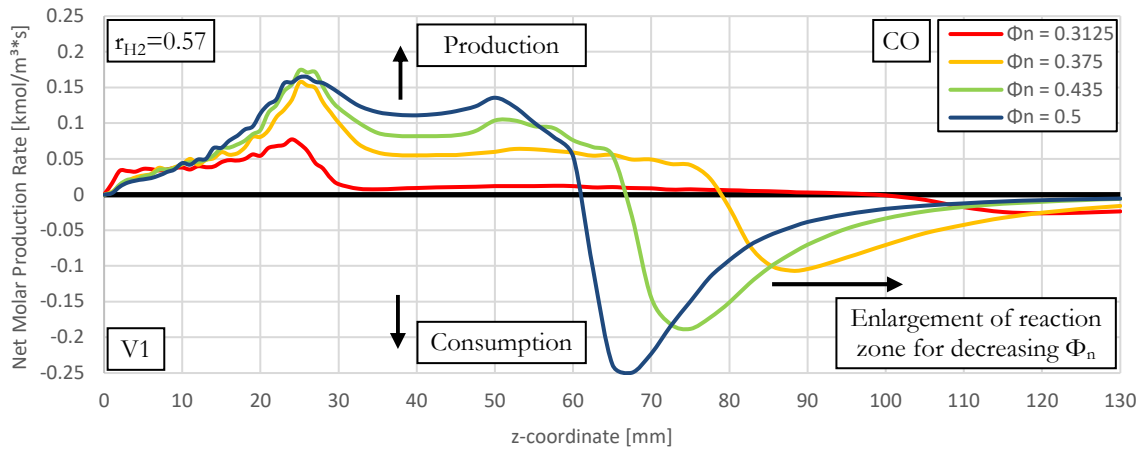


Figure 5-10: Net CO production rate for 4 operating points with $r_{H_2}=0.57$

In Figure 5-11, the regarded unburned fuel components and CO are summarized in the combustion efficiency η . The presented horizontal and vertical error bars indicate measurement accuracies for all experimental data points, but are partly very small. For determining η , the thermal power lost by emission of CO and the unburned fuel components H₂ and CH₄ is put in relation to the potential thermal power introduced to the combustor by both fuel components.

$$\eta = 1 - \frac{\sum_{j=1}^m (\dot{m}_{out,tot} * g_j * LHV_j)}{\sum_{i=1}^n (\dot{m}_{fuel\ i,tot} * LHV_i)} \quad 5.1$$

For pure hydrogen combustion, the combustion efficiency is maximum and almost constant over the complete investigated operating range, exceeding 99.6%.

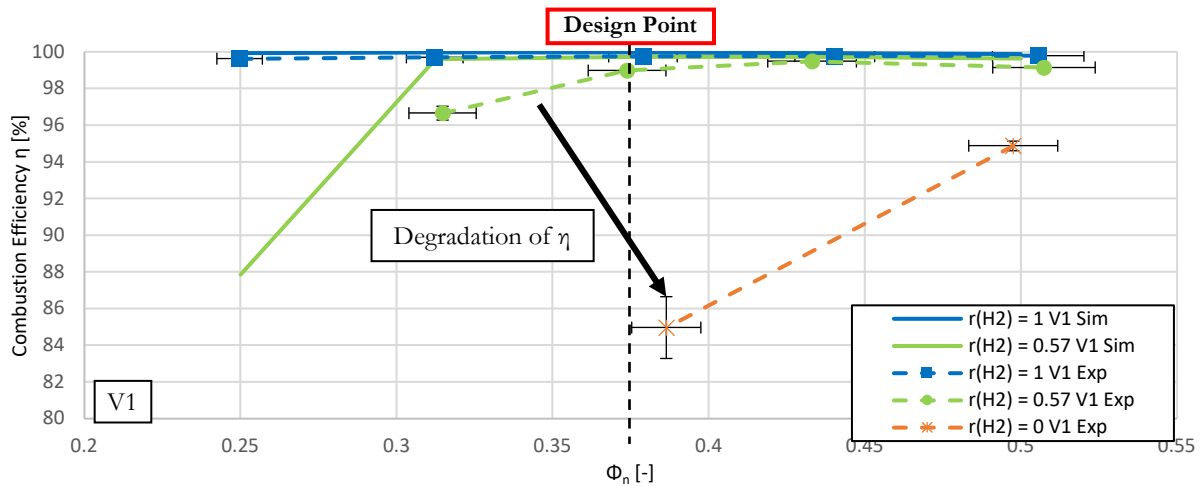


Figure 5-11: Experimental and simulation results of combustion efficiency for 3 fuel mixtures

As discussed earlier, with increasing amounts of methane in the fuel (r_{H_2} reduced), the unburned fuel and CO emissions rise (cf. Figure 5-7), which reduces the general level of combustion efficiency. Since the lower temperatures at part-load operation result in a decrease of all reaction rates, incomplete combustion occurs at low equivalence ratios, especially once generally slowly

reacting methane is present in the fuel mixture (cf. Figure 5-10). As a consequence, less heat is released during combustion, which amplifies this effect and shifts the apparent decrease of combustion efficiency at part-load operation with high methane contents to higher equivalence ratios. The deviations in the numerical prediction of the combustion efficiency result directly from the discrepancy for the unburned fuel and CO emission levels.

Thus, with increasing concentrations of methane in the fuel, lean off-design operation with high combustion efficiency becomes more and more challenging, leading ultimately to flame lean blow out (cf. Figure 5-6). The enlargement of the reaction zone, where CH₄ is broken down, and the existence of a post-flame zone, where CO is oxidized to CO₂, are two unfavorable effects for Micromix combustion. All applied design laws aim at miniaturization of the flames for keeping NO_x emissions at a minimum. Enlargement of the flames for optimizing the combustion process at increased CH₄ portion is a conflicting design goal towards low NO_x emissions with hydrogen-rich fuels.

5.1.3 Nitrogen Oxide Emissions

Apart from high combustion efficiency, low NO_x performance of Micromix combustors is the premier design goal. In order to be a viable solution for near-future industrial-scale hydrogen-enriched methane or natural gas combustion, the MMX principle under flexible-fuel operation must show emission levels well below the legal limit of 25 ppm (corrected to 15% O₂) [135]. Since this limit is defined for pressurized gas turbine operation, it needs to be scaled down to meet the atmospheric conditions present for the experimental assessment in the framework of this thesis. As a reference for scaling, the L30A gas turbine manufactured by Kawasaki Heavy Industries, Ltd. is chosen. It offers the world's highest electrical efficiency level in the 20-35 MW class and is capable of flexible-fuel operation with up to 60 vol.% hydrogen in the fuel at a pressure ratio of 24.5 [136, 137].

According to Lefebvre [43], NO_x emissions of conventional gas turbine combustors scale approximately with the square root of the pressure ratio. When scaling down the legal NO_x limit of 25 ppm from 24.5 bar to atmospheric pressure, the NO_x target for atmospheric testing of MMX combustors is 5.05 ppm at the combustors design point.

In the following, the NO_x emission characteristic of the initial combustor geometry V1 is evaluated. Figure 5-12 shows the NO_x emissions obtained by experimental testing and NO emission obtained by combustion and flow simulations at various combustor operating conditions over the complete fuel mixture range. The NO/NO_x emissions are corrected to 15 vol.% O₂.

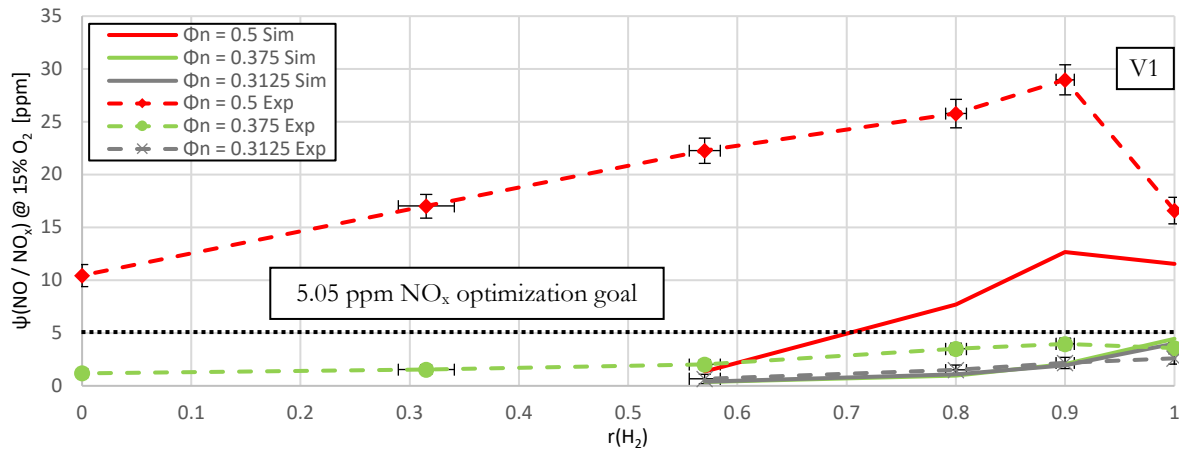


Figure 5-12: Experimental and simulation results of NO/NO_x corrected to 15% O₂ for V1

The first Micromix FuelFlex prototype shows a significant low NO_x performance at part-load and full-load operating conditions, with peak emission levels of 4 ppm at $\Phi_n = 0.375$ and $r_{H_2} = 0.9$. There are three particular phenomena in the emission characteristics that need to be discussed in the following:

- I. At part-load operation ($\Phi_n=0.3125$), the amount of hydrogen in the fuel mixture correlates to the NO_x emission level. The highest NO_x emissions are present for pure hydrogen combustion. These characteristics are well met by the results of the combustion and flow simulations.
- II. When the operating point is shifted from part-load to full-load ($\Phi_n=0.375$) and overload ($\Phi_n=0.5$) conditions, the NO_x emission level rises, independently from the fuel mixture. This trend is also met by the simulations, but an underestimation of the correct level occurs.
- III. At the combustor design point and overload, the correlation between the hydrogen content in the fuel and the NO_x level is complemented by a superimposed phenomenon that delivers the highest NO_x emissions at 90% H₂ ($r_{H_2}=0.9$), instead of 100% H₂ ($r_{H_2}=1.0$). Despite the present deviations in predicting the quantitative NO_x level, this added effect can also be seen in the simulation results for the overload operating point $\Phi_n=0.5$.

When changing the fuel from pure hydrogen to methane at a constant thermal power output of the combustor module, the exhaust gas temperature increases. In Figure 5-13, the adiabatic exhaust gas temperature T_4 is plotted for the boundary conditions specified in chapter 4.2.1.

The suggested increase of NO_x emissions for methane-rich fuels related to the increased exhaust gas temperature is not backed by the experimental evidence (cf. Figure 5-12). Despite the higher idealized mean exhaust gas temperature, NO_x emissions are lowest for pure methane fuel. This correlation between increasing hydrogen content and increasing NO_x level is also stated in [138]. Cozzi et al. suggest that hydrogen's higher reactivity causes this distinct trend.

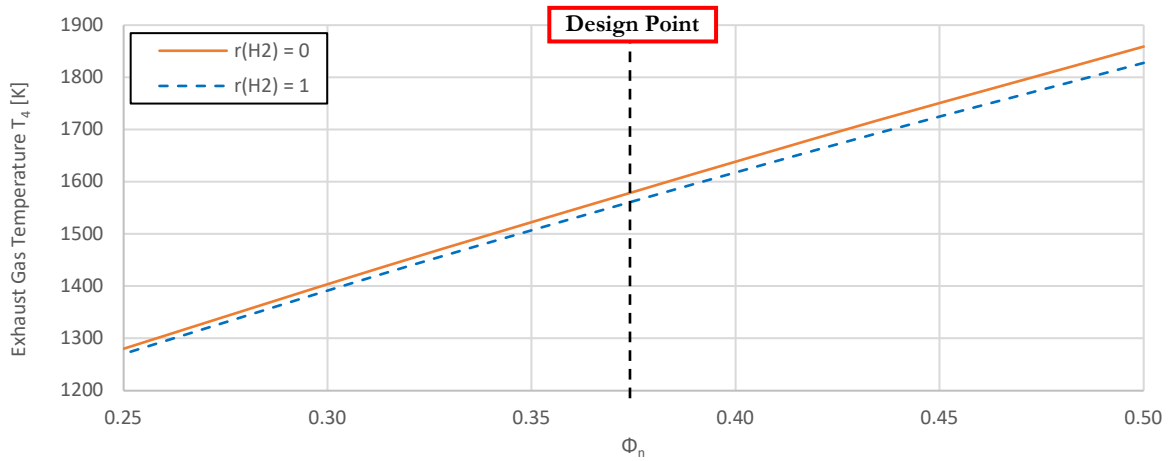


Figure 5-13: Theoretical exhaust gas temperature T_4 for H₂ and CH₄ combustion

As discussed in detail in chapter 5.1.2, hydrogen combustion releases heat in less space and time when compared to hydrogen methane fuel mixtures. The increased combustion efficiency of hydrogen-rich fuels has an additional effect.

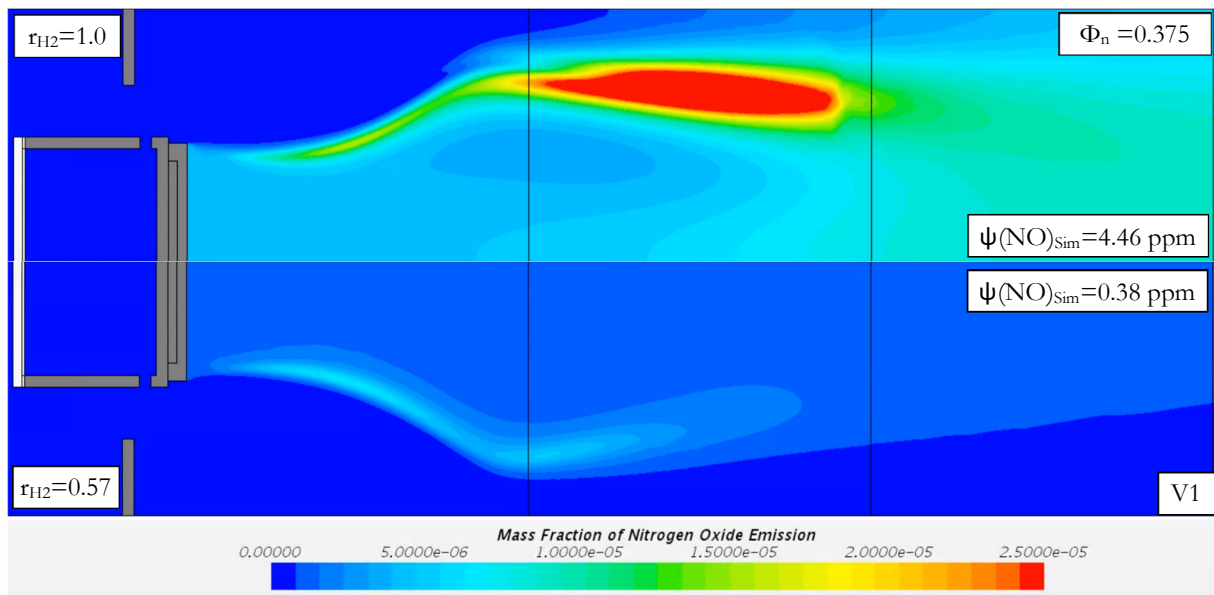


Figure 5-14: Simulated NO mass fraction on the symmetry plane at $\Phi_n=0.375$ for V1

As a result, higher peak flame temperatures are present for hydrogen combustion (cf. Figure 5-9). For the two fuel mixtures at $\Phi_n = 0.375$, presented in Figure 5-9, the resulting NO distribution on the central symmetry plane is given in Figure 5-14. The peak NO level, as well as the overall formation region are significantly enlarged for pure hydrogen combustion.

The applied combustion modeling approach considers thermal NO formation (cf. chapter 3.2.5), which rises with the temperature. For pure hydrogen, the increased peak flame temperature and the more extensive high-temperature regime significantly promote NO formation. In order to keep the thermal power output constant, pure hydrogen is combusted at leaner conditions than

methane-rich fuels (cf. Figure 4-5). At leaner conditions, higher amounts of the NO_x precursors oxygen and nitrogen are supplied to the combustor. In combination with the increased flame temperatures, this yields a significant increase in the resulting NO emissions at the combustor outlet.

When shifting the operating point towards rich combustion conditions for any given fuel mixture composition, the NO_x emission level rises (cf. Figure 5-12). Higher thermal power output at higher equivalence ratios leads to higher combustion temperatures, as less excess air is present for cooling (cf. Figure 5-13). This results in increased NO_x formation, which is especially apparent when reaching overload conditions at $\Phi_n = 0.5$.

Apart from the dependence of NO_x formation on the temperature, there is a superimposed effect that is specific for MMX combustion. Figure 5-15 shows the simulated temperature and NO distribution on the central symmetry plane for 4 operating points with 90% H₂ fuel.

For part-load ($\Phi_n=0.3125$) and full-load ($\Phi_n=0.375$) operation, the simulation shows miniaturized Micromix flames with small high-temperature areas and comparably cold recirculation zones, leading to overall low NO emissions. The overload operating point at $\Phi_n = 0.5$ shows a different characteristic. Instead of only gradually gaining in size and temperature, two opposing flames suddenly merge and form one large-scale flame. For confirmation of the resulting phenomenon of vertical flame merging, an extreme overload point at $\Phi_n = 0.588$ is included, which could not be evaluated in the experiment due to overheating of the combustor module. The extremely enlarged flame does not stabilize in the wake region of the fuel supply segment but anchors at the air guiding panel at $\Phi_n = 0.588$. The temperatures in the merged flame exceed 2000 K in a vast region, leading to significantly increased NO formation.

When moving from part-load to overload conditions, the fuel mass flow is increased, whereas the air mass flow stays constant. According to equation 4.20, the increased fuel mass flow raises the fuel velocity, the momentum flux ratio, and ultimately, the injection depth of the fuel jet into the air crossflow. At sufficiently low injection depth, as present for part-load and full-load operation, the fuel-air mixture can discharge freely into the combustion zone, where miniaturized, clearly separated flames are formed. When reaching a critical injection depth, parts of the fuel jet start penetrating the shear layer between the air crossflow and the upper recirculation zone (cf. chapter 1.4). In consequence, fuel and hot exhaust gas are accumulated in the upper vortex, indicated by the increased temperature level at $\Phi_n = 0.5$.

If the fuel jet is injected even further at $\Phi_n = 0.588$, the flame loses its anchoring point in the wake region of the fuel supply segment and stabilizes itself behind the air guiding panel, leading to an extremely enlarged flame and significant heating of the air guiding panel structure.

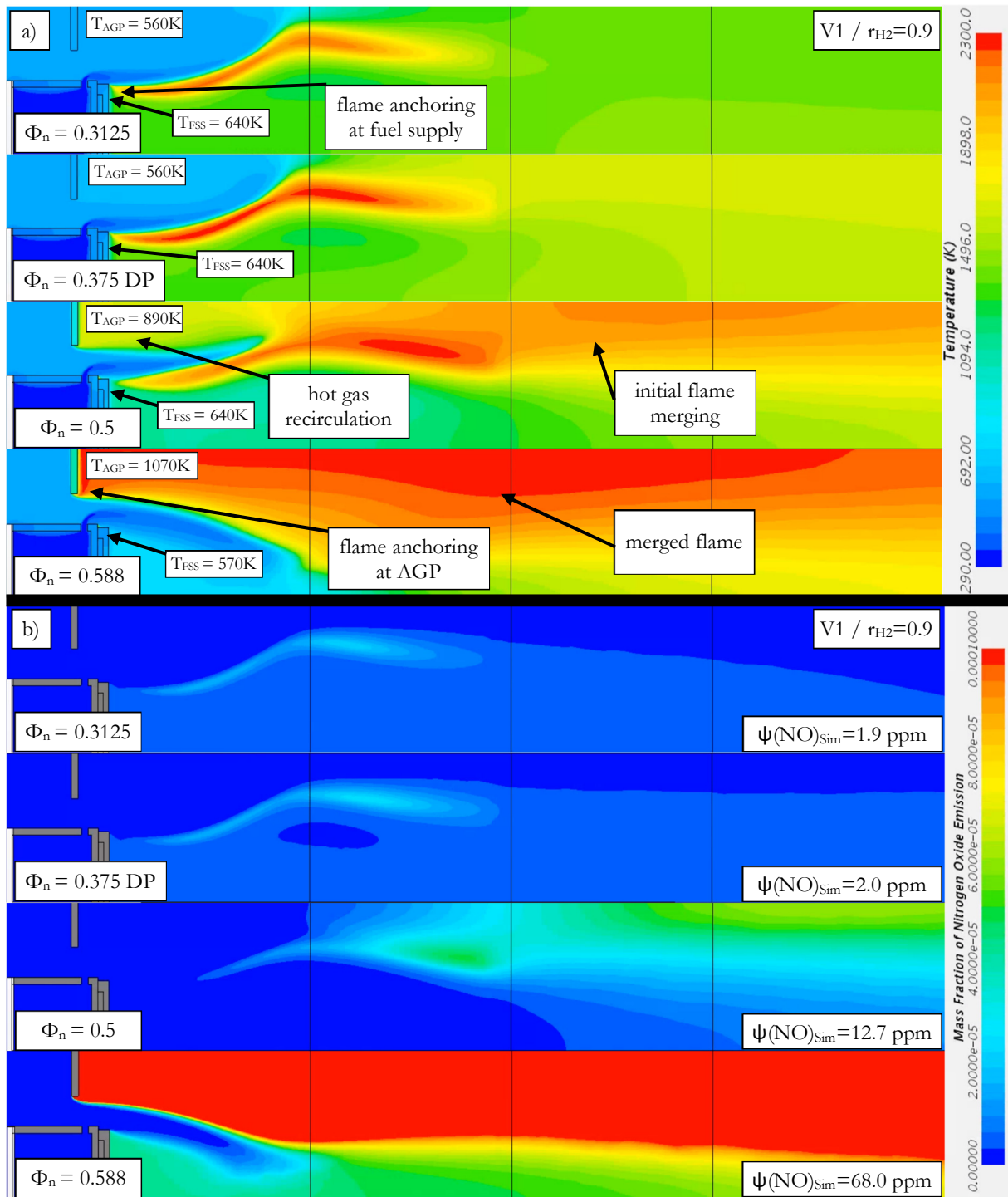


Figure 5-15: Simulated temperature (a) and NO distribution (b) at $r_{H_2}=0.9$ for geometry V1

The phenomenon of flame merging is predicted by the combustion and flow simulations and is also clearly visible during the experimental testing. Figure 5-16 shows the visual flame appearance of merged Micromix flames anchoring in front of the air guiding panel at overload conditions, obtained with a 90% H₂ fuel mixture. The hot recirculation zone leads to heating of the air guiding panel structure that finally was permanently deformed. In contrast, part-load operation leads to clearly separated flames stabilizing in the wake region behind the fuel supply segment.

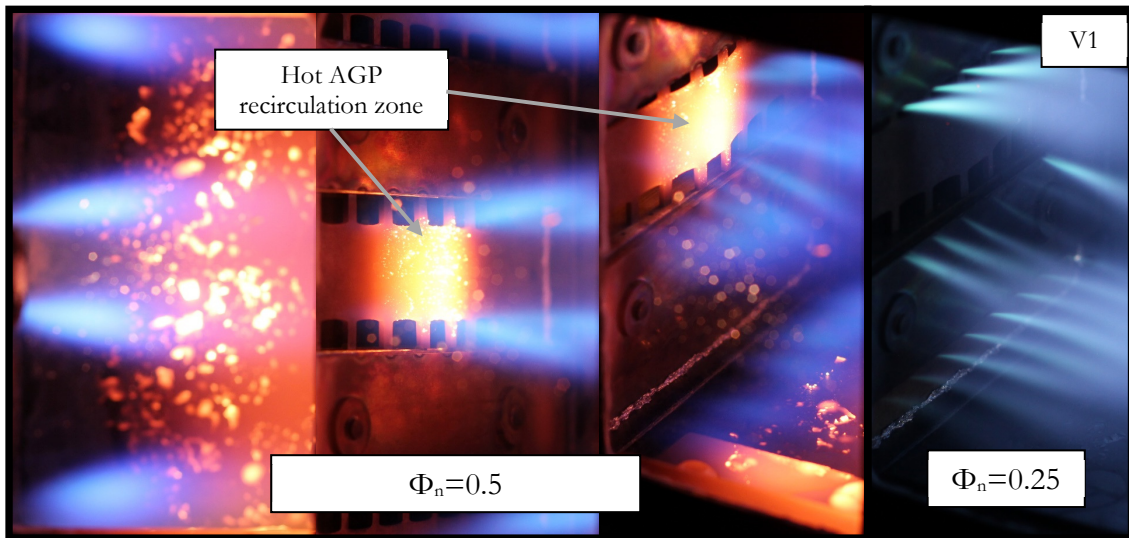


Figure 5-16: Merged flames anchoring at AGP for $\Phi_n=0.5$ and separated flames at $\Phi_n=0.25$ for geometry V1 and $r_{H_2}=0.9$

The injection depth-dependent NO_x formation is also responsible for the specific emission characteristic at $\Phi_n = 0.375$ and $\Phi_n = 0.5$ displayed in Figure 5-12. In contrast to part-load operation ($\Phi_n = 0.3125$), where NO_x emissions increase with the hydrogen content in the fuel, the experimental and numerical results show peak NO_x emissions for 90% H₂ in the fuel, instead of 100%.

Figure 5-17 shows the simulated temperature and NO distribution on the central symmetry plane for the three fuel mixtures 80%, 90% and 100% H₂ at the overload operating point $\Phi_n = 0.5$.

For 80 and 90 vol.% H₂ in the fuel, the upper recirculation zones are significantly hotter than for pure hydrogen. This phenomenon indicates a deeper injection of the fuel jet into the air crossflow due to the present higher momentum flux ratios for fuels containing 80-90 vol.% H₂ (cf. Figure 4-7). The increased injection depth leads to a changed flame stabilization that facilitates hot gas recirculation. With the higher momentum flux ratio, combustion with 90 vol.% H₂ fuel at $\Phi_n=0.5$ is closer to flame merging than combustion with 100 vol.% H₂, leading to higher temperatures and ultimately higher NO formation in a region downstream of the MMX flame.

Despite having the same momentum flux ratio and comparable hot gas recirculation, 80% H₂ results in significantly lower NO_x emission than 90% H₂, in both the experiment and the simulation. This is due to the already discussed superimposed effect of decreasing reactivity with increasing methane content in the fuel. As a result, the peak temperatures in the flame and consequently, the NO_x emissions are reduced.

In the experiment, the discussed injection depth-dependent NO_x formation mechanism is present for the full-load and the overload operating point. During part-load operation, the injection depth is small enough over the entire fuel mixture range that no penetration of the shear layer by the fuel

jet occurs. Thus, at part-load conditions, there is no superimposed injection depth-dependent NO_x formation complementing the already discussed fuel mixture dependent NO_x increase (increasing NO_x emissions with an increasing amount of H₂).

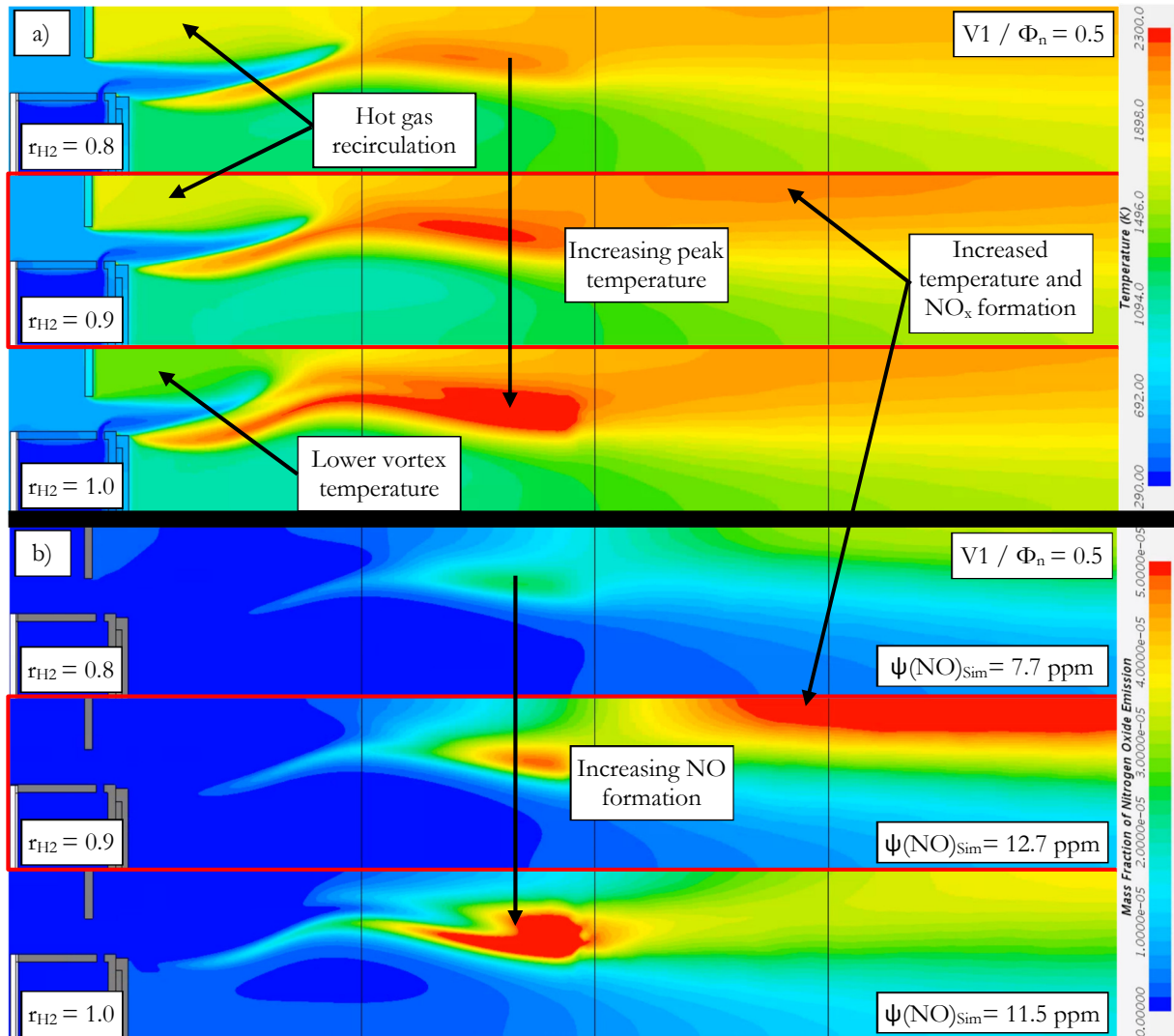


Figure 5-17: Simulated temperature (a) and NO distribution (b) at $\Phi_n = 0.5$ for geometry V1

The general phenomenon of flame merging and the accompanying sudden increase in NO_x emissions is captured very well by the combustion and flow simulation, but the steep NO_x increase is shifted to higher equivalence ratios, as can be seen in Figure 5-18. Due to the limitations of RANS simulations, this shift causes the deviation in the prediction of the NO_x emission level and of the injection depth-dependent NO_x increase at $\Phi_n = 0.375$.

In contrast to recent studies, the current numerical approach also includes modeling of conjugate heat transfer. Preheating the fuel mass flow by the heat flux from the combustion zone through the combustor walls results in decreasing flame peak temperatures [107]. In combination with the applied thermal NO model, the resulting NO emission level is in considerably better agreement with the experimental results than the results presented in the past [49, 117].

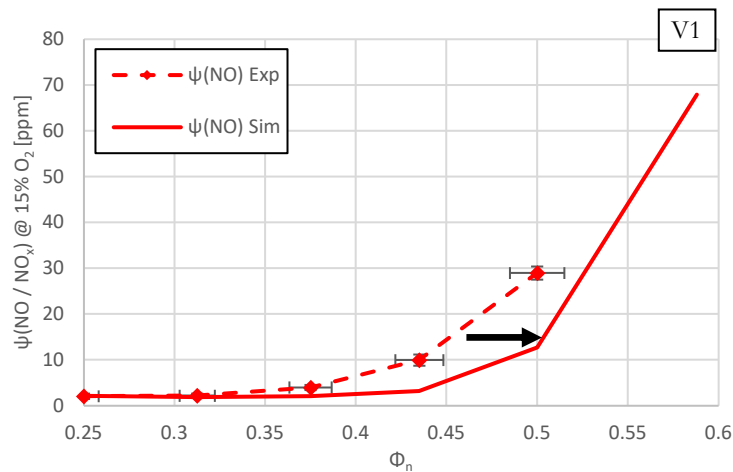


Figure 5-18: Experimental and simulated NO/NO_x emissions at $r_{\text{H}_2}=0.9$ for geometry V1

5.1.4 Conclusion

Despite the design compromise, that takes into account the significantly different fuel and combustion properties of the applied H₂/CH₄ mixtures in one single combustor geometry, the test results of the first Micromix FuelFlex prototype show promising operating behavior, combustion efficiency and pollutant emission levels for flexible-fuel operation. Pure hydrogen combustion yields the highest combustion efficiencies, whereas methane-rich fuel produces the lowest NO_x emissions.

With increasing the amount of methane in the fuel, the unburned fuel and CO emissions rise. The lower temperatures at part-load conditions lead to incomplete combustion, especially once methane is present in the fuel mixture. With increasing methane content, lean off-design operation with high combustion efficiency becomes more and more challenging, leading ultimately to flame blow out (cf. Figure 5-6).

The enlargement of the reaction zone, where CH₄ is broken down, and the existence of a post-flame zone, where CO is oxidized to CO₂, are two unfavorable effects for Micromix combustion. All applied design laws for 100% H₂ aim at miniaturization of the flames for keeping NO_x emissions at a minimum. Enlargement of the flames for optimizing the combustion process at increased CH₄ portion is a conflicting design goal towards low NO_x emissions with hydrogen-rich fuels.

At part-load operation, NO_x emissions increase with the hydrogen content in the fuel. At full- and overload conditions, there is a superimposed injection depth-dependent NO_x effect related to hot gas recirculation and vertical flame merging, generating the highest NO_x emissions at 90% H₂ in the fuel. The phenomenon of flame merging and the accompanying sudden increase in NO_x emissions is captured very well by the combustion and flow simulation, but the steep NO_x increase

is shifted to higher equivalence ratios.

The fundamental characterization of flexible-fuel operation with the baseline Micromix FuelFlex combustor V1 confirms promising operating behavior for a first prototype, but also shows the potential for optimization in several directions:

- I. The general NO_x emission level at the design point barely meets the 5 ppm limit and requires a further reduction in order to establish a safety margin.
- II. The design point of geometry V1 is located in a transition zone, where small deviations towards rich combustion conditions lead to sudden flame merging phenomena and steep increases in NO_x emissions. For guaranteeing low-NO_x MMX combustion over the entire operating range, this transition region must be avoided with an optimized design.
- III. Flame merging at overload conditions produces hot gas recirculation leading to hot spots on the air guiding panel. The resulting thermal stresses exceed the limits for safe operation and restrict the operating range of geometry V1 to $\Phi_n \leq 0.5$. For an optimized geometry, hot gas recirculation in front of the AGP needs to be avoided in order to ensure safe operation over the entire operating range from part-load to overload conditions.
- IV. With increasing amounts of methane in the fuel, the combustion efficiency deteriorates, especially at lean off-design conditions. In order to be a viable fuel option for MMX operated gas turbines, the combustion efficiency of methane-rich fuels needs to be enhanced in a way that they can be utilized at comparable efficiency as hydrogen-rich fuels.

5.2 Optimization of Micromix FuelFlex Combustion

When optimizing the Micromix combustion process for flexible-fuel operation, several design considerations and optimization goals need to be carefully balanced. The potential optimization targets, applicable to MMX flexible-fuel combustion, are summarized in Figure 5-19.

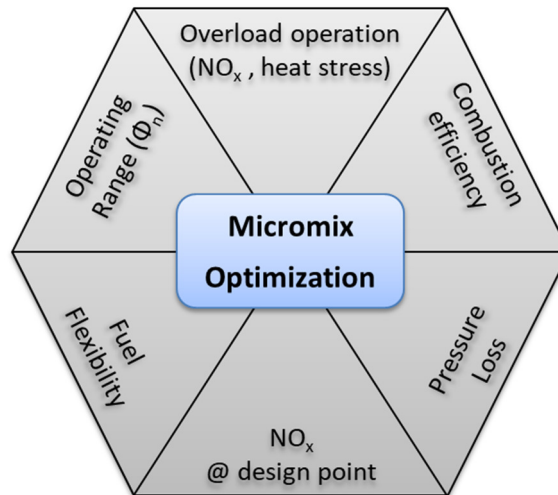


Figure 5-19: Design goals in the Micromix optimization process

The Micromix Combustion Principle is designed for application in industrial gas turbines. Thus, NO_x emission limits are of particular interest as they are a binding requirement for the design process. The NO_x emission target of 5.05 ppm (corrected to 15 vol.% O₂) at the design point needs to be met (with a certain safety margin), in order to enable the MMX principle as a viable option for implementation in industrial gas turbines.

Industrial-scale MMX gas turbine combustors offer, in contrast to the smaller scale low-pressure test burners applied in this thesis, many hundreds of injector nozzles and air gates. However, local deviations from the global equivalence ratio occur at single injectors due to inhomogeneities in the air distribution by the compressor and in the fuel supply system. When the combustor's design point is located in a transition region where small deviations towards rich combustion conditions lead to sudden flame merging phenomena, excessive heating of structural components and steep increases in NO_x emissions can be the consequence. To avoid increased NO_x emissions and structural damage of the combustor module that may lead to an outage of the gas turbine, an essential design goal is to make the combustion system tolerant against inhomogeneities of the fuel and air supply and local deviations from the combustor equivalence ratio.

The research on future gas turbine combustion systems is driven by ecological and economic considerations. In order to be a viable option for industrial gas turbine applications, MMX combustors must operate at high combustion efficiencies. If a single combustor geometry is

applied, this requirement needs to be carefully balanced with the aim for high fuel flexibility, as enhancing the combustion process for hydrogen-rich fuels (in terms of NO_x emissions, overload performance, combustion efficiency) may deteriorate the combustion efficiency for methane-rich fuels. Pure methane combustion yields a very restricted operating range with flame blow out occurring at moderate part-load operation (cf. 5.1.2). Furthermore, the aim of this thesis is to provide a bridge technology with a significant CO₂ reduction potential for a prospective CO₂-free power generation based on low emission gas turbine combustion systems. Since only hydrogen-rich combustion is a viable option for substantial CO₂ reduction (cf. Figure 1-4), the fuel range for the following optimization study is narrowed to 31.5-100 vol.% hydrogen in the fuel with particular focus laid on hydrogen-rich mixtures between 57 vol.% and 100 vol.% H₂.

A second parameter affecting the overall efficiency of a gas turbine is the relative total pressure loss in the combustion chamber. A higher loss in total pressure in the combustion chamber needs to be compensated by a higher pressure level from the gas turbine compressor. The added power for driving the compressor reduces the usable power output of the gas turbine for thrust (in aviation gas turbines) or mechanical work (in stationary gas turbines for energy production). Thus, the pressure loss must be carefully balanced with other design targets, like NO_x emission level. Apparently, design trade-offs are inevitable as there are partly opposing design targets, which restrict a single combustor design from showing peak performance in every respect. The aim of the optimization process presented in the following chapters is to find the best trade between these design targets with the following requirements:

- NO_x emissions at the design point ($\Phi_n=0.375$) well below 5 ppm at 15 vol.% O₂
- Safe overload operation up to $\Phi_n=0.588$ with no steep increase in NO_x emissions and no excessive thermal stress on the combustor's structural components
- High combustion efficiency in a fuel range between 31.5 and 100% H₂
- Tolerable pressure loss

Based on these requirements, the first optimization step applies an increase in the air gate velocity (and corresponding relative total pressure loss) to reduce NO_x emissions, especially at overload conditions, and to increase the combustion efficiency at high methane contents (cf. chapter 5.2.1). After an initial evaluation of the influence of the air gate velocity and the momentum flux ratio on the general combustion characteristics, a modified air gate geometry (V2.2) is applied for extending the safe operating range at overload conditions (cf. chapter 5.2.2).

In a second optimization step, presented in chapter 5.2.3, the lessons learned during this first optimization at increased pressure loss are applied to generate a combustor geometry (V1.1) that

operates at a comparable pressure loss as the baseline design (V1), with significantly improved combustion characteristics in terms of lower NO_x emissions, a wider operating range, and higher combustion efficiencies at high methane contents.

5.2.1 Air Gate Velocity Variation

According to eq. 4.20, the airstream velocity directly influences the momentum flux ratio that determines the injection depth of the fuel jet into the air crossflow. Higher air gate velocities lead to a reduction of the momentum flux ratio.

In the preceding chapter, the influence of injection depth on NO_x emissions at overload conditions of the combustor geometry V1 has been established. In the following, this initial assessment is expanded by a geometric parameter variation that targets the velocity of the airstream flowing through the air guiding panels. For this design space exploration, the MMX combustor is equipped with modified air guiding panels that allow relative air velocities between 87.5% and 125% (V4, V3, V2) with the baseline design (V1) operating at 100%. Between these geometric variations, only the air gate width is modified to change the flow velocity. The overall air mass flow, as well as other geometric parameters, remain constant. The blockage ratios of the combustor module are kept constant to ensure comparable flame stabilization between the vortex structures.

For the design space exploration presented in this chapter, a variation of the equivalence ratio is conducted for each combustor variant over a wide fuel mixture range. A complete set of flame images obtained during experimental testing is included in appendix 8.6.

5.2.1.1 Nitrogen Oxide Emissions

In Figure 5-20, the numerical NO and experimental NO_x emission levels at the design point and two overload operating points are depicted as columns for four different air gate velocities.

At constant air gate velocity, the combustor's operating point affects NO_x formation in two ways. Firstly, richer combustion conditions result in increased combustion temperatures, which promote NO_x formation. Secondly, higher equivalence ratios at constant air mass flow result in a higher fuel jet velocity and injection depth. At a critical injection depth, vertical flame merging occurs that brings along significantly increased NO_x emissions (cf. Figure 5-15). For geometry V1, the design point of the combustor lies in a transition region where small deviations towards rich combustion conditions lead to sudden flame merging phenomena and steep increases in NO_x emissions.

This characteristic changes when the air gate velocity is increased, leading to overall lower NO_x emissions levels. Lowest NO_x emissions are obtained for the highest air gate velocity. For example, NO_x emissions at $\Phi_n = 0.375$ decrease by 89% when going from 87.5% to 125% relative air velocity. Besides, the gradient of NO_x emission versus equivalence ratio is significantly reduced. At a relative air velocity of 87.5%, the NO_x emissions increase by 67% from $\Phi_n = 0.375$ to $\Phi_n = 0.435$.

At 125% air velocity, this increase is only 13.9%. At 87.5%, the overload operating point at $\Phi_n = 0.5$ could not be tested due to overheating of the combustor.

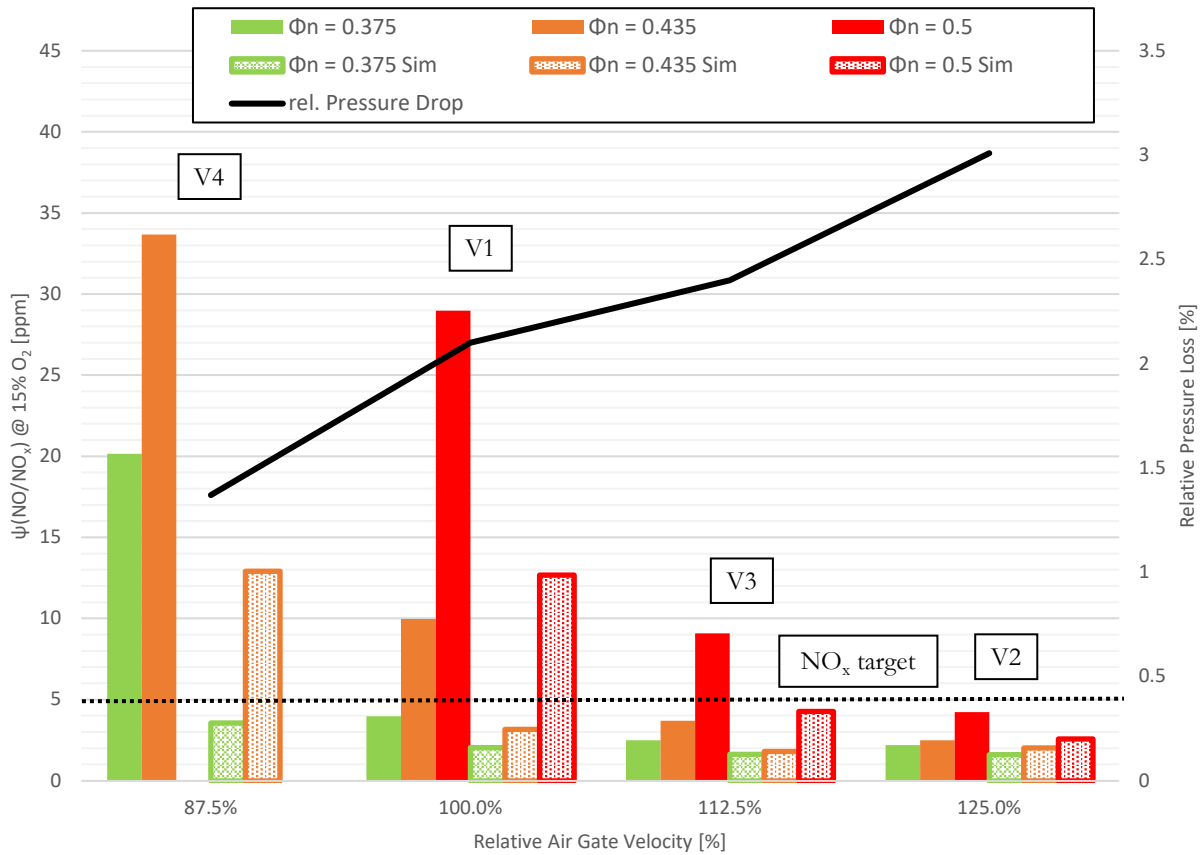


Figure 5-20: NO_x emissions and pressure loss for variable air velocities and $r_{H_2}=0.9$

The cost for this significant improvement in NO_x performance is the pressure loss in the air stream that rises proportionally to the air velocity (cf. Figure 5-20).

$$\Delta p_{t,rel} = \frac{p_{3t} - p_{4t}}{p_{3t}} * 100\% \quad 5.2$$

Since pressure loss in the combustor is a parameter affecting the overall efficiency of a gas turbine, it must be carefully balanced with other design targets, like NO_x emission level.

The simulation results show an underestimation of the quantitative emission levels, but the design trends between different air velocities and equivalence ratios are accurately predicted. As already discussed, the shift of the injection depth-dependent NO_x increase towards higher equivalence ratios causes the present deviations (cf. Figure 5-18).

The phenomenological interpretation of the experimental results based on combustion and flow simulations focuses on the geometries V1 and V2, being the initial combustor geometry with 100% relative air velocity and the preliminary optimum concerning NO_x emissions, with 125% relative air velocity.

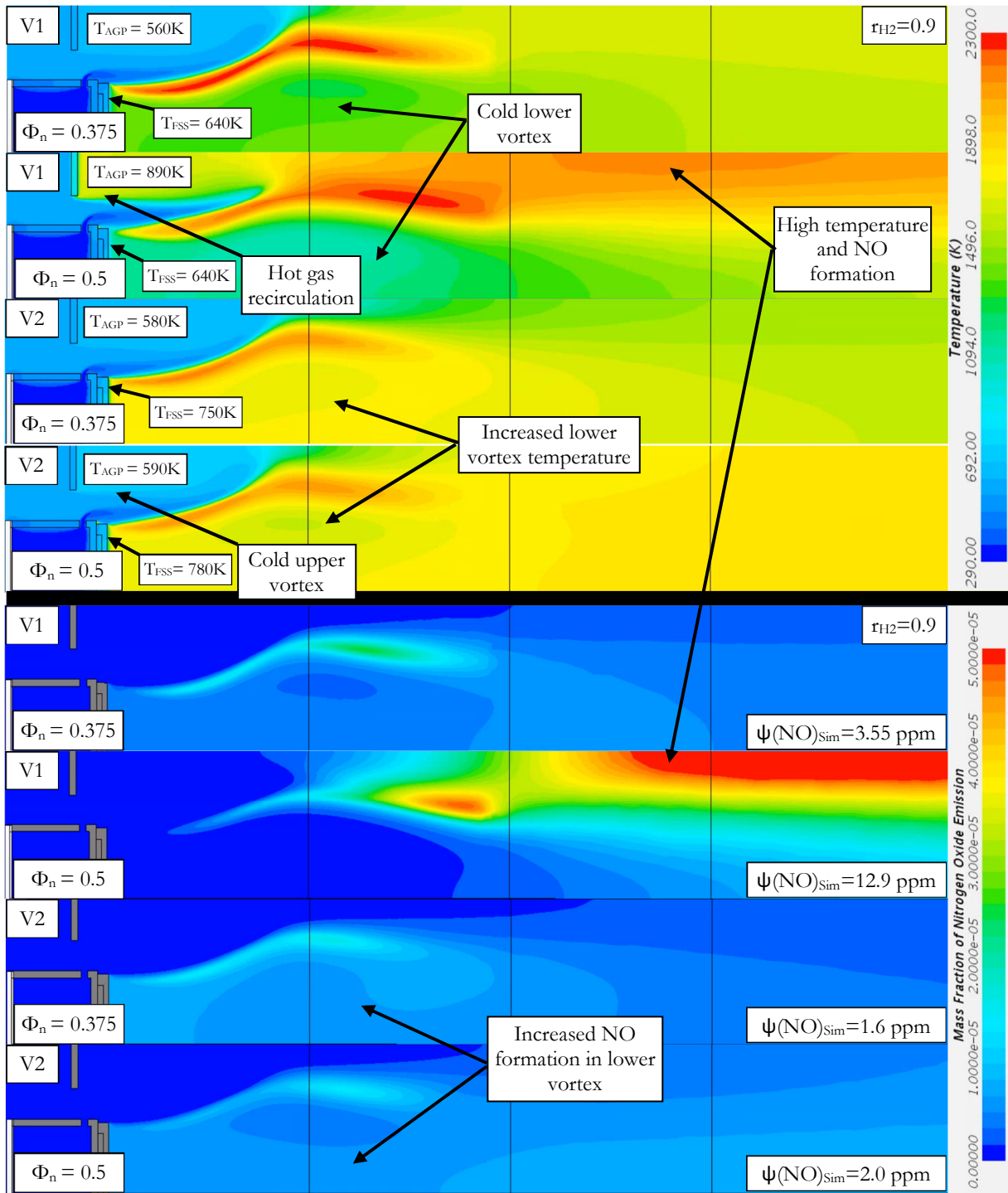


Figure 5-21: Simulated temperature (top) and NO distribution (bottom) on the symmetry plane for V1 and V2 at $r_{H_2}=0.9$

When increasing the air velocity from 100% to 125%, a change in the flame stabilization and the resulting temperature distribution occurs (cf. Figure 5-21). The hot gas recirculation and merging of opposing flames, present for geometry V1 at $\Phi_n = 0.5$ are eliminated with geometry V2. As merged flames bring along a vast high-temperature region where NO_x formation is promoted, they are correlated to the steep increase of NO_x emissions towards overload operating conditions with V1 (cf. chapter 5.1.3). Due to the lower momentum flux ratio of the fuel jet in air crossflow

injection, resulting from the increased air velocity, V2 effectively suppresses flame merging and the correlated NO_x formation.

Where geometry V1 is prone to form hot gas recirculation that heats the upper vortex in front of the air guiding panel, V2 shows increased temperatures of the lower vortex system in front of the fuel supply segment. This phenomenon and the correlated heating of structural components is predicted by the simulation and is also present in the experiment, where it can be seen by the formation of hotspots on the AGP for geometry V1 and on the fuel supply segment for geometry V2 (cf. Figure 5-22). In addition, the location where the flames anchor changes from the top of the air gates (V1) to the fuel supply segment (V2).

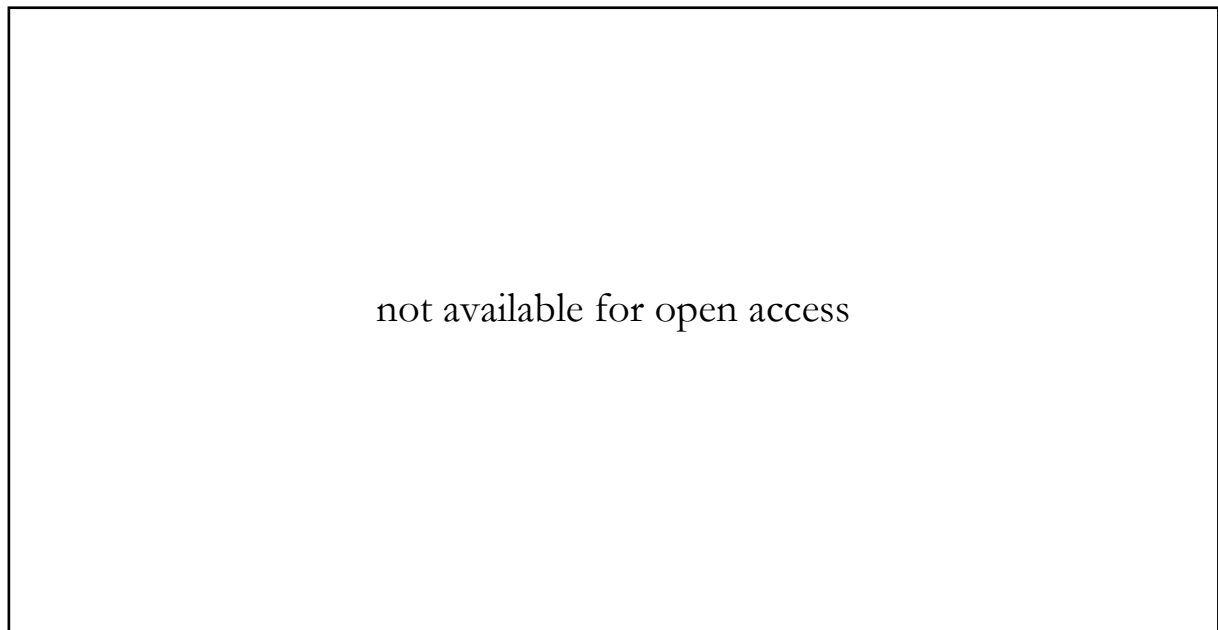


Figure 5-22: Formation of hotspots at $\Phi_n=0.375$ and $r_{H_2}=0.9$ for V1 (a) and V2 (b)

The fuel supply segments are cooled internally by the fuel, and besides, they are equipped with heat shields made from a temperature-resistant nickel-base alloy. Thus, higher flow temperatures located in the lower vortex are much more acceptable than in front of the air guiding panels, that are prone to buckling if exceeding a limit temperature.

In the following, the physical principles that lead to the formation of a high-temperature vortex in front of the fuel supply segment for geometry V2 are discussed based on the conducted combustion and flow simulations. The entering stream of air that does not oxidize the fuel is guided sideways and bypasses the high-temperature flame region. The upper part of this stream is led directly to the outlet, whereas the lower part of the cooling air stream is sucked inside the lower vortex (cf. Figure 5-5).

Figure 5-23 combines the velocity fields on the central symmetry plane for the geometries V1 and V2 with an illustration of the temperature and the vertical velocity component on several cross-

sections in the z-direction of the combustor domain. The velocity vectors on the top and bottom velocity field for V1 and V2 clearly show the two counter-rotating vortices. As demanded by design, V2 shows elevated mean as well as the peak velocities of the air stream passing the air guiding panel. When looking at the cross-sectional temperature distribution between z=-4 and 30 mm, differences in the cold air penetration of the lower vortex structure are apparent. For V1, there is a distinct stream of cold air that bypasses the flame and enters the lower vortex structure, thus leading to a cooling of the recirculation zone. In contrast, this cooling air penetration is much more reduced for V2, leading to several 100 K higher temperatures in the lower vortex.

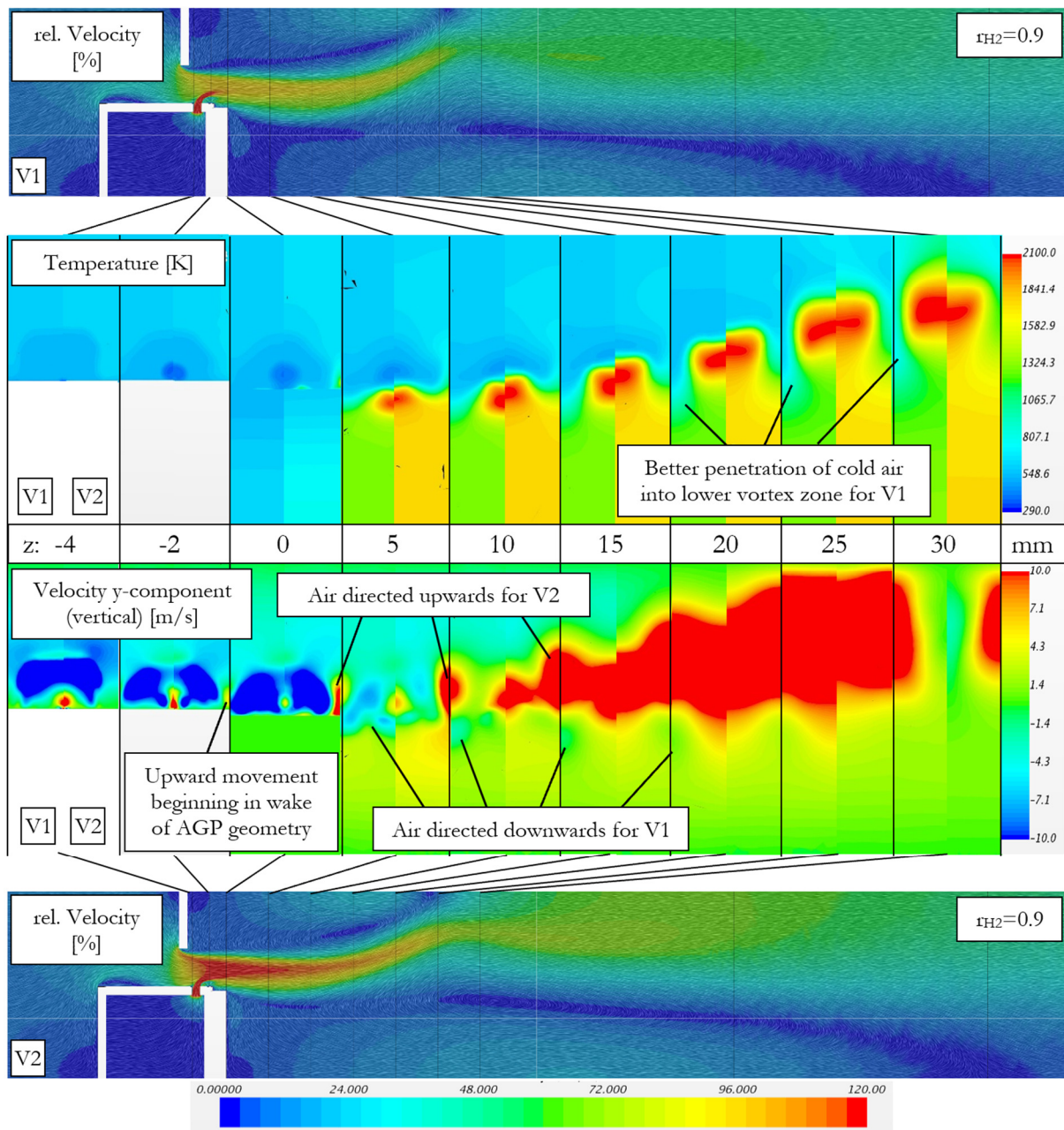


Figure 5-23: Velocity profile on symmetry plane and section-wise temperature and vertical velocity distribution for geometry V1 and V2 at $\Phi_n=0.375$ and $r_{H_2}=0.9$

The reason why air can more easily enter the lower vortex can be found in the illustration of the vertical velocity component of the flow. A positive vertical velocity correlates to a velocity vector pointing in an upward direction (red). A downward-facing flow is illustrated in blue (negative sign). At $z = -4\text{mm}$, directly behind the air gate, the center airflow is directed downwards due to the contraction of the airflow by the air guiding panel. The sideways expansion of this downward-moving stream of air is broader for V1, due to the wider air passage with lower flow velocities at constant air mass flow.

At $z = -2\text{mm}$, the downward movement expands over the whole width of the combustor for V1. In the wake region at the sides of the AGP of V2, an upward-moving airstream develops, due to the interaction with the upper vortex structure.

Further downstream, this upward moving component on the side of the combustor domain gets more dominant. The upward motion of the bypassing airstream reduces the amount of cooling air that is transported to the lower vortex structure. With less cold air input, higher temperatures in the lower recirculation zone are the consequence. In contrast, a dominant downward-moving component in the airstream leads to better cooling of the lower vortex for geometry V1.

Since for geometry V2, the temperatures in the lower vortex do not lead to excessive heating of the combustor's structural components, and no increased NO_x formation in the lower recirculation area, V2 is regarded as an optimized configuration.

5.2.1.2 *Combustion Efficiency*

For configuration V2, operating at a relative air velocity of 125%, the changes in the level of unburned fuel and CO emissions are shown in Figure 5-24 with reference to the initial geometry V1, operating at 100% relative air velocity. In addition to the experimental results, exemplary simulation results at $r_{\text{H}_2} = 0.57$ are included.

Since no flame merging or hot gas recirculation in the upper vortex occurs with V2, no excessive heating of the air guiding panel is detected even at the overload operating point $\Phi_n = 0.588$. Thus, with the change towards V2, the safe operating range of the MMX principle could be significantly extended towards overload combustion conditions with no penalty in the lifetime of structural combustor components or NO_x emissions (cf. Figure 5-20). As seen in Figure 5-24, a by-product of the velocity increase is a significant improvement in the level of all regarded emissions. The most significant improvements are present for the highest methane content regarded during this test campaign ($r_{\text{H}_2} = 0.57$). For the complete operating range, a significant reduction of H₂, CH₄, and CO emissions is achieved, with the most dominant emission reduction at part-load conditions.

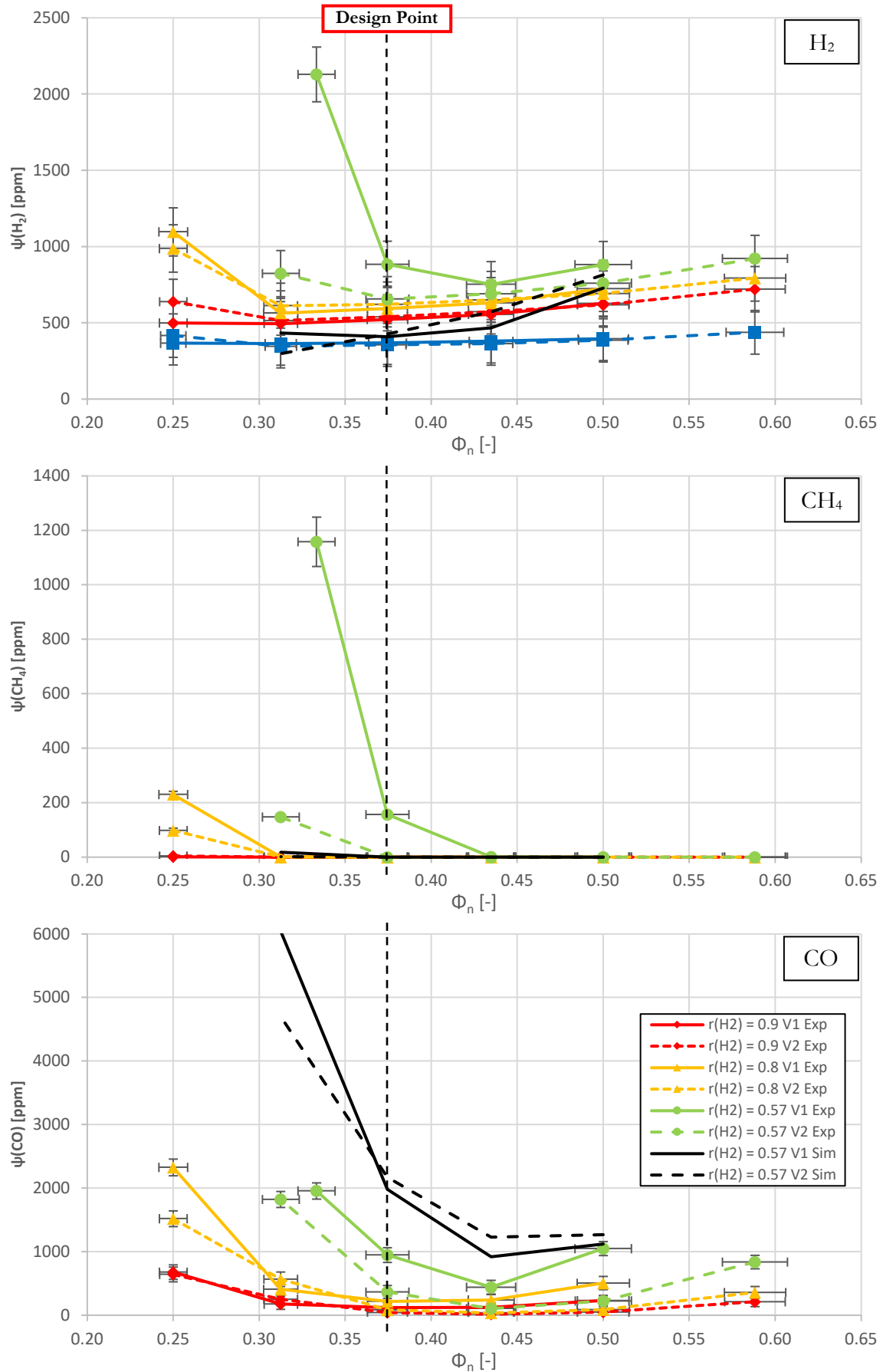


Figure 5-24: Experimental and simulation results of H₂, CH₄ and CO emissions for variable fuel mixtures

Here the increased air velocity at V2 leads to a decrease of H₂ emission by approx. 61% and of CH₄ by 87%. For high hydrogen contents, the differences between the emission levels of both geometries lie in the range of the measurement accuracies.



Figure 5-25: Flame images at $r_{H_2}=0.57$ and $\Phi_n = 0.375$ for V1 (a) and V2 (b)

Since the thermodynamic boundary conditions, as well as all geometric parameters influencing the proportions of the flame stabilizing vortex system remained constant between both geometries, the apparent improvement is related to the increased air velocity. With increasing velocity, the turbulence level rises and leads to an intensified mixing between fuel and air. With a better mixture homogeneity, the combustion process is enhanced, leading to distinct (but still enlarged) MMX flames for geometry V2 that offer a high combustion efficiency instead of indistinct flames with a vast expansion, as seen for geometry V1 (cf. Figure 5-25).

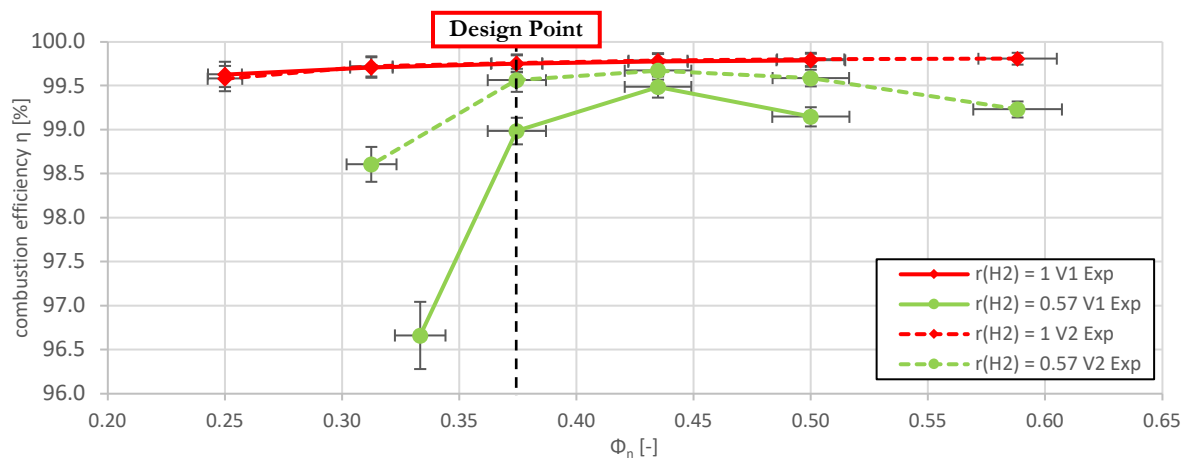


Figure 5-26: Experimental results of combustion efficiency for V1 and V2

With an increased velocity, the operating range where Micromix flames are formed is extended to higher methane contents leading to optimized fuel and CO emissions at $r_{H_2} = 0.57$. For V2, the combustion efficiency exceeds 98.5% over the entire operating range for all tested fuel mixtures between 57% and 100% hydrogen in the fuel.

In Figure 5-24, simulation results are included for $r_{H_2} = 0.57$ as black solid and dotted lines. In contrast to previous numerical assessments, the present results do not give a clear indication about the performance improvement from V1 to V2, which was confirmed by the experiment. For part-load operation, V2 yields less unburned fuel and CO emissions than V1, but for overload conditions, this trend changes. While the physical and thermodynamic influences of the fuel mixture composition and the operating point on the emission trends of unburned fuel and CO emissions are very well captured (cf. chapter 5.1.2), the turbulence effect related to the changed air velocity cannot be resolved adequately by the RANS simulations. Limitations of the applied numerical approach are likely to be the cause since unsteady turbulence effects are not resolved by the numerical grid but modeled by a $k-\epsilon$ turbulence model. Especially flame quenching resulting from local aerodynamic and mixing effects that cause elevated unburned fuel emission levels is presumably not accurately predicted. Thus, it is to state, that the numerical approach shows limitations for predicting and optimizing the combustion characteristics of the MMX combustion principle at higher air gate velocities.

5.2.1.3 Influence of the Momentum Flux Ratio J

The results discussed so far reveal that many of the observed phenomena share a common background. Most of them can be traced back to being a result of the interdependency of the accelerated airflow and the perpendicularly injected fuel jet. The momentum flux ratio indicates how strong this mutual influence is and to which extent jet and crossflow deflect each other.

Figure 5-27 shows the influence of the relative airstream velocity and the operating point (Φ_n) on the momentum flux ratio. When shifting the operating condition towards rich combustion, the momentum flux ratio is increased due to the increased fuel velocity (cf. equation 4.20). In contrast, at constant operating conditions, the momentum flux ratio decreases with an increase in the airstream velocity. Thus, part-load combustion at high air velocities yields the smallest momentum flux ratio, whereas rich conditions at low velocities yield the maximum. As discussed in chapter 5.2.1.1, a high injection depth of the fuel jet into the air crossflow, related to a high momentum flux ratio, favors the formation of hot gas recirculation, leading to heat stress of the combustor's structural components, and flame merging, resulting into a significant increase in NO_x emissions.

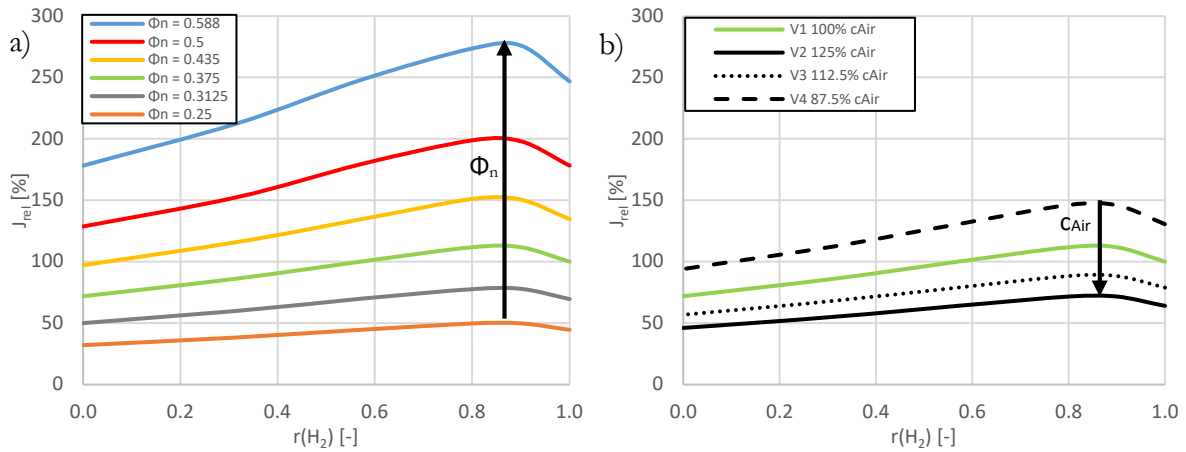


Figure 5-27: Relative momentum flux ratio for variable Φ_n (a) and c_{Air} (b)

Figure 5-28 shows the correlation between NO_x emissions and the square root of the momentum flux ratio for different operating conditions. The square root of the momentum flux ratio is chosen since the discussed effects are related to the injection depth, which, according to eq. 4.19 is dependent on \sqrt{J} . This parameter is expressed as a relative value with respect to the momentum flux ratio obtained with geometry V1 at pure hydrogen combustion at the design point $\Phi_n = 0.375$.

$$\sqrt{J}_{rel} = \frac{\sqrt{J}}{\sqrt{J_{V1, r_{H2}=1, \Phi_n=0.375}}} * 100\% \quad 5.3$$

Figure 5-28 highlights the strong correlation between \sqrt{J} and the measured NO_x emissions for the variation of the normalized equivalence ratio (at 100% rel. air velocity) and the air velocity variation at the design point ($\Phi_n=0.375$). Lower air velocities (e.g., present for V4 in Figure 5-28 b)) lead to higher NO_x emissions, as the momentum flux ratio and consequently, the injection depth is high. The fuel jet can exceed a critical injection depth, leading gradually to the formation of merged flames with increased NO_x emissions. At constant air velocity, an increase in the fuel mass flow by shifting the operating point from part-load to overload has a comparable effect (cf. Figure 5-28 a)).

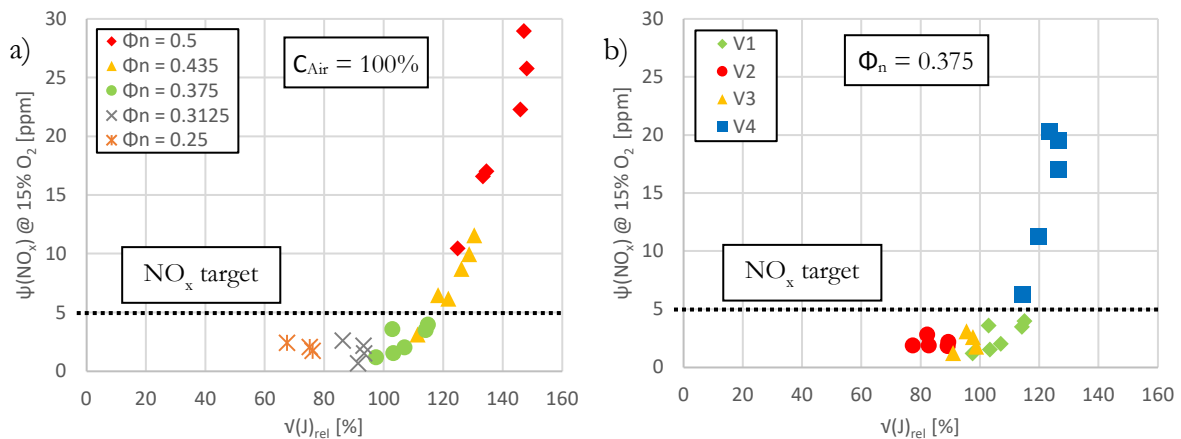


Figure 5-28: Exp. NO_x results versus \sqrt{J}_{rel} for V1 with varying Φ_n (a) and for V1-V4 at $\Phi_n=0.375$ (b)

In Figure 5-29, the NO_x emissions obtained during the design space exploration with the 4 combustor geometries V1-V4 are expressed as a function of \sqrt{J} . The figure combines the results of the full operating range between part-load and overload conditions at varying fuel compositions for all 4 geometries. There is a distinct correlation between NO_x emissions and the injection depth, expressed by the square root of the momentum flux ratio. Higher momentum flux ratios result in increased NO_x formation due to the already discussed vertical flame merging effects. This analysis is also supported by the flame images taken during the experiment (cf. Figure 5-22).

One operating point is highlighted in Figure 5-29 for all 4 combustor variants V1-V4 as diamond-shaped symbols ($\psi_{H_2}=0.9$, $\Phi_n = 0.435$). Despite these operating points having the same thermal power output and the same exhaust gas temperature, the NO_x emissions differ. With geometry variant V2, NO_x emissions at this operating point are 2.5 ppm. When the operating range of a combustor is located at too high momentum flux ratios, as apparent for V4, the NO_x emissions are significantly increased, leading to an emission level of 33.6 ppm.

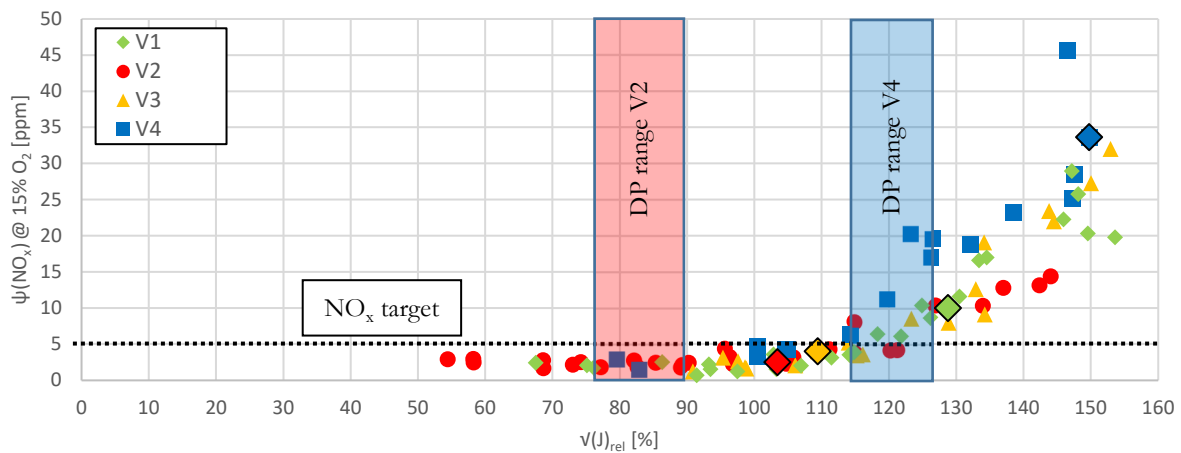


Figure 5-29: Exp. NO_x results versus \sqrt{J}_{rel} for V1-V4 for all measured combinations of r_{H_2} and Φ_n

When exceeding a critical momentum flux ratio, located at approx. $\sqrt{J}_{rel} = 115\%$ NO_x emissions begin to rise steeply. Keeping the momentum flux ratio sufficiently low over a wide combustor operating range, ensures low NO_x performance, as proven for combustor geometry V2 with a relative air velocity of 125%. The excessive NO_x emissions for geometry V4, operating at a relative air velocity of 87.5% with very high momentum flux ratios, substantiates this theory. For V4, even the design point at $\Phi_n=0.375$, indicated in Figure 5-29 as a mixture dependent design point range, lies beyond this critical limit value. Only part-load operation with V4 falls below the limit of 115% and results in low NO_x emissions. For V2, the design point range lies well below the limit value and enables low NO_x emissions over a wide operating range, even at moderate overload conditions.

5.2.1.4 Conclusion

With the conducted design space exploration targeting the air gate velocity in the MMX combustor, the dominant dependence of NO_x emissions on the momentum flux ratio of the jet-in-crossflow mixing process is deduced. Higher momentum flux ratios relate to an increased injection depth of the fuel jet into the air crossflow that facilitates a distinct MMX-specific NO_x increase, once a critical injection depth is exceeded. Keeping the momentum flux ratio sufficiently low ensures low NO_x performance, as proven by the two geometry variants V2 and V4. V2 operates at 125% relative air velocity with momentum flux ratios well below the derived limit value $\sqrt{J_{rel}} = 115\%$. It shows low NO_x performance over a wide operating range up to moderate overload conditions. V4 operates at 87.5% relative air velocity, with even the design point at $\Phi_n=0.375$ exceeding the momentum flux ratio limit of 115%. Drastically increased NO_x emissions at the design point and overload conditions are the consequence.

With increasing the air velocity by 25%, not only the NO_x emission level at the design point, but also the NO_x increase towards overload combustion conditions can be significantly reduced (cf. Figure 5-20). For V2, the design point does not lie in a transition region where deviations towards rich combustion conditions lead to flame merging phenomena. Since vertical flame merging is effectively suppressed, the operating range is extended towards heavy overload ($\Phi_n=0.588$), where no excessive heating or damage of structural components occurs.

Additionally, the level of the unburned fuel and CO emissions is decreased (cf. Figure 5-24). This improvement is related to turbulence effects that influence the mixing process between fuel and air. Despite operating at a higher combustor pressure loss, geometry V2 is regarded as a preliminary optimum concerning combustion efficiency and NO_x emissions. The pressure loss penalty requires further optimization.

5.2.2 Air Gate Height Variation

Evolving from the initial geometry V1 ($c_{\text{Air}}=100\%$) to higher air velocities (V2, $c_{\text{Air}}=125\%$) results in better combustion efficiency and lower NO_x emissions. Increasing the air velocity at constant operating conditions leads to a decrease in the momentum flux ratio. With a lower momentum flux ratio comes a lower injection depth, and therefore a lower risk of fuel breaking through the shear layer and promoting flame merging and the related increase in NO_x emissions.

The critical injection depth is interconnected with the height of the air gate and the resulting position of the shear layer between the upper recirculation zone and the air crossflow (cf. Figure 1-6). With increasing the air gate height, the critical momentum flux ratio increases as well (cf. Figure 4-10), leading to a presumably better NO_x performance at overload conditions.

To test this hypothesis, 2 geometry variants based on the preliminary optimum geometry V2, operating at 125% relative air velocity, are created. Geometry V2.1 explicitly violates the stated design philosophy by lowering the air gate height. This design has a low critical injection depth and leaves less height for the fuel jet to discharge into the combustor zone. In consequence, NO_x emissions are anticipated to increase significantly at lower equivalence ratios in comparison to geometry V2.

The second design variant V2.2 respects the design considerations deduced in the preceding chapter. With a higher but narrower air gate, the critical injection depth is increased, giving the fuel jet more height for discharge even at heavy overload conditions with high momentum flux ratios. With this design, vertical flame merging and related sudden NO_x increases are expected to be suppressed.

While the width and height of the air gate are changed, the air gate cross-section for V2, V2.1, and V2.2 is kept constant in order to ensure comparable air velocities between the geometries.

5.2.2.1 Combustion Efficiency

Figure 5-30 shows the combustion efficiencies obtained with the two combustor geometries V2 and V2.2. Despite the adapted geometrical layout, both combustor variants operate at combustion efficiencies above 98.5% over the entire investigated operating range, with deviations between both geometries close to the magnitude of the measurement accuracy. Supplemental diagrams containing the emission levels of unburned fuel and CO are included in appendix 8.2 - 8.4.

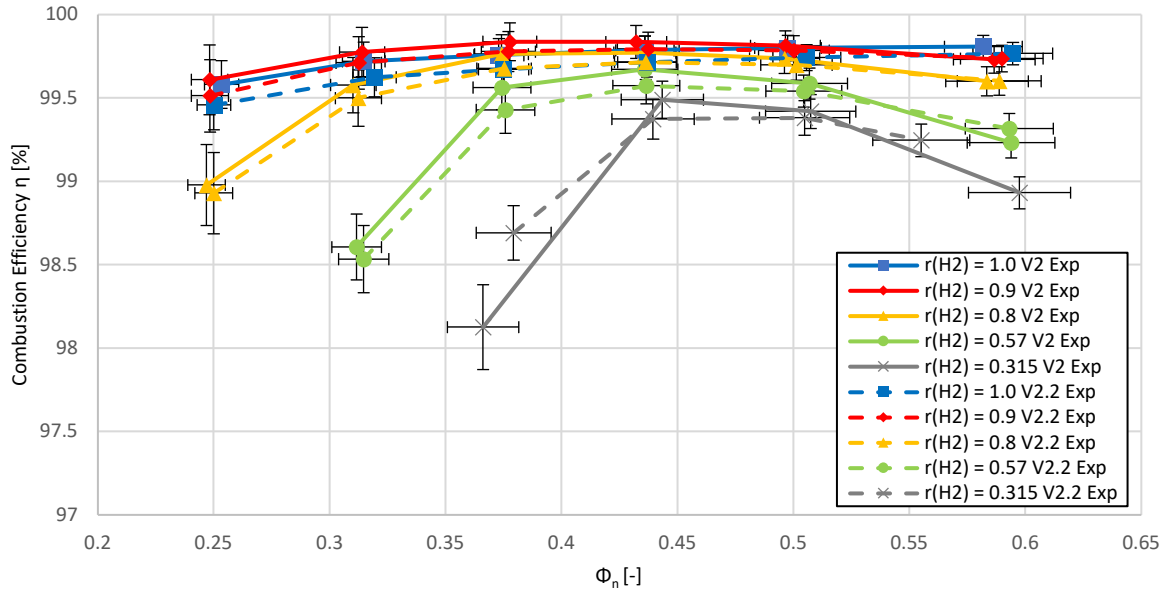


Figure 5-30: Experimental results of combustion efficiency for geometry V2 and V2.2

5.2.2.2 Nitrogen Oxide Emissions

In Figure 5-31, the experimental NO_x emission levels at the design point and 3 overload operating points are depicted as columns for the geometries V2, V2.1, and V2.2. As representative fuel mixtures composition $r_{H_2} = 0.9$ is chosen. Diagrams showing the NO_x emissions over the entire operating range are included in appendix 8.1. Between the 3 geometries tested, the air gate velocity stays constant while the air gate geometries become gradually narrower but higher from V2.1 over V2 to V2.2. Only the air guiding panels are modified, thus leaving all boundary conditions, especially air mass flow and overall thermal power output constant.

As predicted, the NO_x formation is drastically increased using the AGPs with the lower air gates (V2.1). Not only the general emission level at full-load operating conditions ($\Phi_n = 0.375$) is increased but also the gradient towards fuel-rich combustion conditions. With V2.1, the overload operating point at $\Phi_n = 0.588$ could not be tested due to overheating of the combustor's air guiding panels (cf. Figure 5-32).

By applying higher but narrower air gates at a constant air stream velocity with geometry V2.2, the already decent NO_x performance towards heavy overload of geometry V2 is optimized further with a slight decline of the emission level at full- and moderate overload operating conditions. When going from $\Phi_n=0.5$ to $\Phi_n=0.588$, the NO_x emission level increases by only 2.8 ppm, whereas the preliminary optimum V2 showed an increase of 10.2 ppm. By the implemented design modification in V2.2, exceeding the critical injection depth by the fuel jet is effectively avoided due to the higher air gate geometry.

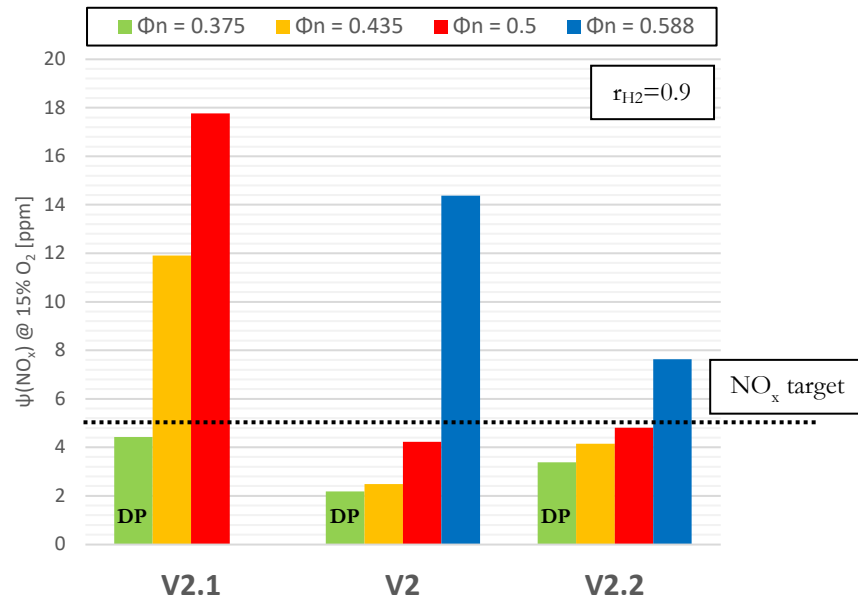


Figure 5-31: NO_x emissions at full- and overload for V2.1, V2, and V2.2 at r_{H2}=0.9

As can be seen from flame images at overload conditions ($\Phi_n = 0.5$) and $r_{H_2} = 0.9$, no glowing of the AGP, indicating hot gas recirculation or flame merging effects due to an excess of the critical injection depth, is present for V2.2 (cf. Figure 5-32 c)).

The trend, established in chapter 5.2.1.1, that narrowing the air gates and thus increasing the sideward wake regions, enhances heating of the lower vortex region is substantiated by the flame images. The slight glowing of the fuel supply segments present for V2 (cf. Figure 5-32 b)), indicating hot gas recirculation in the vortex in front of the fuel supply segment, is intensified for geometry V2.2, but still acceptable, due to the applied heat shield design.

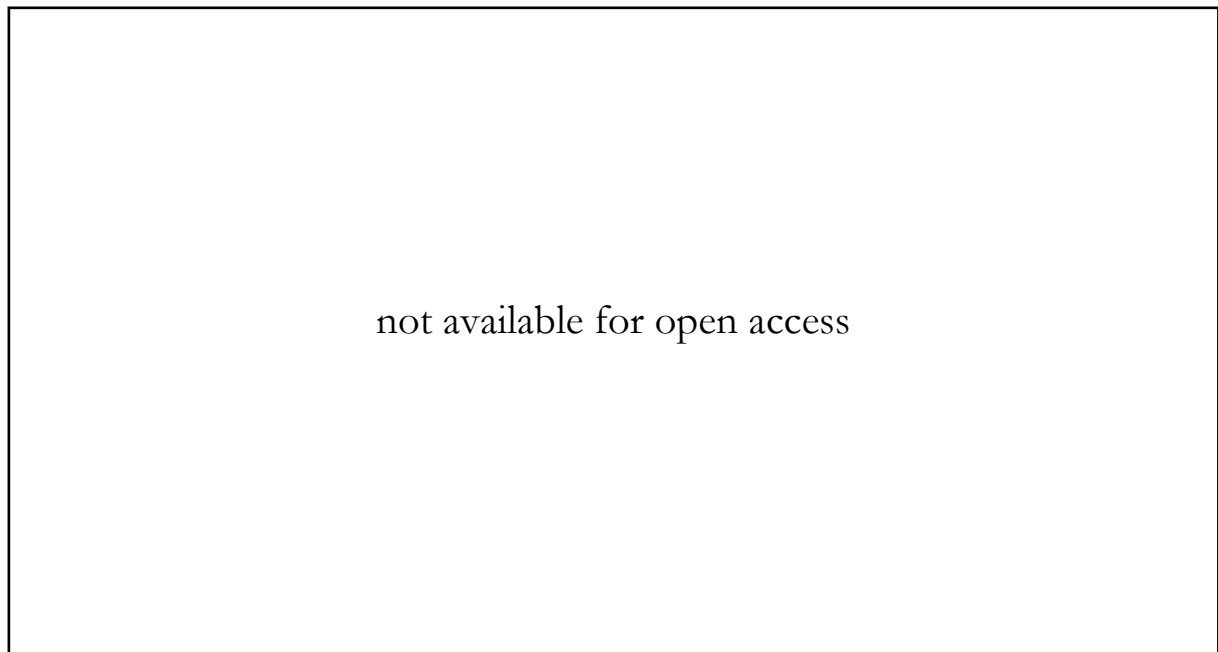


Figure 5-32: Flame images for V2.1 (a), V2 (b), and V2.2 (c) at r_{H2}=0.9 and Φ_n=0.5

For geometry V2.1, exceeding the critical injection depth at overload conditions leads to a shift of the flame anchoring position to the top of the air gate and resulting hot gas recirculation in the upper vortex region, explaining the glowing AGPs in Figure 5-32 a). The excessive heating led to buckling and permanent deformation of the AGPs at $\Phi_n = 0.5$.

5.2.2.3 Influence of the Air Gate Height

Figure 5-33 a) shows the correlation between NO_x emissions and the square root of the momentum flux ratio for the 3 tested combustor geometries V2, V2.1 and, V2.2 at operating conditions corresponding to part-, full- and overload conditions with variable fuel mixtures. The momentum flux ratios at the combustors design points ($\Phi_n = 0.375$) are indicated in Figure 5-33 as mixture dependent design point ranges. Since the critical injection depth is not only dependent on the momentum flux ratio, but also on the air gate height that determines the position of the shear layer between the recirculation zone and the air crossflow (cf. Figure 1-6), the illustration of NO_x emissions as a function of \sqrt{J} gives no clear indication on a specific limit momentum flux ratio that ensures low NO_x performance.

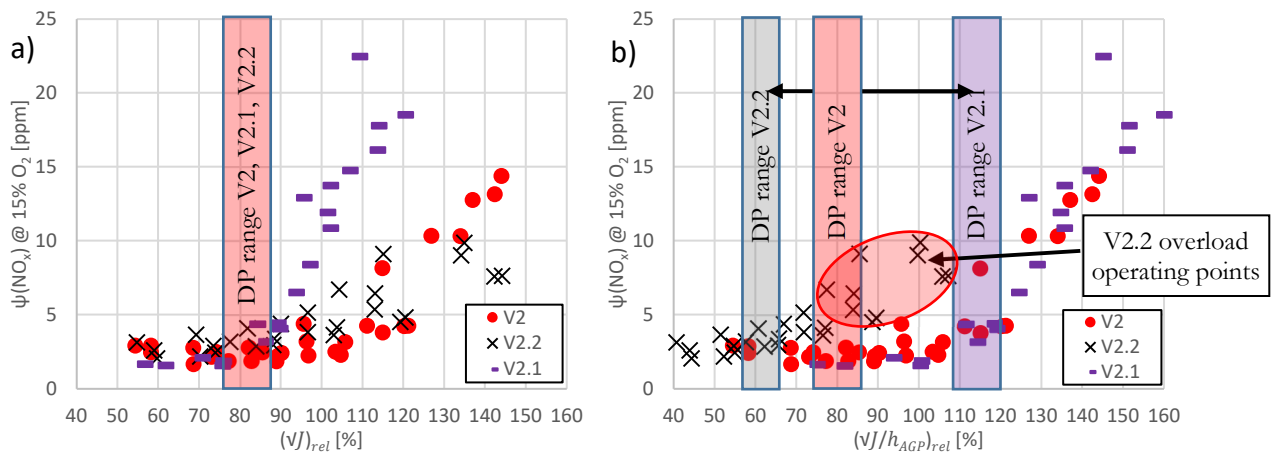


Figure 5-33: Experimental NO_x results versus \sqrt{J}_{rel} (a) and $\left(\frac{\sqrt{J}}{h_{AGP}}\right)_{rel}$ (b) for V2, V2.1 and V2.2 at varying Φ_n and r_{H2}

Based on the momentum flux ratio J , the parameter $\left(\frac{\sqrt{J}}{h_{AGP}}\right)_{rel}$ is defined. For comparing different combustor geometries with changing air gate proportions, it takes into account the height of the air gate, which is related to the critical injection depth. It is put in relation to the design momentum flux ratio of geometry V1 at a normalized equivalence ratio of $\Phi_n = 0.375$ and $r_{H2} = 1$ and the corresponding air gate height of V1.

$$\left(\frac{\sqrt{J}}{h_{AGP}}\right)_{rel} = \frac{\frac{\sqrt{J}}{h_{AGP}}}{\frac{\sqrt{J_{V1,r,H2=1;\Phi_n=0.375}}}{h_{AGP,V1}}} * 100\% \quad 5.4$$

In Figure 5-33 b), the NO_x emissions for the three regarded combustor geometries are given as a function of $\left(\frac{\sqrt{J}}{h_{AGP}}\right)_{rel}$. Since the air gate geometry is regarded in this parameter, the design point ranges for the three geometries with varying air gate heights change. With increasing air gate height, the normalized momentum flux ratios are reduced, resulting in the lowest design point range for geometry V2.2 and the highest for V2.1. With a higher air gate at constant momentum flux ratio, the safety margin towards the critical injection depth is increased.

For V2.1, the design point is shifted inside the transition region (towards higher values of $\left(\frac{\sqrt{J}}{h_{AGP}}\right)_{rel}$), where a small change in the equivalence ratio leads to a sharp increase in NO_x emissions. As discussed earlier, with gas turbine integration in mind, locating the design point in this transition region needs to be avoided, since naturally occurring inhomogeneities in the fuel and air supply of a gas turbine combustion chamber may result in local variations of the equivalence ratio.

For V2.2 the operating point is shifted well outside this transition region (towards lower values of $\left(\frac{\sqrt{J}}{h_{AGP}}\right)_{rel}$), making it safe against vertical flame merging and the related sudden NO_x increase towards overload conditions. Despite being predominant for MMX combustion, the injection depth-dependent NO_x formation is only one effect leading to increased NO_x emissions. The second, being the thermal conditions in the combustion chamber, related to the equivalence ratio, can also be seen in Figure 5-33 b) for geometry V2.2. This quite unconventional design with very narrow and high air gates is safe against vertical flame merging effects. With effectively suppressing the MMX-specific injection depth-dependent NO_x increase, only the general temperature-dependent NO_x formation towards high equivalence ratios is present. Under heavy overload conditions, NO_x formation is promoted even if the injection depth criterion is not exceeded.

5.2.2.4 Conclusion

With the conducted air gate geometry variation, a dependence between NO_x emissions and the normalized momentum flux ratio $\left(\frac{\sqrt{J}}{h_{AGP}}\right)_{rel}$ is derived. Since vertical flame merging is related to an excess of the critical injection depth, the momentum flux ratio is put in relation to the air gate height, which determines the position of the shear layer between the recirculation zone and the air

crossflow. Keeping the normalized momentum flux ratio sufficiently low, ensures low NO_x performance over a wide operating range.

With the geometrical optimization towards V2.2, a significant improvement in the MMX combustor's overload performance is achieved at the cost of slightly increased NO_x emissions at full- and moderate overload, while keeping the unburned fuel and CO emission level nearly constant. V2.2 still operates at a relative air velocity of 125%, resulting in an increased pressure loss in comparison to the first combustor geometry V1. The pressure loss penalty of design V2.2 is the subject of the final optimization step, presented in the following chapter.

5.2.3 Pressure Loss Optimization - V1.1

With the lessons learned from the fundamental characterization of the MMX combustion principle (cf. chapter 5.1) and the optimization studies in chapter 5.2.1 and 5.2.2, the final optimized geometry V1.1 is deduced. The air gate velocity is lowered in order to achieve a comparable pressure loss as the initial combustor V1. By adapting the combustor's air gate geometry (higher but narrower air gates in comparison to V1), the operating range of V1.1 is shifted to lower normalized momentum flux ratios $\left(\frac{\sqrt{J}}{h_{AGP}}\right)_{rel}$. With this shift, the safety margin towards exceeding the critical injection depth is increased. As demonstrated for V2.2 (cf. chapter 5.2.2), this effectively suppresses vertical flame merging and the associated steep NO_x increase at overload conditions.

5.2.3.1 Pressure Loss

In the last optimization step, the air velocity and resulting pressure loss, that was initially raised to lower the NO_x emission level, is reduced to a level comparable to geometry V1, while keeping the improvements obtained with geometry V2.2. Like V1, the optimized geometry V1.1 is operated at 100% rel. air velocity but offers narrower but higher air gates, in order to suppress the injection depth-dependent sudden NO_x increase at overload conditions.

With the decrease of the velocity from 125% to 100%, a reduction of the relative pressure loss is achieved. As substantiated by the experimental results presented in Table 7, V1.1 operates with approx. 1.9% at a comparable pressure loss as V1.

Table 7: Relative total pressure loss for V1, V1.1, V2, and V2.2 at $\Phi_n = 0.375$ and $r_{H_2}=0.9$

	V1	V2	V2.2	V1.1
relative total pressure loss [%]	2.1	3	2.9	1.9

5.2.3.2 Nitrogen Oxide Emissions

In Figure 5-34, a comparison between V1 and V1.1 concerning experimental NO_x emissions is presented. The assessment focuses on the combustor design point at $\Phi_n = 0.375$ and overload conditions. With the optimized geometry, not only the general emission level at the design point is lowered, but also the sudden increase of NO_x emissions at overload conditions, as present for V1, is effectively suppressed. At the design point, NO_x emissions below 1.8 ppm are achieved over the complete investigated fuel range between 31.5% and 100% H₂, whereas the initial combustor geometry delivered 4 ppm at the same thermal power output. The most significant improvement

is apparent for the combustor's overload performance. At an equivalence ratio of $\Phi_n = 0.5$, V1 produces 29 ppm NO_x at $r_{H_2} = 0.9$. At the same operating point, V1.1 generates just 4.4 ppm.

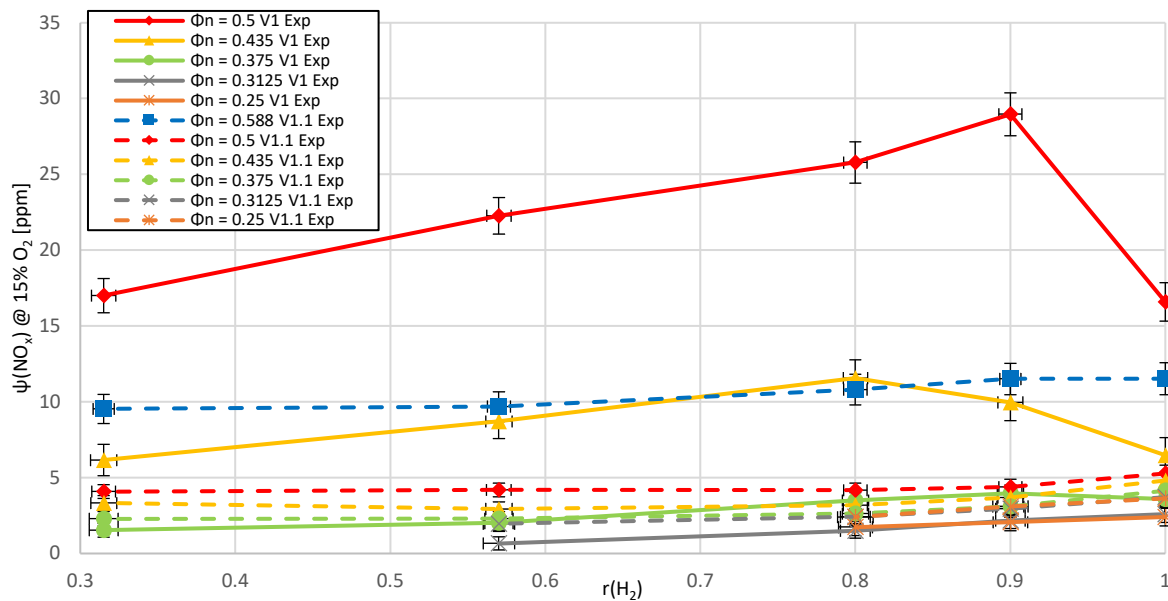


Figure 5-34: Experimental results of NO_x corrected to 15% O₂ for V1 and V1.1

Additionally, the injection depth dependence of NO_x (cf. 5.1.3) that yields the highest emissions for V1 at 80-90% H₂, is not present for V1.1, whereas it is dominant for V1 at the design point and overload conditions. For V1.1, NO_x formation at part- full- and overload conditions ($\Phi_n \leq 0.5$) is driven by the increased peak temperatures of hydrogen-rich fuel combustion. At heavy overload operation, the MMX-specific injection depth-dependent NO_x formation becomes dominant when the injection depth exceeds a critical level, and flame merging effects begin to occur.

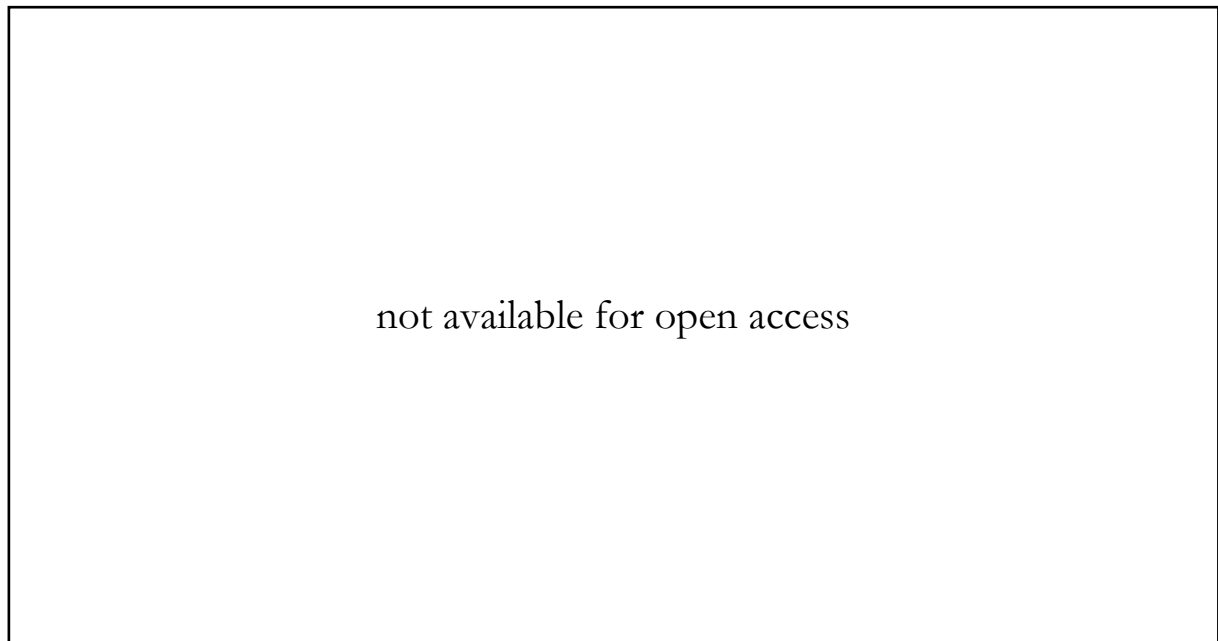


Figure 5-35: Flame images for V1 (a) and V1.1 (b) at $\Phi_n = 0.5$ $r_{H_2} = 0.9$

By increasing the air gate height for geometry V1.1, the critical injection depth is raised in a way that over the entire operating range, no significant injection depth-dependent NO_x formation and no vertical flame merging occurs. The shift of the critical injection depth can be expressed by the normalized momentum flux ratio $\left(\frac{\sqrt{J}}{h_{AGP}}\right)_{rel}$. In Figure 5-36, the operating range of V1.1 is shifted towards lower normalized momentum flux ratios leading to a higher safety margin towards exceeding the critical injection depth.

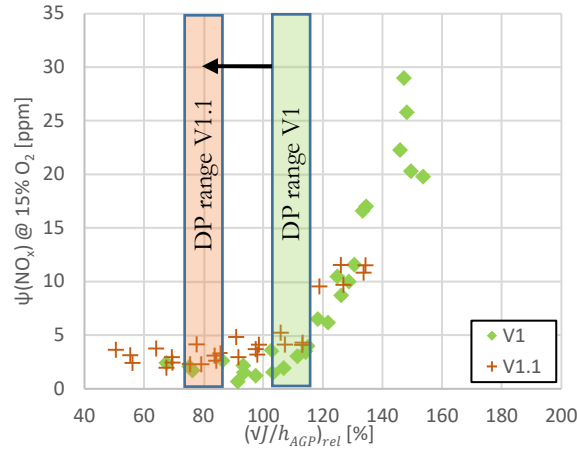


Figure 5-36: Experimental NO_x results versus $\left(\frac{\sqrt{J}}{h_{AGP}}\right)_{rel}$ for V1 and V1.1 at varying Φ_n and r_{H2}

In consequence, the optimized geometry V1.1 can be operated even at the heavy overload operating point at $\Phi_n = 0.588$ without vertical flame merging. This effectively suppresses the steep increase of NO_x emissions and overheating of the combustor's structural components. V1, in contrast, is limited to a maximum equivalence ratio of $\Phi_n = 0.5$ since overheating of the AGPs occurs (cf. Figure 5-35).

In Figure 5-37, the NO_x emissions obtained with all tested combustor geometries over the entire operating and fuel mixture range are plotted as a function of $\left(\frac{\sqrt{J}}{h_{AGP}}\right)_{rel}$. Below a particular limit value, that is approx. 115%, low NO_x combustion is achieved with little influence of the fuel mixture composition and the operating conditions. When exceeding this limit value, flame merging effects start to occur, resulting in injection depth-dependent NO_x formation. The higher the relative normalized momentum flux ratio, the higher the obtained NO_x emissions. For instance, the operating range of geometry V4 or V2.1 lies mostly beyond this limit value, explaining the high emission levels measured throughout the experimental assessment.

The quite unconventional design V2.2 with very narrow and high air gates is safe against flame merging effects, but the temperature-dependent NO_x formation towards high equivalence ratios is apparent. Under heavy overload conditions, NO_x formation is promoted even if the injection depth

criterion is not exceeded for V2.2. For all other, less extreme geometries, the injection-depth dependent NO_x increase is dominant.

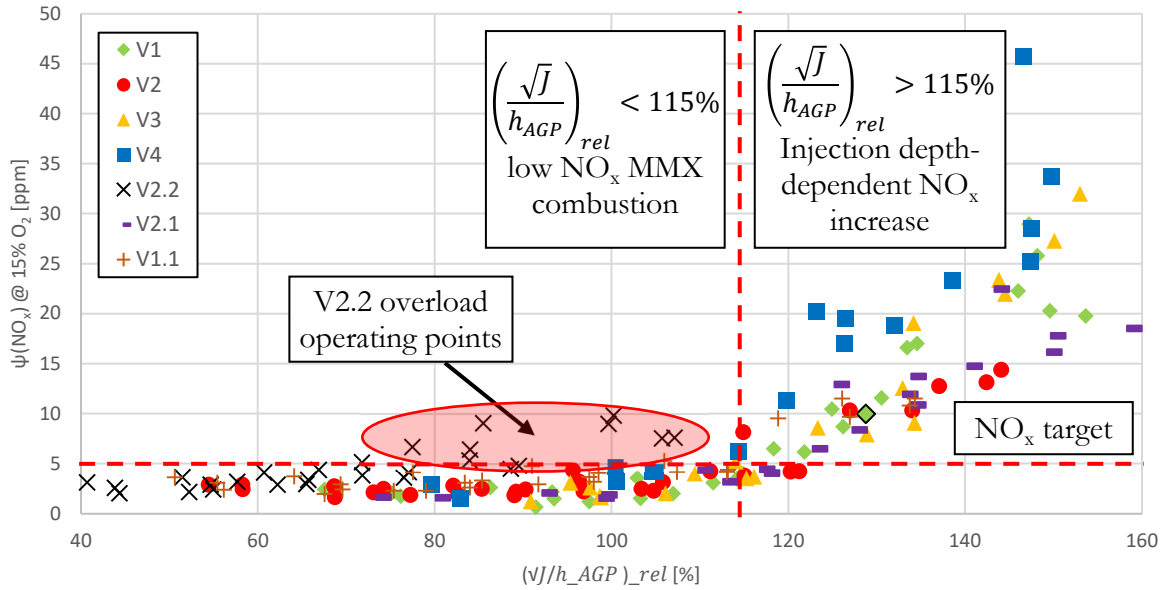


Figure 5-37: Experimental NO_x results versus $\left(\frac{\sqrt{J}}{h_{AGP}}\right)_{rel}$ for all geometries at varying Φ_n and r_{H2}

With the normalized momentum flux ratio $\left(\frac{\sqrt{J}}{h_{AGP}}\right)_{rel}$, a design criterion is derived that is useful for the design process of future MMX combustors operated with variable fuel mixtures of hydrogen and methane. Within limits set by the design and manufacturing process, the momentum flux ratio should be chosen in a way that no steep NO_x increase occurs in the intended operating range.

In Figure 5-38, the experimental and simulated NO/NO_x emissions are presented for the combustor geometries V1 and V1.1. As discussed in chapter 5.1.3, there is a distinct shift of the steep NO_x increase towards higher equivalence ratios for V1 due to the injection depth-dependent NO_x formation, which is dominant for V1. This injection depth effect is not captured accurately due to the limitations of the applied numerical approach.

With suppressing this NO_x formation effect by modifying the combustor geometry, also the prediction of the NO_x level and the trend is in much better agreement for V1.1. NO_x formation is mostly driven by the reactivity of the applied fuel and the resulting peak temperatures and residence times of NO_x precursors. Apparently, these effects are captured very well by the chosen approach of using a steady RANS solver with detailed chemistry, a thermal NO model, and conjugate heat transfer modeling. Thus, with the general chemistry model able to predict the NO_x emission level quite accurately, a challenge for further research is the accurate prediction of the jet-in-crossflow process, which will make the implementation of higher-order methods like LES necessary.

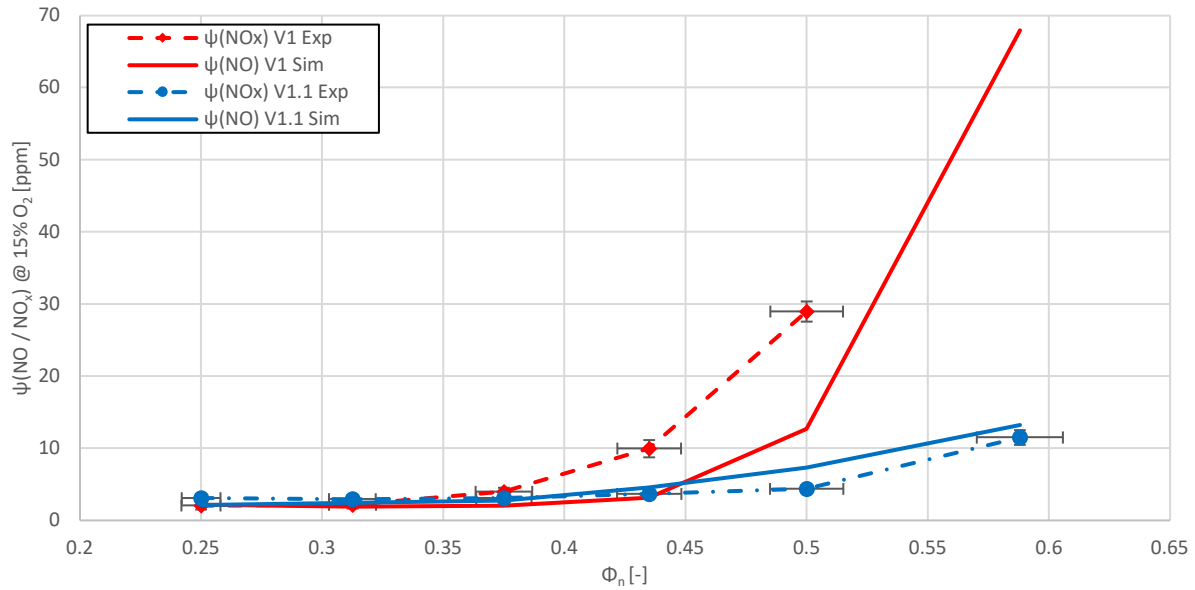


Figure 5-38: Experimental and simulated NO/NO_x emissions for V1 and V1.1 at $r_{H_2}=0.9$

5.2.3.3 Combustion Efficiency

In addition to the significant improvement concerning the general NO_x emission level and the overload performance, also the combustion efficiency is enhanced by the optimized combustor geometry V1.1. In Figure 5-39, the combustion efficiencies for fuel mixtures between 31.5% and 100% H₂ are presented for the geometries V1 and V1.1.

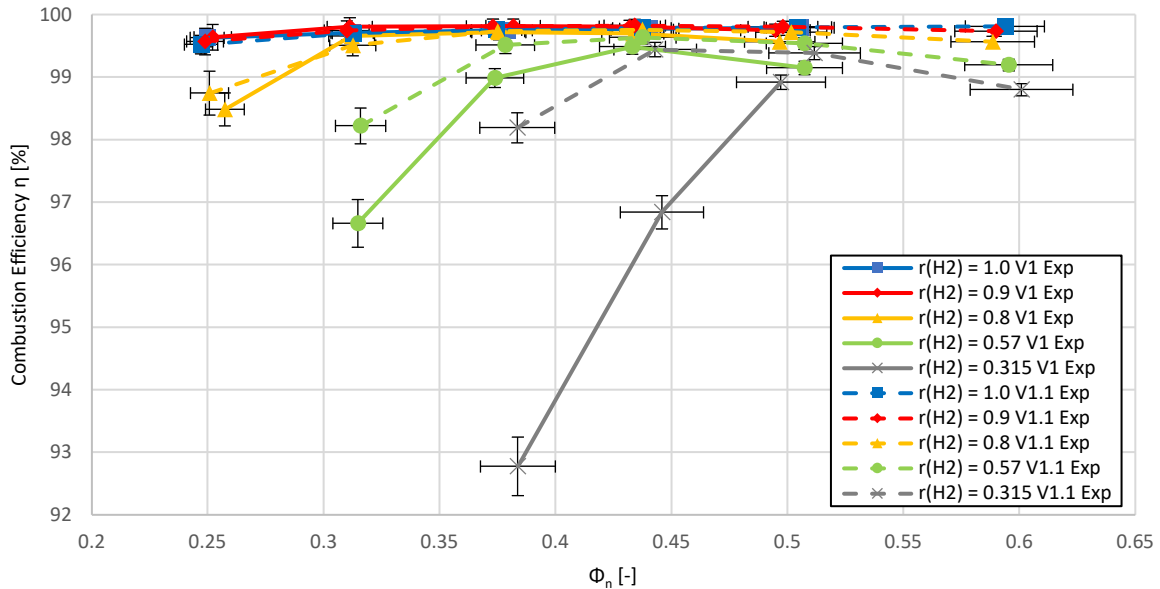


Figure 5-39: Experimental results of combustion efficiency for geometry V1 and V1.1

For high hydrogen contents in the fuel, the combustion efficiencies are almost constant between both geometries. With increasing amounts of methane, the optimized combustor V1.1 shows a

considerably better combustion efficiency as a result of reduced emissions of unburned fuel components and CO. The full set of measured data is included in appendix 8.2 - 8.4. With geometry V1.1, even combustion at $r_{H_2} = 0.3125$ could be maintained with combustion efficiencies exceeding 98%, whereas V1 operated with $\eta=92.8\%$ under the same conditions.

5.2.3.4 Conclusion

Based on the lessons learned during the characterization of the MMX combustion principle for hydrogen methane mixtures, an optimization of the combustor geometry was performed. By modifying the air gate height while keeping the cross-section and therefore the air velocity constant, a correlation between the combustor's momentum flux ratio, air gate height and resulting NO_x emissions is established. With the parameter $\left(\frac{\sqrt{J}}{h_{AGP}}\right)_{rel}$, a limit value of 115% is defined that ensures low NO_x performance with no flame merging effects. Below this value, low NO_x combustion is achieved with little influence of the fuel mixture composition and the operating conditions. When exceeding this limit, flame merging effects start to occur, resulting in injection depth-dependent NO_x formation.

With the final combustor geometry V1.1, an optimum concerning fuel flexibility, pressure loss, combustion efficiency, and NO_x emissions is finally found. In comparison to the baseline combustor V1, it shows a considerably better combustion efficiency, exceeding 98% over the entire tested operating range for fuel mixtures between 31.5 and 100% H₂.

NO_x emissions below 1.8 ppm are achieved at the design point ($\Phi_n=0.375$) over the complete investigated fuel range, leaving a high safety margin towards the 5 ppm emission limit, which was initially set as a requirement. At the same operating point, the baseline combustor V1 generates a maximum of 4.4ppm at $r_{H_2}=0.9$.

The most significant improvement is apparent for the combustor's overload performance. At an equivalence ratio of $\Phi_n = 0.5$, V1 emits 29.0 ppm NO_x at $r_{H_2}=0.9$. At the same conditions, V1.1 operates at 4 ppm NO_x emissions, which amounts to a reduction of 25 ppm. Additionally, V1.1 shows no flame merging effects, which leaves the operating range towards heavy overload conditions unrestricted. Apparently, the design point lies well outside the transition region where NO_x emissions increase rapidly as a consequence of vertical flame merging when the equivalence ratio changes towards rich combustion conditions. This characteristic makes the final combustor geometry V1.1 eligible for application under full scale pressurized gas turbine conditions in future research work.

Finally, also the favorable pressure loss level of the initial combustor V1 is maintained while all other combustion characteristics could be improved with geometry V1.1.

Concluding, Table 8 summarizes the improvements (+) and degradations (-) of all investigated combustor variants concerning several optimization targets with respect to the baseline geometry V1. Apparently, V1.1 combines the benefits of the significantly improved overload performance and combustion efficiency obtained with geometry V2.2, with the low pressure loss level of the baseline design.

Table 8: Comparison of the combustion characteristics for all tested geometries

	V1	V2	V3	V4	V2.1	V2.2	V1.1
Pressure loss	O	- -	-	+	- -	- -	O
NO_x @ DP	O	+	+	- -	-	+	+
Overload operation (NO_x, Heat stress)	O	++	+	-	-	++	++
Combustion efficiency (level)	O	+	+	+	+	+	+
Operating range (Φ_n)	O	++	+	-	-	++	++
Fuel Flexibility	O	++	+	O	O	++	++

Based on the lessons learned from the design space exploration and the optimization loops conducted in the framework of this thesis, further optimization of pressure loss and NO_x emission level by adapting the air gate geometry seems possible. A further pressure loss reduction would require lower air velocities, which results in increased momentum flux ratios at constant equivalence ratio. As seen in the preceding chapters, this favors hot gas recirculation in front of the combustor's air guiding panel. A proven method to counteract hot gas recirculation would be a further increase in air gate height. This is possible up to a point, where the flame stabilization between the counter-rotating vortices is influenced adversely. As the air gate height is increased more and more, the vortex in its wake region becomes smaller. At a certain point, flame stabilization collapses, which results in combustion instabilities, noise and a deterioration of the combustion efficiency. With a certain safety margin, this point represents the limit of a potential pressure loss optimization, but even prior to that, the gradual relocation of the flame can influence the combustion and emission characteristics adversely.

6

Conclusion & Outlook

With the prospective abatement of fossil energy carriers, gas turbines operated with hydrogen and hydrogen-rich fuel mixtures pave the way for a CO₂-free energy production in the future. Low emission gas turbines operated with hydrogen and methane that is generated with excess renewable energy by power-to-gas applications, facilitate a direct energy recovery while preserving most of the existing natural gas infrastructure. However, the challenging properties of hydrogen make changes to the gas turbine combustors necessary to facilitate low emission and flexible-fuel operation.

Against this background, the Dry-Low-NO_x-Micromix combustion technology has been developed at Aachen University of Applied Sciences for hydrogen-rich fuels. In contrast to the majority of industrially available gas turbine combustors, the Micromix principle achieves dry low NO_x emissions with diffusion flames without using dilution or steam injection. Fuel and air are not premixed but introduced separately into the combustion chamber, where they are mixed rapidly by jet-in-crossflow mixing directly before combustion in miniaturized flames. Hence, the MMX combustion principle is inherently safe against flashbacks.

Based on previous research work at AcUAS, targeting low emission combustion of hydrogen and hydrogen-rich syngas (H₂/CO), the Micromix combustion principle was characterized and optimized for low NO_x combustion with variable fuel mixtures of hydrogen and methane in the framework of this thesis. The scientific approach combined low-pressure combustor testing with numerical combustion and flow simulations. Within an interactive research cycle, steady RANS simulations were used in the context of parametric studies for generating optimized burner geometries and for the phenomenological interpretation of the experimental results. Experimental investigations with test burners under atmospheric pressure conditions established the combustion

characteristics of the Micromix combustion principle with variable H₂/CH₄ fuel mixtures and provided the basis for validation of the applied numerical methods.

Considering the significantly changing fuel characteristics of variable hydrogen methane mixtures, an initial combustor prototype (V1) was designed. Despite the design compromise for achieving flexible-fuel operation with a single combustor geometry, the results of a design space exploration at a fuel mixture range between 100% hydrogen and 100% methane at operating conditions corresponding to gas turbine part-, full, and overload conditions showed promising initial results but also the potential for optimization. Especially NO_x emissions at overload conditions and the combustion efficiency for methane-rich fuels under part-load operation were optimization targets during a subsequent study.

Within a first optimization step, the air gate velocity of the Micromix combustor was adapted by geometric modification of the Micromix air guiding panels. An increase in the air velocity led to a reduction of the NO_x emissions, especially at overload conditions, and to an increase in the combustion efficiency at high methane contents. The momentum flux ratio of the jet-in-crossflow mixing process was identified as the main driver for NO_x emissions at overload conditions. Higher momentum flux ratios relate to an increased injection depth of the fuel jet into the air crossflow. When exceeding a specific critical injection depth, flame merging effects occur that go along with an MMX-specific NO_x increase.

Focusing on the momentum flux ratio as a central design parameter, a second optimization of the overload performance could be achieved by modifying the air gate geometry. With narrower but higher air gates, the critical injection depth was increased, leaving more space for the injected fuel jet to discharge in the combustor zone, without the formation of merged flames. With this design, a safety margin towards the critical injection depth was established, making the derived design V2.2 safe against flame merging effects and the resulting increase of NO_x emissions towards overload operating conditions.

With the conducted air gate geometry variation, a dependence between NO_x emissions and the normalized momentum flux ratio $\left(\frac{\sqrt{J}}{h_{AGP}}\right)_{rel}$ was derived, which takes into account the momentum flux ratio as a measure for the injection depth, and the air gate height as a measure for the critical injection depth. Taking into account all conducted geometry variations, a limit value was derived. Below this value, low NO_x combustion is achieved with little influence of the fuel mixture composition and the operating conditions. When exceeding this limit, flame merging effects start to occur, resulting in injection depth-dependent NO_x formation.

With the combustor geometry V1.1, an optimum concerning fuel flexibility, pressure loss, combustion efficiency, and NO_x emissions was finally established. In comparison to the baseline

combustor V1, it shows a considerably better combustion efficiency, exceeding 98% over the entire tested operating range for fuel mixtures between 31.5 and 100% H₂. NO_x emissions below 1.8 ppm are achieved at the design point ($\Phi_n=0.375$) for the complete investigated fuel range, leaving a high safety margin towards the 5 ppm emission limit, which was set as a requirement. The most significant improvement was demonstrated for the combustor's overload performance. Flame merging effects and the related steep NO_x increase were effectively suppressed by application of the derived design laws. During the optimization, the favorable low pressure loss of the initial combustor prototype was maintained.

Concerning the numerical analyses that complemented the experimental testing in the framework of this thesis, it is to state that the physical and thermodynamic influences of the fuel mixture composition and the operating point on the emission trends of unburned fuel and CO emissions are very well captured by the applied RANS modeling in combination with detailed chemistry and conjugate heat transfer. As long as NO_x formation is driven by the reactivity of the applied fuel and the resulting peak temperatures and residence times of NO_x precursors, the applied thermal NO model is in close agreement with the experimental results.

The numerical approach shows limitations in predicting turbulence effects of the jet-in-crossflow mixing process. Inaccuracies in the predicted amount of unburned fuel and CO emissions at higher air gate velocities are the consequence. The general phenomenon of injection-depth dependent flame merging and the accompanying sudden increase in NO_x emissions is captured very well by the applied modeling approach with deviations concerning the exact emission level. Thus, a challenge for further research is the accurate prediction of the jet-in-crossflow process, which will make the implementation of higher-order methods like Large Eddy Simulation necessary.

In the framework of this thesis, a fundamental characterization of the Micromix combustion principle has been conducted under atmospheric pressure conditions. With low-pressure testing, extensive design space explorations and optimization with many geometries were possible. By this approach, the main design drivers were derived.

This is the first step for demonstrating the capabilities of the MMX combustion principle applied to flexible-fuel operation with hydrogen methane mixtures. In subsequent research projects, the influence of pressure levels corresponding to gas turbine operating conditions on the combustion process needs to be assessed during high-pressure testing. Finally, the operability, reliability, and emission characteristics of this combustion principle must be demonstrated during full-scale gas turbine operation.

7

References

- [1] T. Stocker, Ed., *Climate change 2013: The physical science basis Working Group I contribution to the Fifth assessment report of the Intergovernmental Panel on Climate Change*. New York: Cambridge University Press, 2014.
- [2] K. Aleklett *et al.*, “The Peak of the Oil Age – Analyzing the world oil production Reference Scenario in World Energy Outlook 2008,” *Energy Policy*, vol. 38, no. 3, pp. 1398–1414, 2010.
- [3] H. Khatib, “IEA World Energy Outlook 2010—A comment,” *Energy Policy*, vol. 39, no. 5, pp. 2507–2511, 2011.
- [4] L. Hughes and J. Rudolph, “Future world oil production: growth, plateau, or peak?,” *Current Opinion in Environmental Sustainability*, vol. 3, no. 4, pp. 225–234, 2011.
- [5] U.S. Energy Information Administration, “International Energy Outlook 2017,” Washington, D.C. USA, 2017.
- [6] R. K. Pachauri and L. Mayer, Eds., *Climate change 2014: Synthesis report*. Geneva, Switzerland: Intergovernmental Panel on Climate Change, 2015.
- [7] J. E. Penner, Ed., *Aviation and the global atmosphere: A special report of IPCC Working Groups I and III in collab. with the Scientific Assessment Panel to the Montreal Protocol on Substances that Deplete the Ozone Layer*. Cambridge: Cambridge University Press, 1999.
- [8] F. Barbir, “Transition to renewable energy systems with hydrogen as an energy carrier,” *Energy*, vol. 34, no. 3, pp. 308–312, 2009.
- [9] J. M. Carrasco *et al.*, “Power-Electronic Systems for the Grid Integration of Renewable Energy Sources: A Survey,” *IEEE Trans. Ind. Electron.*, vol. 53, no. 4, pp. 1002–1016, 2006.

-
- [10] J.-F. Hake, J. Linssen, and M. Walbeck, "Prospects for hydrogen in the German energy system," *Energy Policy*, vol. 34, no. 11, pp. 1271–1283, 2006.
- [11] Y. Li, H. Chen, X. Zhang, C. Tan, and Y. Ding, "Renewable energy carriers: Hydrogen or liquid air/nitrogen?," *Applied Thermal Engineering*, vol. 30, no. 14-15, pp. 1985–1990, 2010.
- [12] E. Lopez, F. Isorna, and F. Rosa, "Optimization of a solar hydrogen storage system: Exergetic considerations," *International Journal of Hydrogen Energy*, vol. 32, no. 10-11, pp. 1537–1541, 2007.
- [13] S. A. Sherif, F. Barbir, and T. N. Veziroglu, "Wind energy and the hydrogen economy—review of the technology," *Solar Energy*, vol. 78, no. 5, pp. 647–660, 2005.
- [14] Ø. Ulleberg, T. Nakken, and A. Eté, "The wind/hydrogen demonstration system at Utsira in Norway: Evaluation of system performance using operational data and updated hydrogen energy system modeling tools," *International Journal of Hydrogen Energy*, vol. 35, no. 5, pp. 1841–1852, 2010.
- [15] A. Züttel, A. Remhof, A. Borgschulte, and O. Friedrichs, "Hydrogen: the future energy carrier," *Philosophical transactions. Series A, Mathematical, physical, and engineering sciences*, vol. 368, pp. 3329–3342, 2010.
- [16] T. Nejat Veziroglu, "Quarter century of hydrogen movement 1974–2000," *International Journal of Hydrogen Energy*, vol. 25, no. 12, pp. 1143–1150, 2000.
- [17] A. Midilli, M. Ay, I. Dincer, and M. A. Rosen, "On hydrogen and hydrogen energy strategies: I: current status and needs," *Renewable and Sustainable Energy Reviews*, vol. 9, no. 3, pp. 255–271, 2005.
- [18] A. Midilli, M. Ay, I. Dincer, and M. A. Rosen, "On hydrogen and hydrogen energy strategies II: future projections affecting global stability and unrest," *Renewable and Sustainable Energy Reviews*, vol. 9, no. 3, pp. 273–287, 2005.
- [19] B. D. Solomon and A. Banerjee, "A global survey of hydrogen energy research, development and policy," *Energy Policy*, vol. 34, no. 7, pp. 781–792, 2006.
- [20] J. E. Mason, "World energy analysis: H₂ now or later?," *Energy Policy*, vol. 35, no. 2, pp. 1315–1329, 2007.
- [21] M. Zerta, P. Schmidt, C. Stiller, and H. LANDINGER, "Alternative World Energy Outlook (AWEO) and the role of hydrogen in a changing energy landscape," *International Journal of Hydrogen Energy*, vol. 33, no. 12, pp. 3021–3025, 2008.
- [22] P. Moriarty and D. Honnery, "Hydrogen's role in an uncertain energy future," *International Journal of Hydrogen Energy*, vol. 34, pp. 31–39, 2009.

-
- [23] SoCalGas, *Power-to-Gas*. [Online] Available: <https://www3.socalgas.com/smart-energy/renewable-gas/power-to-gas>.
- [24] C. Tang, Y. Zhang, and Z. Huang, "Progress in combustion investigations of hydrogen enriched hydrocarbons," *Renewable and Sustainable Energy Reviews*, vol. 30, pp. 195–216, 2014.
- [25] Katsuyoshi Tada, Kei Inoue, Tomo Kawakami, Keijiro Saitoh, Satoshi Tanimura, "Expanding Fuel Flexibility in MHPS' Dry Low NO_x Combustor: GT2018-77164," Oslo, Norway, Proceedings of the ASME Turbo Expo 2018, Jun. 2018.
- [26] K. Zhao *et al.*, "Effects of hydrogen addition on methane combustion," *Fuel Processing Technology*, vol. 89, no. 11, pp. 1142–1147, 2008.
- [27] H. KIM, V. ARGHODE, and A. GUPTA, "Flame characteristics of hydrogen-enriched methane–air premixed swirling flames," *International Journal of Hydrogen Energy*, vol. 34, no. 2, pp. 1063–1073, 2009.
- [28] M. ILBAS, I. YILMAZ, and Y. KAPLAN, "Investigations of hydrogen and hydrogen–hydrocarbon composite fuel combustion and emission characteristics in a model combustor," *International Journal of Hydrogen Energy*, vol. 30, no. 10, pp. 1139–1147, 2005.
- [29] P. Griebel, E. Boschek, and P. Jansohn, "Lean blowout limits and NO_x emissions of turbulent, lean premixed, hydrogen-enriched methane/air flames at high pressure," *Journal of engineering for gas turbines and power*, vol. 129, no. 2, pp. 404–410, 2007.
- [30] T. C. Lieuwen, V. Yang, and R. A. Yetter, *Synthesis gas combustion: Fundamentals and applications*. Boca Raton: CRC Press, 2010.
- [31] M. Skottene and K. E. Rian, "A study of NO_x formation in hydrogen flames," *International Journal of Hydrogen Energy*, vol. 32, no. 15, pp. 3572–3585, 2007.
- [32] J. Warnatz and U. Maas, *Combustion*. Berlin: Springer, 2010.
- [33] G. E. Andrews, "Ultra-low nitrogen oxides (NO_x) emissions combustion in gas turbine systems," in *Modern Gas Turbine Systems*: Elsevier, 2013, pp. 715–790.
- [34] S. Börner, "Optimization and testing of a low NO_x hydrogen fuelled gas turbine," PhD Thesis, Université libre de Bruxelles, Ecole polytechnique de Bruxelles – Mécanicien, Bruxelles, 2013.
- [35] S. Gadde *et al.*, "Syngas Capable Combustion Systems Development for Advanced Gas Turbines," in *Proceedings of the ASME Turbo Expo 2006: Presented at the 2006 ASME Turbo Expo : May 6-11, 2006, Barcelona, Spain*, ASME International Gas Turbine Institute, Ed., New York, N.Y: ASME, 2006, pp. 547–554.

-
- [36] J. Wu *et al.*, “Advanced Gas Turbine Combustion System Development for High Hydrogen Fuels,” in *Proceedings of the ASME Turbo Expo 2007*, vol. 2, *Combustion And Fuels, Electric Power*, ASME International Gas Turbine Institute, Ed., New York, NY: ASME, 2007, pp. 1085–1091.
- [37] Q. Wang, V. McDonnell, E. Steinthorsson, A. Mansour, and B. Hollon, “Correlating Flashback Tendencies for Premixed Injection of Hydrogen and Methane Mixtures at Elevated Temperature and Pressure,” in *Proceedings of the ASME Turbo Expo 2009*, ASME International Gas Turbine Institute, Ed., New York, N.Y.: ASME, 2009, pp. 401–410.
- [38] J. Brand, S. Sampath, F. Shum, R.I. Bayt, and J. Cohen, “Potential Use of Hydrogen in Air Propulsion,” AIAA 2003-2879, 2003.
- [39] F. Suttrop and G. Dahl, “Liquid Hydrogen Fuelled Aircraft - System Analysis - Cryoplane: Combustion Chamber and Emissions - Estimated NO_x Reduction Potential of Hydrogen Fuelled Aircraft Engines,” Task Technical Report, FH Aachen, Jun. 2001.
- [40] J. Keinz, “Optimization of a Dry Low NO_x Micromix Combustor for an Industrial Gas Turbine Using Hydrogen-Rich Syngas Fuel,” PhD Thesis, Ecole polytechnique de Bruxelles – Mécanicien, Université Libre de Bruxelles (ULB), Bruxelles, 2018.
- [41] H. H. W. Funke *et al.*, “Experimental and Numerical Study on Optimizing the Dry Low NO_x Micromix Hydrogen Combustion Principle for Industrial Gas Turbine Applications,” *J. Thermal Sci. Eng. Appl*, vol. 9, no. 2, 2017.
- [42] A. Haj Ayed *et al.*, “Improvement study for the dry-low-NO_x hydrogen micromix combustion technology,” *Propulsion and Power Research*, vol. 4, no. 3, pp. 132–140, 2015.
- [43] A. H. Lefebvre and D. R. Ballal, *Gas turbine combustion: Alternative fuels and emissions*, 3rd ed. Boca Raton: Taylor & Francis, 2010.
- [44] H. H.-W. Funke *et al.*, “Numerical and Experimental Characterization of Low NO_x Micromix Combustion Principle for Industrial Hydrogen Gas Turbine Applications,” *ASME Turbo Expo 2012*, pp. 1069–1079, 2012.
- [45] A. Haj Ayed *et al.*, “Numerical Study on Increased Energy Density for the DLN Micromix Hydrogen Combustion Principle: GT2014-25848,” Düsseldorf, Proceedings of the ASME Turbo Expo 2014, Jun. 2014.
- [46] H. H.-W. Funke, N. Beckmann, J. Keinz, and S. Abanteriba, “Comparison of Numerical Combustion Models for Hydrogen and Hydrogen-rich Syngas Applied for Dry-Low-NO_x-Micromix-Combustion,” in *Proceedings of the ASME Turbo Expo 2016*, ASME International Gas Turbine Institute, Ed., New York, N.Y.: ASME, 2016.

-
- [47] H. H.-W. Funke, S. Börner, J. Keinz, P. Hendrick, and E. Recker, “Low NO_x Hydrogen combustion chamber for industrial gas turbine applications,” Honolulu, 14th International Symposium on Transport Phenomena and Dynamics of Rotating Machinery, ISROMAC-14 th, 2012.
- [48] H. H.-W. Funke *et al.*, “Experimental and Numerical Characterization of the Dry Low NO_x Micromix Hydrogen Combustion Principle at Increased Energy Density for Industrial Hydrogen Gas Turbine Applications,” in *ASME Turbo Expo 2013: Turbine Technical Conference and Exposition*, San Antonio, Texas, USA, Monday Jun. 2013.
- [49] H. H. W. Funke, N. Beckmann, J. Keinz, and S. Abanteriba, “Numerical and Experimental Evaluation of a Dual-Fuel Dry-Low-NO_x Micromix Combustor for Industrial Gas Turbine Applications,” *J. Thermal Sci. Eng. Appl.*, vol. 11, no. 1, 2019.
- [50] M. Boudellal, “Global energy consumption,” in *Power-to-Gas*, M. Boudellal, Ed., Berlin, Boston: De Gruyter, 2018, pp. 2–25.
- [51] M. Boudellal, “Electricity of renewable origin,” in *Power-to-Gas*, M. Boudellal, Ed., Berlin, Boston: De Gruyter, 2018, pp. 26–56.
- [52] M. Boudellal, “Principle of power-to-gas,” in *Power-to-Gas*, M. Boudellal, Ed., Berlin, Boston: De Gruyter, 2018, pp. 57–62.
- [53] M. Götz *et al.*, “Renewable Power-to-Gas: A technological and economic review,” *Renewable Energy*, vol. 85, pp. 1371–1390, 2016.
- [54] R. C. Mulready, “Liquid Hydrogen Engines,” in *Technology and Uses of Liquid Hydrogen*, R. B. Scott, W. H. Denton, and C. M. Nicholls, Eds.: Pergamon Press, 1964, pp. 149–179.
- [55] K. von Gersdorff, K. Grasmann, and T. Benecke, *Flugmotoren und Strahltriebwerke: Entwicklungsgeschichte der deutschen Luftfahrtantriebe von den Anfängen bis zu den europäischen Gemeinschaftsentwicklungen*. Munich: Bernard & Graefe, 1981.
- [56] V. Sosounov and V. Orlov, “Experimental Turbofan Using Liquid Hydrogen and Liquid Natural Gas as Fuel,” AIAA 90-2421, Washington DC, Jul. 1990.
- [57] F. Svensson and R. Singh, “Effects of Using Hydrogen on Aero Gas Turbine Pollutant Emissions, Performance and Design,” in *Proceedings of the ASME Turbo Expo 2004: Presented at the 2004 ASME Turbo Expo : June 14-17, 2004, Vienna, Austria*, ASME Turbo Expo, Ed., New York, N.Y: ASME, 2004, pp. 107–116.
- [58] F. Svensson and R. Singh, “Design of hydrogen-fuelled aero gas turbines for low environmental impact,” in *Proceedings / XVII International Symposium on Air Breathing Engines (ISABE): September 4 - 9, 2005, Munich, Germany*, 2005.

-
- [59] A. Westenberger, "Liquid Hydrogen Fuelled Aircraft - System Analysis: CRYOPLANE - Final Technical Report, Report No. GRD1-1999-10014," Airbus Deutschland GmbH, Hamburg, Germany, 2003.
- [60] F. Suttrop and G. Dahl, "Liquid Hydrogen Fuelled Aircraft - System Analysis - Cryoplane: Combustion Chamber and Emissions Review of Proposed Hydrogen Combustors, Benefits and Drawbacks," Task Technical Report, FH Aachen, Jun. 2001.
- [61] T. Komori, S. Shiozaki, N. Yamagami, Y. Kitauchi, and W. Akizuki, *CO₂ Emission Reduction Method Through Various Gas Turbine Fuel Applications*. [Online] Available: <http://www.mhi.co.jp/technology/review/pdf/e441/e441006.pdf>.
- [62] S. Taamallah *et al.*, "Fuel flexibility, stability and emissions in premixed hydrogen-rich gas turbine combustion: Technology, fundamentals, and numerical simulations," *Applied Energy*, vol. 154, pp. 1020–1047, 2015.
- [63] P. Chiesa, G. Lozza, and L. Mazzocchi, "Using Hydrogen as Gas Turbine Fuel," *J. Eng. Gas Turbines Power*, vol. 127, no. 1, pp. 73–80, 2005.
- [64] M. Huth and A. Heilos, "Fuel flexibility in gas turbine systems: impact on burner design and performance," in *Modern Gas Turbine Systems*: Elsevier, 2013, pp. 635–684.
- [65] R. Tuccillo, M. C. Cameretti, R. de Robbio, F. Reale, and F. Chiariello, "Methane-Hydrogen Blends in Micro Gas Turbines: Comparison of Different Combustor Concepts," in *Proceedings of the ASME Turbo Expo 2019*, ASME International Gas Turbine Institute, Ed., New York, N.Y.: ASME, 2019.
- [66] M. Ilbas, İ. Yılmaz, T. N. Veziroglu, and Y. Kaplan, "Hydrogen as burner fuel: Modelling of hydrogen-hydrocarbon composite fuel combustion and NO_x formation in a small burner," *Int. J. Energy Res.*, vol. 29, no. 11, pp. 973–990, 2005.
- [67] S. F. Ahmed, J. Santner, F. L. Dryer, B. Padak, and T. I. Farouk, "Computational Study of NO_x Formation at Conditions Relevant to Gas Turbine Operation, Part 2: NO_x in High Hydrogen Content Fuel Combustion at Elevated Pressure," *Energy Fuels*, vol. 30, no. 9, pp. 7691–7703, 2016.
- [68] C. Lhuillier *et al.*, "Hydrogen Enriched Methane Combustion Diluted With Exhaust Gas and Steam: Fundamental Investigation on Laminar Flames and NO_x Emissions," in *Proceedings of the ASME Turbo Expo 2017*, ASME International Gas Turbine Institute, Ed., New York, N.Y.: ASME, 2017.
- [69] D. Kroniger, M. Lipperheide, and M. Wirsum, "Effects of Hydrogen Fueling on NO_x Emissions: A Reactor Model Approach for an Industrial Gas Turbine Combustor," in

-
- Proceedings of the ASME Turbo Expo 2017*, ASME International Gas Turbine Institute, Ed., New York, N.Y.: ASME, 2017.
- [70] J. H. H. K. Klaus Döbbling, “25 YEARS OF BBC/ABB/ALSTOM LEAN PREMIX COMBUSTION TECHNOLOGIES,” ASME Turbo Expo, Reno-Tahoe, Nevada, USA, Power for Land, Sea and Air GT2005-68269, Jun. 2005.
- [71] L. D. Pfefferle and W. C. Pfefferle, “Catalysis in Combustion,” *Catalysis Reviews*, vol. 29, no. 2-3, pp. 219–267, 1987.
- [72] Y. Ozawa *et al.*, “Development of a low NO_x catalytic combustor for a gas turbine,” *Catalysis Today*, vol. 26, no. 3-4, pp. 351–357, 1995.
- [73] S. Etemad, H. Karim, L. L. Smith, and W. C. Pfefferle, “Advanced technology catalytic combustor for high temperature ground power gas turbine applications,” *Catalysis Today*, vol. 47, no. 1, pp. 305–313, 1999.
- [74] M. Lyubovsky *et al.*, “Catalytic combustion over platinum group catalysts: Fuel-lean versus fuel-rich operation,” *Catalysis Today*, vol. 83, no. 1-4, pp. 71–84, 2003.
- [75] L. L. Smith, H. Karim, M. J. Castaldi, S. Etemad, and W. C. Pfefferle, “Rich-Catalytic Lean-burn combustion for fuel-flexible operation with ultra low emissions,” *Catalysis Today*, vol. 117, no. 4, pp. 438–446, 2006.
- [76] B. Baird, S. Etemad, H. Karim, S. Alavandi, and W. C. Pfefferle, “Gas turbine engine test of RCL® catalytic pilot for ultra-low NO_x applications,” *Catalysis Today*, vol. 155, no. 1-2, pp. 13–17, 2010.
- [77] T. Lecomte *et al.*, “Best Available Techniques (BAT) Reference Document for Large Combustion Plants - Industrial Emissions Directive 2010/75/EU (Integrated Pollution Prevention and Control),” European Union, Luxembourg, 2017.
- [78] M. Klassen and T. Lieuwen, “Gas Turbine Combustion Fundamentals - ASME Turbo Expo,” San Antonio, USA, 2013.
- [79] T. C. Lieuwen and V. Yang, *Gas turbine emissions*. Cambridge: Cambridge University Press, 2013.
- [80] B. Tripod, K. Döbbling, C. Pfeiffer, and R. Heimerl, “Increasing Power Generation Efficiency in Russia and CIS Countries through Further Development of the Alstom GT13E2 Gas Turbine,” Moscow, Russia Power Conference, 2012.
- [81] W. D. York, W. S. Ziminsky, and E. Yilmaz, “Development and Testing of a Low NO_x Hydrogen Combustion System for Heavy-Duty Gas Turbines,” *J. Eng. Gas Turbines Power*, vol. 135, no. 2, 2013.

-
- [82] S. R. Hernandez *et al.*, “Micro Mixing Fuel Injectors for Low Emissions Hydrogen Combustion,” in *Proceedings of the ASME Turbo Expo 2008*, ASME International Gas Turbine Institute, Ed., New York, N.Y: ASME, 2008.
- [83] H. Lee *et al.*, “Development of Flashback Resistant Low-Emission Micro-Mixing Fuel Injector for 100% Hydrogen and Syngas Fuels,” in *Proceedings of the ASME Turbo Expo 2009*, ASME International Gas Turbine Institute, Ed., New York, N.Y: ASME, 2009, pp. 411–419.
- [84] S. Dodo *et al.*, “Combustion Characteristics of a Multiple-Injection Combustor for Dry Low-NO_x Combustion of Hydrogen-Rich Fuels Under Medium Pressure,” in *ASME 2011 Turbo Expo: Turbine Technical Conference and Exposition*, Vancouver, British Columbia, Canada, Jun. 2011, pp. 467–476.
- [85] T. Asai *et al.*, “Performance of Multiple-Injection Dry Low-NO_x Combustors on Hydrogen-Rich Syngas Fuel in an IGCC Pilot Plant,” *J. Eng. Gas Turbines Power*, vol. 137, no. 9, p. 91504, 2015.
- [86] K.-K. Lam, P. Geipel, and J. Larfeldt, “Hydrogen Enriched Combustion Testing of Siemens Industrial SGT-400 at Atmospheric Conditions,” *J. Eng. Gas Turbines Power*, vol. 137, no. 2, 2015.
- [87] A. Lantz *et al.*, “Investigation of hydrogen enriched natural gas flames in a SGT-700/800 burner using oh plif and chemiluminescence imaging,” in *Proceedings of the ASME Turbo Expo 2014*, Düsseldorf, Germany, 2014.
- [88] V. Iyer, J. Haynes, P. May, and A. Anand, “Evaluation of Emissions Performance of Existing Combustion Technologies for Syngas Combustion,” in *Proceedings of the ASME Turbo Expo 2005*, ASME International Gas Turbine Institute, Ed., New York, N.Y: ASME, 2005.
- [89] M. Cerutti, S. Cocchi, R. Modi, S. Sigali, and G. Bruti, “Hydrogen Fueled Dry Low NO_x Gas Turbine Combustor Conceptual Design,” in *Proceedings of the ASME Turbo Expo 2014*, ASME International Gas Turbine Institute, Ed., New York: ASME, 2014.
- [90] N. Weiland, R.-H. Chen, and P. Strakey, “Effects of coaxial air on nitrogen-diluted hydrogen jet diffusion flame length and NO_x emission,” *Proceedings of the Combustion Institute*, vol. 33, no. 2, pp. 2983–2989, 2011.
- [91] D. E. Giles, S. Som, and S. K. Aggarwal, “NO_x emission characteristics of counterflow syngas diffusion flames with airstream dilution,” *Fuel*, vol. 85, no. 12-13, pp. 1729–1742, 2006.

-
- [92] J. Park, J.-G. Choi, S.-I. Keel, and T.-K. Kirn, "Flame structure and NO emissions in gas combustion of low calorific heating value," *Int. J. Energy Res.*, vol. 27, no. 15, pp. 1339–1361, 2003.
- [93] C. Galletti, A. Parente, M. Derudi, R. Rota, and L. Tognotti, "Numerical and experimental analysis of NO emissions from a lab-scale burner fed with hydrogen-enriched fuels and operating in MILD combustion," *International Journal of Hydrogen Energy*, vol. 34, no. 19, pp. 8339–8351, 2009.
- [94] A. Cavaliere and M. de Joannon, "Mild Combustion," *Progress in Energy and Combustion Science*, vol. 30, no. 4, pp. 329–366, 2004.
- [95] J.A. Wüning and J.G. Wüning, "Flameless oxidation to reduce thermal no-formation," *Progress in Energy and Combustion Science*, vol. 23, no. 1, pp. 81–94, 1997.
- [96] A. K. Agarwal, S. De, A. Pandey, and A. P. Singh, *Combustion for Power Generation and Transportation*. Singapore: Springer Singapore, 2017.
- [97] M. Derudi, A. Villani, and R. Rota, "Mild Combustion of Industrial Hydrogen-Containing Byproducts," *Ind. Eng. Chem. Res.*, vol. 46, no. 21, pp. 6806–6811, 2007.
- [98] P. Sabia, M. de Joannon, S. Fierro, A. Tregrossi, and A. Cavaliere, "Hydrogen-enriched methane Mild Combustion in a well stirred reactor," *Experimental Thermal and Fluid Science*, vol. 31, no. 5, pp. 469–475, 2007.
- [99] E. Lemmon, M. McLinden und D. Friend, *Thermophysical Properties of Fluid Systems - NIST Chemistry WebBook, NIST Standard Reference Database Number 69*. [Online] Available: <http://webbook.nist.gov>. Accessed on: Jul. 12 2017.
- [100] N. T. Weiland, T. G. Sidwell, and P. A. Strakey, "Testing of a Hydrogen Diffusion Flame Array Injector at Gas Turbine Conditions," *Combustion Science and Technology*, vol. 185, no. 7, pp. 1132–1150, 2013.
- [101] *Directive 2010/75/EU of the European Parliament and of the Council of 24 November 2010 on industrial emissions (integrated pollution prevention and control)*, 2010.
- [102] ABB Automation GmbH, "Advanced Optima 2000 User Manual: 42/24-10 DE Rev.9," Frankfurt a. M., 2009.
- [103] Eco Physics Inc., "CLD 700 el ht User Manual,"
- [104] X. Gao, "A Parallel Solution-adaptive Method for Turbulent Non-premixed Combusting Flows," Ph.D. thesis, University of Toronto, Toronto, Canada, 2008.
- [105] D. A. Venditti and D. L. Darmofal, "Grid adaptation for functional outputs: application to two-dimensional inviscid flows," *Journal of Computational Physics*, vol. 176, no. 1, pp. 40–69, 2002.

-
- [106] H. H.-W. Funke, N. Beckmann, J. Keinz, S. Abanteriba, “Numerical and Experimental Evaluation of a Dual-Fuel Dry-Low-NO_x Micromix Combustor for Industrial Gas Turbine Applications,” in *Proceedings of the ASME Turbo Expo 2017*, ASME International Gas Turbine Institute, Ed., New York, N.Y.: ASME, 2017.
- [107] C. Striegan, A. Haj Ayed, K. Kusterer, H. H.-W. Funke, S. Loechle, M. Kazari, A. Horikawa, K. Okada, K. Koga, “Numerical Combustion and Heat Transfer Simulations and Validation for a Hydrogen Fueled "Micromix" Test Combustor in Industrial Gas Turbine Applications,” in *Proceedings of the ASME Turbo Expo 2017*, ASME International Gas Turbine Institute, Ed., New York, N.Y.: ASME, 2017.
- [108] CD-adapco, *Star-CCM+ Documentation Version 10.02*. Melville, NY, USA: CD-adapco, 2015.
- [109] S. Arrhenius, “Über die Reaktionsgeschwindigkeit bei der Inversion von Rohrzucker durch Säuren,” *Zeitschrift für Physikalische Chemie*, vol. 4, pp. 226–248, 1889.
- [110] J. H. Ferziger and M. Perić, *Computational Methods for Fluid Dynamics*. Berlin, Heidelberg: Springer Berlin Heidelberg, 2002.
- [111] H. K. Versteeg and W. Malalasekera, *An introduction to computational fluid dynamics: The finite volume method*, 2nd ed. Harlow England, New York: Pearson Education Ltd, 2007.
- [112] A. Haj Ayed *et al.*, “Experimental and numerical investigations of the dry-low-NO_x hydrogen micromix combustion chamber of an industrial gas turbine,” *Propulsion and Power Research*, vol. 4, no. 3, pp. 123–131, 2015.
- [113] A. Penkner, “Thermische Totaldruckverluste durch Wärmezufuhr in Drallströmungen,” Dissertation, RWTH Aachen, Aachen, 2018.
- [114] D. Fernández-Galisteo, A. L. Sánchez, A. Liñán, and F. A. Williams, “One-step reduced kinetics for lean hydrogen–air deflagration,” *Combustion and Flame*, vol. 156, no. 5, pp. 985–996, 2009.
- [115] B. F. Magnussen, “The Eddy Dissipation Concept a Bridge Between Science and Technology,” Ph.D. thesis, Norwegian University of Science and Technology Trondheim, Trondheim, Norway, 2005.
- [116] J. A. van Oijen, “Flamelet-generated manifolds: development and application to premixed laminar flames,” PhD Thesis, Technische Universiteit Eindhoven, Eindhoven, 2002.
- [117] H. H. W. Funke, N. Beckmann, J. Keinz, and S. Abanteriba, “Comparison of Numerical Combustion Models for Hydrogen and Hydrogen-Rich Syngas Applied for Dry-Low-NO_x -Micromix-Combustion,” *J. Eng. Gas Turbines Power*, vol. 140, no. 8, 2018.

- [118] A. R. Masri, *Bluff-Body Flows and Flames*. [Online] Available: <http://web.aeromech.usyd.edu.au/thermofluids/bluff.php>. Accessed on: Nov. 12 2018.
- [119] B. B. Dally, D. F. Fletcher, and A. R. Masri, "Flow and mixing fields of turbulent bluff-body jets and flames," *Combustion Theory and Modelling*, vol. 2, no. 2, pp. 193–219, 1998.
- [120] F. Wang, J. Mi, P. Li, and C. Zheng, "Diffusion flame of a CH₄/H₂ jet in hot low-oxygen coflow," *International Journal of Hydrogen Energy*, vol. 36, no. 15, 2011.
- [121] C. Safta and C. K. Madnia, "Autoignition and structure of nonpremixed CH₄/H₂ flames: Detailed and reduced kinetic models," *Combustion and Flame*, vol. 144, no. 1-2, pp. 64–73, 2006.
- [122] D. A. Lysenko, I. S. Ertesvåg, K. E. Rian, B. Lilleberg, and D. Christ, "Numerical simulation of turbulent flames using the Eddy Dissipation Concept with detailed chemistry," *Computational mechanics, Trondheim*, pp. 159–178, 2013.
- [123] A. Mardani and S. Tabejamaat, "Effect of hydrogen on hydrogen–methane turbulent non-premixed flame under MILD condition," *International Journal of Hydrogen Energy*, vol. 35, no. 20, 2010.
- [124] B. Yang and S. B. Pope, "An investigation of the accuracy of manifold methods and splitting schemes in the computational implementation of combustion chemistry," *Combustion and Flame*, vol. 112, no. 1-2, pp. 16–32, 1998.
- [125] R. Sankaran, E. R. Hawkes, J. H. Chen, T. Lu, and C. K. Law, "Structure of a spatially developing turbulent lean methane–air Bunsen flame," *Proceedings of the Combustion Institute*, vol. 31, no. 1, pp. 1291–1298, 2007.
- [126] A. Kazakov and M. Frenklach, *Reduced Reaction Sets based on GRI-Mech 1.2*. [Online] Available: <http://www.me.berkeley.edu/drm/>. Accessed on: Nov. 12 2018.
- [127] T. Lu and C. K. Law, "A criterion based on computational singular perturbation for the identification of quasi steady state species: A reduced mechanism for methane oxidation with NO chemistry," *Combustion and Flame*, vol. 154, no. 4, pp. 761–774, 2008.
- [128] G. P. Smith *et al.*, *GRI-MECH 3.0*. [Online] Available: <http://combustion.berkeley.edu/gri-mech/version30/text30.html>. Accessed on: Nov. 12 2018.
- [129] E. L. Petersen *et al.*, "Methane/propane oxidation at high pressures: Experimental and detailed chemical kinetic modeling," *Proceedings of the Combustion Institute*, vol. 31, no. 1, pp. 447–454, 2007.
- [130] H. H.-W. Funke, J. Keinz, S. Börner, P. Hendrick, and R. Elsing, "Testing and Analysis of the Impact on Engine Cycle Parameters and Control System Modifications Using

- Hydrogen or Methane as Fuel in an Industrial Gas Turbine,” in *Progress in propulsion physics - Volume 8*, Les Ulis: EDP sciences, 2016.
- [131] E. R. Norster, “Second Report on Jet Penetration and Mixing studies,” The College of Aeronautics Granfield, Granfield PD7JP 2, Mar. 1964.
- [132] R.W. Schefer, W.D. Kulatilaka, B.D. Patterson, and T.B. Settersten, “Visible emission of hydrogen flames,” *Combustion and Flame*, vol. 156, no. 6, pp. 1234–1241, 2009.
- [133] T. S. Cheng, C.-Y. WU, Y.-H. LI, and Y.-C. CHAO, “Chemiluminescence Measurements Of Local Equivalence Ratio In A Partially Premixed Flame,” *Combustion Science and Technology*, vol. 178, no. 10-11, pp. 1821–1841, 2006.
- [134] E. C. W. Smith, “The emission spectrum of hydrocarbon flames,” *Proc. R. Soc. Lond. A*, vol. 174, no. 956, pp. 110–125, 1940.
- [135] VDMA Motoren und Systeme, “Abgasgesetzgebung Diesel- und Gasmotoren,” Frankfurt a. M., Jan. 2017.
- [136] Kawasaki Heavy Industries Ltd., “Kawasaki Launches New State of the Art 30MW Class Gas Turbine - Kawasaki L30A,” Tokyo, Jun. 2012.
- [137] Kawasaki Heavy Industries Ltd., *L30A-01D/DLH Gas Turbine*. [Online] Available: https://global.kawasaki.com/en/corp/sustainability/green_products/L30A-01D_DLH.html.
- [138] F. COZZI and A. COGHE, “Behavior of hydrogen-enriched non-premixed swirled natural gas flames,” *International Journal of Hydrogen Energy*, vol. 31, no. 6, pp. 669–677, 2006.

8

Appendix

8.1 Supplemental Diagrams: NO_x Emissions

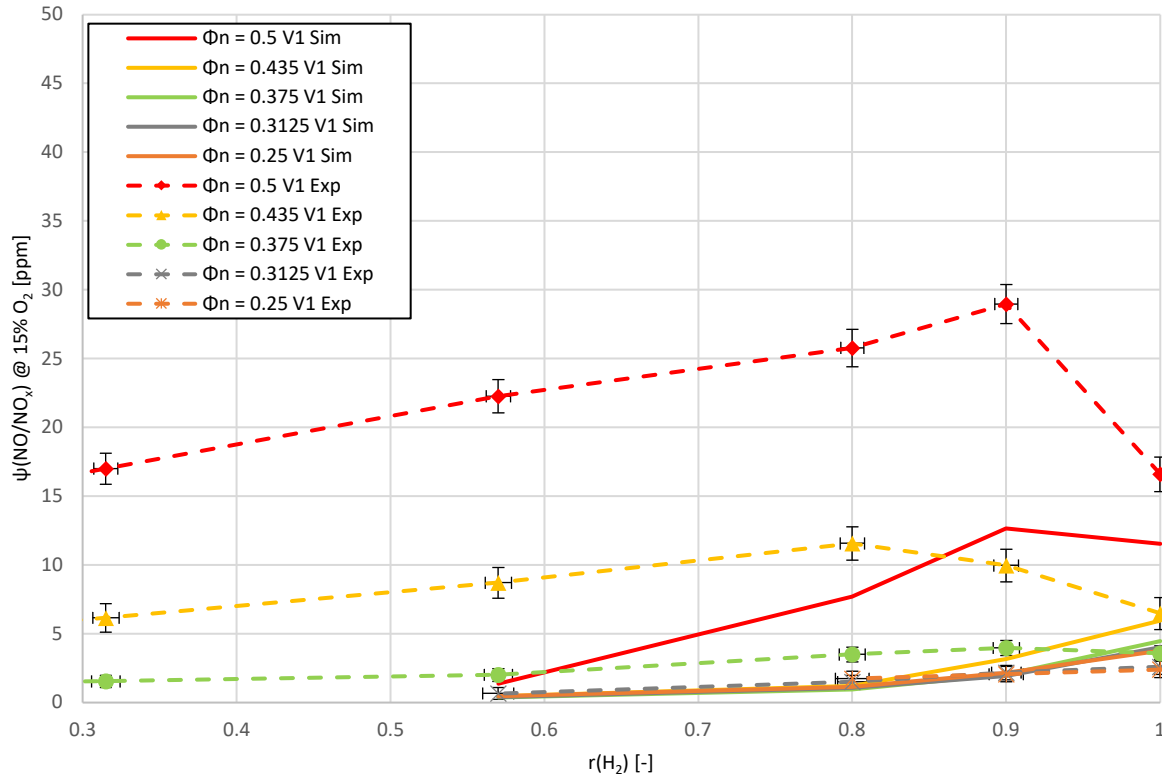


Figure 8-1: Experimental and simulation results of NO/NO_x corrected to 15% O₂ for V1

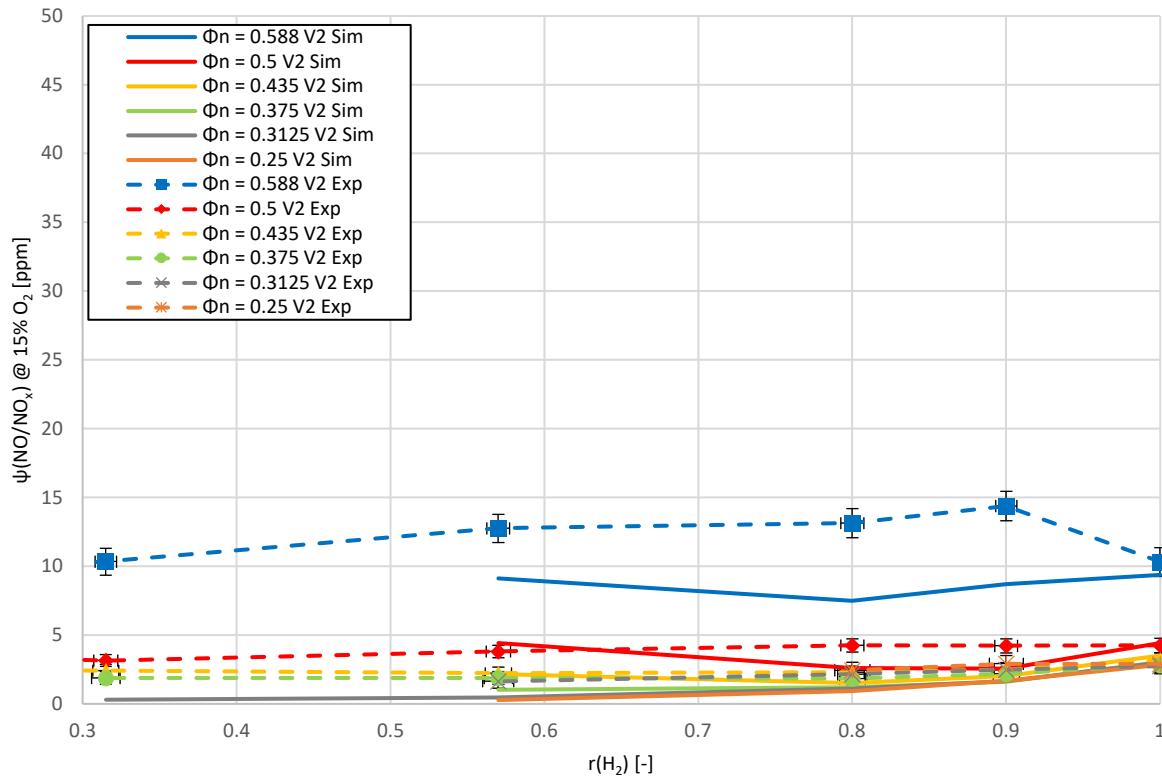


Figure 8-2: Experimental and simulation results of NO/NO_x corrected to 15% O₂ for V2

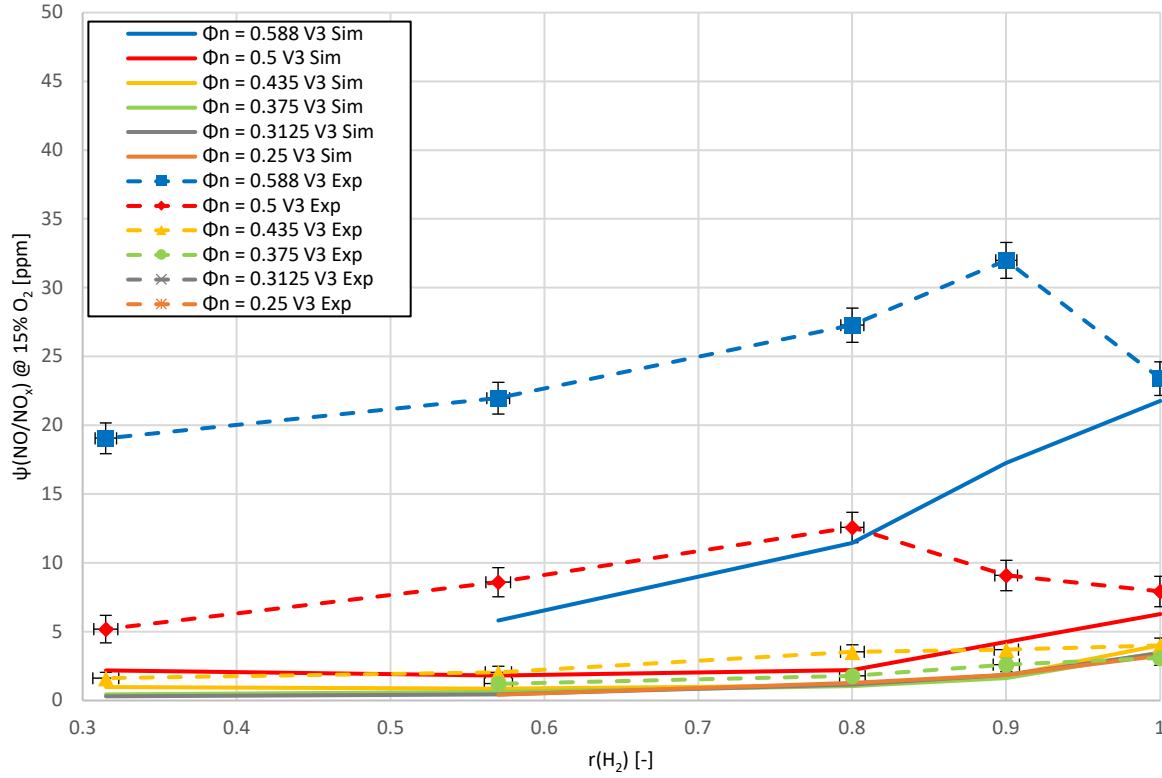


Figure 8-3: Experimental and simulation results of NO/NO_x corrected to 15% O₂ for V3

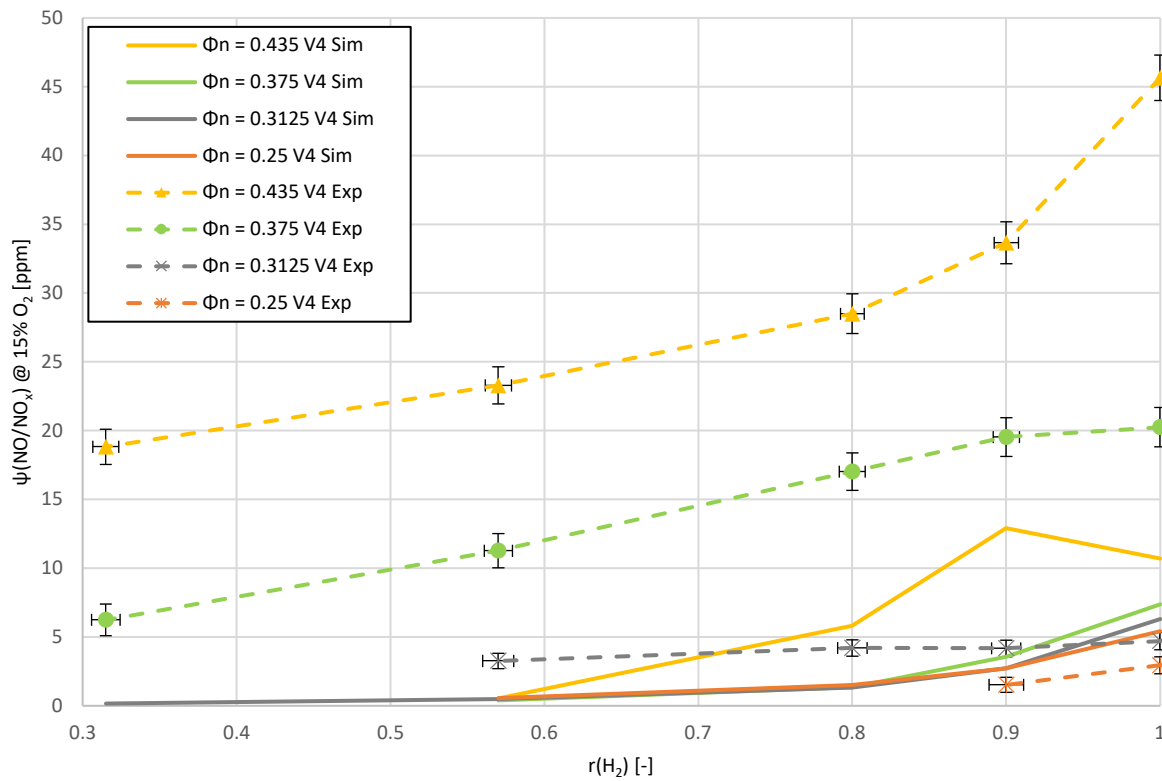


Figure 8-4: Experimental and simulation results of NO/NO_x corrected to 15% O₂ for V4

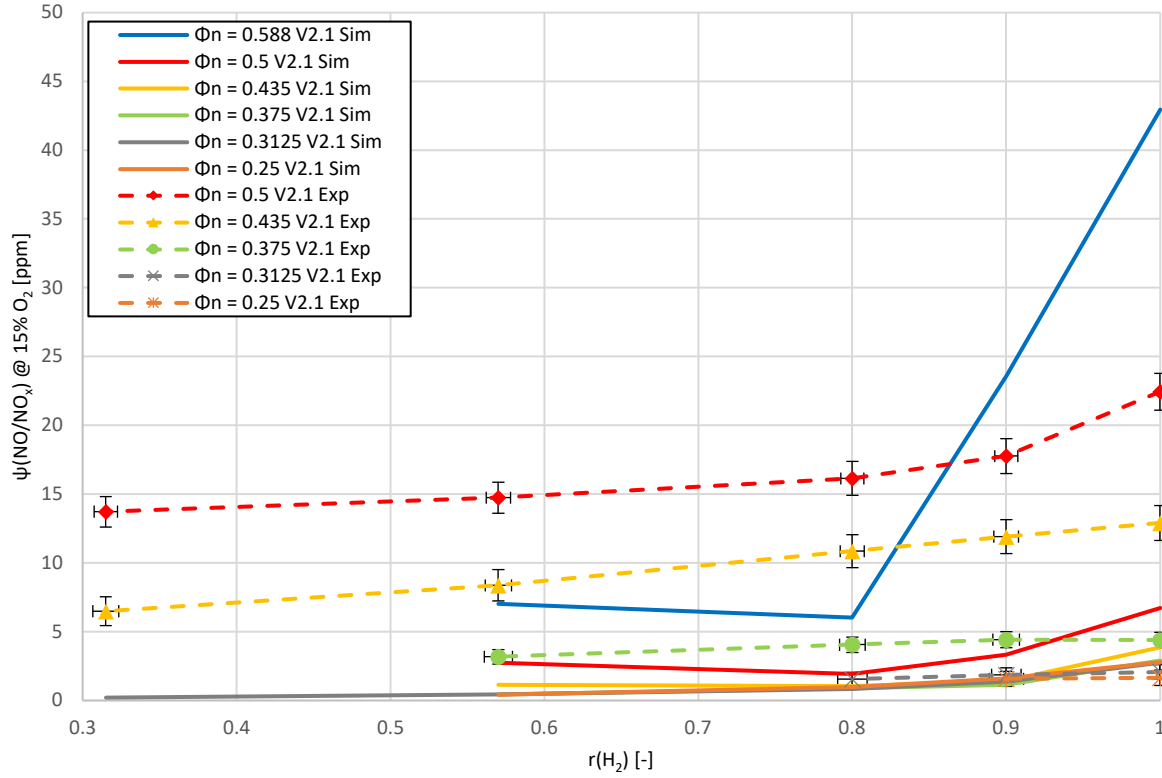


Figure 8-5: Experimental and simulation results of NO/NO_x corrected to 15% O₂ for V2.1

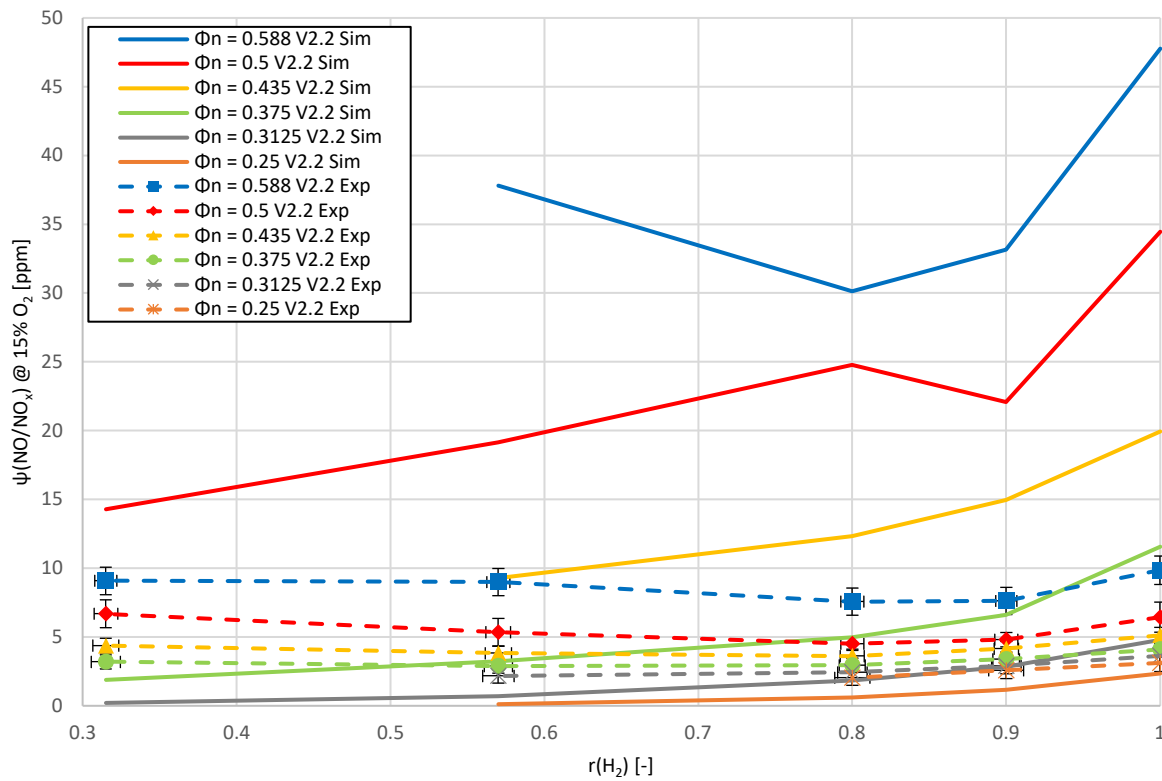


Figure 8-6: Experimental and simulation results of NO/NO_x corrected to 15% O₂ for V2.2

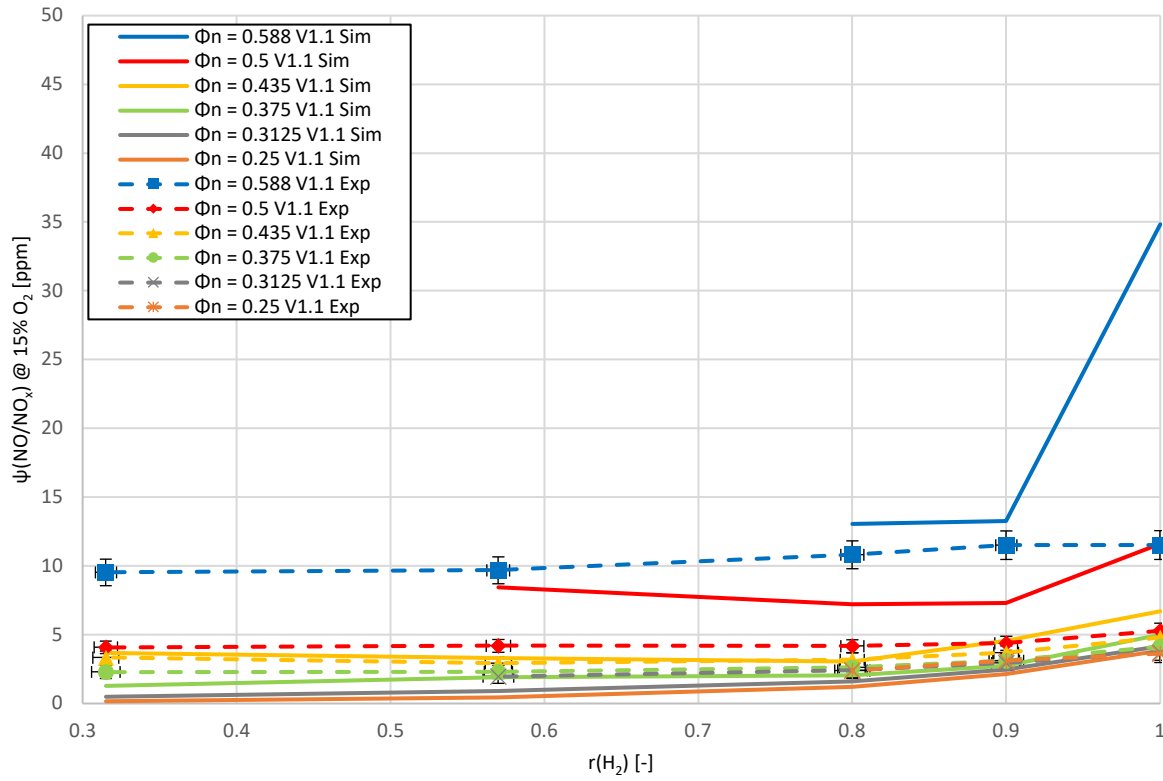


Figure 8-7: Experimental and simulation results of NO/NO_x corrected to 15% O₂ for V1.1

8.2 Supplemental Diagrams: CO Emissions

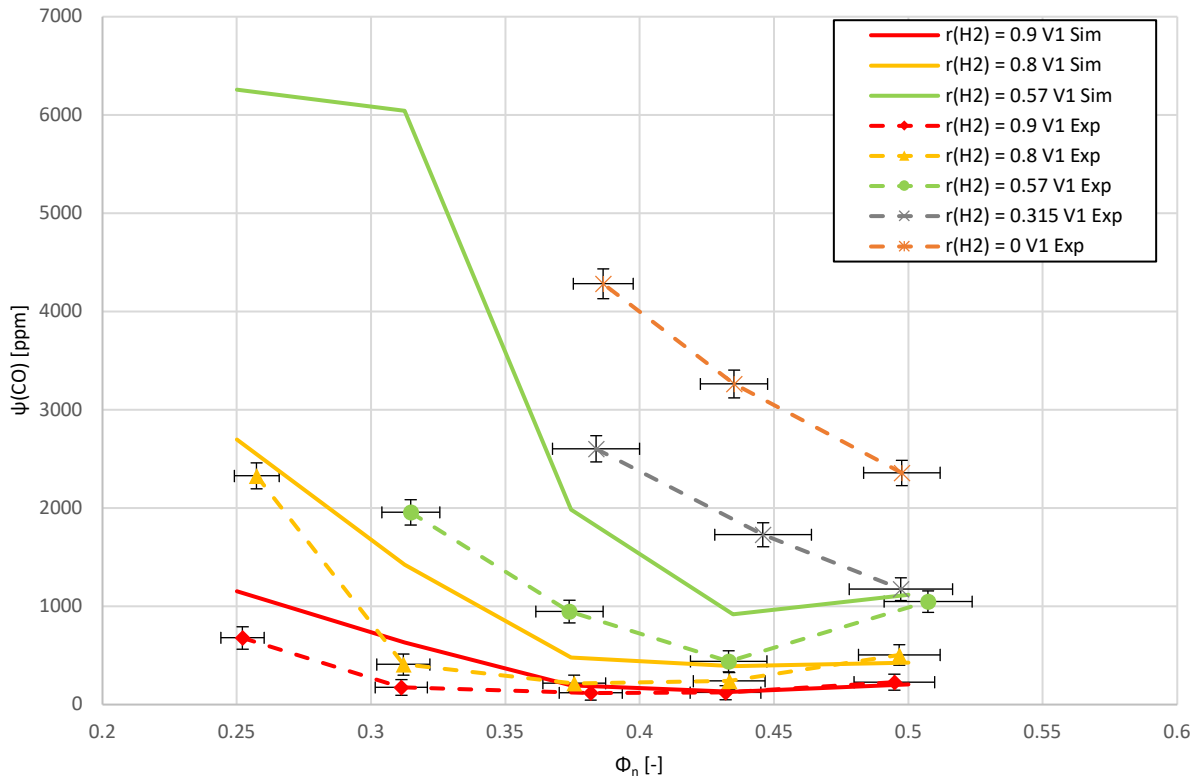


Figure 8-8: Experimental and simulation results of mole fraction CO for V1

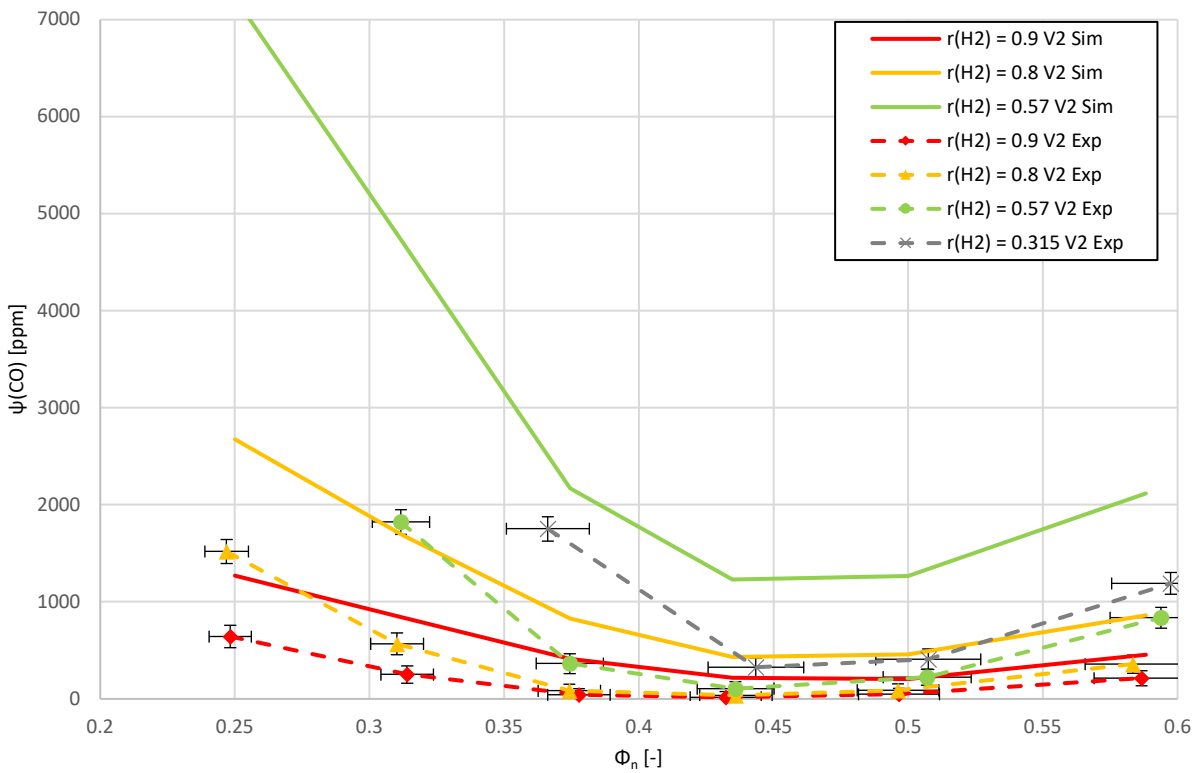


Figure 8-9: Experimental and simulation results of mole fraction CO for V2

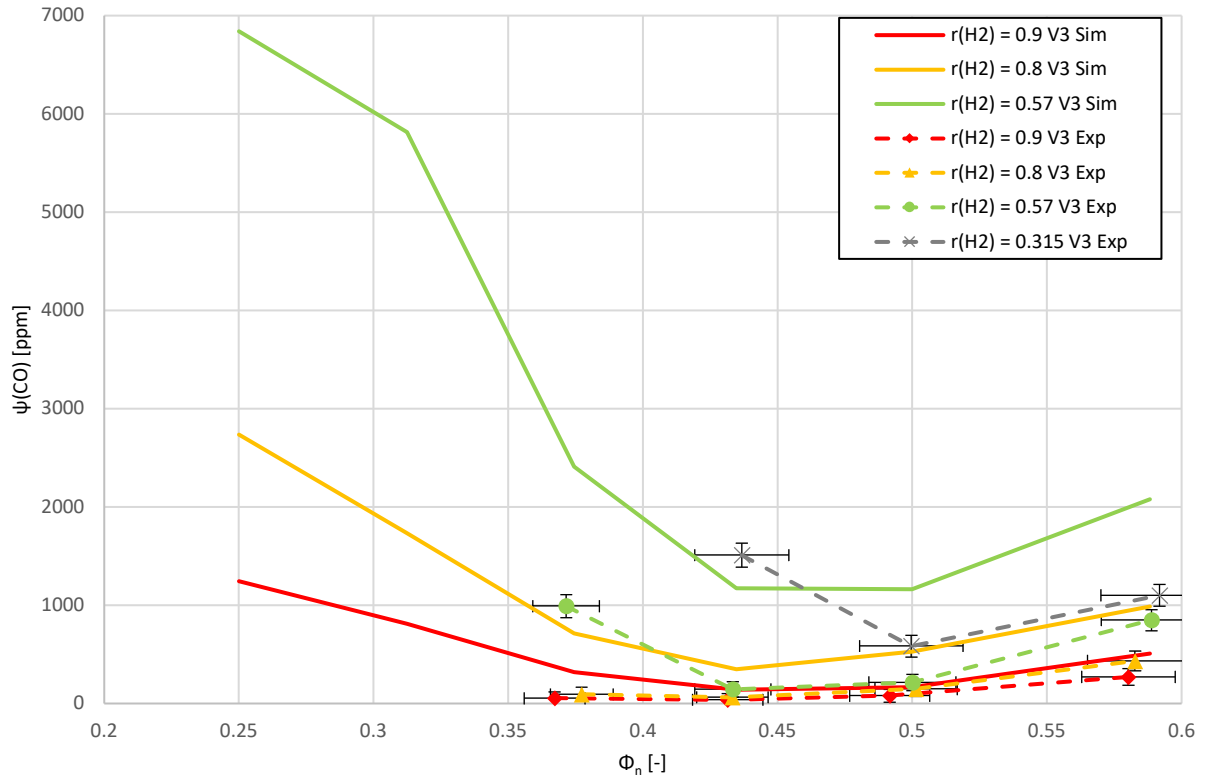


Figure 8-10: Experimental and simulation results of mole fraction CO for V3

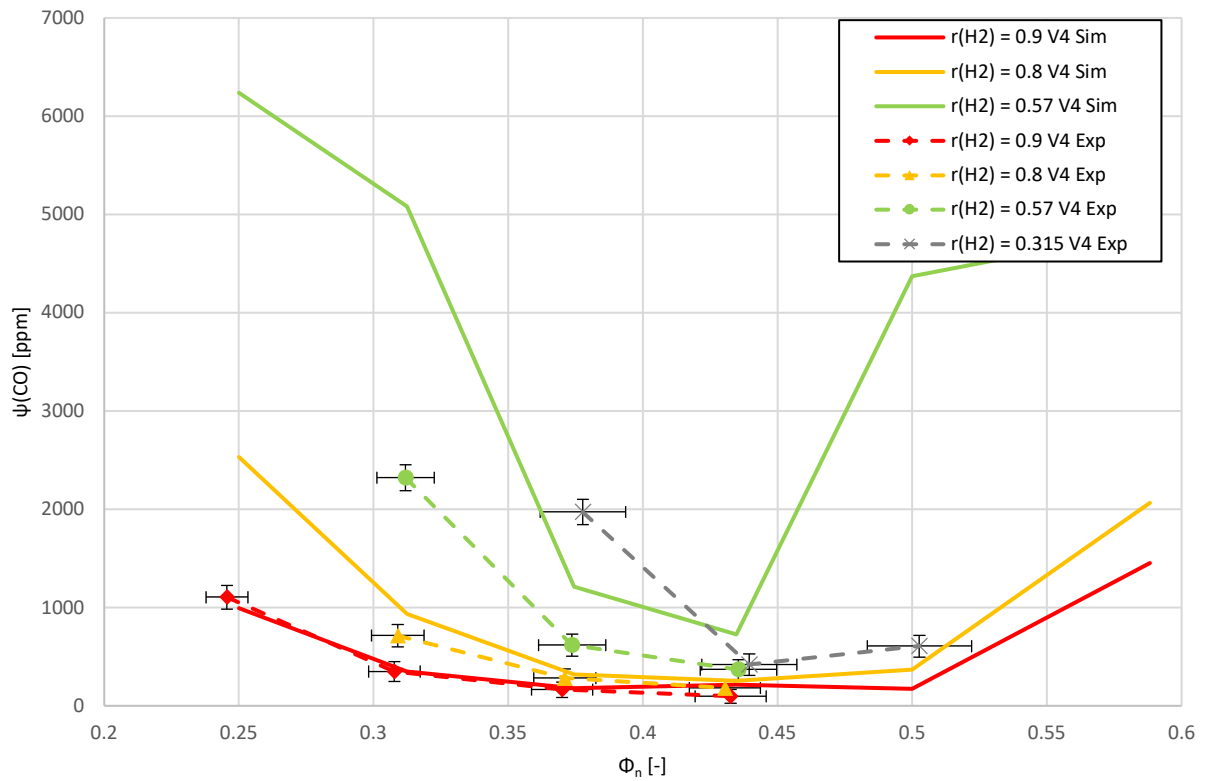


Figure 8-11: Experimental and simulation results of mole fraction CO for V4

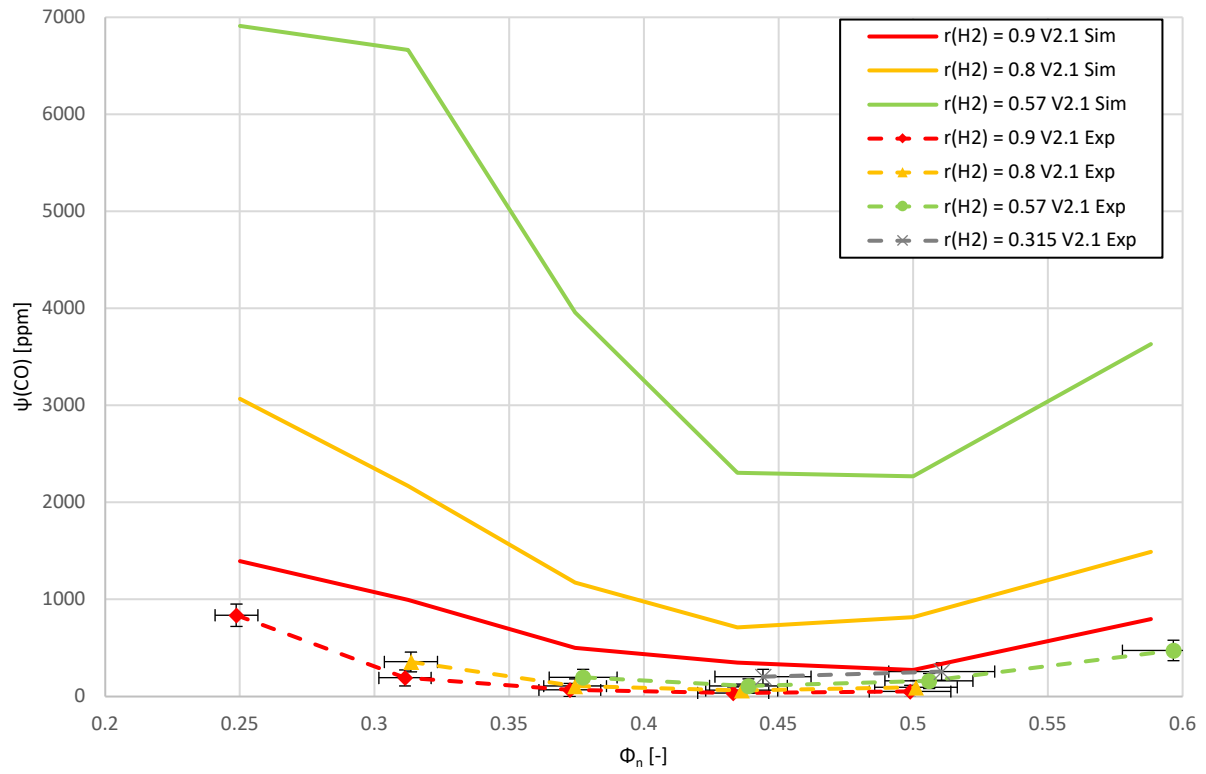


Figure 8-12: Experimental and simulation results of mole fraction CO for V2.1

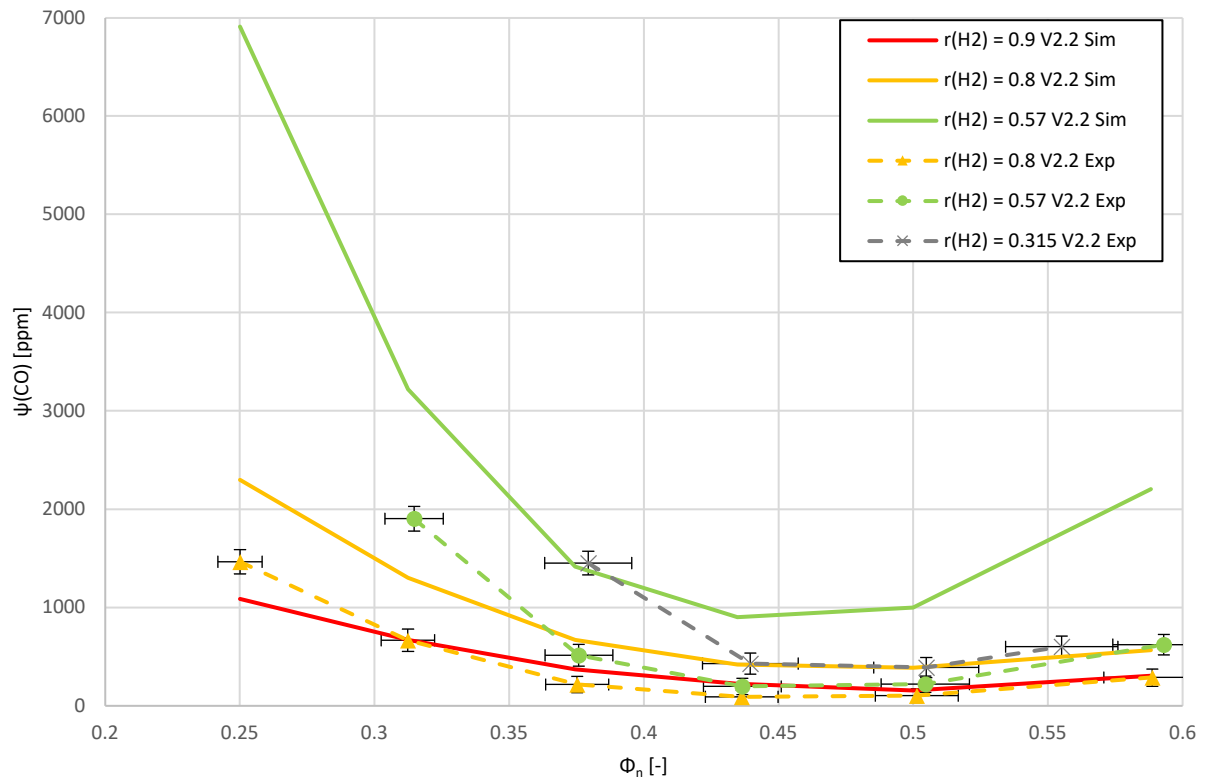


Figure 8-13: Experimental and simulation results of mole fraction CO for V2.2

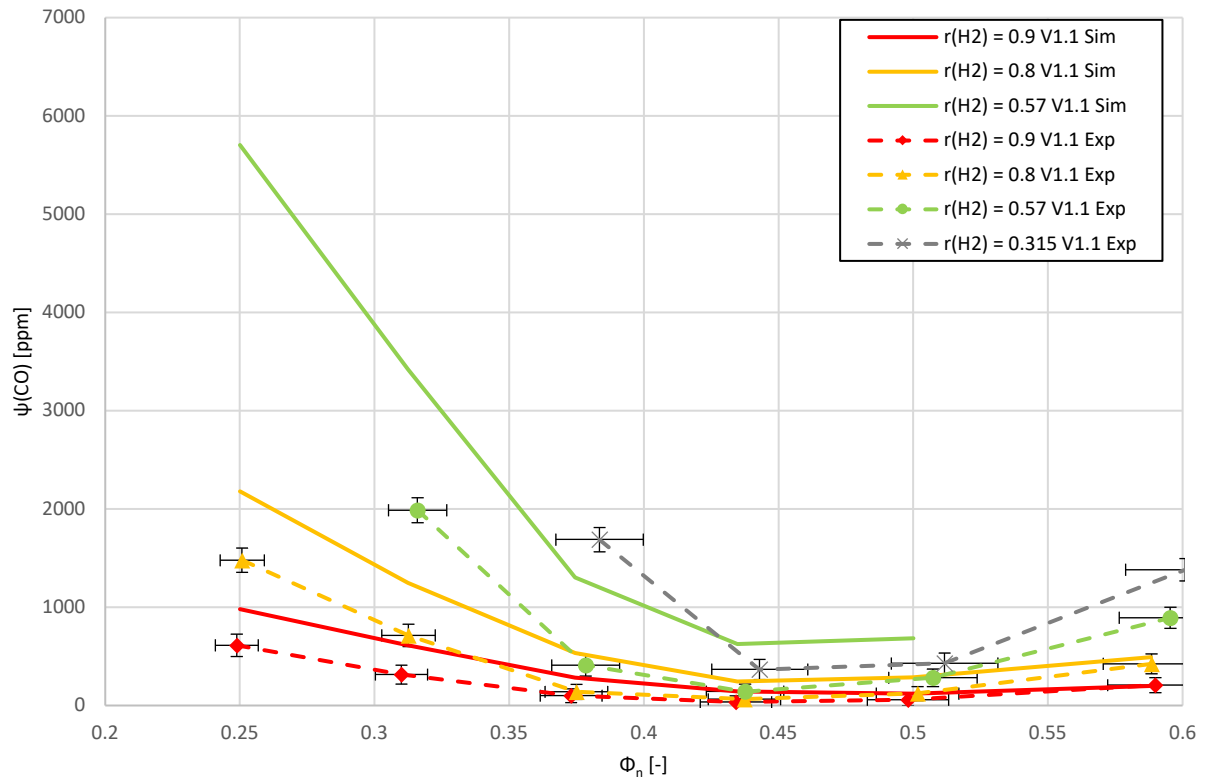


Figure 8-14: Experimental and simulation results of mole fraction CO for V1.1

8.3 Supplemental Diagrams: CH₄ Emissions

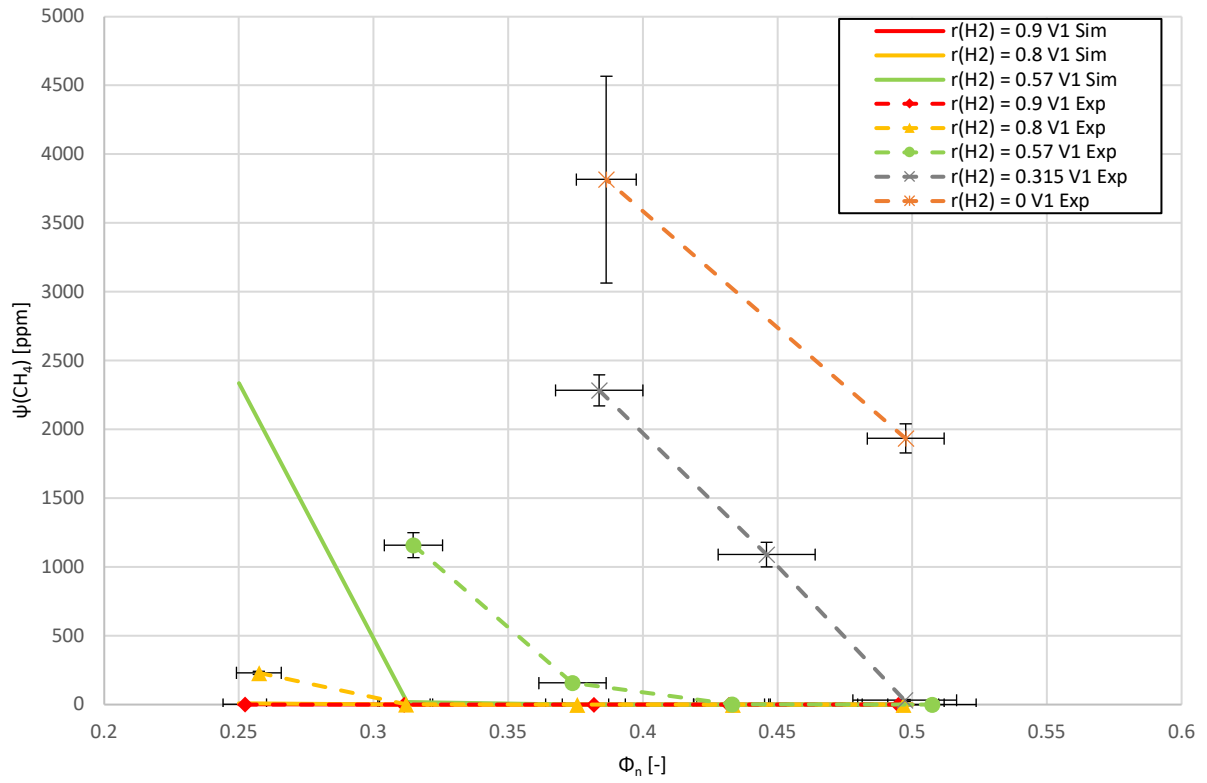


Figure 8-15: Experimental and simulation results of mole fraction CH₄ for V1

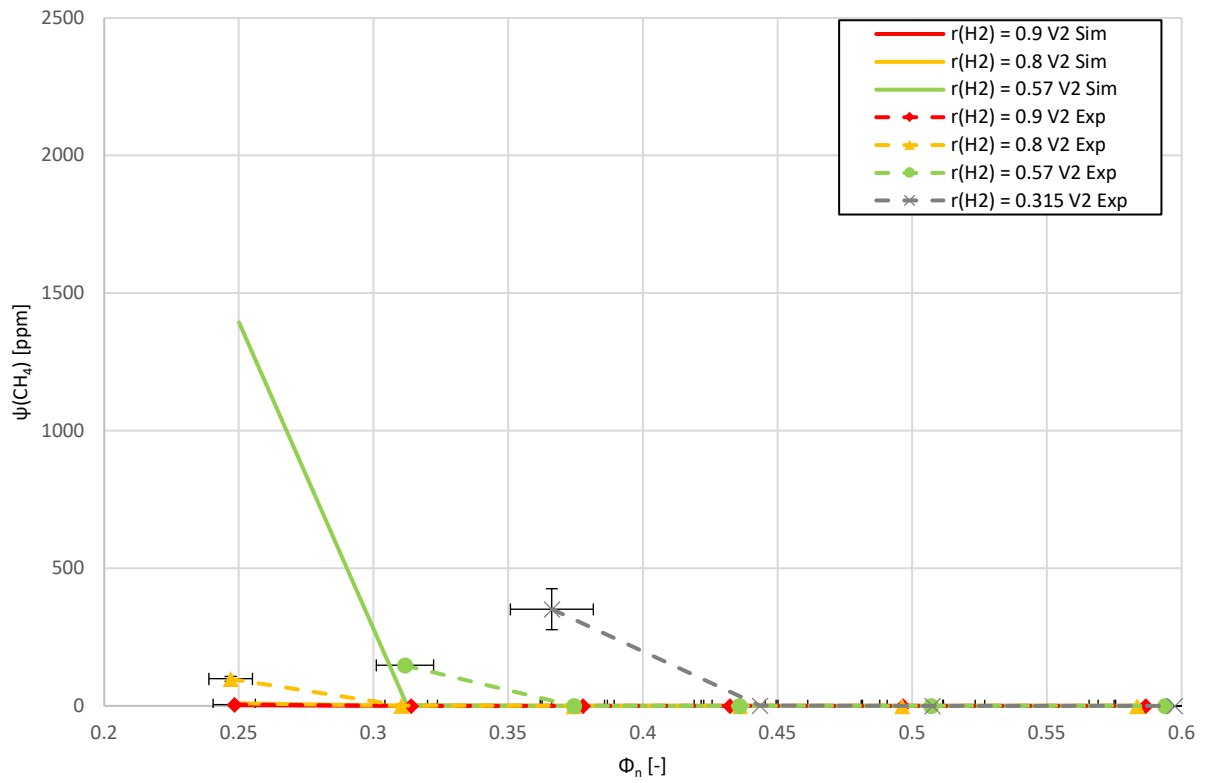


Figure 8-16: Experimental and simulation results of mole fraction CH₄ for V2

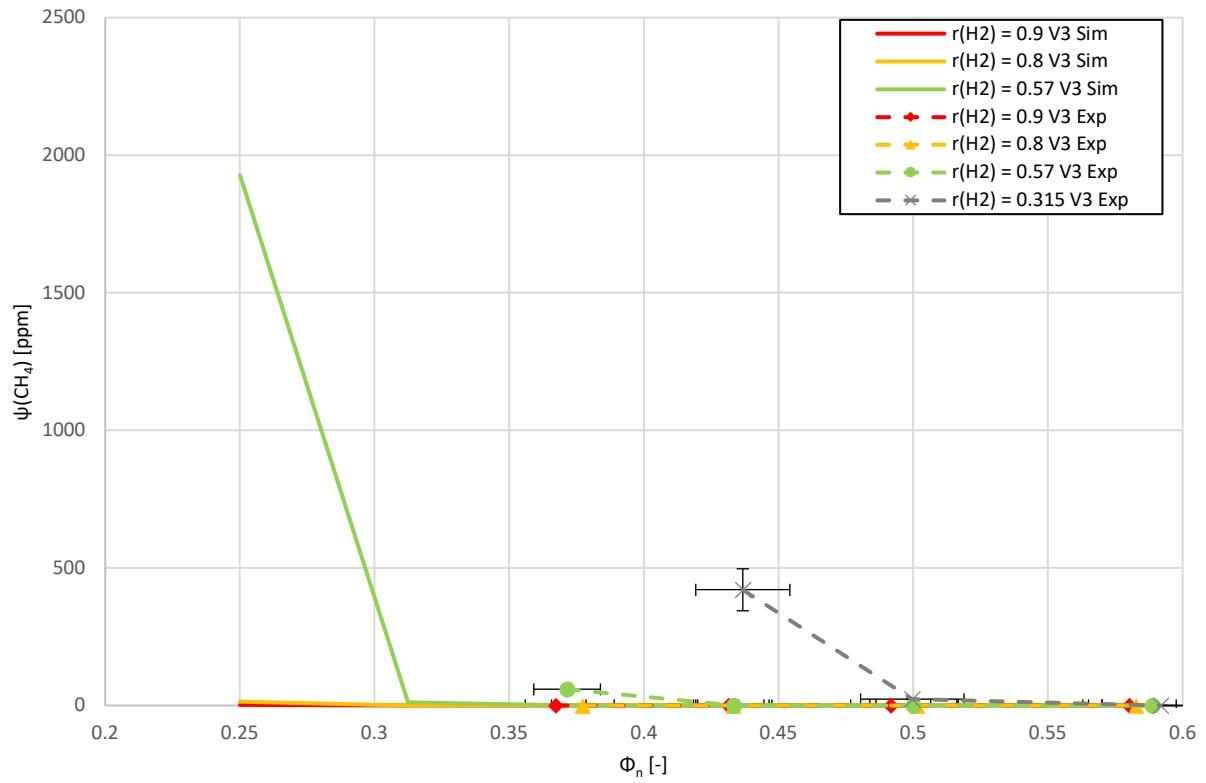


Figure 8-17: Experimental and simulation results of mole fraction CH₄ for V3

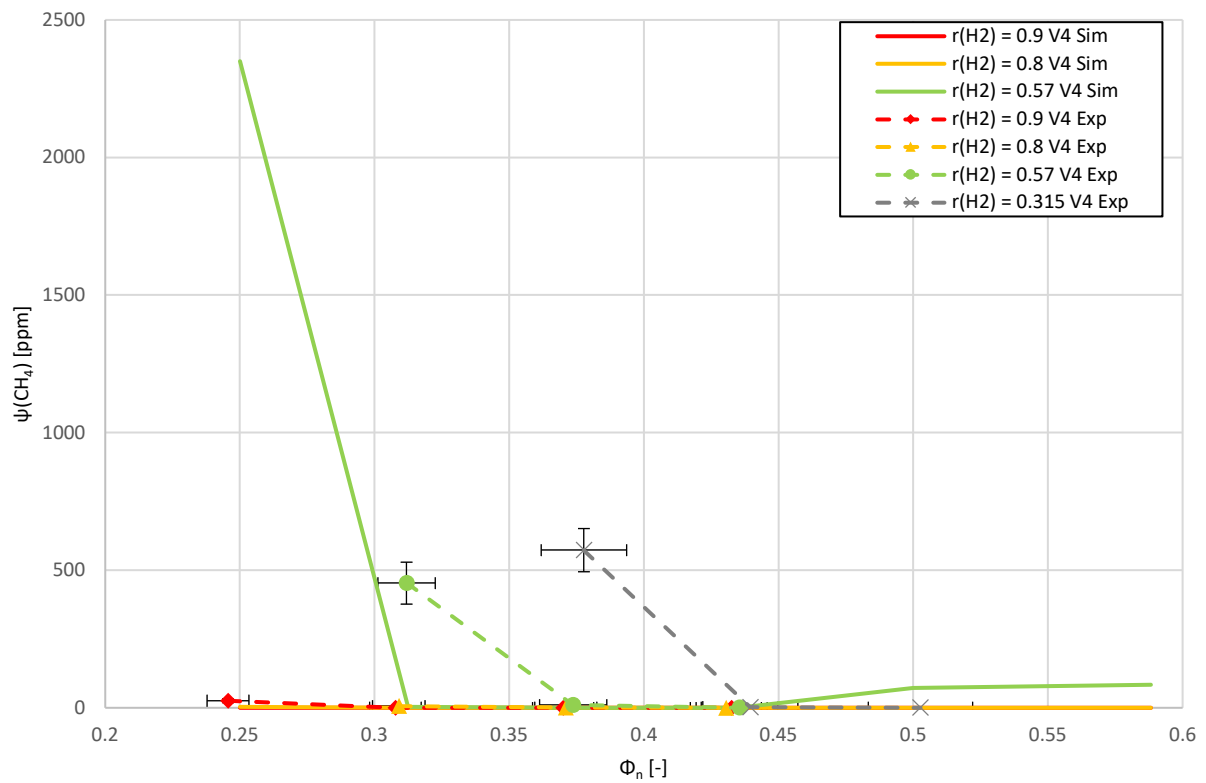


Figure 8-18: Experimental and simulation results of mole fraction CH₄ for V4

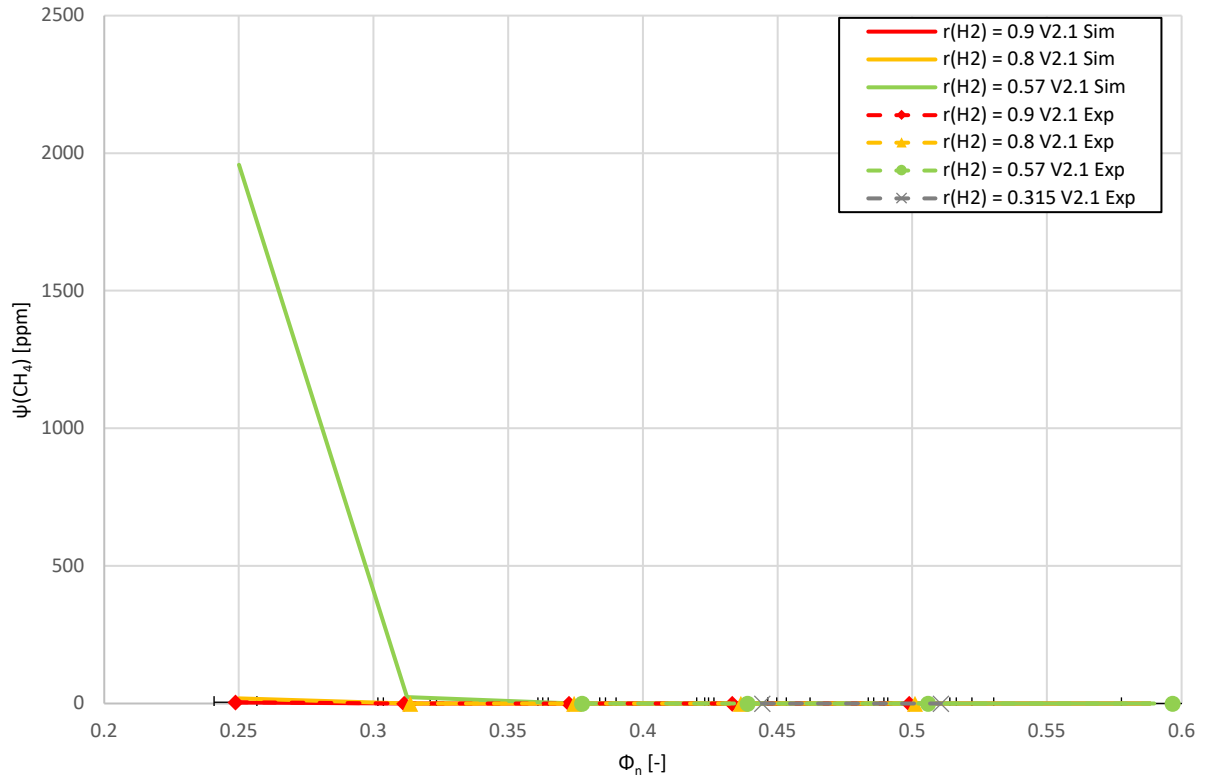


Figure 8-19: Experimental and simulation results of mole fraction CH₄ for V2.1

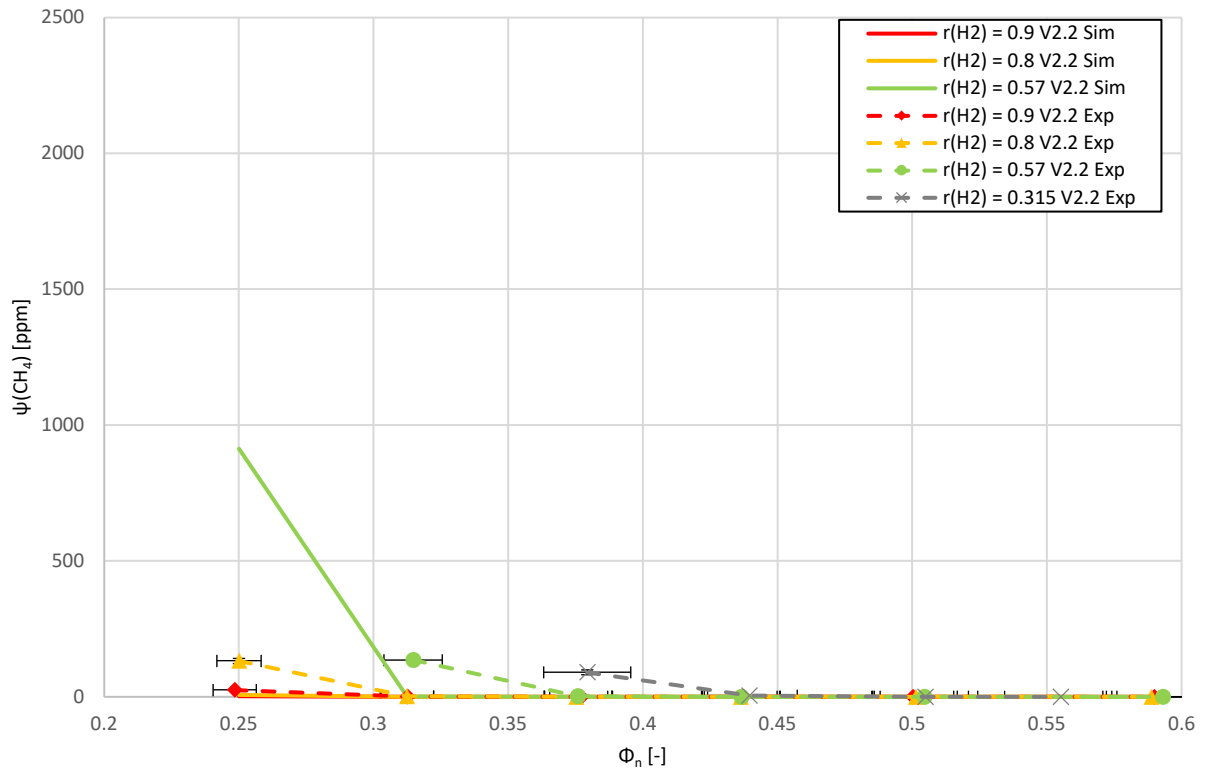


Figure 8-20: Experimental and simulation results of mole fraction CH₄ for V2.2

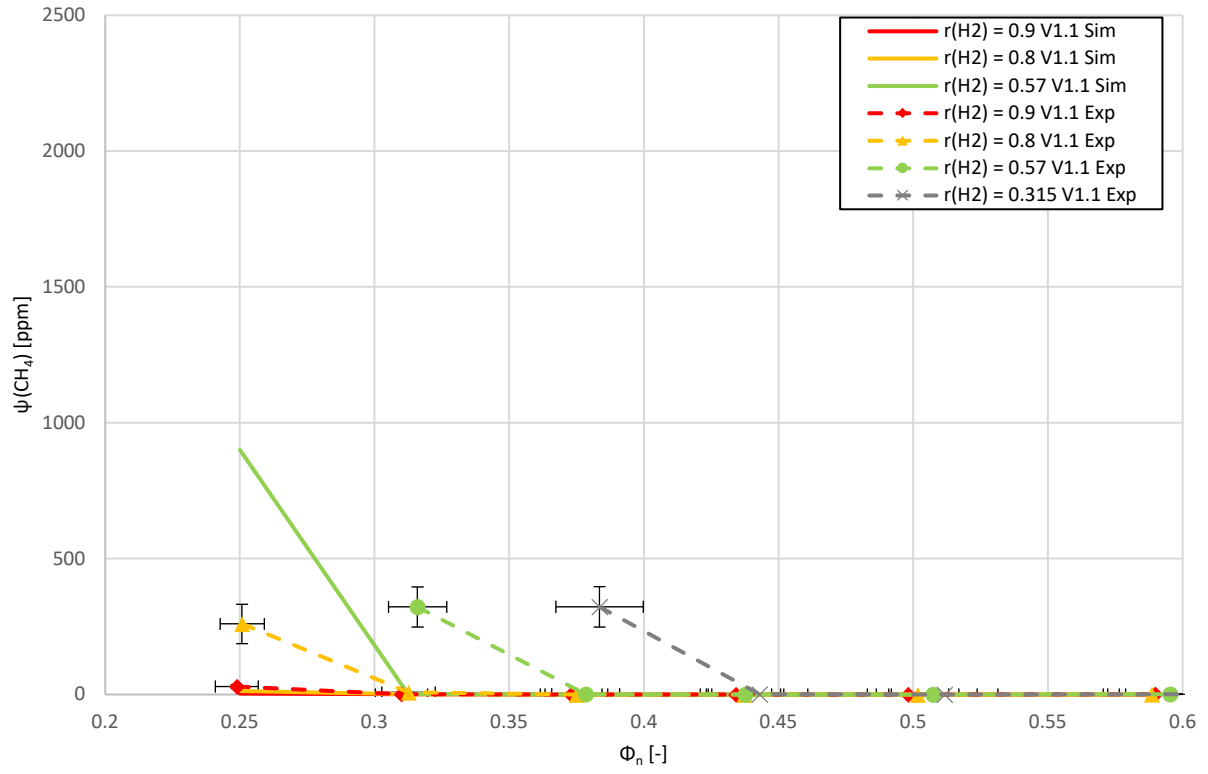


Figure 8-21: Experimental and simulation results of mole fraction CH₄ for V1.1

8.4 Supplemental Diagrams: H₂ Emissions

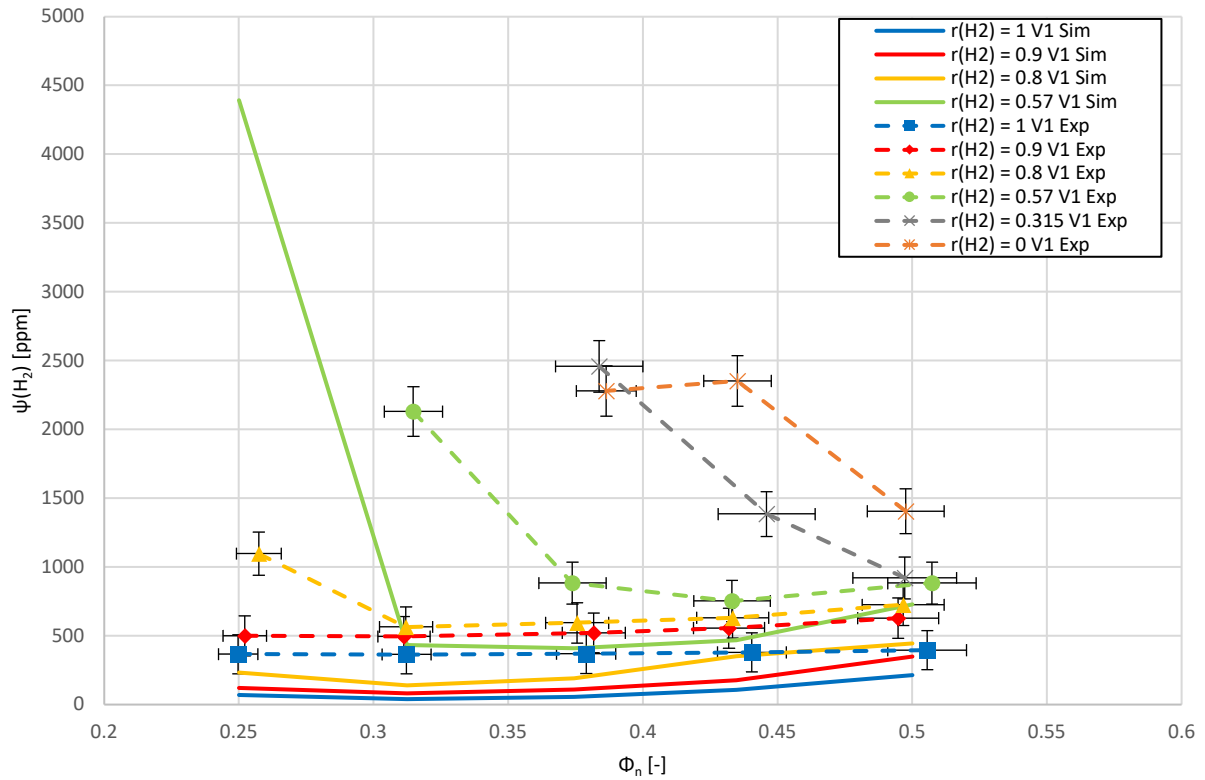


Figure 8-22: Experimental and simulation results of mole fraction H₂ for V1

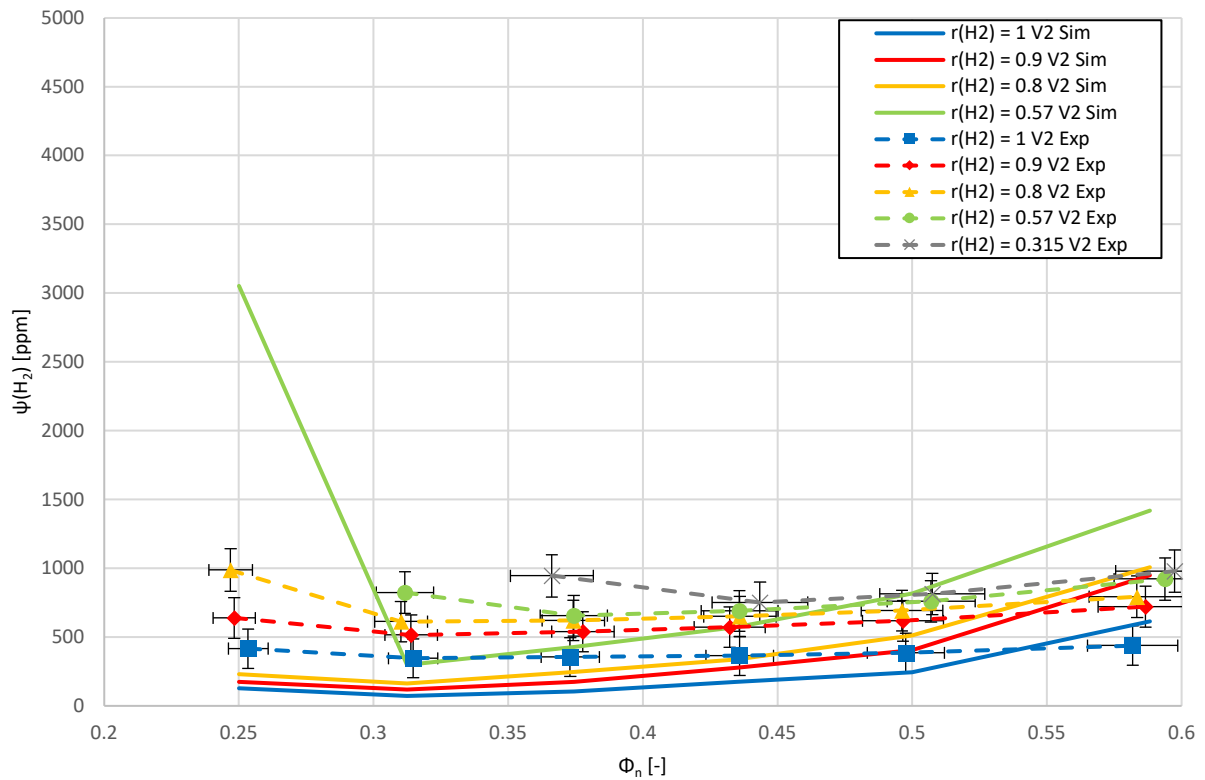


Figure 8-23: Experimental and simulation results of mole fraction H₂ for V2

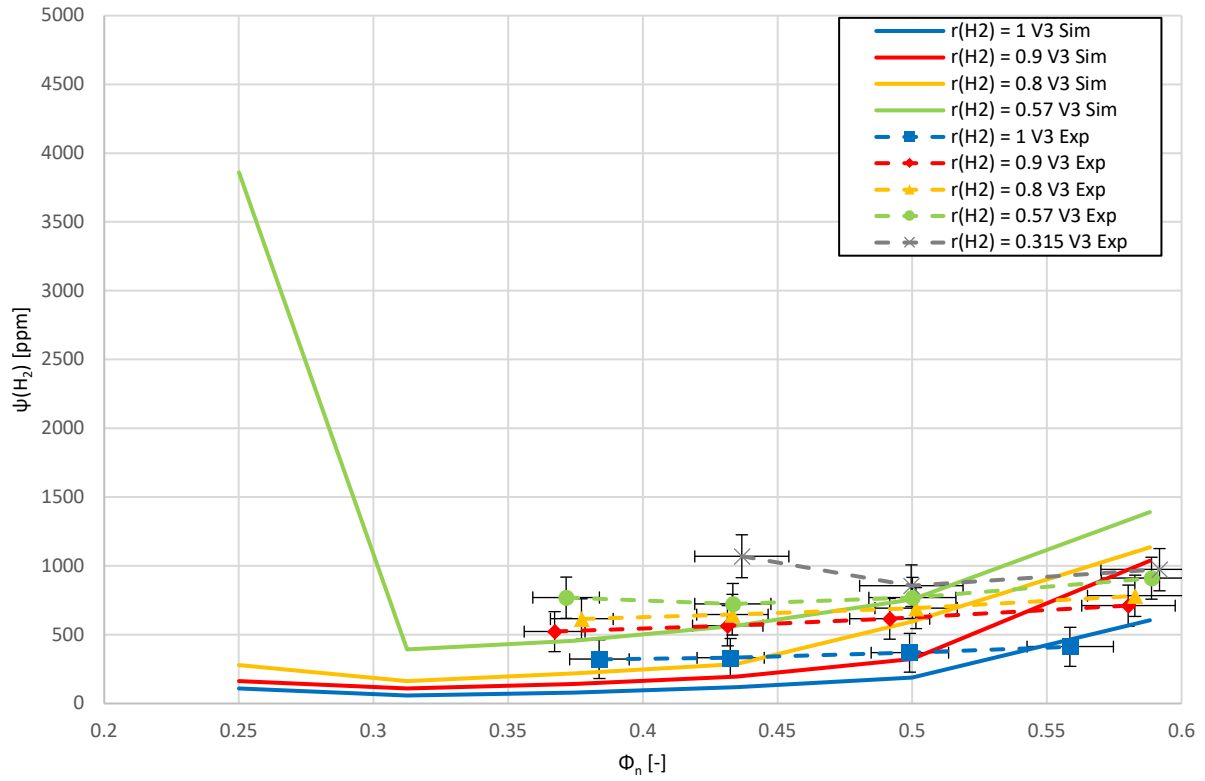


Figure 8-24: Experimental and simulation results of mole fraction H₂ for V3

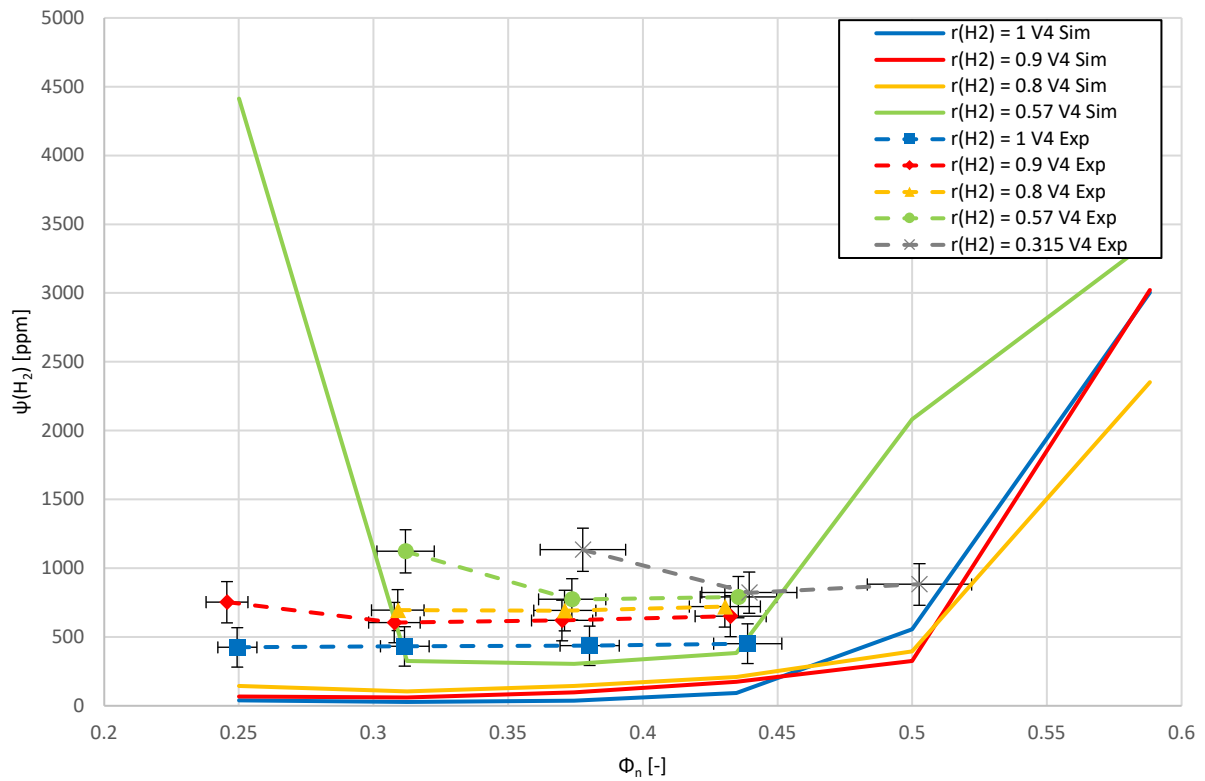


Figure 8-25: Experimental and simulation results of mole fraction H₂ for V4

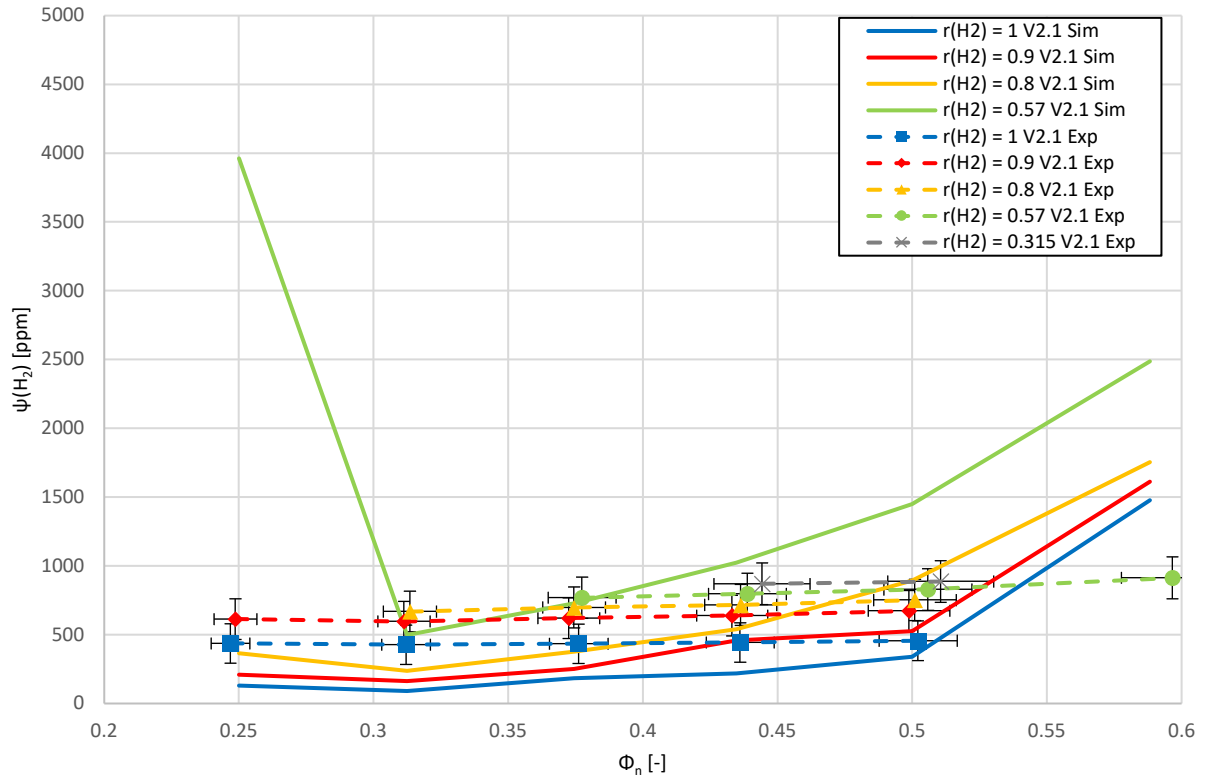


Figure 8-26: Experimental and simulation results of mole fraction H₂ for V2.1

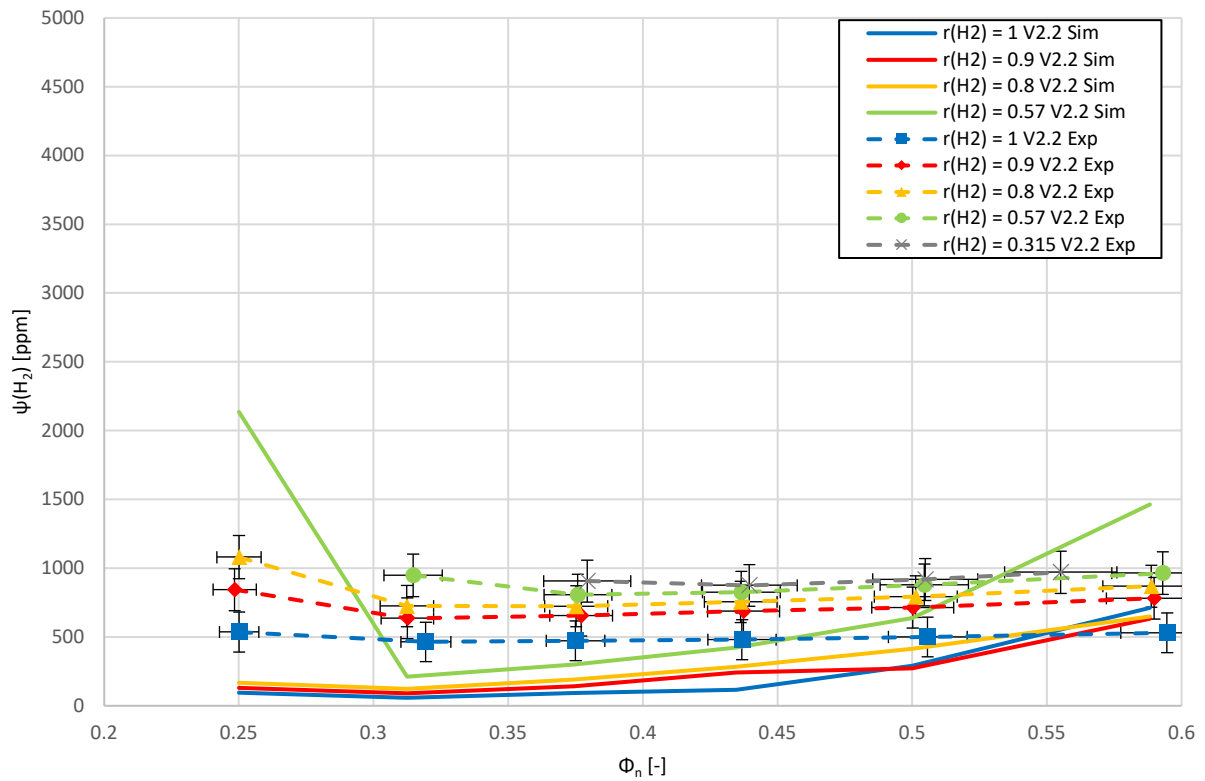


Figure 8-27: Experimental and simulation results of mole fraction H₂ for V2.2

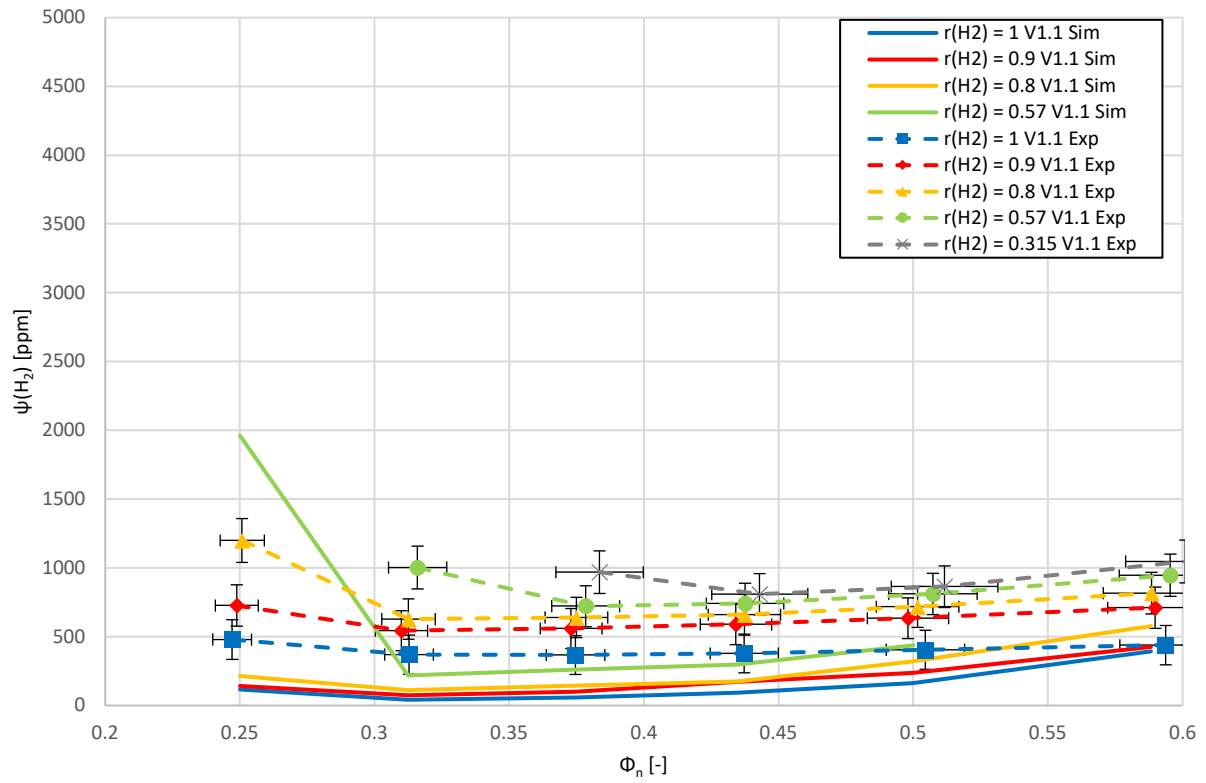


Figure 8-28: Experimental and simulation results of mole fraction H₂ for V1.1

8.5 Supplemental Diagrams: Combustion Efficiency

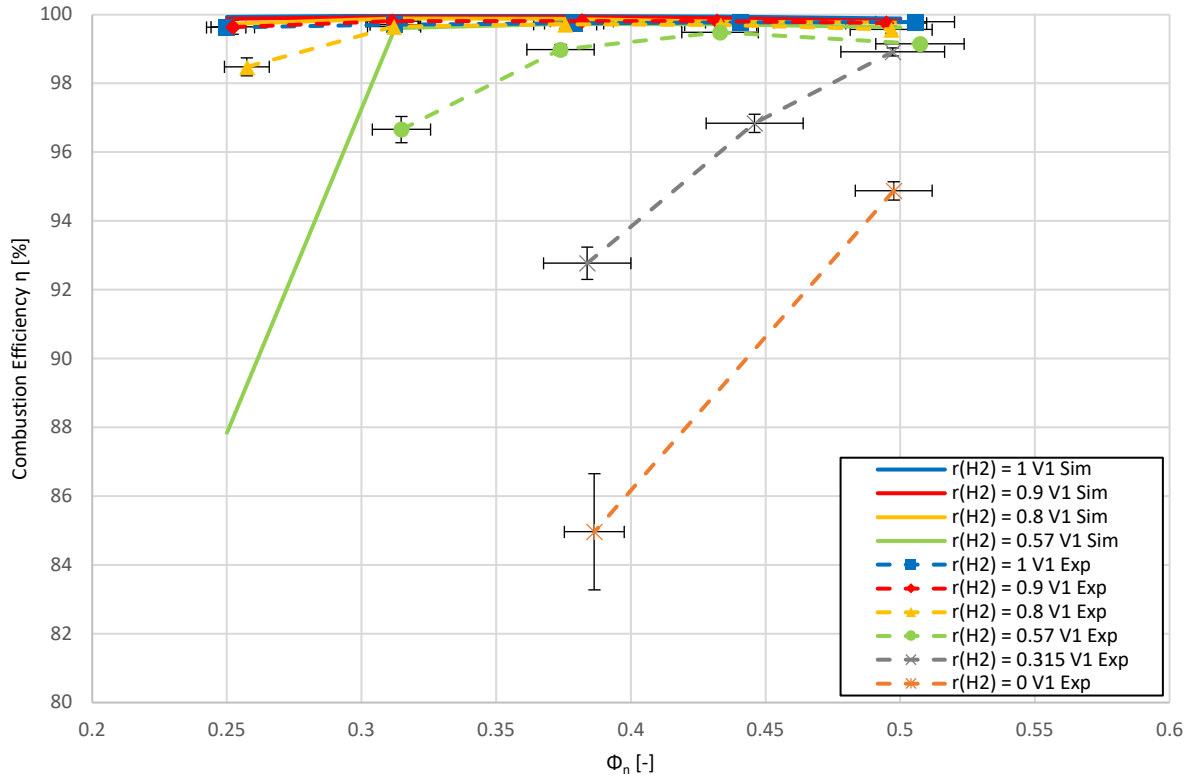


Figure 8-29: Experimental and simulation results of combustion efficiency η for V1

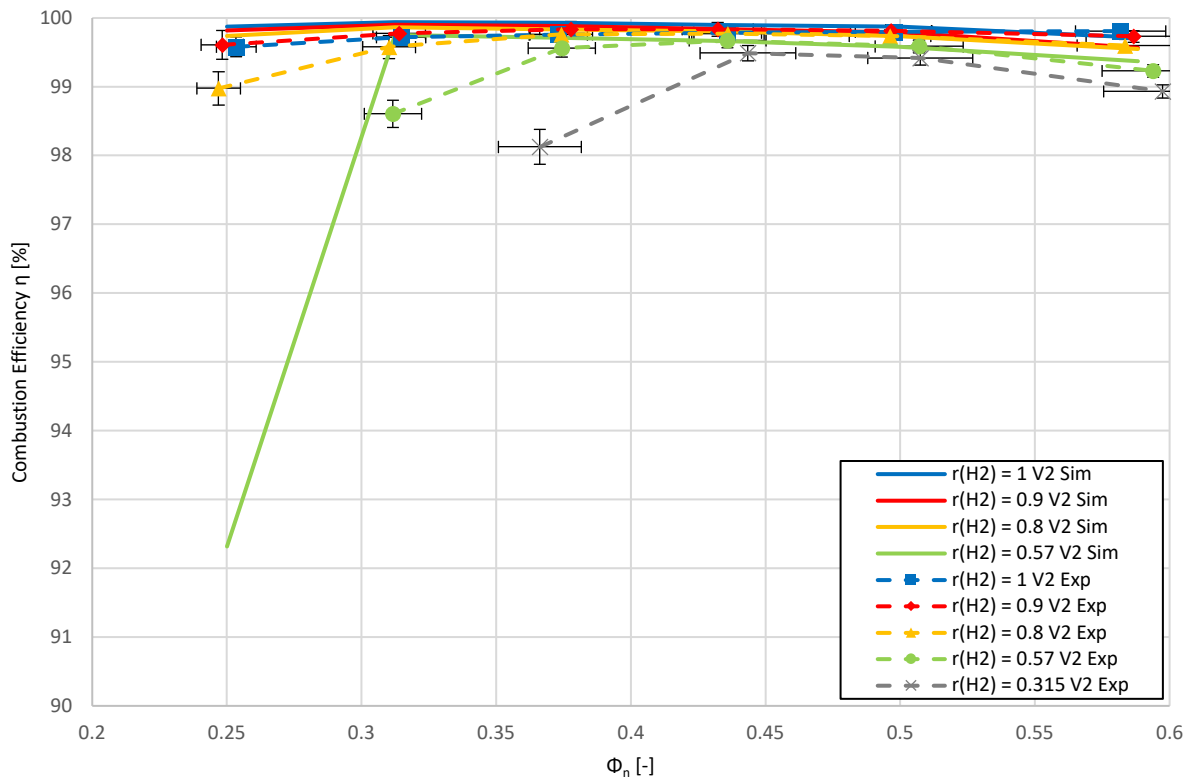


Figure 8-30: Experimental and simulation results of combustion efficiency η for V2

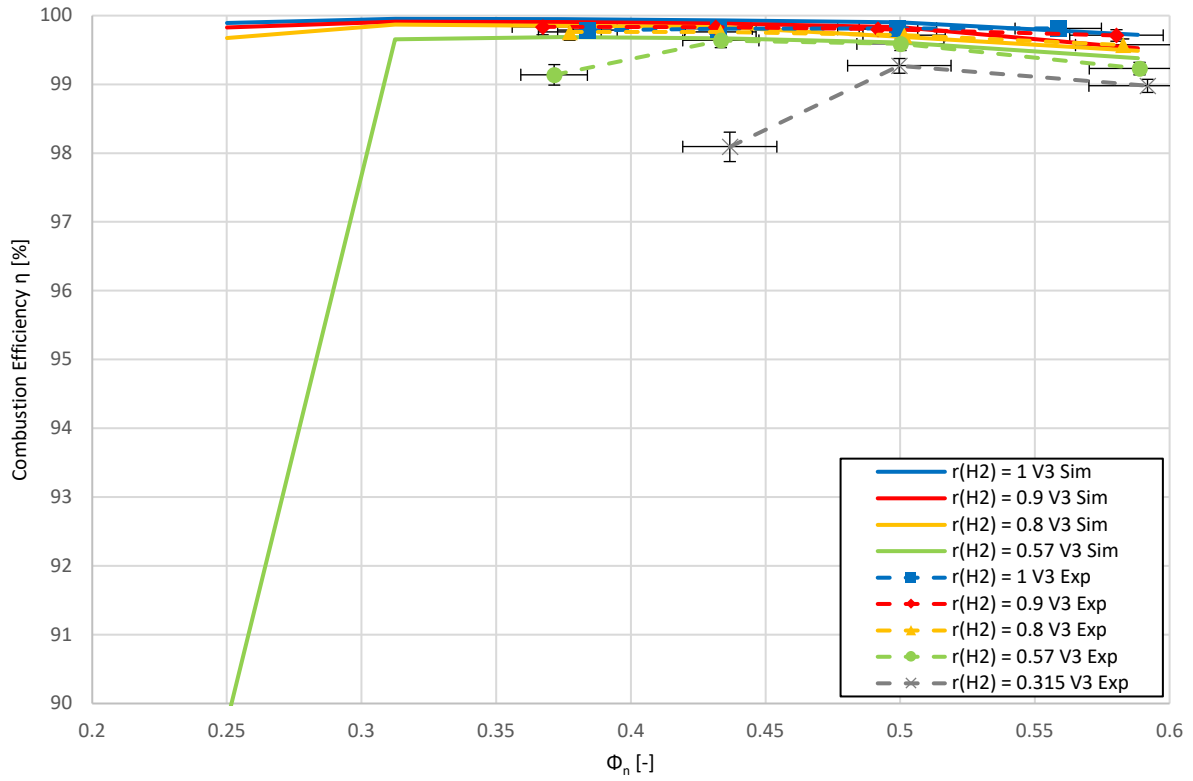


Figure 8-31: Experimental and simulation results of combustion efficiency η for V3

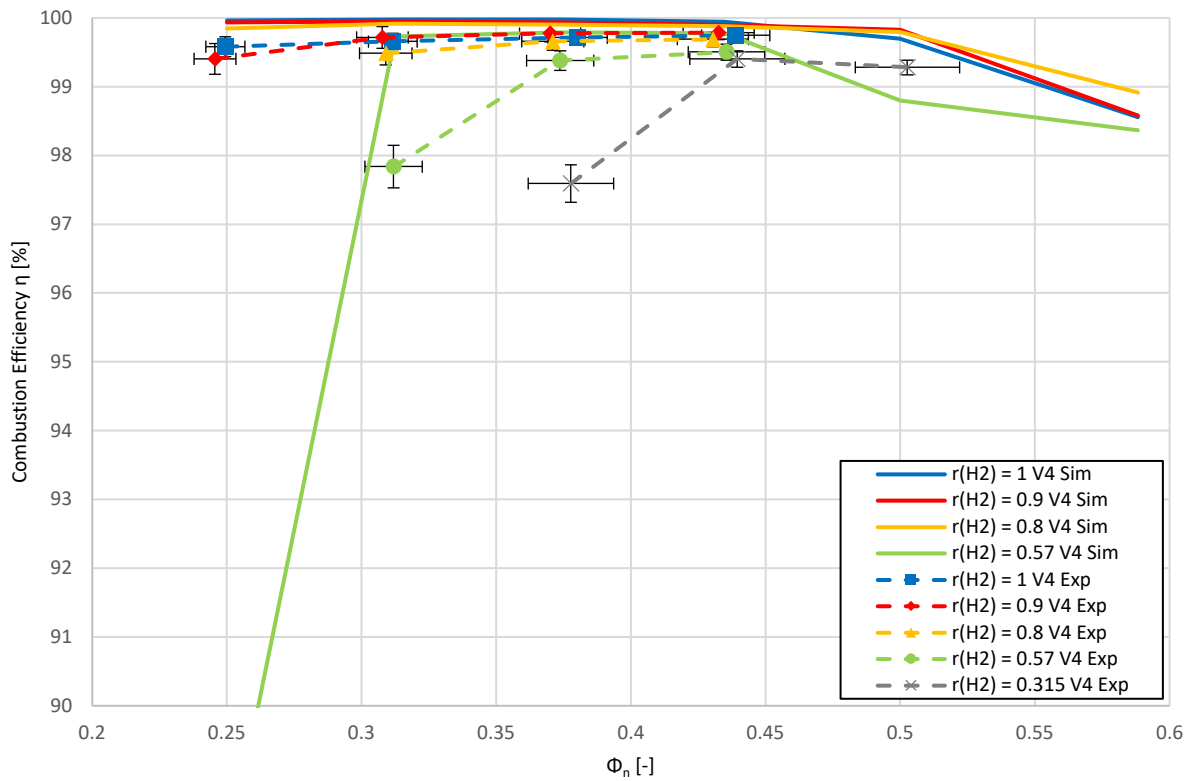


Figure 8-32: Experimental and simulation results of combustion efficiency η for V4

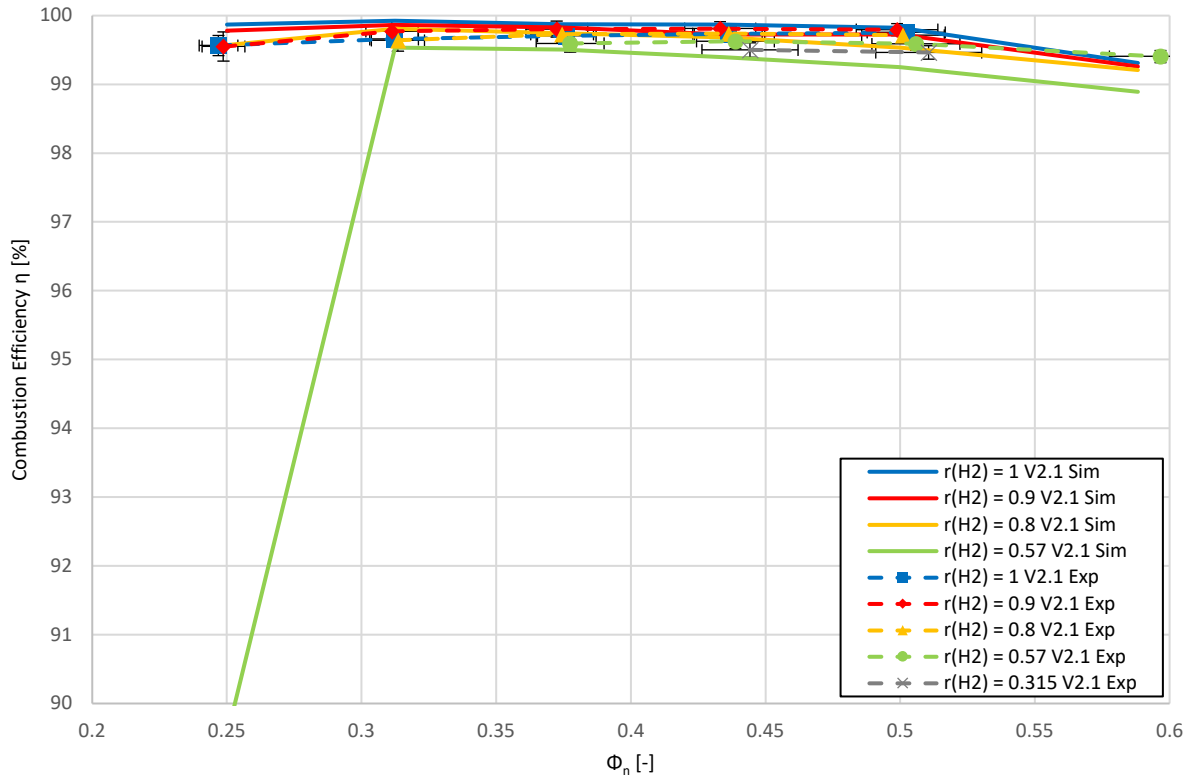


Figure 8-33: Experimental and simulation results of combustion efficiency η for V2.1

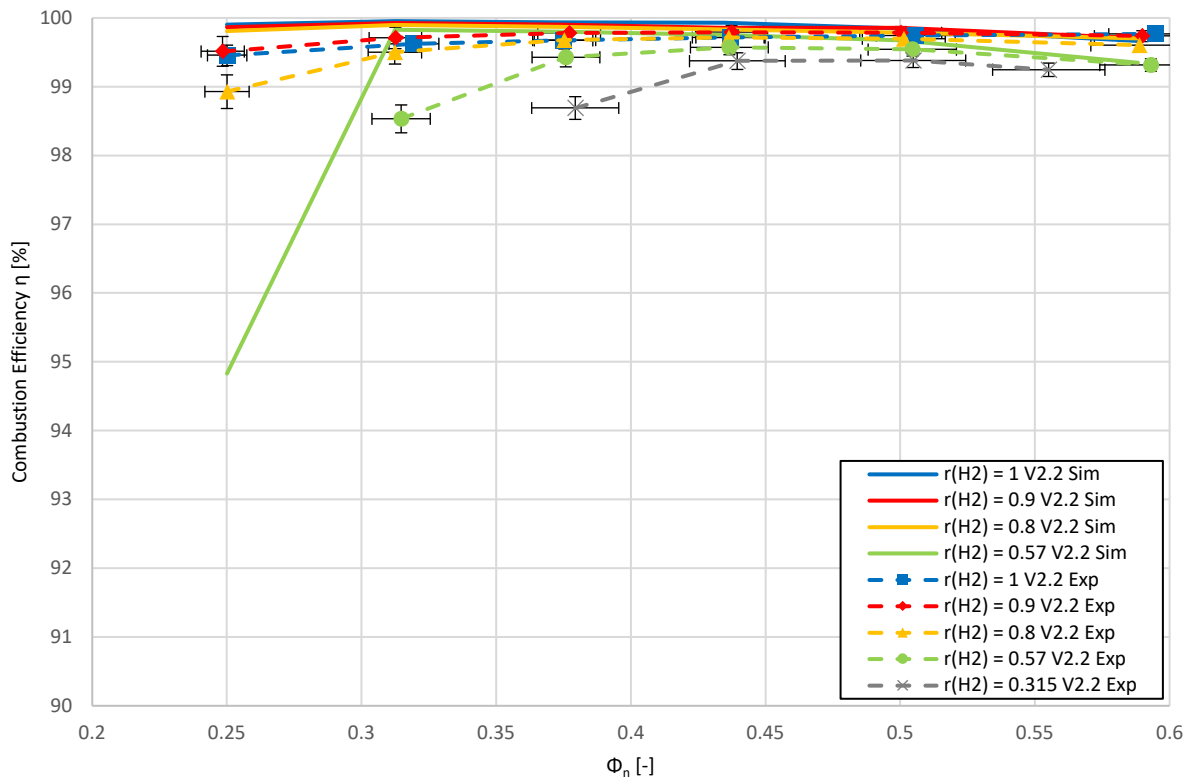


Figure 8-34: Experimental and simulation results of combustion efficiency η for V2.2

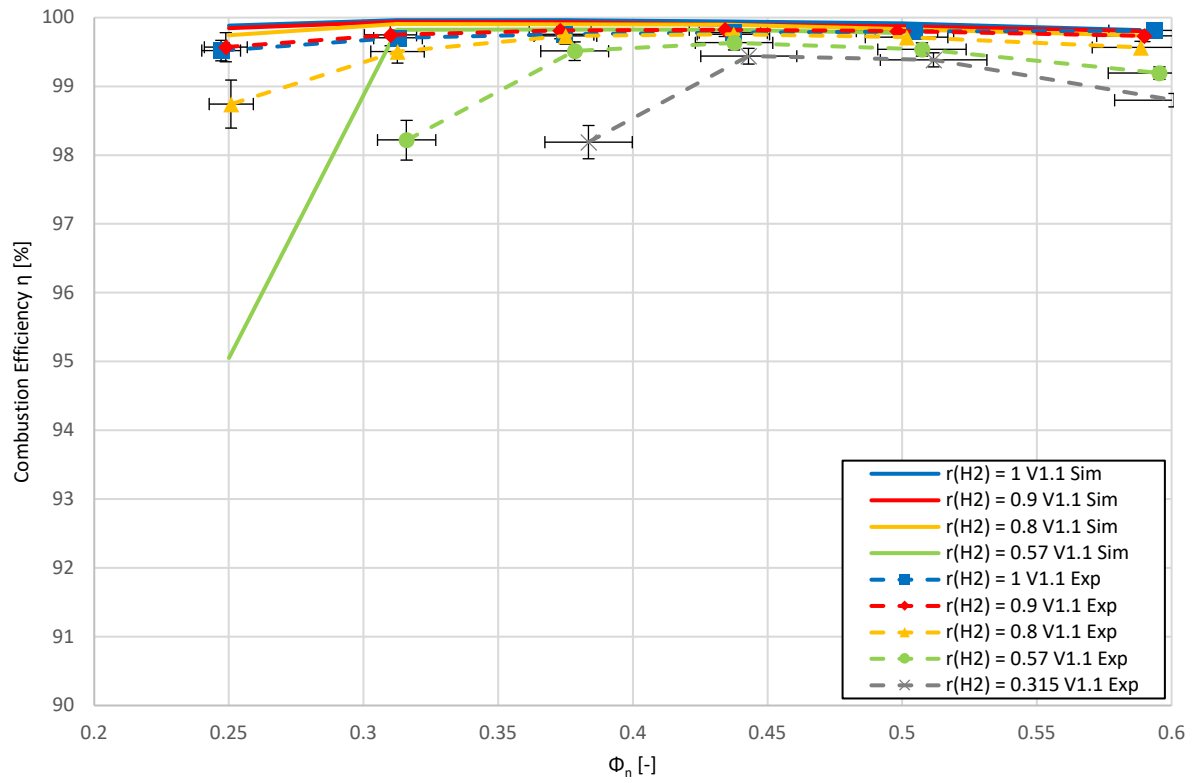


Figure 8-35: Experimental and simulation results of combustion efficiency η for V1.1

8.6 Flame Images

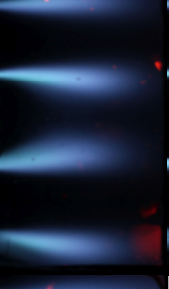
Φ_n r_{H2}	0.588	0.5	0.435	Design Point 0.375	0.3125	0.25
1.0						
0.9						
0.8						
0.57						Flame Blow Out
0.315					Flame Blow Out	Flame Blow Out

Figure 8-36: Flame images with variable H₂/CH₄ fuel mixtures for V2

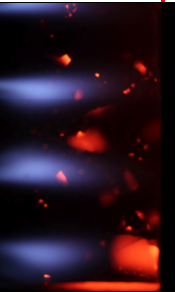
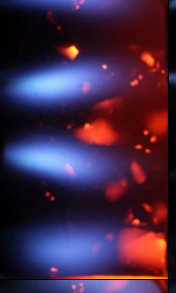
Φ_n r_{H_2}	0.588	0.5	0.435	Design Point 0.375	0.3125	0.25
1.0					Not Tested	Not Tested
0.9					Not Tested	Not Tested
0.8					Not Tested	Not Tested
0.57					Not Tested	Not Tested
0.315				Flame Blow Out	Not Tested	Not Tested

Figure 8-37: Flame images with variable H₂/CH₄ fuel mixtures for V3

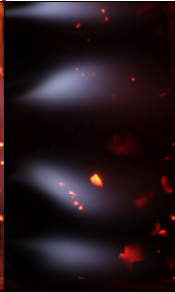
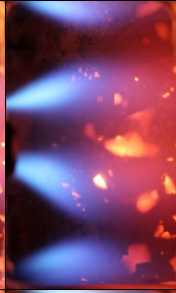
Φ_n r_{H2}	0.588	0.5	0.435	Design Point 0.375	0.3125	0.25
1.0	Not Tested	Not Tested				
0.9	Not Tested	Not Tested				
0.8	Not Tested	Not Tested				Flame Blow Out
0.57	Not Tested	Not Tested				Flame Blow Out
0.315	Not Tested				Flame Blow Out	Flame Blow Out

Figure 8-38: Flame images with variable H₂/CH₄ fuel mixtures for V4

		Design Point					
Φ_n r_{H2}		0.588	0.5	0.435	0.375	0.3125	0.25
1.0	Not Tested						
0.9	Not Tested						
0.8	Not Tested						Flame Blow Out
0.57						Flame Blow Out	Flame Blow Out
0.315	Not Tested					Flame Blow Out	Flame Blow Out

Figure 8-39: Flame images with variable H₂/CH₄ fuel mixtures for V2.1

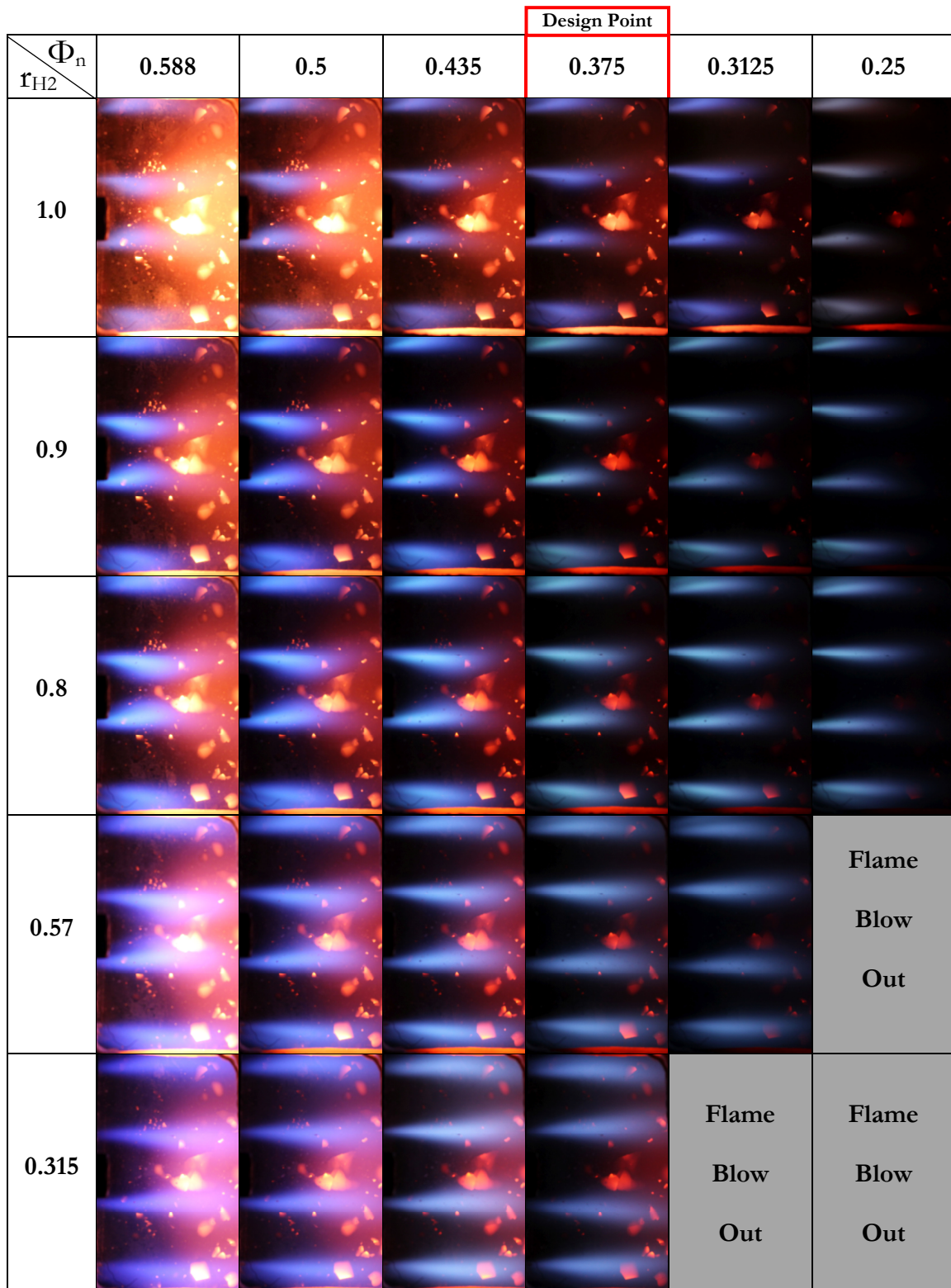


Figure 8-40: Flame images with variable H₂/CH₄ fuel mixtures for V2.2

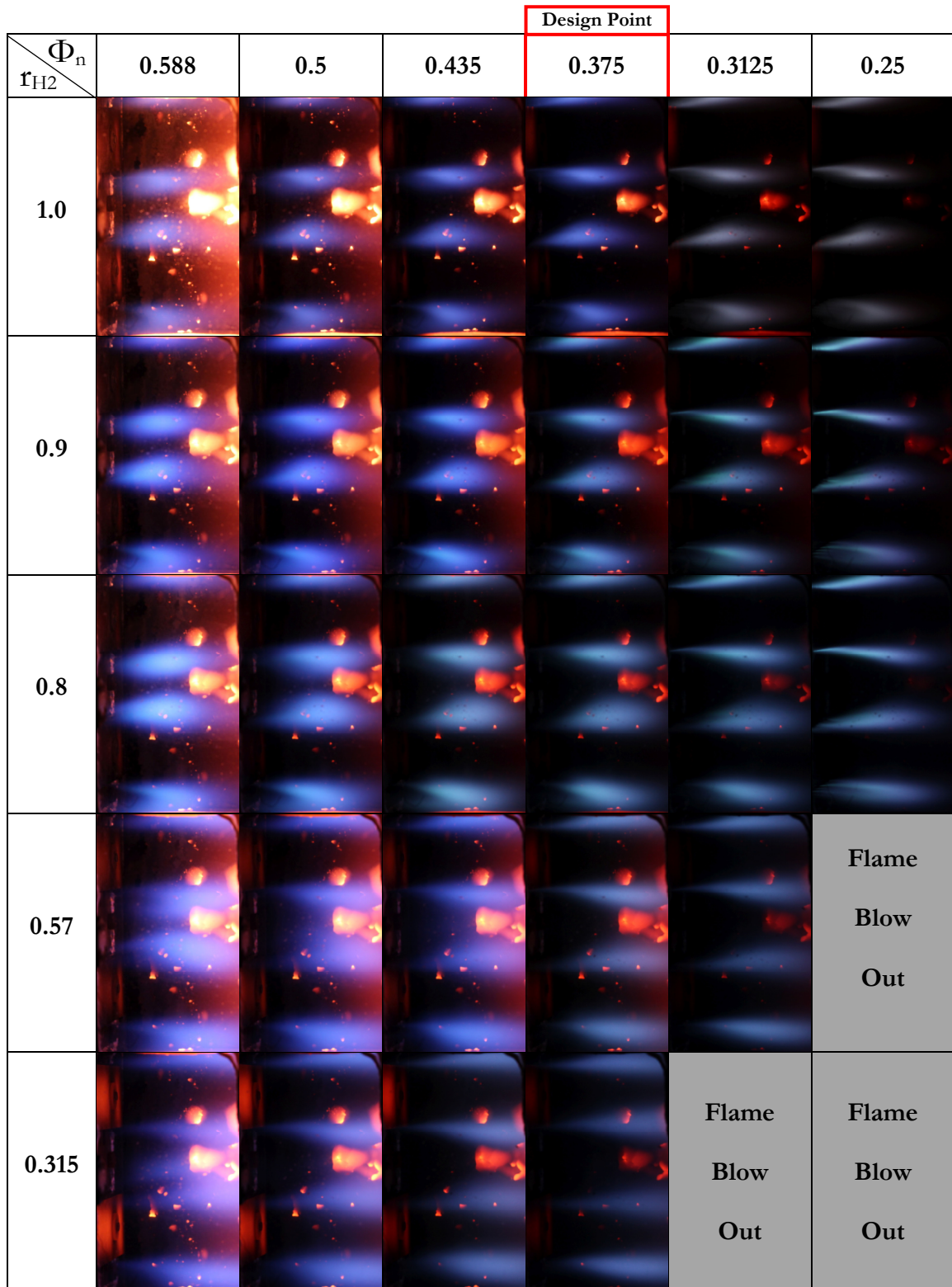


Figure 8-41: Flame images with variable H₂/CH₄ fuel mixtures for V1.1